THE UNIVERSITY OF QUEENSLAND
AUSTRALIA

Micro-resonator Optomechanics with Superfluid Helium

Xin He

B. Eng.

A thesis submitted for the degree of Doctor of Philosophy at
The University of Queensland in 2019
School of Mathematics and Physics,
ARC Centre of Excellence for Engineered Quantum Systems (EQuS)

Abstract

Cavity optomechanics studies the interaction between light and the motion of mechanical oscillators, which can have mass ranging from cold atom clouds to kilogram-scale mirrors. By optimizing the optomechanical interaction and engineering the mechanical oscillators, researchers have generated macroscopic quantum states, and developed techniques for high precision sensing of mass, displacement and electric and magnetic fields. One of the most influential examples of precision optomechanical sensing was the detection of gravitational waves. The technique of cavity optomechanics can also be leveraged to investigate superfluids. Owing to its zero viscosity, low optical absorption and high thermal conductivity, superfluid helium is an excellent candidate for the mechanical oscillator of an optomechanical system. With the rich physics in superfluid helium, the superfluid optomechanical system can be an ideal platform to study the interdisciplinary field between quantum physics and condense matter physics.

The general optomechanical interaction is mediated by the optical forces exerted on the mechanical oscillator, which typically exist in the form of radiation pressure and photothermal effects. In the first experiment reported in this thesis, a silica Whispering Gallery Mode (WGM) resonator is covered in a thin film of superfluid helium. Optical absorption in the WGM microtoroid resonator causes superfluid flow and evaporation, resulting in a recoil force that exceeds the radiation pressure force by one order of magnitude. Using this superfluid-enhanced optical force, we demonstrate feedback cooling of a bulk mechanical mode of the microtoroid with final mode temperature as low as 137 mK and final mechanical occupancy of 2110 ± 40.

In addition to using superfluid to control the motion of bulk modes of a microtoroid, we also explore the native surface acoustic waves (third sound) that reside on the superfluid film condensed on the surface of the WGM resonator. Including the aforementioned advantages of superfluid helium, the small mass and the self-assembling nature of the thin superfluid film enable third sound to be a mechanical oscillator of high quality and large optomechanical coupling. We have theoretically developed a superfluid optomechanical system comprised of third sound waves and a WGM disk resonator, and estimated that the system is capable to achieve an ultra-strong coupling, *i.e.* the single photon optomechanical rate larger than the mechanical frequency. Further, we theoretically and experimentally demonstrate that quantized vortices in the thin superfluid film can interact with the third sound waves and lift the degeneracy of third sound modes. With the optical field and vortices bridged by third sound, the vortex dynamics can be probed using this superfluid optomechanical system. Experimentally, by monitoring the third sound frequency splitting we interrogate the coherent evolution of an ensemble of 17 vortices on the superfluid optomechanical resonator. The investigation of the coherent vortex dynamics in a nanometer-scale thin superfluid confined at microscale allows us to study the fascinating physics in strongly-interacting superfluids, and build practical applications like high-precision inertial sensors.

Finally a major work in this thesis is to study the Brillouin interaction between phase-matched travelling light and sound. The conventional Brillouin interaction is limited by the large Young's modulus of solid materials, which constrains the electrostrictive compression of the material in response to light. The large mechanical compliance of the thin superfluid film affords us a strong Brillouin interaction between the travelling light and third sound confined on a superfluid optomechanical disk resonator. Enabled by the strong Brillouin interaction a superfluid Brillouin laser is experimentally demonstrated to have the lowest so-far-recorded lasing threshold power of 1.8 μW, with harmonics of the Brillouin scattering observed up to the 6th order at 5.6 μW. Furthermore, the combination of a strong Brillouin interaction and large Brillouin lasing amplitude allows the strength of the Brillouin-induced coupling between counter-propagating optical waves to exceed the optical damping rate for the first time. This strong optical coupling has potential applications for all-optical reconfigurable optomechanical circuits and the generation of microwave frequency synthesis.

Declaration by author

This thesis is composed of my original work, and contains no material previously published or written by another person except where due reference has been made in the text. I have clearly stated the contribution by others to jointly-authored works that I have included in my thesis.

I have clearly stated the contribution of others to my thesis as a whole, including statistical assistance, survey design, data analysis, significant technical procedures, professional editorial advice, financial support and any other original research work used or reported in my thesis. The content of my thesis is the result of work I have carried out since the commencement of my higher degree by research candidature and does not include a substantial part of work that has been submitted to qualify for the award of any other degree or diploma in any university or other tertiary institution. I have clearly stated which parts of my thesis, if any, have been submitted to qualify for another award.

I acknowledge that an electronic copy of my thesis must be lodged with the University Library and, subject to the policy and procedures of The University of Queensland, the thesis be made available for research and study in accordance with the Copyright Act 1968 unless a period of embargo has been approved by the Dean of the Graduate School.

I acknowledge that copyright of all material contained in my thesis resides with the copyright holder(s) of that material. Where appropriate I have obtained copyright permission from the copyright holder to reproduce material in this thesis and have sought permission from co-authors for any jointly authored works included in the thesis.

Publications during candidature

Peer-reviewed research papers

1. [1] D. L. McAuslan, G. I. Harris, C. Baker, Y. Sachkou, **X. He**, E. Sheridan, and W. P. Bowen, Microphotonic Forces from Superfluid Flow, *Physical Review X*, 6(2):021012, 2016.
2. [2] C. G. Baker, G. I. Harris, D. L. McAuslan, Y. Sachkou, **X. He** and W. P. Bowen, Theoretical framework for thin film superfluid optomechanics: towards the quantum regime, New Journal of Physics, 18(12):123025, 2016.
3. [3] S. Forstner, Y. Sachkou, M. Woolley, G. I. Harris, **X. He**, W. P. Bowen, C. G. Baker, Modelling of vorticity, sound and their interaction in two-dimensional superfluids, New Journal of Physics, 21(5):053029, 2019.

Submitted manuscripts included in this thesis

1. [4] **X. He**, G. I. Harris, C. G. Baker, A. Sawadsky, Y. P. Sachkou, Y. Sfendla, S. Forstner, W. P. Bowen, Strong optical coupling through superfluid Brillouin lasing, submitted to a journal in July 2019.
2. [5] Y. P. Sachkou, C. G. Baker, G. I. Harris, O. R. Stockdale, S. Forstner, M. T. Reeves, **X. He**, D. L. McAuslan, A. S. Bradley, M. J. Davis, W. P. Bowen, Coherent vortex dynamics in a strongly-interacting superfluid on a silicon chip, submitted to a journal in February 2019.

Preprints

1. [4] **X. He**, G. I. Harris, C. G. Baker, A. Sawadsky, Y. P. Sachkou, Y. Sfendla, S. Forstner, W. P. Bowen, Strong optical coupling through superfluid Brillouin lasing, arXiv 1907.06811, 2019.
2. [5] Y. P. Sachkou, C. G. Baker, G. I. Harris, O. R. Stockdale, S. Forstner, M. T. Reeves, **X. He**, D. L. McAuslan, A. S. Bradley, M. J. Davis, W. P. Bowen, Coherent vortex dynamics in a strongly-interacting superfluid on a silicon chip, arXiv 1902.04409, 2019.

Other publications during candidature

None

Conference abstracts

1. **X. He** *et al.*, Phonon Confinement by the Force of Light. APPC-AIP Joint 14th Asia Pacific Physics Conference and 22nd Australian Institute of Physics Congress, Perth, Australia, 9-13 December, (2018) - talk accompanied by abstract.

2. **X. He** *et al.*, Phonon Confinement by the Force of Light. CLEO Pacific Rim 2018 Conference, Hong Kong, China, 29 July-03 August, (2018) - talk accompanied by abstract.

3. **X. He** *et al.*, Cavity eigen-optomechanics with superfluid. Gordon Research Conference, Mechanical Systems in the Quantum Regime, Ventura, CA, USA, 24 February -2 March, (2018) - poster accompanied by abstract.

4. **X. He** *et al.*, Detecting Superfluid Josephson Oscillations by Cavity Optomechanics. ARC Center of Excellence for Engineered Quantum Systems (EQuS) workshop, Noosa, Australia, 8-10 December, (2016) - poster accompanied by abstract.

5. **X. He** *et al.*, Microphotonic force from the control of superfluid flow. APPC-AIP Joint 13th Asia Pacific Physics Conference and 22nd Australian Institute of Physics Congress, Brisbane, Australia, 4-8 December, (2016) - talk accompanied by abstract.

5\. **X. He** *et al.*, Enhanced Optical Forces From Superfluid Flow. Gordon Research Conference, Mechanical Systems in the Quantum Regime, Ventura, CA, USA, 6-11 March (2016) - poster accompanied by abstract.

7\. **X. He** *et al.*, Enhanced Optical Forces From Superfluid Flow. Engineering Quantum Systems annual Workshop, Gold Coast, Australia, 9-11 December, (2015) - poster accompanied by abstract.

8\. **X. He** *et al.*, Enhanced Optical Forces From Superfluid Flow. the International Optical Society of America Network of Students (IONS) conference KOALA (Conference on Optics, Atoms and Laser Applications), Auckland, New Zealand, 22-27 November, (2015) - talk accompanied by abstract.

Publications included in this thesis

1. [1] D. L. McAuslan, G. I. Harris, C. Baker, Y. Sachkou, **X. He**, E. Sheridan, and W. P. Bowen, Microphotonic Forces from Superfluid Flow, *Physical Review X*, 6(2):021012, 2016.

   A major part of this paper is incorporated as Chapter 4. The break-downs of the published paper are shown below. Chapter 4 is was prepared by X. He by compiling the relevant data, modifying the figures and re-writing 80% of the text.

Contributor	Statement of contribution	%
D. L. McAuslan	Conception and design	20
	Analysis and interpretation	20
	Drafting and production	20
G. I. Harris	Conception and design	20
	Analysis and interpretation	20
	Drafting and production	20
C. Baker	Conception and design	15
	Analysis and interpretation	25
	Drafting and production	20
Y. Sachkou	Conception and design	10
	Analysis and interpretation	10
	Drafting and production	10
X. He	Conception and design	15
	Analysis and interpretation	10
	Drafting and production	10
E. Sheridan	Conception and design	5
	Analysis and interpretation	0
	Drafting and production	0
W. P. Bowen	Conception and design	15
	Analysis and interpretation	15
	Drafting and production	20

2. [2] C. G. Baker, G. I. Harris, D. L. McAuslan, Y. Sachkou, **X. He** and W. P. Bowen, Theoretical framework for thin film superfluid optomechanics: towards the quantum regime, New Journal of Physics, 18(12):123025, 2016.
   A major part of this paper is incorporated as Chapter 5. The break-downs of the published paper are shown below. Chapter 5 was prepared by X. He by modifying the figures and re-writing 90% of the text.

Contributor	Statement of contribution	%
C. G. Baker	Conception and design	40
	Analysis and interpretation	45
	Drafting and production	45
G. I. Harris	Conception and design	10
	Analysis and interpretation	10
	Drafting and production	10
D. L. McAuslan	Conception and design	10
	Analysis and interpretation	0
	Drafting and production	0
Y. Sachkou	Conception and design	10
	Analysis and interpretation	10
	Drafting and production	10
X. He	Conception and design	10
	Analysis and interpretation	15
	Drafting and production	15
W. P. Bowen	Conception and design	20
	Analysis and interpretation	20
	Drafting and production	20

3. [3] S. Forstner, Y. Sachkou, M. Woolley, G. I. Harris, **X. He**, W. P. Bowen, C. G. Baker, Modelling of vorticity, sound and their interaction in two-dimensional superfluids, New Journal of Physics, 21(5):053029, 2019.

   A part of this paper is incorporated as Chapter 5. The break-downs of the published paper are shown below. Chapter 5 was prepared by X. He by modifying the figures and re-writing 80% of the text.

Contributor	Statement of contribution	%
S. Forstner	Conception and design	20
	Analysis and interpretation	20
	Drafting and production	35
Y. Sachkou	Conception and design	20
	Analysis and interpretation	20
	Drafting and production	10
M. Woolley	Conception and design	10
	Analysis and interpretation	0
	Drafting and production	5
G. I. Harris	Conception and design	0
	Analysis and interpretation	10
	Drafting and production	5
X. He	Conception and design	15
	Analysis and interpretation	15
	Drafting and production	5
W. P. Bowen	Conception and design	15
	Analysis and interpretation	10
	Drafting and production	10
C. G. Baker	Conception and design	20
	Analysis and interpretation	25
	Drafting and production	30

Contributions by others to the thesis

Prof. Warwick P. Bowen, Dr Christopher G. Baker, Dr Glen I. Harris, and Dr Andreas Sawadsky provided critical feedback, editing, and supervision throughout my candidature.
Dr Christopher G. Baker supplied rendered images (acknowledged throughout the text).
All other contributions have been acknowledged in the publication list.

Statement of parts of the thesis submitted to qualify for the award of another degree

None

Research involving human or animal subjects

No animal or human subjects were involved in this research.

Acknowledgments

First I would like to thank my supervisor Prof Warwick Bowen for introducing me to the field of quantum physics. Now I find physics is like classical music, whereas engineering is like pop songs. I am grateful for your supervision and the chance you gave me to work in the world-class lab and do research in the cutting-edge field of optomechanics and superfluid. I was really inspired by your wide knowledge, and also by your enthusiasm and persistent pursuit for physics.

I sincerely appreciate the valuable suggestions, explanations and hands-on help from my co-supervisor Chris Baker during the four years in the lab. I was greatly benefited from your ability to explain every physics “problem” with an intuitive and beautiful picture. You are always supportive, optimistic and humorous. Without your jokes my PhD life would be much less happy. I would also like to thank my unofficial supervisor Glen Harris for teaching me lots of quantum optics experimental skills in the early stage. Huge thank you to other superfluid team members too: Eugene Sachkou, Andreas Sawadsky, Stefan Forstner, Yasmine Sfendla and David McAusland. Particular thanks to Eugene and Chris for the unforgettable “happy hours” with the two cryostats. So amazing to see physics works with all of you!

Queensland Quantum Optics Lab is an excellent research group full of nice and brilliant people. I not only learned physics but also got happiness from working with every colleague from the group, especially Lars Madsen, James Bennett, Erick Romero, Nicolas Mauranyapin, Christiaan Bekker, Beibei Li, Rachpon Kalra, Varun Prakash, George Brawley, Michael Vanner, Catxere Casacio, Kiran Khosla, Muhammad Waleed, Chao Meng, Sahar Esfahani and Gian-Marco Schnuriger. Thank you also for having lunch with me in the amazing Great Court, no matter it’s rainy or sunny. I am so lucky to meet you guys here!

I would also like to thank Kaerin Gardner, Angela Bird and Lisa Laletina for their administrative assistances; Dave Perkins, Rob Webb, Alan Reid from the mechanical workshop for fabricating lots of mechanical components for me to set up the dilution fridge. Many thanks to the building manager Erinn Osmond too. Without your assistance, my experiment would have been badly delayed, or even destroyed.

I had a memorable non-physics life in Brisbane with both lab mates and friends outside the lab, such as Daiqin Su, Xiuwen Zhou, Wenjun Zhu, Rui Ran, Larry, Shu Zhang, Ming Su, Shaoli Zhu, Shuying Chen and Lin Tian. Thank all of you for cooking, fishing, hiking, chatting with me on weekends and holidays.

My parents Luncai Hu and Zuyi He are always providing me unconditional support and understanding. am deeply grateful to you. Also to my two uncles for their time spent with me. I also sincerely thank my girlfriend Yue for her support during my writing.

Last but not least, I would like to thank Wong Ka Kui, a Hong Kong rock musician mostly active between 1980s and early 1990s. Since my school age, his music has always encouraged me to go to the woods to live deliberately.

Financial support

- Australian Research Council and Lockheed Martin Corporation through the Australian Research Council Linkage Grant LP140100595.
- Australian Research Council through the Centre of Excellence for Engineered Quantum Systems(EQuS, CE110001013)
- The University of Queensland (UQRTTUIT - UQ Research and Training Tuition Fee Offset)

Keywords

superfluid, Brillouin laser, quantized vortex, quantum optics, cavity optomechanics, microresonator

Australian and New Zealand Standard Research Classifications (ANZSRC)

ANZSRC code: 020604, Quantum optics, 40%
ANZSRC code: 020499, Condensed Matter Physics not elsewhere classified, 30%
ANZSRC code: 020699, Quantum Physics not elsewhere classified, 30%

Fields of Research (FoR) Classification

FoR code: 0206, Quantum Physics, 70%
FoR code: 0204, Condensed Matter Physics, 30%

Form is emptiness, emptiness is form.

'Vacuum Fluctuation' in the words of Buddhism

Contents

List of figures

List of abbreviations

Abbreviations	
AC	Alternating Current
DC	Direct Current
dB	Decibel
CW	Clockwise
CCW	Counter-clockwise
AM	Amplitude Modulation
PM	Phase Modulation
NA	Network Analyzer
SA	Spectrum Analyzer
BS	Beam Splitter
PD	Photodetector
SNR	Signal-to-Noise Ratio
LO	Local Oscillator
TE	Transverse Electric
TM	Transverse Magnetic
WGM	Whispering Gallery Mode
BEC	Bose Einstein Condensate
ZPF	Zero Point Motion
FSR	Free Spectral Range
SMF	Single-Mode Fibre
PTC	Pulse-Tube Cooler
VDW	Van der Waals
ODE	Ordinary Differential Equation
RWA	Rotating Wave Approximation
FEM	Finite-Element Modelling
HF	Hydrofluoric Acid
EOM	Electro-Optic Modulator
SEM	Scanning Electron Microscope
HMDS	Hexamethyldisilazane

List of symbols

Symbols	
$\hbar$	Reduced Planck constant
k_B	Boltzmann constant
K	Kelvin
G	Optical frequency shift per unit mechanical displacement
g_0	Single-photon optomechanical coupling rate
g	Multi-photon optomechanical single-photon coupling rate
c_3	Third sound speed
Δ	Laser detuning from the cavity resonance
κ	Superfluid circulation quantum or total cavity intensity decay rate
$\kappa_{\mathrm{ext\,(int)}}$	Cavity input coupling (intrinsic) loss rate
ω_{cav}	Cavity resonance frequency
ω_L	Laser frequency
Ω_m	Mechanical frequency
Γ	Mechanical damping rate
Γ_{opt}	Mechanical damping rate induced by optomechanical interaction
x_{ZPF}	Mechanical zero-point fluctuation amplitude
a	Photon annihilation operator
a_{in}	Photon input annihilation flux operator
b	Phonon annihilation operator
n	Average number of phonons stored in the mechanical resonator
n_{cav}	Average intracavity photon number
n_{th}	Average phonon number in thermal equilibrium
P_{in}	Incoming laser power
$S_{xx}(\omega)$	Power spectrum
C	Cooperativity
Q	Quality factor
κ_b	Backscattering rate
α, β	Coherent amplitude
α_{vdw}	van der Waals constant
χ_m	Mechanical susceptibility

ϵ_0 (ϵ_r)	Vacuum (relative) permittivity
λ	Wavelength
σ	Surface tension
$\mathcal{F}$	Finesse of an optical cavity
ρ	Density of the material
k	Wavenumber
$\mathbf{E}$	Electric Field

Chapter 1

Introduction

What is the difference between signals and noise? This is a subjective question, because signals are just something in the measurement which we are interested in, whereas noise is not. For example, if we shine a laser beam directly onto a photodetector, the photocurrent generated by the photodetector will always drift over some time scale, due to the "pick-up" of the environmental noise (e.g. from vibrations of the optical table, sound in the lab, lab temperature, etc.). Some particular "pick-up" from vibrations can be our signal, if we are interested in them. On the other hand, the signals imprinted by vibrations in the environment on the bare laser beam are typically very weak, since environmental vibrations generally have very low frequency, and are spectrally broad (have low quality). The low quality factor of the environmental vibrations is due to that they are a continuum of normal (eigen) mechanical modes, which are poorly defined and leaky into the ports of the environment. What's more, a bare laser beam generally has very low detection sensitivity making us not able to resolve all these weak signals.

In the cavity optomechanics community, researchers are interested in particular mechanical vibrations, and they then distinguish them from noise by engineering mechanical oscillators which support high quality mechanical modes. These modes are defined by the boundary condition of the mechanical oscillators, thus they are distinct normal modes instead of a continuum. In addition to increasing the quality factor of mechanical modes, researchers also improve the measurement sensitivity by employing an optical cavity, in which light circulates for a large number of round-trips (namely, the finesse of the cavity which ranges typically from several thousand up to several million), and thus interacts with the mechanical motion an equivalent number of times.

This is the simple understanding of cavity optomechanics, which is composed of an optical cavity and a mechanical oscillator. The resonance frequency of the cavity ranges from microwave ($\sim$ GHz) up to optical ($\sim$ several hundred THz), while the mechanical frequency ranges from Hz to tens of GHz, and the mass of the mechanical oscillator from dilute atom clouds to kg mirrors.

Cavity optomechanics has been widely explored in both practical and scientific cases of scenario. For the practical case, cavity optomechanics is used for mechanical position measurement, which is exhibited as the influence of the mechanical motion on the light. This has enabled many practical applications, like precision sensing of masses [6], forces [7], and gravitational waves [8]. For the case of fundamental science, cavity optomechanics is used to investigate the interplay between the mechanical oscillator and light, where the backaction of light affects the mechanical motion, and is used to generate and control the quantum state of the mechanical motion. With the dynamical backaction people have demonstrated a wide range of fundamental physics, including ground state cooling, squeezing and entanglement of macroscopic mechanical oscillators, etc [9–14].

Here in this thesis, instead of usual bulk solid materials, thin superfluid helium films are explored to form an optomechanical system with a silica Whispering Gallery Mode (WGM) resonator. Superfluid helium is a type of Bose Einstein condensate, in which all the constituent atoms at the energy ground state are described by one wavefunction, when helium gas is cooled below a critical temperature of 2.17 K. Compared with solid materials, superfluid helium has several advantages, such as zero viscosity [15], low optical absorption [16], high thermal conductivity [17], the self-assembling nature of superfluid films [18], and it has very rich and fascinating physics like Berezinskii–Kosterlitz–Thouless topological phase transition [19, 20], and quantum turbulence and quantized vortices [21–24].

With the fascinating superfluid optomechanical system, many experimental and theoretical results have been demonstrated in our lab. The ones related to this thesis are as following. In the first work included in this thesis, the superfluid fountain effect (see § 3.2.2) is utilized to enhance the optical force by one order of magnitude larger than radiation pressure, and using the enhanced optical force we demonstrate feedback cooling of a mechanical mode of the WGM resonator down to a phonon occupancy of 2110 ± 40 [1]. Next, to exploit the advantages of superfluid helium, in contrast to conventional optomechanical systems we study a superfluid optomechanical system, where surface acoustic waves on the thin superfluid film evanescently interact with the intracavity optical field [2]. We theoretically estimate that the superfluid optomechanical system can operate in the ultra-strong coupling regime, where the single photon optomechanical coupling rate g_0 is larger than the mechanical frequency Ω_m. Further, we theoretically investigate the vortex-sound interaction and show that the splitting of sound modes can be detected using this optomechanical system. With the vortex-sound interaction we also experimentally demonstrate the probing of the dynamics of an ensemble of 17 quantized vortices [5]. Last, we theoretically and experimentally demonstrate ultra-low threshold Brillouin lasing in the mechanically compliant superfluid thin film, in contrast to solid materials where the electrostrictive force of light strains the material to amplify the Brillouin acoustic wave. The Brillouin lasing in the superfluid thin film can mediate the strong coupling of two counter-propagating optical modes, and can be potentially used to stir superfluid vortices.

Thesis Outline

There are seven chapters in this thesis.

Chapter 2 summarizes the basic concepts and experimental skills involved in the superfluid optomechanics experiment during my PhD.

Chapter 3 presents the basic theoretical formulation for cavity optomechanics, and gives a brief introduction to superfluid helium.

Chapter 4 presents a conventional cavity optomechanics experiment, where we use the superfluid fountain effect to enhance the optical force exerted on the mechanical motion of the optical resonator.

Chapter 5 presents the theory developed for the optomechanical coupling between light and superfluid acoustic waves. Based on the superfluid optomechanical coupling the probing of vortex dynamics is both theoretically and experimentally demonstrated.

Chapter 6 presents the theory and experiment on the ultra-low threshold Brillouin lasing in a thin superfluid film, where a superfluid surface acoustic mode, which matches well with the intensity nodes of a WGM optical mode, and thus gets amplified by the optical field.

Chapter 7 concludes the thesis and gives the outlook for future superfluid optomechanics experiments.

Chapter 2

Shopping List for an Optomechanics Experiment

This chapter summarizes important optical components and useful techniques for cavity optomechanics experiments. For example, beam splitters are the critical component for interferometers, which are widely used to measure weak optical signals and detect the quantum state of light, as explained in the following section for homodyne and heterodyne detection. Optical cavities are another type of powerful optical component, which is used to enhance light-matter interaction. Basic concepts of the Fabry-Perot cavity and the Whispering Gallery Mode resonator are explained. Then the frequency locking technique and the fabrication process for WGM resonators are introduced.

2.1 Beam Splitter

Beam splitters are the most common optical device in optical physics experiments, and they are mostly used in interferometers. Fig. 2.1 illustrates a classical lossless beam splitter made of a silica slide with a reflective dielectric coating. The dielectric constant of the three materials

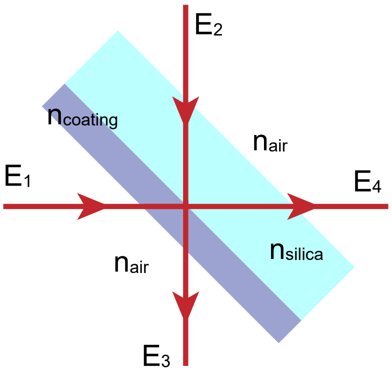

Figure 2.1: Illustration of a beam splitter (the reflection at the two interfaces between the beam splitter and air is neglected due to further anti-reflective coating).

have such relation: $n_{\text{silica}} > n_{\text{coating}} > n_{\text{air}}$, such that the two input electric fields (E_1 and E_2), and two output fields (E_3 and E_4) of the beam splitter obey a linear relation:

$$\begin{bmatrix} E_3 \\ E_4 \end{bmatrix} = \boldsymbol{S} \cdot \begin{bmatrix} E_1 \\ E_2 \end{bmatrix}, \text{ where } \boldsymbol{S} = \begin{bmatrix} -r & t \\ t & r \end{bmatrix} \tag{2.1}$$

is the transformation matrix of the beam splitter, r and t are respectively the amplitude reflection and transmission coefficients along a particular path through the beam splitter. Note that the minus sign in S_{11} is due to the π phase shift acquired from the reflection by a higher refractive index material back into the lower refractive index material (the Fresnel equations). As the beam splitter is assumed to be lossless, energy conservation requires that $\sum_i S_{ij}^* S_{ik} = \delta_{jk}$.

2.2 Modulators

2.2.1 Amplitude Modulation

Amplitude modulation is widely used in optical experiments and commercial telecommunication applications. The modulation of the amplitude of an electromagnetic field can be expressed as below:

$$E = E_0(1 + \beta \cos \Omega t) e^{-i\omega_L t} = E_0 \left[1 + \frac{\beta}{2}\left(e^{-i\Omega t} + e^{i\Omega t}\right)\right] e^{-i\omega_L t}, \tag{2.2}$$

where β is the modulation depth, ω_L is the carrier frequency (original laser frequency), and Ω is the modulation frequency. As shown by the definition equation, amplitude modulation generates two side bands of frequencies $\omega_L - \Omega$ and $\omega_L + \Omega$. Note that at $t = 0$, the two sidebands point to the same direction in the phasor diagram with the carrier.

2.2.2 Phase Modulation

Phase modulation is another common modulation. Mathematically, it takes the form as below, and with the Taylor expansion at small angle limit, we have:

$$E = E_0 e^{-i(\omega_L t + \beta \cos \Omega t)} \approx E_0 \left[1 - \frac{i\beta}{2}\left(e^{-i\Omega t} + e^{i\Omega t}\right)\right] e^{-i\omega_L t}. \tag{2.3}$$

Note that although phase modulation also generates two sidebands, the two sidebands have $\pi/2$ phase difference with the carrier at $t = 0$.

2.3 Detection Methods

2.3.1 Direct Detection

Direct detection is the simplest way to measure an optical signal E_{sig} by shining the light directly onto a semiconductor photodiode. Let us assume the photodiode converts the incident photons into electrons with a perfect efficiency. This eventually generates a photocurrent i_{out}, which is given by:

$$i \propto \bar{E}_{\text{sig}}^2 + \bar{E}_{\text{sig}}(\delta E_{\text{sig}}^* + \delta E_{\text{sig}}) \tag{2.4}$$

where the optical signal E_{sig} is decomposed into a real-valuded average component $\bar{E}_{\text{sig}}$ and a fluctuating part δE_{sig}.

Although the cannonical quantization of electromagnetic waves is formally introduced later in Chapter 3, to avoid the confusion of variables, here please allow me to briefly express the electric field operator of an electromagnetic wave with continuum frequency in terms of the annihilation $\hat{a}$ and creation $\hat{a}^\dagger$ operators [25]:

$$\hat{E}(t,x) = i\int_0^\infty \mathrm{d}\omega \left(\frac{\hbar\omega}{4\pi\epsilon_0 cA}\right)^{1/2} \left[\hat{a}(\omega)e^{-i\omega(t-x/c)} - \hat{a}^\dagger(\omega)e^{i\omega(t-x/c)}\right], \tag{2.5}$$

where x is the propagation direction, A is the cross-section area of the laser beam or the fiber core where the laser light is confined, ϵ_0 is the vacuum permittivity, c is the speed of light. If the signal light is assumed to be a single frequency (ω_L) and propagate only in $+x$ direction, we can find this relation between the classical electric field and the mean value (α) of the annihilation operator: $|E|^2 = \frac{\hbar\omega}{4\pi\epsilon_0 cA}|\alpha|^2$. Then we can also decompose the annihilation operator $\hat{a}_{\text{sig}}$ of the signal field into a real-valued average component α_{sig} and a fluctuating component $\delta\hat{a}_{\text{sig}}$. Inserting them into the photocurrent equation, we have

$$i \propto \underbrace{\alpha_{\text{sig}}^2}_{DC} + \underbrace{\alpha_{\text{sig}}\hat{X}(t)}_{AC}. \tag{2.6}$$

where $\hat{X} = \delta\hat{a}_{\text{sig}} + \delta\hat{a}_{\text{sig}}^\dagger$ is the fluctuations on the amplitude quadrature of the signal. Note that this equation tells that we can increase the amplitude of the fluctuating photocurrent by increasing the average input optical power.

From the detector's point of view, the photocurrent is defined as:

$$i(t) = \frac{n_e(t)\,e}{\Delta t} = \frac{\eta P(t)e}{\hbar\omega_L} \tag{2.7}$$

where η is the photodiode's quantum efficiency of converting incoming photons into electrons, e is the electron charge, $n_e(t)/\Delta t$ is the number of the photoelectrons generated by the detector during a time interval Δt, η is the detector quantum efficiency, $P(t)$ is the optical power proportional to $|E_{\text{sig}}(t)|^2$, and $P(t)/(\hbar\omega_L)$ is the incoming photon rate. The average photocurrent $\bar{i} = \langle i(t)\rangle$ is proportional to the average optical power $\bar{P}$, and eventually proportional to α_{sig}^2. Fourier transform of Eq. 2.4 gives the spectrum of the photocurrent: $i(\omega) \propto \alpha_{\text{sig}}^2 + \alpha_{\text{sig}}\hat{X}(\omega)$.

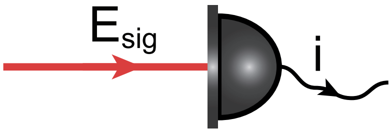

Figure 2.2: Illustration of direct measurement of the amplitude of an optical signal

The fluctuating term $\alpha_{\mathrm{sig}}\hat{X}(\omega)$, which can be measured using a spectrum analyzer, is generally what we are interested in.

The fluctuations of the optical signal can be quantitatively analyzed using its variance $\mathrm{Var}(i(t))$ [26]:

$$\mathrm{Var}(i(t)) = \Delta\left(\frac{n_e(t)\,e}{\Delta t}\right)^2 = \frac{\Delta(n_e(t))^2\,e^2}{\Delta t^2}. \tag{2.8}$$

Assuming all the photoelectrons are independently generated, the counting statistics of the photoelectrons obeys a Poissonian distribution with variance $\Delta(n_e(t))^2 = n_e = \bar{i}\Delta t/e$. For large numbers of electrons, this becomes a Gaussian distribution in each measurement interval Δt with variance given by:

$$\mathrm{Var}(i(t)) = \frac{\bar{i}\,e}{\Delta t}. \tag{2.9}$$

In order to investigate the spectrum of the fluctuating component of the photocurrent, we define the measurement bandwidth B from the Shannon theorem $B = \frac{1}{2\Delta t}$ [27]. Then this leads the photocurrent variance to

$$\mathrm{Var}(i(t)) = 2\,\bar{i}\,eB. \tag{2.10}$$

This is the formula for *shot noise* for all electronics, and is also true for photodetection. Note that this formula can be derived for any stream of independently generated electrons. Although the shot noise of the photocurrent comes from the random generation of electrons, it is not a property of the detector. It reflects the statistics of the light fluctuations as long as the detector quantum efficiency η is high. When $\eta = 1$, the photoelectrons have the same statistics with the incoming photons.

2.3.2 Homodyne Detection

Literally, homodyne can be understood as same (‘homo’) color (‘dyne’). Homodyne detection measures signals by using an interferometer with two arms of the same frequency. Homodyne detection measures the phase signal ($\delta\phi_{\mathrm{sig}}$) on the weak arm by comparing to the high power arm (Local Oscillator (LO)), which carries no signal and is from the same laser source with signal beam [28]. Fig. 2.3 illustrates a homodyne detection setup composed of a beam splitter and a balanced detector. The balanced detector measures the optical intensity of the two output port (E_3 and E_4), and subtract the corresponding photocurrent (i_3 and i_4) from one another, such that the DC photocurrent generated by the two input beam is subtracted, and only the oscillating component is kept.

Assuming a 50/50 beam splitter and a constant relative phase difference $\Delta\phi$ between the two input fields (E_{sig} and E_{LO}), the two output fields are given by:

$$E_3 = \frac{1}{\sqrt{2}}\left(E_{0,LO}\,e^{-i(\omega_L t+\Delta\phi)} - E_{0,\mathrm{sig}}e^{-i(\omega_L t+\delta\phi_{\mathrm{sig}})}\right) \tag{2.11a}$$

$$E_4 = \frac{1}{\sqrt{2}}\left(E_{0,LO}\,e^{-i(\omega_L t+\Delta\phi)} + E_{0,\mathrm{sig}}e^{-i(\omega_L t+\delta\phi_{\mathrm{sig}})}\right), \tag{2.11b}$$

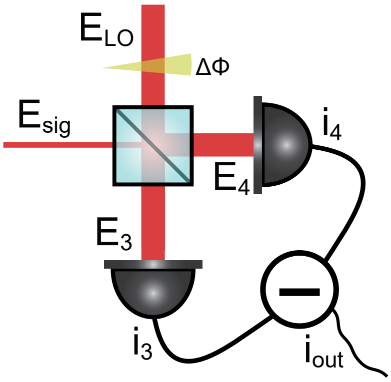

Figure 2.3: Illustration of a balanced homodyne detector.

where $E_{0,LO}$ and $E_{0,\mathrm{sig}}$ are respectively the real-valued amplitude of the LO and signal fields.

As the photocurrent is proportional to the mod-square of the field, so the output photocurrent generated by the balanced detector is:

$$i_{homo} \propto |E_4|^2 - |E_3|^2 = E_{0,LO}e^{i\Delta\phi}\, E_{0,\mathrm{sig}}e^{-i\delta\phi_{\mathrm{sig}}} + E_{0,LO}e^{-i\Delta\phi}\, E_{0,\mathrm{sig}}e^{i\delta\phi_{\mathrm{sig}}} \;. \tag{2.12}$$

Since the homodyne detection method is able to detect different quadratures of the signal, we decompose the signal field $E_{0,\mathrm{sig}}e^{i\delta\phi_{\mathrm{sig}}}$ into its amplitude and phase quadratures: $X + iY = E_{0,\mathrm{sig}}\cos(\delta\phi_{\mathrm{sig}}) + iE_{0,\mathrm{sig}}\sin(\delta\phi_{\mathrm{sig}})$. Thus, the output photocurrent of the balanced detector is further simplified as:

$$i_{homo} \propto 2E_{0,LO}\left[X cos(\Delta\phi) + Y sin(\Delta\phi)\right]. \tag{2.13}$$

This equation shows two advantages of homodyne detection over direct amplitude detection. First, the weak signal is boosted by the large amplitude of the LO beam. Second, by adjusting the constant phase difference $\Delta\phi$, we are able to measure an arbitrary quadrature of the signal. For example, if the signal and LO arms of the interferometer is locked to have a constant $\pi/2$ phase difference, the homodyne detector measures the fluctuations imprinted on the Y quadrature of the signal. Whereas, when the two arms are locked to have zero phase difference, we measure the fluctuations on the X quadrature.

2.3.3 Heterodyne Detection

Heterodyne detection is another useful approach to measure optical signals in quantum optics experiments. Heterodyne detection is composed of an interferometer with two arms of different frequencies. It has lower signal-to-noise ratio (SNR) than homodyne detection, given the same experimental conditions. However, heterodyne detection can shift low frequency signals to higher frequency band, and thus the technical noise dominating in the low frequency band can be avoided. The heterodyne detection setup is almost the same as the homodyne detection setup in Fig. 2.3, except that an additional Acousto-Optic Modulator (AOM) shifts the LO frequency from ω_L to $\omega_L+\Omega$, where Ω is the AOM modulation frequency. With this, the output fields of the balanced beamsplitter in Fig. 2.3 are:

$$E_3 = \frac{1}{\sqrt{2}}\left(E_{0,LO}\, e^{-i(\omega_L t+\Omega t)} - E_{0,\mathrm{sig}} e^{-i(\omega_L t+\delta\phi_{\mathrm{sig}})}\right) \tag{2.14a}$$

$$E_4 = \frac{1}{\sqrt{2}}\left(E_{0,LO}\, e^{-i(\omega_L t+\Omega t)} + E_{0,\mathrm{sig}} e^{-i(\omega_L t+\delta\phi_{\mathrm{sig}})}\right), \tag{2.14b}$$

and the corresponding photocurrent is:

$$i_{hetero} \propto |E_4|^2 - |E_3|^2 = E_{0,LO} e^{i\Omega t}\, E_{0,\mathrm{sig}} e^{-i\delta\phi_{\mathrm{sig}}} + E_{0,LO} e^{-i\Omega t}\, E_{0,\mathrm{sig}} e^{i\delta\phi_{\mathrm{sig}}}\ . \tag{2.15}$$

Then the heterodyne photocurrent has the final form:

$$i_{hetero} \propto 2E_{0,LO}E_{0,\mathrm{sig}}\, cos(\Omega t - \delta\phi_{\mathrm{sig}}), \tag{2.16}$$

where the phase signal $\delta\phi_{\mathrm{sig}}$ is up-shifted to be the sidebands of the AOM frequency Ω. Compared with the homodyne photocurrent [Eq. (2.16)], the heterodyne photocurrent signal is rotating in the phasor diagram of the signal at the frequency of Ω. Thus, its root-mean-square (RMS) sensitivity to a particular quadrature is $\sqrt{2}$ times smaller than the sensitivity of homodyne detection. The advantage of heterodyne detection is that it allows us to resolve Stokes and anti-Stokes sidebands separately, as the two sidebands would be located respectively at the two sides of the AOM frequency Ω.

2.4 Fabry-Perot Cavity

Fabry-Perot cavities are the most common and well-studied cavities in optical physics [29–31]. Although the cavities used in this thesis are Whispering Gallery Mode (WGM) micro-resonators, the transmitted field of a tapered fiber evanescently coupled to a WGM resonator has the same input-output relation with the reflected field of the Fabry-Perot cavity [32].

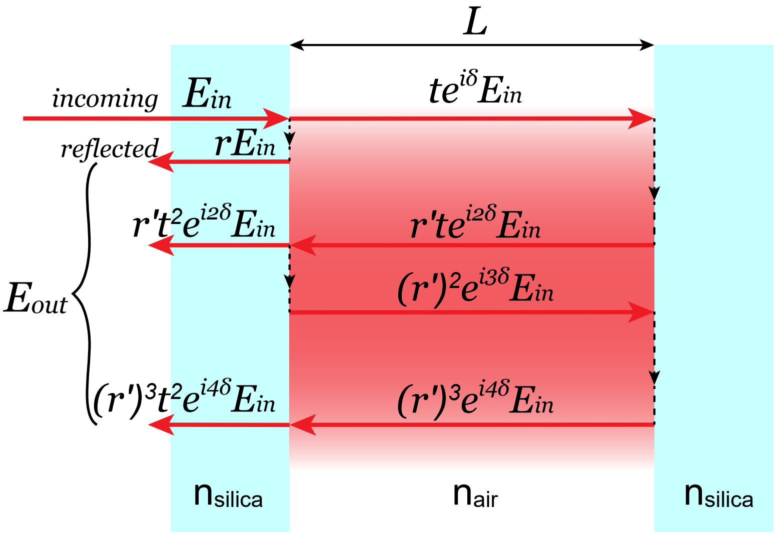

Figure 2.4: Illustration of a Fabry-Perot cavity with optical fields reflecting between the two mirrors.

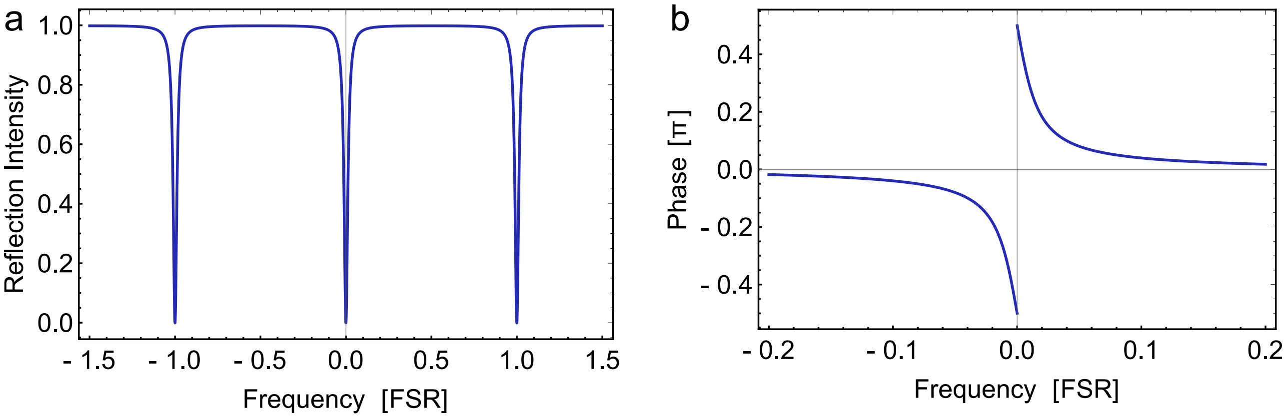

Figure 2.5: Spectral response of a Fabry-Perot cavity with the amplitude reflection coefficient $r = 0.96$ ($\mathcal{F} = 38.5$): (a) $|R(\omega)|^2$, (b) $-\arctan[\mathrm{Im}(R)/\mathrm{Re}(R)]$.

Let us take the Fabry-Perot cavity with no internal loss (Fig. 2.4) as the example. The cavity length is L, the amplitude reflection coefficient from glass to air is r, and from air to glass is $r' = -r$. For simplicity, the two mirrors are assumed to have the same reflection coefficient (critical coupling). For a laser with frequency ω_L, the phase acquired by the field for a one-way trip in the cavity is $\delta = L\,\omega_L/c = 0.5\omega/\Delta\nu_{\mathrm{FSR}}$, and $\Delta\nu_{\mathrm{FSR}} = \frac{c}{2L}$ is the Free Spectral Range (FSR) of the cavity. The input field is $E_{in} = E_0 e^{-i\omega_L t}$, and the output field $E_{out} = E_0' e^{-i(\omega_L t+\phi)}$ is the sum over all the reflected fields after each round-trip in the cavity in Fig. 2.4, while all the transmitted fields (not shown) to the right side are treated as cavity loss. The sum over from the second reflected field to the field with infinite round-trips is the power series of $\frac{1}{(1-(r')^2 e^{i2\delta}}$. Thus the amplitude reflection coefficient (transfer function) of the cavity is calculated:

$$R(\omega) = E_{out}/E_{in} = \frac{r\left(1 - e^{i2\delta}\right)}{1 - r^2 e^{i2\delta}} \tag{2.17}$$

Using this equation, intensity and phase (ϕ) response of a typical Fabry-Perot cavity is plotted in Fig. 2.5.

The finesse $\mathcal{F}$ of an optical cavity is proportional to the average number of round-trips each photon can circulate inside. It quantifies the quality of the cavity, and quantifies the enhancement of light-matter interaction by the cavity via Purcell effect [33]. For a Fabry-Perot cavity with no internal loss, the finesse has the form:

$$\mathcal{F} = \frac{\Delta\nu_{\mathrm{FSR}}}{\kappa} = \frac{\pi r}{1 - r^2}, \tag{2.18}$$

where κ is the Full Width Half Maximum (FWHM) of the cavity resonances, and is also called the bandwidth of the cavity.

2.5 Whispering Gallery Mode Resonator

Whispering Gallery Mode (WGM) resonators are another type of optical cavity, where the light is not reflecting between two mirrors, but is confined by Total Internal Reflection (TIR) inside a circular geometry, which can have many forms, such as microtoroids, microspheres, microdisks, ring resonators, and race-track resonators, etc [32, 34–41]. Fig. 2.6 illustrates a WGM disk resonator evanescently coupled to a tapered fiber. The tapered region is much thinner than a normal fiber, such that the optical field inside is less confined and evanescently extend up to a few micrometers into the air. In experiments when the taper and WGM resonator are brought close to each other using nanopoistioning stages, the absorption spectrum can be observed on the output light a_{out} by sweeping the laser wavelength through the resonance wavelengths. The absorption dips happen when the laser is on resonance with one optical mode by meeting such condition: $2\pi n_{\mathrm{eff}} r \simeq m\lambda$, where n_{eff} and r are respectively the effective refractive index and radius of the resonator, m is the azimuthal number resulting from the angular dependence of the solution of the electromagnetic wave equation for the circular geometry. In addition to the azimuthal number, the dependence of the solution on the radial direction is exhibited as the radial number p, corresponding the number of field maxima along the radial direction. Fig. 2.7 shows the simulation of WGMs confined on the circumference of a 5 μm radius micropillar using Finite Element Modelling (FEM). Fig. 2.7(a) is a principle mode, the field of which is mostly localized to the rim of the micropillar, whereas (b) is a third order mode with the electric field energy mostly distributed inside of the micropillar.

Coupled Mode Theory for WGM resonators

The coupling of two WGMs is quite common, for example the coupling induced by the backscattering caused by imperfections of the resonator geometry such as sidewall roughness [42]. Unlike the mechanically induced optical coupling, this type of coupling is stationary, so we define a fixed mutual coupling strength κ_b between the forward and backward propagating optical modes a_k and a_{-k}. The Hamiltonian of the system derived from coupled mode theory is:

$$H = \hbar\omega_k a_k^\dagger a_k + \hbar\omega_{-k} a_{-k}^\dagger a_{-k} + \hbar\kappa_b \left(a_k^\dagger a_{-k} + a_k a_{-k}^\dagger \right), \tag{2.19}$$

where ω_k and ω_{-k} are the bare eigen frequencies of the two optical modes, and the associated a is the annihilation operator of each mode. κ_b is the coupling rate. The subscript k is the wave

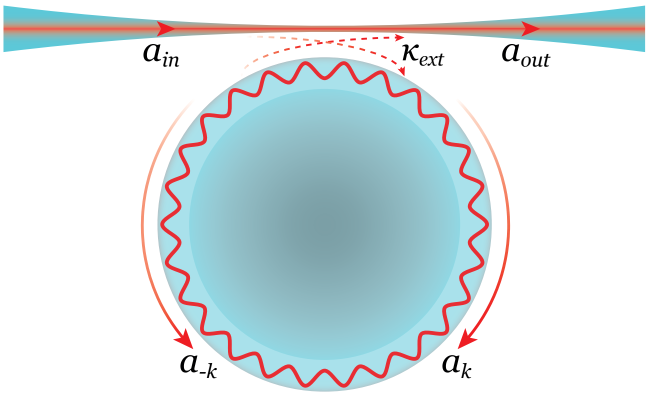

Figure 2.6: Illustration of a Whispering Gallery Mode resonator coupled to a fiber taper.

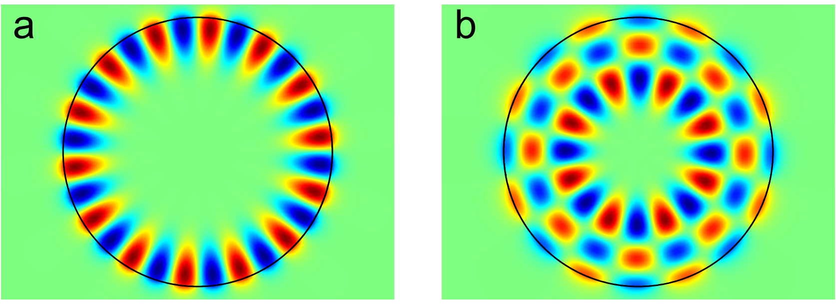

Figure 2.7: Two dimensional FEM simulation (out of plane electric field E_z) of WGMs confined at the circumference of a silica micropillar. (a) $m = 14$ and $p = 1$; (b) $m = 8$ and $p = 3$.

number of the optical modes, with the signs in the front indicating directions. The interaction term is a beamsplitter interaction between the two optical modes.

Equations of motion

Including dissipation and drive, the equations of motion for the two coupled optical cavity modes are obtained using Heisenberg equations of motion from the Hamiltonian [Eq. (2.19)] [43]:

$$\begin{aligned}\dot{a}_k &= i\Delta_k a_k - \frac{\kappa_k}{2} a_k - i\kappa_b a_{-k} + \sqrt{\kappa_{ext}}\, a_{in} && (2.20)\\ \dot{a}_{-k} &= i\Delta_{-k} a_{-k} - \frac{\kappa_{-k}}{2} a_{-k} - i\kappa_b a_k, && (2.21)\end{aligned}$$

where $\Delta_{k(-k)} = \omega_L - \omega_{k(-k)}$ is the detuning, $\kappa_{k(-k)} = \kappa_{int}^{k(-k)} + \kappa_{ext}$ is the total optical decay rate for the k $(-k)$ optical mode. κ_{ext} is the coupling rate to the tapered optical fibre, and κ_{int} is the intrinsic optical cavity decay rate. The pump field a_{in} drives the forwards propagating mode a_k via the fiber taper and its quantum noise is neglected. The amplitude of the pump field a_{in} is related to the incoming photon flux in the tapered fibre, via $|a_{in}|^2 = \frac{P_{in}}{\hbar\omega}$, with P_{in} the input laser power. Solving the equations of motion in the steady state, the forwards propagating mode a_k has the solution:

$$a_k = \frac{\sqrt{\kappa_{ext}}\ a_{in}}{-i\Delta + \kappa_k/2 + \frac{\kappa_b^2}{-i\Delta + \kappa_{-k}/2}}. \tag{2.22}$$

The amplitude of the backscattered field a_{-k} travelling in the opposite direction can be expressed as a function of a_k:

$$a_{-k} = \frac{-i\,\kappa_b\,a_k}{-i\Delta + \kappa_{-k}/2}. \tag{2.23}$$

Using the input-output theorem, the output light in the fiber after the cavity is [32]:

$$a_{out} = a_{in} - \sqrt{\kappa_{ext}}\,a_k\,. \tag{2.24}$$

Thus, the normalised transmission spectrum in the fiber after the WGM cavity is:

$$\begin{aligned}T &= \left|\frac{a_{out}}{a_{in}}\right|^2\\ &= \left|1 - \frac{\sqrt{\kappa_{ext}}\,a_k}{a_{in}}\right|^2\end{aligned} \tag{2.25}$$

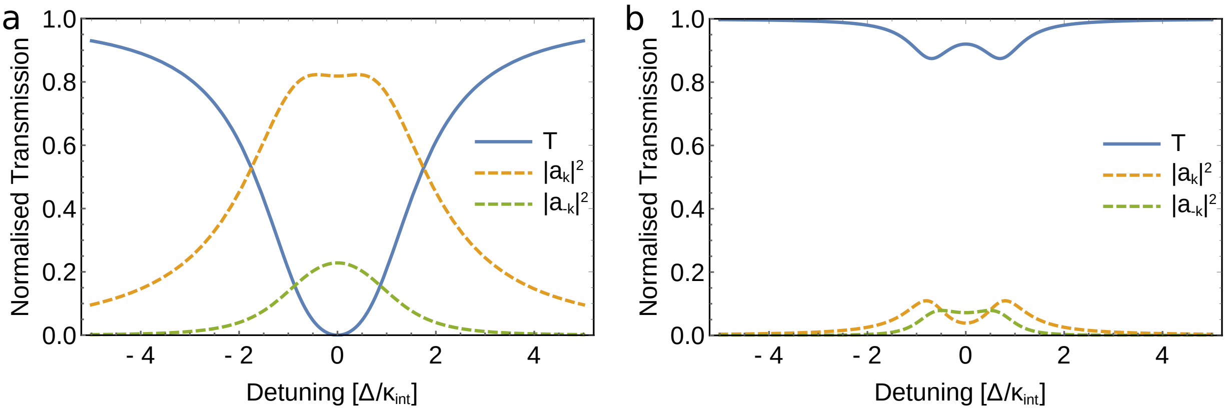

Figure 2.8: Normalised WGM transmission spectrum in the presence of backscattering, plotted using Eq. (2.25). Blue: Normalized transmission. Yellow and green dashed lines refer respectively to the forwards and backwards propagating field intensities $|a_k|^2$ and $|a_{-k}|^2$ in arbitrary units, obtained from Eqs (2.22) and (2.23). (a) Intrinsic optical linewidth κ_{int}: 104 MHz, taper coupling rate κ_{ext}: 180 MHz, backscattering rate κ_b: 75 MHz.(b) Undercoupled regime with intrinsic optical linewidth κ_{int}: 104 MHz, taper coupling rate κ_{ext}: 6.4 MHz, backscattering rate κ_b: 75 MHz.

The effect of the taper coupling rate κ_{ext} on the ratio of forwards to backwards travelling light intensity is illustrated in Fig. 2.8. This figure is plotted using typical experimental parameters: an optical mode with an unloaded optical decay rate $\kappa_{int} = 104$ MHz, and a backscattering coupling rate $\kappa_b = 75$ MHz. When the taper coupling rate is set to $\kappa_{ext} = 180$ MHz, the resulting cavity transmission is plotted in Fig. 2.8(a). Because the total dissipation rate $\kappa = \kappa_{int} + \kappa_{ext}$ is larger than κ_b, the mode splitting is not resolvable in the cavity transmission (blue curve). For the same reason, the intracavity intensity of the forwards propagating optical field (yellow line) is around four times larger than that of the field propagating in the opposite direction (green line). This intensity difference of the two optical modes leads to a net forwards travelling optical field in the cavity. In contrast, when the taper coupling rate is reduced such that the total dissipation rate is now comparable to the backscattering rate, the lifted degeneracy between forwards and backwards propagating fields is revealed, as shown the transmission in Fig. 2.8(b). In this regime, both optical fields are similarly populated, resulting in a predominantly standing optical field.

2.6 Locking Techniques

2.6.1 Thermal Locking

The easiest way to lock the laser frequency on resonance with a WGM resonator is to use the thermo-optic effect [44, 45]. Thermo-optic effect is due to the thermo-expansion of the WGM resonator size due to the passive heating from optical absorption. This effect happens when the laser frequency is swept from the blue-detuning side of an optical mode. As the laser detuning decreases, the intracavity optical power increases, leading to stronger optical absorption and

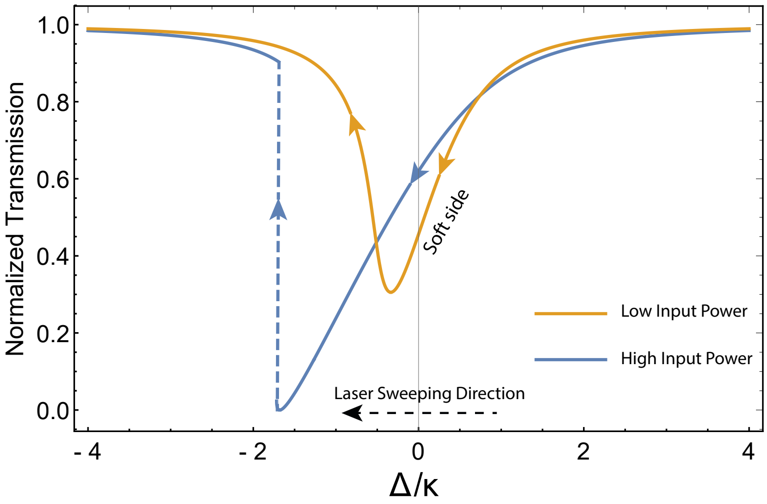

Figure 2.9: Examples of WGM resonator thermo-optic effect shown by the transmission spectra.

thermo-expansion, pushing the optical resonance to slightly lower frequency. This phenomenon is illustrated in Fig. 2.9 as the soft side (blue-detuning side) of the optical mode. The thermo-expansion eventually reaches an upper limit and the laser frequency snaps away from the lowest resonance frequency the optical mode can be, as shown by the blue dashed line.

In optomechanics experiments, the soft side is a naturally stable side where the laser frequency can be "locked", owing to the natural negative feedback from the thermo-optic effect. The advantage of thermal locking is its simplicity, but it has several disadvantages. First, it does not work at low optical power. Second, since the laser frequency is stabilized on the blue-detuning side, the measurement is limited for amplitude signals, and there will be dynamical heating for mechanical modes. Third, it does not work at cryogenic temperatures.

2.6.2 Pound-Drever-Hall Locking

The Pound-Drever-Hall technique is a very powerful way to lock the laser frequency on resonance with an optical cavity [46]. The full PDH locking setup is shown in Fig. 2.10. The modulated laser light is coupled to a WGM resonator via a tapered fiber and the transmitted

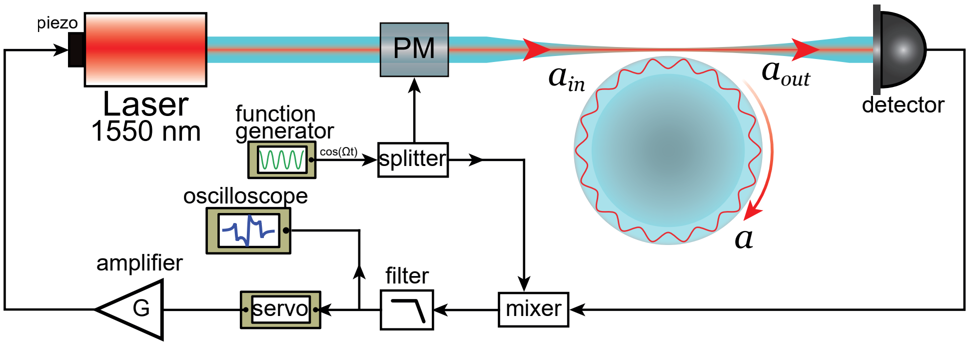

Figure 2.10: Schematic of an optical setup with the laser locked on resonance with a WGM resonator using PDH technique (PM: phase modulator).

light through the fiber is measured by a photodetector. The error signal is generated via mixing the photocurrent with the initial RF signal sent to the phase modulator. Assuming the RF signal is $\cos \Omega t$ and the modulation depth β, the modulated optical field sent to the resonator has a form like Eq. (2.3). Then in the frame rotating at the carrier frequency ω_L, the three independent equations of motion respectively for the three tones in the modulated optical field are:

$$\dot{a}_0 = i\Delta a_0 - \frac{\kappa}{2}a_0 + \sqrt{\kappa_{ext}}\, a_{in,ca} \tag{2.26a}$$

$$\dot{a}_1 = i(\Delta+\Omega)a_1 - \frac{\kappa}{2}a_1 + \sqrt{\kappa_{ext}}\,(-i)a_{in,si}e^{-i\Omega t} \tag{2.26b}$$

$$\dot{a}_2 = i(\Delta-\Omega)a_2 - \frac{\kappa}{2}a_2 + \sqrt{\kappa_{ext}}\,(-i)a_{in,si}e^{i\Omega t}, \tag{2.26c}$$

where $\Delta = \omega_L - \omega_{cav}$ is the detuning of the carrier frequency, Ω is the modulation frequency, the amplitude of $a_{in,ca}$ is proportional to the amplitude of the carrier tone E_0, the amplitude of $a_{in,si}$ is proportional to the amplitude of the two sideband tones $\frac{\beta}{2}E_0$, and the factor of $-i$ in the sideband tones is due to the phase modulation. Solving the equations of motion for the steady-state, and applying the input-output relation [Eq. (2.24)] yields the output fields:

$$a_{out,0} = F(\Delta)a_{in,ca} = \frac{-i\Delta}{-i\Delta+\kappa/2}a_{in,ca} \tag{2.27a}$$

$$a_{out,1} = F(\Delta+\Omega)(-i)a_{in,si}e^{-i\Omega t} = \frac{-i(\Delta+\Omega)}{-i(\Delta+\Omega)+\kappa/2}(-i)a_{in,si}e^{-i\Omega t} \tag{2.27b}$$

$$a_{out,2} = F(\Delta-\Omega)(-i)a_{in,si}e^{i\Omega t} = \frac{-i(\Delta-\Omega)}{-i(\Delta-\Omega)+\kappa/2}(-i)a_{in,si}e^{i\Omega t}, \tag{2.27c}$$

where the resonator is assumed to be critically coupled ($\kappa_{ext} = 0.5\kappa$).

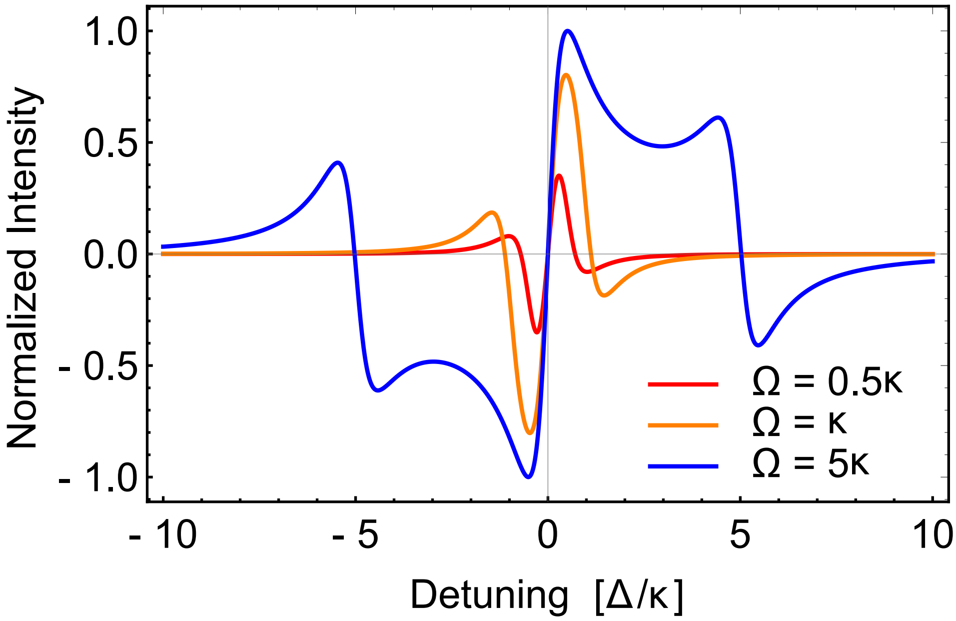

Figure 2.11: Normalized PDH error signals with different phase modulation frequencies Ω.

The photocurrent i_{out} is proportional to $|a_{out,0}+a_{out,1}+a_{out,2}|^2$, which can be expanded as:

$$\begin{aligned} i_{out} \propto\ & |a_{in,ca}|^2|F(\Delta)|^2+|a_{in,si}|^2\{|F(\Delta+\Omega)|^2+|F(\Delta-\Omega)|^2\} \\ & +2|a_{in,ca}||a_{in,si}|Re\{F(\Delta)[-iF(\Delta+\Omega)]^*+F^*(\Delta)[-iF(\Delta-\Omega)]\}\cos\Omega t \\ & +2|a_{in,ca}||a_{in,si}|Im\{F(\Delta)[-iF(\Delta+\Omega)]^*+F^*(\Delta)[-iF(\Delta-\Omega)]\}\sin\Omega t+(2\Omega\ terms)\,. \end{aligned}$$

Mixing down the photocurrent with the initial RF signal ($\cos\Omega t$) pulls out the term that is proportional to $\cos\Omega t$. Therefore, neglecting the DC terms and the 2Ω terms, the error signal ϵ has the following form:

$$\epsilon=2|a_{in,ca}||a_{in,si}|Re\{F(\Delta)[-iF(\Delta+\Omega)]^*+F^*(\Delta)[-iF(\Delta-\Omega)]\}\,. \tag{2.28}$$

Using this equation, Fig. 2.11 plots the normalized error $\frac{\epsilon}{2|a_{in,ca}||a_{in,si}|}$ with various phase modulation frequencies.

Then we connect the error signal to a servo, and afterwards an amplifier. By connecting the amplified error signal to the piezo of the laser, the feedback loop forms a complete PDH frequency locking setup.

2.7 Fabrication of WGM Resonators

The fabrication of WGM silica microresonators is a standard photolithography process, and is well described in this reference [47]. Here, I briefly summarize how we fabricate the silica microdisk resonators used in our superfluid optomechanics experiments.

We use a 500 μm-thick silicon handling wafer with a two-micron thick thermal oxide layer (Virginia Semiconductor) as illustrated in Fig. 2.12(a). Silica microdisks are fabricated via the photomicrography process steps in Fig. 2.12(b)-(e):

b HMDS adhesion promoter and subsequently AZ1518 positive photoresist are spin-coated on the wafer. Then the coating [pink layer in Fig. 2.12(b)] is heated at 100 degrees Celsius for 2 minutes to prepare the photoresist for UV exposure.

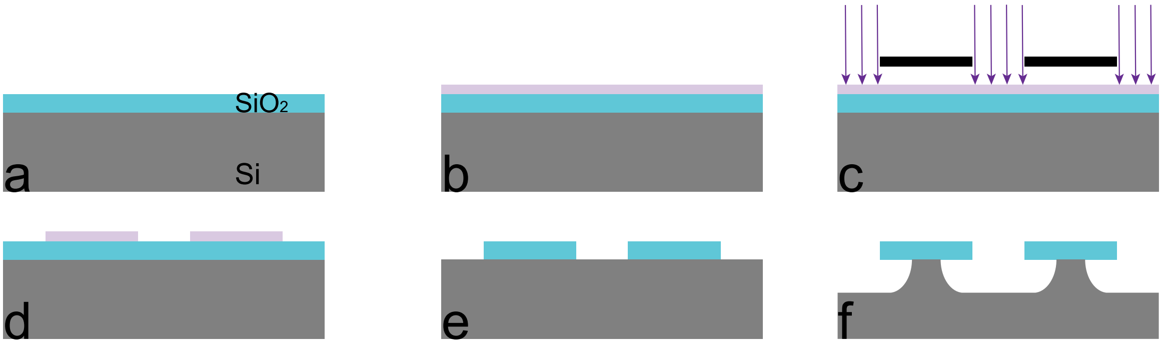

Figure 2.12: Illustration of the fabrication process for WGM microdisk resonators.

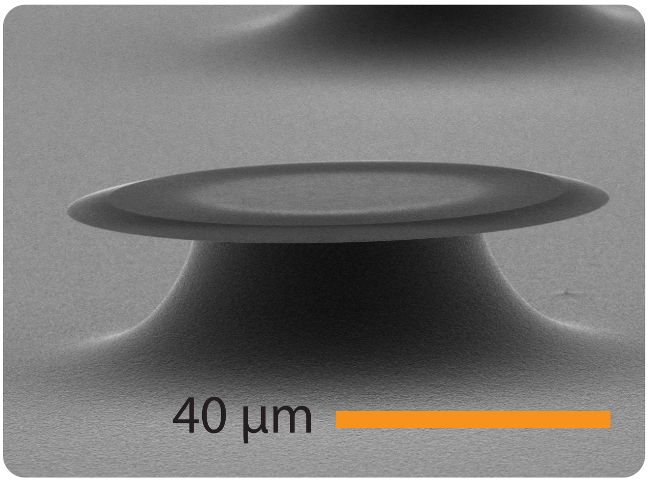

Figure 2.13: Scanning Electron Microscope (SEM) image of a silica WGM resonator on the silicon chip (radius 40 μm, thickness 2 μm).

c Fig. 2.12(c) shows the UV exposure process, where the black layer above the wafer is the cross-section of the ultra-fine mask. After UV exposure, the wafer is heated at 110 degrees Celsius for 1 minute.

d Then after development with AZ726 for 25 seconds and photoresist removal, only the unexposed regions of the photoresist are left [Fig. 2.12(d)]. Then we heat the wafer again to slightly melt the remaining photoresist to smooth its edges. This heating step is called photoresist reflow, which is necessary for making high quality (high finesse) disk resonators.

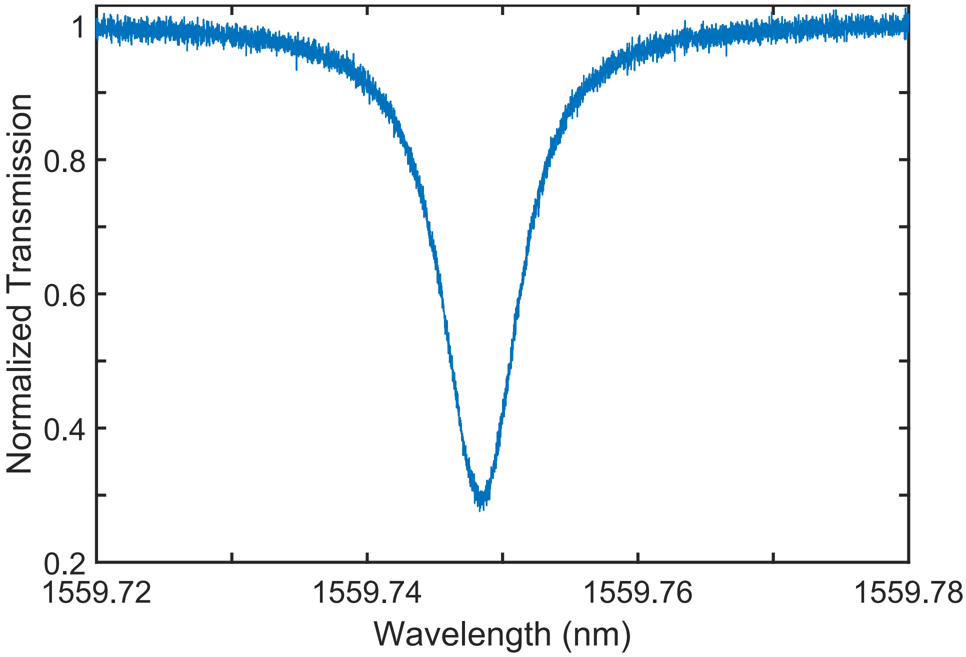

Figure 2.14: Example of the transmission spectrum of an optical mode from a 40 μm radius microdisk resonator (Q $\approx 3 \times 10^5$).

e Hydrofluoric acid (HF) wet-etch will transfer the mask pattern to the silica layer. After washing away the remaining photoresist with acetone and deionized water, the cross-section of the wafer will have silica microdisks atop the silicon substrate as shown by Fig. 2.12(e).

f Finally we under-cut the silicon substrate using XeF_2 gas-phase etch, so that the silica disks are released from the substrate. The XeF_2 etch time determines the size of the silicon pedestal, which affects quality-factor of the microdisk mechanical modes, as the pedestal is a loss channel to the mechanical motion of the silica disk.

Fig. 2.14 shows the Scanning Electron Microscope (SEM) image of a silica microdisk resonator sample. The wedged edge of the microdisk sample is due to the isotropic HF wet-etch as it etches also horizontally under the edge of the photoresist in Fig. 2.12(d). In the experiments, the fabricated devices generally show a number of WGM families, with optical quality factors in the 10^5 to low 10^7 range.

Chapter 3

Theoretical Basics of Cavity Optomechanics and Superfluid Helium

This chapter introduces the basic background knowledge on cavity optomechanics and superfluid helium-4. The knowledge will be useful for the following experimental chapters, as it includes important definitions, mathematical conventions to follow, and basic theory and characteristic phenomena of cavity optomechanics and superfluid. First, the cavity optomechanics literature is reviewed and the motivation is explained. Then I will describe why the two elements (light and mechanics) are both simple harmonic oscillators, and how they couple to each other. With that, the Hamiltonian and equations of motion for cavity optomechanics are introduced, and solved to explain typical phenomena. In addition, superfluid as another important element for my PhD research is briefly introduced, including its phenomenological description, the Josephson effect, the fountain effect, the acoustic excitations and the quantized vortices in superfluid helium.

3.1 Cavity Optomechanics

3.1.1 Two Simple Harmonic Oscillators

Cavity optomechanics basically studies the interaction between two oscillators, and often they can be treated as linear simple harmonic oscillators with one resonant at optical (microwave) frequency and the other at mechanical frequency (typically kHz to tens of GHz). Here in this section the two constituent oscillators of cavity optomechanics will be introduced separately. From classical to quantum, the two oscillators will be shown to have the exactly same physics: simple harmonic oscillators. First, taking the movable mirror in Fig. 3.1 as an example, the classical Hamiltonian of the harmonic oscillator is expressed as the sum of its kinetic energy

---

[1] The rate of the thermal phonons leaking into the mechanical oscillator from the bath

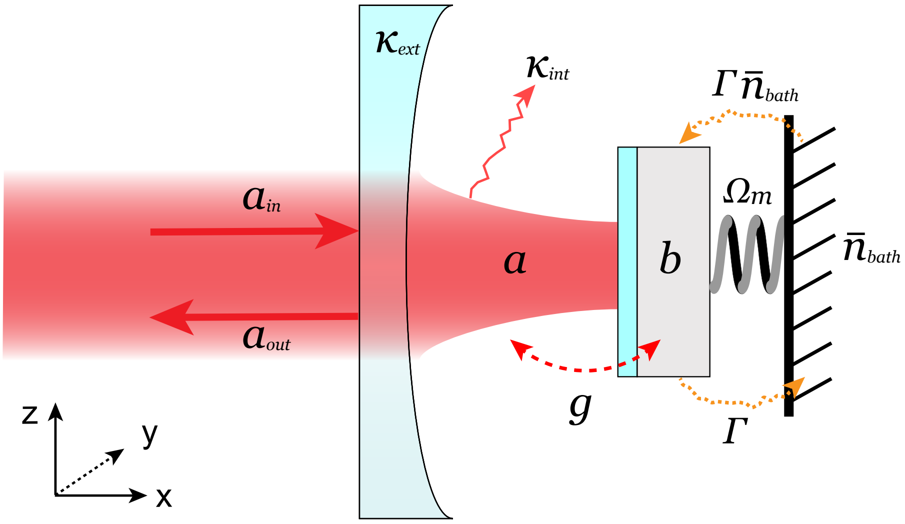

Figure 3.1: Artistic illustration of an optomechanical system composed of a Fabry-Perot cavity with a movable mirror acting as the mechanical oscillator. The notations describing all the optomechanical parameters are: a_{in} input light (including all the optical noises); a_{out} output light; κ_{ext} coupling rate of the cavity determined by the reflectivity of the front mirror; κ_{int} internal loss rate of the cavity (also a channel coupling to vacuum noise); a annihilation operator for the intracavity optical field; b annihilation operator for the mechanical oscillator; Ω_m mechanical resonance frequency; Γ mechanical loss rate; m mass of the movable mirror (not shown); $\bar{n}_{\text{bath}}$ thermal bath occupancy; $\Gamma\bar{n}_{\text{bath}}$ mechanical decoherence rate[1].

and potential energy [43]:

$$\mathcal{H} = \frac{p^2}{2m} + \frac{m\Omega_m^2}{2}q^2, \tag{3.1}$$

where m is the mass of the movable mirror, Ω_m is the frequency of the mechanical oscillator related to the spring constant k by the equation $\Omega_m = \sqrt{k/m}$, q is the position, and the momentum is $p = m\dot{q}$. We can confirm that p is the conjugate variable to q by checking the Hamilton's equations of motion:

$$\dot{q} = \frac{\partial}{\partial p}\mathcal{H} = \frac{p}{m} \tag{3.2a}$$

$$\dot{p} = -\frac{\partial}{\partial q}\mathcal{H} = -m\Omega_m^2 q \tag{3.2b}$$

satisfy the equations of motion of the mechanical oscillator: $\ddot{q} + \Omega_m^2 q = 0$. By putting a hat on q and p, and imposing the usual canonical commutation relation:

$$[\hat{q}, \hat{p}] = i\hbar\,, \tag{3.3}$$

we have the Heisenberg equations of motion

$$\dot{\hat{q}} = \frac{1}{i\hbar}\left[\hat{q}, \hat{\mathcal{H}}\right] = \frac{\hat{p}}{m} \tag{3.4a}$$

$$\dot{\hat{p}} = -\frac{1}{i\hbar}\left[\hat{p}, \hat{\mathcal{H}}\right] = -m\Omega_m^2\hat{q}, \tag{3.4b}$$

which have the same form as the Hamilton-Jacobi equations.

The annihilation b and creation $b^\dagger$ operators for the quantum harmonic oscillator are introduced as

$$b = \sqrt{\frac{m\Omega_m}{2\hbar}}\,\hat{q} + \frac{i\hat{p}}{\sqrt{2\hbar m\Omega_m}}, \quad b^\dagger = \sqrt{\frac{m\Omega_m}{2\hbar}}\,\hat{q} - \frac{i\hat{p}}{\sqrt{2\hbar m\Omega_m}} \tag{3.5}$$

with the commutation relation: $[b, b^\dagger] = 1$. Using these expressions in Eq. (3.1), the Hamiltonian becomes

$$\hat{\mathcal{H}} = \frac{\hbar\Omega_m}{2}(bb^\dagger + b^\dagger b) = \hbar\Omega_m(b^\dagger b + \frac{1}{2}). \tag{3.6}$$

Two important parameters of the mechanical oscillator are its zero point motion and phonon occupancy. From Eq. (3.5), the position operator is expressed as: $\hat{q} = x_{\mathrm{ZPF}}(b + b^\dagger)$, where

$$x_{\mathrm{ZPF}} = \sqrt{\frac{\hbar}{2m\Omega_m}} \tag{3.7}$$

is the zero point motion: the characteristic mechanical amplitude in the ground state. The phonon occupancy is defined from Eq. (3.6) to be $\hat{n} = b^\dagger b$, while $\frac{1}{2}\hbar\Omega_m$ is the zero point energy (the energy from vacuum fluctuations).

Similarly, a single-mode intracavity optical field of the free space (vacuum) Fabry-Perot cavity (see Fig. 3.1) can also be treated as a quantum harmonic oscillator [48]. Assuming the standing electromagnetic wave in the cavity has electric field polarized in the y direction (pointing inwards), and has the form

$$\mathbf{E}(x,t) = \hat{\mathbf{y}} q(t)\sqrt{\frac{2\omega_{\mathrm{cav}}^2}{\epsilon_0 V}}\,\sin(Kx)\,, \tag{3.8}$$

where K is the wavenumber and V is the mode volume. For this field to obey the wave equation $\nabla^2\mathbf{E} - \frac{1}{c^2}\frac{\partial^2}{\partial t^2}\mathbf{E} = 0$, the cavity resonance frequency must be $\omega_{\mathrm{cav}} = cK = c(m\pi/L)$, where c is the speed of light, m is an integer, and L is the length of the Fabry-Perot cavity, and the time-dependent amplitude must obey the simple harmonic oscillator equation $\ddot{q} + \omega_{\mathrm{cav}}^2 q = 0$. Based on Ampere's law of Maxwell's equations and Eq. (3.8), the corresponding magnetic component is:

$$\mathbf{B}(x,t) = \hat{\mathbf{z}}\frac{\dot{q}(t)}{c\,\omega_{\mathrm{cav}}}\sqrt{\frac{2\omega_{\mathrm{cav}}^2}{\epsilon_0 V}}\,\cos(Kx)\,. \tag{3.9}$$

While the electric and magnetic field distributions describe the common case of a free-space Fabri-Perot cavity, the case of a Whispering Gallery Mode (WGM) resonator used in our experiment follows a similar derivation with minor changes such as taking into account the material permittivity (see Chapter 5). The sum of the energy of the electric and magnetic fields gives the total energy of the intracavity optical field:

$$\begin{aligned}\mathcal{H} &= \frac{\epsilon_0}{2}\int dV\left(\mathbf{E}^2 + c^2\mathbf{B}^2\right)\\ &= \frac{1}{2}\left(\omega_{\mathrm{cav}}^2 q^2 + p^2\right),\end{aligned} \tag{3.10}$$

where q is again the "position", whereas the "momentum" is defined as $p = \dot{q}$. Note that Eq. (3.10) only refers to a vacuum cavity as illustrated in Fig. 3.1. In the case of a non-vacuum cavity with spatially varying refractive index, $\epsilon(r)$ should be inside the integral. Comparing this Hamiltonian with the Hamiltonian for the mechanical oscillator Eq. (3.1), we see that they both describe simple harmonic oscillators, with the energy oscillating back and forth between q and p.

Quantization happens again with the canonical commutation relation Eq. (3.3). Then the creation $a^\dagger$ and annihilation a operators for the intracavity optical field are also similarly defined:

$$a^\dagger = \frac{1}{\sqrt{2\hbar\omega_{\mathrm{cav}}}}\left(\omega_{\mathrm{cav}}\hat{q} - i\hat{p}\right); \quad a = \frac{1}{\sqrt{2\hbar\omega_{\mathrm{cav}}}}(\omega_{\mathrm{cav}}\hat{q} + i\hat{p}), \tag{3.11}$$

with the Hamiltonian as:

$$\hat{\mathcal{H}} = \hbar\omega_{\mathrm{cav}}\left(a^\dagger a + \frac{1}{2}\right). \tag{3.12}$$

The electric and magnetic fields in the cavity mode are quantized as below [49]:

$$\hat{\mathbf{E}} = \sqrt{\frac{\hbar\omega_{\mathrm{cav}}}{\epsilon_0 V}}\left(ae^{-i\omega_{\mathrm{cav}}t} + a^\dagger e^{i\omega_{\mathrm{cav}}t}\right)\sin(Kx)\,\hat{\mathbf{z}}, \tag{3.13a}$$

$$\hat{\mathbf{B}} = \sqrt{\frac{\hbar\omega_{\mathrm{cav}}}{c^2\epsilon_0 V}}\left[i\left(a^\dagger e^{i\omega_{\mathrm{cav}}t} - ae^{-i\omega_{\mathrm{cav}}t}\right)\right]\cos(Kx)\,\hat{\mathbf{y}}. \tag{3.13b}$$

Since often people are more interested in the electric field, so we define the electric field amplitude for the positive frequency component as:

$$\hat{\mathcal{E}}_+ = \sqrt{\frac{\hbar\omega_{\mathrm{cav}}}{\epsilon_0 V}}\, a, \tag{3.14}$$

where $\sqrt{\hbar\omega_{\mathrm{cav}}/(\epsilon_0 V)}$ is the electric field for one photon.

3.1.2 Parametric Coupling

After talking about the mechanical and optical oscillators separately, here in this section we discuss how the two simple harmonic oscillators with contrasting frequencies interact with each other. Let's look back at the illustration in Fig. 3.1 and consider a general cavity optomechanics model like the Fabry-Perot cavity with a movable mirror. The intracavity optical field exerts a radiation pressure force (momentum transfer of the photons due to reflection) on the movable mirror, affecting its position, and the mechanical motion of the movable mirror modulates the cavity resonance frequency, affecting the intensity of the intracavity optical field and subsequently the strength of the radiation pressure force. This interplay is essentially the parametric coupling between the intracavity optical field and the mechanical oscillator. Since the mechanical motion modulates the cavity resonance frequency, the output light from the cavity has two sidebands.

Given the average cavity length L and the position of the movable mirror x (see Fig. 3.1), the resonances supported by this cavity have angular frequency $\omega_{\mathrm{cav}} \approx m \cdot \pi \frac{c}{L+x}$, where c is the speed of light and m is the integer mode number. The strength of optomechanical coupling is calibrated by the optical frequency shift per displacement, which is defined as [50]:

$$G = -\frac{\Delta\omega_{\text{cav}}}{\Delta x} = m \cdot \pi \frac{c}{(L+x)^2}\bigg|_{x=0} = \frac{\omega_{\text{cav}}}{L}. \tag{3.15}$$

The Hamiltonian of the optomechanical system illustrated in Fig. 3.1 is the sum of the energy of the intracavity field and the mechanical oscillator:

$$\mathcal{H} = \hbar\omega_{\text{cav}}(x)a^\dagger a + \hbar\Omega_m b^\dagger b, \tag{3.16}$$

where the hat notation on each operator is neglected for convenience. Due to the dispersive coupling between the intracavity field and the mechanical oscillator: $\omega_{\text{cav}}(x) = \omega_{\text{cav}} + x\partial\omega_{\text{cav}}/\partial x + \ldots \approx \omega_{\text{cav}} - xG$, the Hamiltonian including the optomechanical coupling is expressed as:

$$\mathcal{H} = \hbar\left(\omega_{\text{cav}} - xG\right)a^\dagger a + \hbar\Omega_m b^\dagger b, \tag{3.17}$$

where the position operator is as defined in Eq. (3.7): $x = x_{\text{ZPF}}(b + b^\dagger)$. Thus the interaction Hamiltonian, which describes the part of energy in the system sloshing between light and mechanics, is:

$$\mathcal{H}_{\text{int}} = -\hbar g_0 a^\dagger a(b + b^\dagger), \tag{3.18}$$

where

$$g_0 = Gx_{\text{ZPF}} \tag{3.19}$$

is the single photon optomechanical coupling rate, quantifying the fluctuations of cavity resonance frequency due to the mirror's zero point motion. Since the interaction energy is only sloshing between light and mechanics within the system, and does not dissipate out of the system, the dynamics of this closed system are energy conserving, *i.e.* unitary, making radiation-pressure mediated optomechanical systems a promising platform for macroscopic quantum experiments.

From Eq. (3.18), we see that the coupling is between the mechanical amplitude (proportional to $(b + b^\dagger)$) and the intracavity optical intensity (proportional to $a^\dagger a$). Thus the radiation-pressure mediated optomechanical interaction is inherently nonlinear. General optomechanics experiments can be approximated by a linearized model as following. In the limit that the intracavity field is driven to a strong coherent amplitude, then it can be decomposed into an average coherent amplitude $\alpha = \langle a\rangle = \sqrt{n_{\text{cav}}}\ e^{-i\omega_L t}$ (where ω_L is the frequency of the input laser, and n_{cav} is the average intracavity photon number) and a fluctuating term δa for all the optical noise, namely $a = \alpha + \delta a$. The decomposition of the intracavity field leads the interaction Hamiltonian to be:

$$\begin{aligned}\mathcal{H}_{\text{int}} &= -\hbar g_0(\alpha + \delta a)^\dagger(\alpha + \delta a)(b + b^\dagger) \\ &= -\hbar g_0(|\alpha|^2 + \alpha^*\delta a + \alpha\delta a^\dagger + \delta a^\dagger\delta a)(b + b^\dagger),\end{aligned} \tag{3.20}$$

where the first term $-\hbar g_0|\alpha|^2(b + b^\dagger)$ is the product of the DC radiation pressure force ($F_{\text{rad}} = -\hbar G|\alpha|^2$) and the mechanical amplitude $[x_{\text{ZPF}}(b + b^\dagger)]$. This DC effect only offsets the system to a new equilibrium position. Let's first neglect this term for the analysis of the system dynamics. The fourth term is related to the second order of the optical noise, which generally has amplitude much smaller than the coherent amplitude α, thus it is valid to neglect the fourth term. Thus, the interaction Hamiltonian is linearized to be:

$$\mathcal{H}_{\text{int}}^{\text{lin}} = -\hbar g(\delta a^\dagger + \delta a)(b + b^\dagger), \tag{3.21}$$

where α is assumed to be real valued without loss of generality, and $g = \alpha g_0$ is the multi-photon optomechanical coupling rate.

Depending on the detuning, we can take different Rotating Wave Approximations (RWAs). When the laser is red-detuned by the mechanical resonance frequency $\Delta \approx -\Omega_m$, only the sideband which has higher frequency than the laser is on resonance. When the mechanical frequency is larger than the cavity linewidth, by neglecting the non-resonant terms in the interaction Hamiltonian, the RWA yields a beamsplitter-type interaction Hamiltonian:

$$-\hbar g(\delta a^\dagger \, b + \delta a \, b^\dagger). \tag{3.22}$$

When the laser is blue-detuned $\Delta \approx \Omega_m$, only the red sideband is on resonance. Thus the resonant terms after RWA are:

$$-\hbar g(\delta a^\dagger \, b^\dagger + \delta a \, b), \tag{3.23}$$

which corresponds to a "parametric down-conversion" or "two-mode squeezing" interaction. When $\Delta = 0$ or the mechanical frequency is smaller than the cavity linewidth, neither sideband is biased, so we have to keep all the four terms in the linearized interaction Hamiltonian.

3.1.3 Equations of Motion

The original full Hamiltonian for the optomechanical system can be derived from Eq. (3.17). Switching the intracavity optical field to a rotating frame at the input laser frequency ω_L gives the new Hamiltonian:

$$\mathcal{H} = -\hbar\Delta a^\dagger a + \hbar\Omega_m b^\dagger b - \hbar g_0 a^\dagger a(b + b^\dagger), \tag{3.24}$$

where $\Delta = \omega_L - \omega_{\text{cav}}$ is the laser detuning from the cavity resonance frequency. Using Langevin equations of motion, the equations of motion for a and b can be obtained. Including the optical and mechanical damping, the optical and mechanical noises, and the optical drive, the equations of motion have the form [50]:

$$\dot{a} = i\Delta a - \frac{\kappa}{2}a + ig_0 a(b + b^\dagger) + \sqrt{\kappa_{ext}}\, a_{in} + \sqrt{\kappa_{int}}\, f_{in}, \tag{3.25a}$$

$$\dot{b} = -i\Omega_m b - \frac{\Gamma}{2}b + ig_0 a^\dagger a + \sqrt{\Gamma}\, b_{in}, \tag{3.25b}$$

where a_{in} includes the coherent laser drive and the external vacuum fluctuations coupling to the cavity, κ_{ext} is the coupling rate of the cavity to the laser drive, f_{in} is the vacuum fluctuations coupled through the cavity intrinsic loss channel quantified by the intrinsic cavity loss κ_{int}. Thus, the total cavity loss rate [Full Width Half Maximum (FWHM)] is $\kappa = \kappa_{int} + \kappa_{ext}$. b_{in} is the thermal noise coupled to the mechanical oscillator through the mechanical loss channel quantified by the mechanical damping rate Γ (FWHM). In the Markovian limit, these quantum stochastic operators obey the temporal correlations as below [51]:

$$\langle a_{in}(t)a^{\dagger}_{in}(t')\rangle = \delta(t-t'), \tag{3.26a}$$

$$\langle a^{\dagger}_{in}(t)a_{in}(t')\rangle = 0, \tag{3.26b}$$

$$\langle b_{in}(t)b^{\dagger}_{in}(t')\rangle = (n_{th}+1)\delta(t-t'), \tag{3.26c}$$

$$\langle b^{\dagger}_{in}(t)b_{in}(t')\rangle = n_{th}\delta(t-t'), \tag{3.26d}$$

where the correlation relations for f_{in} are the same as those of a_{in}, and n_{th} is the thermal occupancy of the mechanical oscillator. Note that the difference between the optical and mechanical noises is only that the optical frequency is so high that the average thermal occupancy of the optical field is zero ($\hbar\omega_{cav} \gg k_B T$, where k_B is the Boltzmann constant and T is the bath temperature).

Based on the optomechanical coupling rate g, optical linewidth κ, and mechanical linewidth Γ, we introduce the optomechanical cooperativity defined as [52]:

$$C = \frac{4g^2}{\kappa\Gamma}. \tag{3.27}$$

The cooperativity might be the most important figure of merit for cavity optomechanics. Its form is a direct comparison between the optomechanical coupling rate and the optical and mechanical loss rates. In this thesis it will be shown that optical damping/heating of mechanical oscillators, optomechanically induced transparency/amplification discussed in the following section and the Brillouin optomechanical amplification in Chapter 6 can be simply expressed in terms of the optomechanical cooperativity. This figure of merit can be directly used to quantify what regime an optomechanical system can be. For example, with C larger than 1, the optomechanical system is able to generate regenerative oscillation of the mechanical mode, where the intrinsic mechanical linewidth is reduced to zero by the optomechanical amplification. With C larger than the thermal occupancy n_{th}, the optomechanical system can allow quantum experiments, such as ground state cooling of mechanical oscillators [9, 10], observation of radiation pressure shot noise [53], quantum coherent frequency conversion [54], quantum state transfer and processing, etc [55–57].

Often it is useful to neglect the noise terms and have the classical version of the equations of motion, which are valid in the case of large photon numbers. The mechanical annihilation operator b is replaced by the actual position of the mechanical oscillator in such a way:

$$x(t) = 2x_{\mathrm{ZPF}}\mathrm{Re}(\langle b(t)\rangle), \tag{3.28}$$

while the annihilation operator a for light is approximated by the coherent optical amplitude $\alpha(t) = \langle a(t)\rangle$ with all the noise being averaged out. Thus, the equation of motion for the intracavity field in the classical limit can also be derived easily from Eq. (3.16):

$$\dot{\alpha} = i\Delta\alpha - \frac{\kappa}{2}\alpha + iGx\alpha + \sqrt{\kappa_{ext}}\,\alpha_{in}, \tag{3.29}$$

where α_{in} is only the coherent laser drive.

From complex analysis[2], Eq. (3.28) gives $\mathrm{d}\,\mathrm{Re}(\langle b\rangle)/\mathrm{d}t = \mathrm{Re}(\langle\dot{b}\rangle) = \mathrm{Re}[(-i\Omega_m - \Gamma/2)\langle b\rangle + ig_0|\alpha|^2]$, and further $\mathrm{d}^2\mathrm{Re}(\langle b\rangle)/\mathrm{d}t^2 = \mathrm{Re}(\langle\ddot{b}\rangle) = \mathrm{Re}[(-i\Omega_m - \Gamma/2)\langle\dot{b}\rangle]$, where $|\alpha|^2$ is the intracavity photon number n_{cav}. Thus, the equation of motion for the mechanical position can be derived from Eq. (3.25b):

$$\begin{aligned}
\ddot{x} &= 2x_{\mathrm{ZPF}}\mathrm{Re}[(-i\Omega_m - \Gamma/2)\langle\dot{b}\rangle] \\
&= 2x_{\mathrm{ZPF}}\mathrm{Re}[-\frac{\Gamma}{2}\langle\dot{b}\rangle + (-i\Omega_m)\langle\dot{b}\rangle] \\
&= 2x_{\mathrm{ZPF}}\mathrm{Re}\{-\frac{\Gamma}{2}\langle\dot{b}\rangle + (-i\Omega_m)[(-i\Omega_m - \frac{\Gamma}{2})\langle b\rangle + ig_0|\alpha|^2]\} \\
&= 2x_{\mathrm{ZPF}}\mathrm{Re}\{-\frac{\Gamma}{2}\langle\dot{b}\rangle - \Omega_m^2\langle b\rangle - \frac{\Gamma}{2}(-i\Omega_m)\langle b\rangle + \Omega_m g_0|\alpha|^2\}.
\end{aligned} \tag{3.30}$$

In the limit where the mechanical quality factor is very high ($Q_m = \Omega_m/\Gamma \gg 1$), the damping and coupling terms in Eq. (3.25b) can be neglected, such that the approximation $-i\Omega_m b \approx \dot{b}$ is valid. Then the equation of motion for the mechanical position is simplified as:

$$\begin{aligned}
\ddot{x} &= 2x_{\mathrm{ZPF}}\mathrm{Re}\{-\frac{\Gamma}{2}\langle\dot{b}\rangle - \Omega_m^2\langle b\rangle - \frac{\Gamma}{2}\langle\dot{b}\rangle\} + 2\Omega_m G x_{\mathrm{ZPF}}^2|\alpha|^2 \\
&= -\Omega_m^2 x - \Gamma\dot{x} + \frac{G\hbar}{m}|\alpha|^2\,.
\end{aligned} \tag{3.31}$$

3.1.4 Steady-state Solution

As stated in introducing the interaction Hamiltonian in § 3.1.2, these semi-classical equations of motion are also nonlinear because of the α^2 term representing the optomechanical coupling in Eq. (3.31). In order to solve the coupled ODEs, we need to first linearize them by decomposing the coherent optical amplitude and the mechanical position respectively into a constant term for the steady state of the system, and a time-variant term which describes the dynamics of the system. For the optical amplitude, the decomposition is: $\alpha(t) = \bar{\alpha} + \delta\alpha$. The linearization steps for the mechanical position lead to $x(t) = \bar{x} + \delta x$, where $\bar{x}$ is the shift of the mechanical equilibrium position by $G\hbar|\bar{\alpha}|^2/(m\Omega_m^2)$, and $G\hbar|\bar{\alpha}|^2$ is the average radiation pressure force. Inserting the DC shift of the mechanical position into Eq. (3.29) yields an equation for the steady state of the intracavity optical amplitude:

$$\left(i\Delta - \frac{\kappa}{2}\right)\bar{\alpha} + \frac{i\hbar G^2}{m\Omega_m^2}|\bar{\alpha}|^2\bar{\alpha} + \sqrt{\kappa_{ext}}\,\alpha_{in} = 0 \tag{3.32}$$

As shown by this complex equation $\bar{\alpha}$ can have multiple roots (although some of them might not be physical), leading to the optomechanical static bistability of the average intracavity photon number at large input laser drive. This optomechanical bistable behaviour is exhibited as the

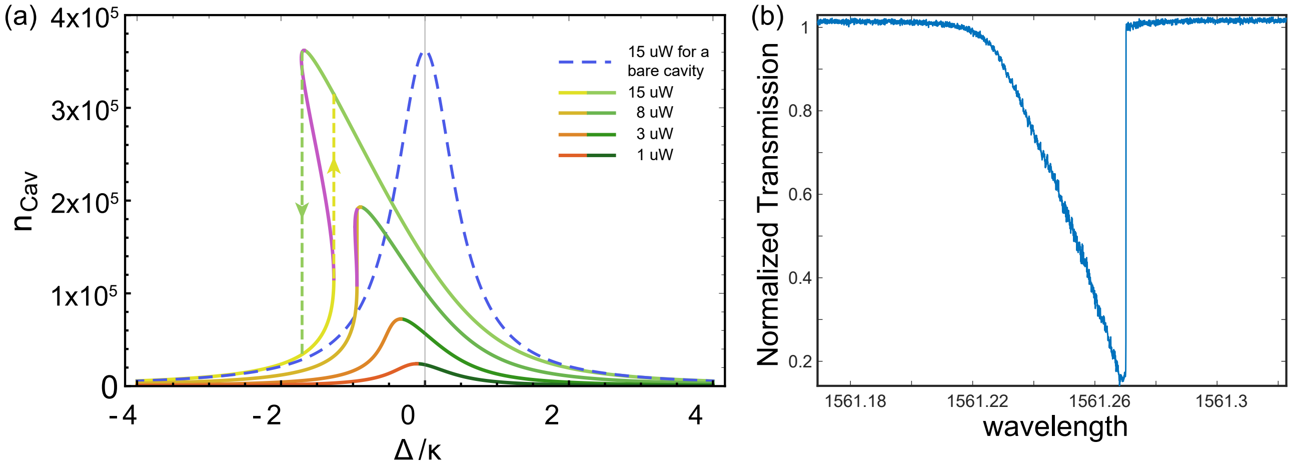

Figure 3.2: (a) Optomechanical bistability of the intracavity photon number versus laser detuning [all the solid lines are direct plot of the mod-square of Eq. (3.32)'s numerical solutions]. The system parameters used in this figuer: $m = 1$ picogram, $\Omega_m/2\pi = 3$ MHz, $\kappa/2\pi = 100$ MHz, $\kappa_{ext}/2\pi = 50$ MHz, $G/2\pi = 0.5$ GHz/nm. (b) Typical optomechanical bistability shown on the experimental transmission spectrum of a WGM resonator.

hysteresis of the average photon number ($n_{cav} = |\bar{\alpha}|^2$) versus laser detuning (Fig. 3.2). Four sets of solutions of Eq. (3.32) at different input power levels are plotted in this figure. Below bistability threshold power the average intracavity photon number curve is composed of one solution, and the intracavity photon number versus laser detuning curve is only skewed, which means the skewed curve will be the same no matter in which direction the laser frequency is swept through the cavity resonance frequency. When the input power is high enough, the green and yellow solutions are disconnected and an unstable second solution (the purple line) appears, resulting in an abrupt jump from one solution to the other when the laser frequency sweeps through the cavity resonance frequency, and the detuning where the abrupt jump happens depends on the laser sweeping direction. This phenomenon is the hysteresis generated by the optomechanical bistability.

In addition to the optomechanical bistability, the steady-state solution also leads to the change of the mechanical frequency (the spring constant). This is because the average intracavity optical amplitude changes with mechanical position, which results in a mechanical-position dependent average radiation pressure force. Since the original restoring force is also position dependent $F(x) = -kx$, the mechanical-position dependent average radiation pressure force modifies the spring constant, and thus the mechanical frequency. From Eq. (3.29) we can obtain the average optical amplitude at a given mechanical position x:

$$\bar{\alpha}(x) = \frac{-\sqrt{\kappa_{ext}}\,\alpha_{in}}{i\Delta - \kappa/2 + iGx}, \tag{3.33}$$

from which the position dependent average radiation pressure force is: $\bar{F}_{rp}(x) = \hbar G|\bar{\alpha}(x)|^2$. Then the extra spring constant induced by the average radiation pressure force is $\delta k =$

---

[2] Assuming a complex function $f(t) = x(t) + iy(t)$, where $x(t)$ and $y(t)$ are real functions, we have $\dot{f} = \dot{x} + i\dot{y}$. Thus, $\mathrm{d}\,\mathrm{Re}(f)/\mathrm{d}t = \mathrm{Re}(\dot{f})$.

$2m\Omega_m\delta\Omega_m = -\mathrm{d}\bar{F}_{rp}/\mathrm{d}x|_{x=0}$, where $x = 0$ is the new equilibrium position. Therefore, the mechanical frequency change induced by the average radiation pressure force is obtained from the derivative of the average radiation pressure force near the new equilibrium position:

$$\delta\Omega_m = \frac{-\mathrm{d}\bar{F}_{rp}/\mathrm{d}x|_{x=0}}{2m\Omega_m} = \frac{2g_0^2\kappa_{ext}|\alpha_{in}|^2\Delta}{(\kappa^2/4+\Delta^2)^2}, \tag{3.34}$$

where $|\alpha_{in}|^2$ is the input photon flux, defined as the incident laser power P_{in} divided by the photon energy $\hbar\omega_L$, and G is replaced by $g_0 x_{\text{ZPF}}$. If we introduce a new variable $n_{cav}^{max} = 4\kappa_{ext}|\alpha_{in}|^2/\kappa^2$ for the maximum average intracavity photon number with zero laser detuning at given input power, the mechanical frequency change can be further simplified to be $8\Delta n_{cav}^{max}\left(\frac{g_0}{\kappa}\right)^2/\left[1+(2\Delta/\kappa)^2\right]^2$. Note that $\delta\Omega_m$ has the same sign as the laser detuning Δ, which means there will be spring hardening with a blue-detuned laser frequency, and spring softening with red detuning.

3.1.5 Solution of the Dynamics

Subtracting the DC terms and neglecting the higher order terms of the dynamics variables from Eq. (3.29) and Eq. (3.31) yields the linearized equations of motion for the system's dynamics:

$$\delta\dot{\alpha} = i\Delta\delta\alpha - \frac{\kappa}{2}\delta\alpha + iG\delta x\bar{\alpha}, \tag{3.35a}$$

$$\delta\ddot{x} = -\Omega_m^2\delta x - \Gamma\delta\dot{x} + \frac{G\hbar}{m}\left(\bar{\alpha}^*\delta\alpha + \bar{\alpha}\delta\alpha^*\right). \tag{3.35b}$$

Using the linearized interaction Hamiltonian (Eq. (3.21)), Heisenberg equations of motion give the linearized equations of motion for the quantum case:

$$\delta\dot{a} = i\Delta\delta a - \frac{\kappa}{2}\delta a + ig(b+b^\dagger) + \sqrt{\kappa_{ext}}\,\delta a_{in}(t) + \sqrt{\kappa_0}\,f(t), \tag{3.36a}$$

$$\dot{b} = -i\Omega_m b - \frac{\Gamma}{2}b + ig\left(\delta a + \delta a^\dagger\right) + \sqrt{\Gamma}\,b_{in}(t). \tag{3.36b}$$

where $g = g_0\sqrt{n_{cav}}$, $\delta a_{in}(t)$ is the external vacuum fluctuations coupled into the cavity, $f(t)$ is the vacuum fluctuations coupled into the cavity through the cavity internal loss channel, and $b_{in}(t)$ is the thermal noise.

The equations of motion are two sets of coupled ODEs, and they are easier to solve in the frequency domain, as the operation of differentiation in the time domain corresponds to multiplication by the frequency. The equations of motion in the frequency domain are obtained by performing a Fourier transform on the equations in time domain. Before proceeding to solving the equations of motion, the convention for the Fourier transform used in this thesis is first defined. Given a function of time, $f(t)$, its Fourier transform is below:

$$\tilde{f}(\omega) = \int_{-\infty}^{\infty} f(t)e^{i\omega t}\mathrm{d}t. \tag{3.37}$$

When this integral converges the function $\tilde{f}(\omega)$ is the Fourier form of the original function $f(t)$, whose magnitude represents the amount of that frequency component presented in the original function, and whose complex argument is the phase offset of the basic sinusoid at that frequency. The inverse Fourier transform given below mathematically synthesises the original function $f(t)$ from the basis of harmonic waves $e^{-i\omega t}$ in the continuum limit:

$$f(t) = \frac{1}{2\pi}\int_{-\infty}^{\infty}\tilde{f}(\omega)e^{-i\omega t}\mathrm{d}\omega. \tag{3.38}$$

It is worth to state the convention that $b(\omega)$ and $b^\dagger(\omega)$ are defined as the Fourier transforms of $b(t)$ and $b^\dagger(t)$ respectively[3], and this convention will be obeyed consistently in this thesis. Following this convention it can be proved that the operators and classical variables obey the relations

$$a^\dagger(\omega) = [a(-\omega)]^\dagger, \tag{3.39a}$$

$$\delta\alpha^*(\omega) = [\delta\alpha(-\omega)]^*. \tag{3.39b}$$

Consistently following this relation in solving the equations of motion is very important.

Using Fourier transform the equations of motion (Eq. (3.35)) in the frequency domain have the form:

$$-i\omega\delta\alpha(\omega) = i\Delta\delta\alpha(\omega) - \frac{\kappa}{2}\delta\alpha(\omega) + iG\bar{\alpha}\,\delta x(\omega), \tag{3.40a}$$

$$-\omega^2\delta x(\omega) = -\Omega_m^2\delta x(\omega) + i\omega\Gamma\delta x(\omega) + \frac{G\hbar}{m}\left[\bar{\alpha}^*\delta\alpha(\omega) + \bar{\alpha}\delta\alpha^*(\omega)\right]. \tag{3.40b}$$

In the linearized case, the optomechanical system is acting as a Linear Time-Invariant (LTI) system [58], such that in the frequency domain the response of the system is equal to the product of the power spectrum of the drive force and the transfer function of the system. The transfer function of the mechanical oscillator is called its *susceptibility*, defined as $\chi_m(\omega) = \delta x(\omega)/F(\omega)$. For a general mechanical oscillator without optomechanical interaction, its susceptibility takes the form of $\chi_m^{-1}(\omega) = m[(\Omega_m^2 - \omega^2) - i\Gamma\omega]$. For a high quality mechanical oscillator ($Q = \Omega_m/\kappa \ll 1$), this can be approximated as $\chi_m^{-1}(\omega) = -i\,m\,\Omega_m[-i(\omega - \Omega_m) + \Gamma]$ [4].

Optical Spring Effect and Optomechanical Cooling

Solving the equations of motion [Eq. (3.40)] with a weak force $F(\omega)$ exerted on the mechanical oscillator, the solution of the mechanical position can be conveniently denoted as:

$$\delta x(\omega) = F(\omega)\cdot\chi_{m,\mathrm{eff}}(\omega), \tag{3.41}$$

where $\chi_{m,\mathrm{eff}}(\omega)$ the effective mechanical susceptibility modified by the optomechanical interaction is defined as $\chi_{m,\mathrm{eff}}^{-1}(\omega) = \chi_m^{-1}(\omega) + \Sigma(\omega)$, $\chi_m^{-1}(\omega)$ is the original mechanical susceptibility, and $\Sigma(\omega)$ is the part contributed by the optomechanical interaction. From the solution of the equations of motion [Eq. (3.40b)], $\Sigma(\omega)$ has the form:

$$\Sigma(\omega) = 2m\Omega_m g^2\left(\frac{1}{\omega + \Delta + i\kappa/2} - \frac{1}{\omega - \Delta + i\kappa/2}\right), \tag{3.42}$$

---

[3] The Fourier transform of the conjugate transpose of an operator is not equal to the conjugate transpose of the Fourier transform of this operator.

[4] Be aware that $\frac{1}{\pi}\frac{\Gamma}{(\omega-\Omega_m)^2+\Gamma^2}$ is a normalized Lorentzian function and its integral is equal to unity.

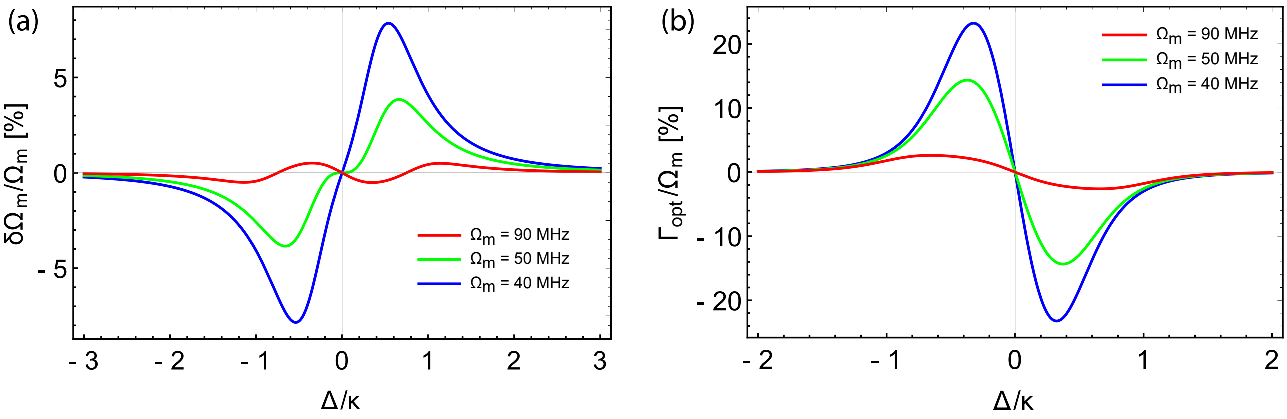

Figure 3.3: (a) optomechanical-interaction induced mechanical frequency shift $\delta\Omega_m(\Omega_m)$ versus optical linewidth normalized laser detuning Δ/κ; (b) optomechanical-interaction induced mechanical damping $\Gamma_{\text{opt}}(\Omega_m)$ versus optical linewidth normalized laser detuning Δ/κ. The system parameters used in this figure: $m = 1$ picogram, input laser power = 100 μW, $\kappa/2\pi = 100$ MHz, $\kappa_{ext}/2\pi = 50$ MHz, $G/2\pi = 1$ GHz/nm.

where $G^2|\bar{\alpha}|^2$ is replaced by g^2/x^2_{ZPF}. The real part of $\Sigma(\omega)$ contributes to the mechanical frequency change (optical spring effect) due to the optomechanical interaction, and the imaginary part corresponds to the mechanical linewidth change (optical damping effect). Thus we can define the two parts of $\Sigma(\omega)$ as: $\Sigma(\omega) = m[2\Omega_m\delta\Omega_m(\omega) - i\omega\Gamma_{\text{opt}}]$. From Eq. (3.42), $\delta\Omega_m(\omega)$ and Γ_{opt} are found to be:

$$\delta\Omega_m(\omega) = g^2\left(\frac{\omega+\Delta}{(\omega+\Delta)^2+\kappa^2/4} - \frac{\omega-\Delta}{(\omega-\Delta)^2+\kappa^2/4}\right), \tag{3.43}$$

$$\Gamma_{\text{opt}}(\omega) = g^2\frac{\Omega_m}{\omega}\left(\frac{\kappa}{(\omega+\Delta)^2+\kappa^2/4} - \frac{\kappa}{(\omega-\Delta)^2+\kappa^2/4}\right). \tag{3.44}$$

In the resolved sideband regime ($\Omega_m \gg \kappa$), when the laser is blue-detuned by the mechanical frequency: $\Delta = \Omega_m$, the mechanical linewidth change is approximately: $\Gamma_{\text{opt}} \approx -\frac{4g^2}{\kappa} = -C\Gamma$, while when the laser is red-detuned by the mechanical frequency the mechanical linewidth change is approximately: $\Gamma_{\text{opt}} \approx C\Gamma$. The result of the optical spring and optomechanical damping effects around the mechanical resonance are plotted in Fig. 3.3 for the unresolved sideband regime ($\kappa > \Omega_m$). In Fig. 3.3(a) spring hardening and softening effects happens at the blue-detuning and red-detuning sides respectively. When the system is deep in the unresolved sideband regime ($\kappa \gg \Omega_m$), Eq. (3.43) is approximately equal to its steady state counterpart [Eq. (3.34)], as shown by the blue curve in Fig. 3.3(a), where the largest frequency shift happens around the two steepest points of the optical detuning. Fig. 3.3(b) shows the optomechanical cooling on the red-detuning side, and the optomechanical heating on the blue-detuning side. Further, when the system approaches the resolved sideband regime, the highest cooling (heating) efficiency detuning transitions from the steepest point of the optical mode to the detuning equal to the mechanical frequency.

Optomechanically Induced Transparency/ Amplification

The optomechanical interaction not only affects the mechanical linewidth and subsequently generates heating and cooling of the mechanical motion, it also affects the effective optical linewidth for some particular detunings, which is termed as Optomechanically Induced Transparency/ Amplification (OMIT/OMIA) depending on whether the optical linewidth is narrowed or broadened at that detuning. To investigate this effect, we need two optical fields: a_1 for the strong pump field and δa_2 for the weak probe field, and assume for simplicity that the system is in the resolved sideband regime ($\Omega_m \gg \kappa$). Then the equations of motion in the frame rotating at the pump field frequency ω_L can be derived from the original optomechanical Hamiltonian [Eq. (3.24)] to have a similar form with the general optomechanical equations of motion [Eq. (3.36)]:

$$\begin{aligned} -i\omega a_1(\omega) &= i\Delta_1 a_1 - \frac{\kappa}{2}a_1 + ig_0\alpha_1(b+b^\dagger) + \sqrt{\kappa_{ext}}\;\alpha_{in,1} && (3.45a)\\ -i\omega \delta a_2(\omega) &= i\Delta_2 \delta a_2 - \frac{\kappa}{2}\delta a_2 + ig_0\alpha_1(b+b^\dagger) + \sqrt{\kappa_{ext}}\;\delta a_{2,in} && (3.45b)\\ -i\omega b(\omega) &= -i\Omega_m b - \frac{\Gamma}{2}b + ig_0\alpha_1(\delta a_2 + \delta a_2^\dagger)\,, && (3.45c)\end{aligned}$$

where $\Delta_1 = \omega_L - \omega_{\text{cav}}$ is the pump field detuning (fixed at $\pm\Omega_m$ respectively for OMIA/T), and $\Delta_2 = \omega_L - \omega_{pr}$ is the frequency difference between the probe and pump fields, $\alpha_{in,1}$ is the drive for the pump field, α_1 is the steady state solution of the pump field. Note that the dynamics of the strong pump field a_1 is neglected, and the optomechanical interaction is boosted by the steady state intracavity field of the strong pump field. To solve for α_1, we neglect the optomechanical interaction for the detuned strong pump field a_1, assuming the steady state of the pump field only changes the equilibrium position of the mechanical oscillator and the optical cavity linewidth stays the same. Thus the pump field's steady state solution is:

$$\alpha_1 = \frac{\sqrt{\kappa_{ext}}\;\alpha_{in,1}}{-i\Delta_1 + \kappa/2}. \tag{3.46}$$

With the rotating wave approximations mentioned in Eq. (3.22), for $\Delta_1 = -\Omega_m$ the solution for δa_2 is:

$$\delta a_2(\omega) = \frac{\sqrt{\kappa_{ext}}\;\delta a_{2,in}}{-i(\omega-\Delta_2) + \kappa/2 + \frac{g^2}{-i(\omega+\Omega_m)+\Gamma/2}}, \tag{3.47}$$

where $g = \alpha_1\, g_0$, and Δ_2 has to be $-\Omega_m$. The output spectrum of the cavity depends on whether the reflection or the transmission is measured as output light, but the relative amplitude (dip-depth) of the OMIT feature shown on the cavity response to the probe field is given by:

$$\frac{\delta a_2(-\Omega_m)}{\delta a_2'(-\Omega_m)} = \frac{1}{1+C}, \tag{3.48}$$

where $\delta a_2'(-\Omega_m) = \frac{\sqrt{\kappa_{ext}}\;\delta a_{2,in}}{\kappa/2}$ is the response of a bare cavity to the probe field, and C is the multi-photon coorperativity.

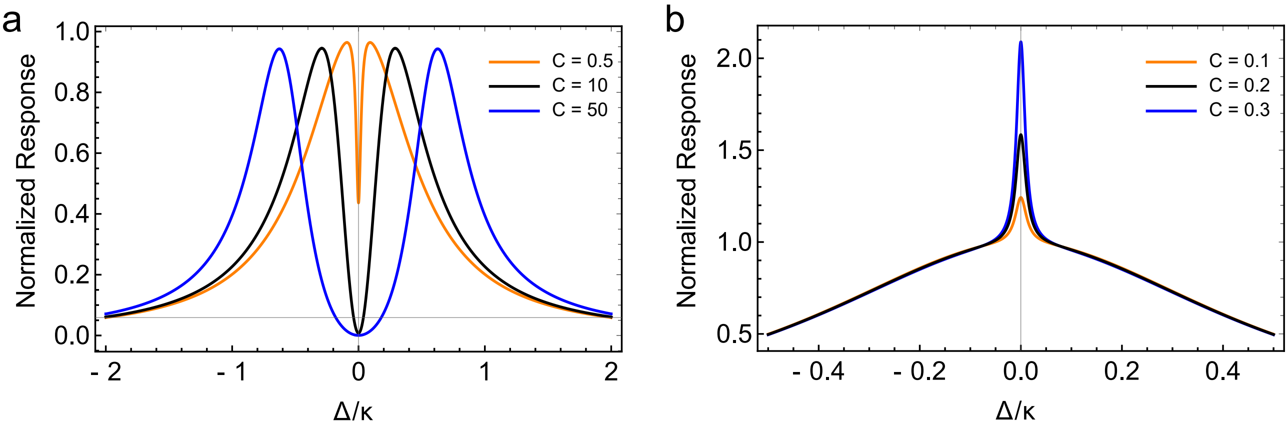

Figure 3.4: OMIT (a) and OMIA (b) exhibited on the normalized cavity intensity responses to the probe field, plotted using the squared modulus of Eq. (3.47) and Eq. (3.49) respectively. The system parameters used in this figure: $m = 1$ picogram, $\kappa/2\pi = 10$ MHz, $\kappa_{ext}/2\pi = 5$ MHz, $\Omega_m/2\pi = 300$ MHz, $\Gamma/2\pi = 300$ kHz, $G/2\pi = 0.5$ GHz/nm..

Similarly for the blue-detuned pump laser $\Delta_1 = \Omega_m$, with the rotating wave approximations mentioned in Eq. (3.23), the solution of δa_2 is:

$$\delta a_2(\omega) = \frac{\sqrt{\kappa_{ext}}\ \delta a_{2,in}}{-i(\omega - \Delta_2) + \kappa/2 - \frac{g^2}{-i(\omega-\Omega_m)+\Gamma/2}}, \tag{3.49}$$

where $g = \alpha_1 \, g_0$, and Δ_2 has to be Ω_m. Then the relative amplitude of the OMIA feature on the cavity response to the probe field is is given by:

$$\frac{\delta a_2(\Omega_m)}{\delta a_2'(\Omega_m)} = \frac{1}{1 - C}. \tag{3.50}$$

Note that the theory for OMIA is only valid for $C < 1$, because when C larger than 1, the effective optical linewidth, which is defined here as $\kappa - 4g^2/\Gamma$ based on the real part of the denominator of Eq. (3.49), will be negative. In reality, when the effective optical linewidth approaches zero, there will be extra optical attenuation from nonlinearities, which can cause saturation. Note also that the OMIA feature appears on the reflected light only when the Fabry-Perot cavity is under-coupled, but appears on the transmitted light for the Fabry-Perot cavity with any coupling. Although the solutions for OMIT and OMIA look very similar, they correspond to the pump laser detuning of different signs. The signs in the denominator of Eq. (3.48) and Eq. (3.50) show the contrasting difference of these two phenomena.

From the results shown in Fig. 3.4, we will find if the strong pump field is blue-detuned by the mechanical frequency and is strong enough to narrow the mechanical linewidth to zero: $\Gamma_{\text{opt}} = -\Gamma$ (*phonon lasing*), the effective optical linewidth (experienced by the probe field) will be substantially narrowed. This phenomenon is called OMIA, which basically can be understood as when the mechanical mode is driven to a strong coherent amplitude, the probe field will be amplified by the coherent mechanical mode through the strongly biased Stokes scattering. Similarly for OMIT, if the strong pump field is red-tuned by $-\Omega_m$ and cools the mechanical mode, the probe field will experience a large effective optical linewidth as it is strongly attenuated by the strongly biased anti-Stokes scattering. OMIT demonstrates that the optical field is strong enough to obtain the coherent optomechanical interaction, equivalently the cooperativity $C = \frac{4g^2}{\kappa\Gamma} \geq 1$.

Spectral Analysis

The solution of $\delta x(\omega)$ not only enables us to explain how the optomechanical interaction affects the mechanical oscillator, it can also directly give the spectral response (power spectral density) of the mechanical system. Before we proceed to calculate the power spectral density, the basic statistics are introduced to deal with the stochastic driving forces in the equations of motion.

First, the autocorrelation is defined as the correlation of a signal at time t with a delayed version of itself at $t+\tau$ as a function of delay τ, which can be intuitively understood as the similarity between observations of the signal as a function of the time lag τ between them. Given a wide-sense stationary random process [5] $\{X_t\}$ with time-independent average μ and variance σ^2, where X_t is the value produced by a given run of the process at time t, the auto-correlation of the random process are mathematically defined as:

$$\mathrm{R}_{XX}(t, t+\tau) = \mathrm{E}[X(t)X^*(t+\tau)], \tag{3.51}$$

and auto-covariance:

$$\mathrm{K}_{XX}(t, t+\tau) = \mathrm{E}[(X(t)-\mu)(X(t+\tau)-\mu)^*] = \mathrm{R}_{XX}(t, t+\tau) - \mu\mu^* \, . \tag{3.52}$$

The power spectral density $S_{bb}(\omega)$ of a fluctuation operator $b(t)$ from a stationary process is defined from the Wiener-Khinchin theorem as [51]:

$$S_{bb}(\omega) = \int_{-\infty}^{\infty} \langle b^\dagger(t) b(0) \rangle e^{i\omega(t-0)} \mathrm{d}t, \tag{3.53}$$

which is the Fourier transform of the autocorrelation of the operator $b(t)$. Following this definition, we prove that the power spectral density $S_{bb}(\omega)$ can also be calculated directly via the Fourier transformed lowering and raising operators:

$$\begin{aligned} S_{bb}(\omega) &= \int_{-\infty}^{\infty} \left\langle \frac{1}{2\pi} \int_{-\infty}^{\infty} b^\dagger(\omega'') e^{-i\omega'' t} \mathrm{d}\omega'' \cdot \frac{1}{2\pi} \int_{-\infty}^{\infty} b(\omega') e^{-i\omega' 0} \mathrm{d}\omega' \right\rangle e^{i\omega t} \mathrm{d}t \\ &= \frac{1}{4\pi^2} \int_{-\infty}^{\infty} \int_{-\infty}^{\infty} \int_{-\infty}^{\infty} \langle b^\dagger(\omega'') b(\omega') \rangle e^{-i\omega'' t} \mathrm{d}\omega'' \, e^{i\omega t} \, \mathrm{d}t \, \mathrm{d}\omega' \\ &= \frac{1}{2\pi} \int_{-\infty}^{\infty} \langle b^\dagger(\omega) b(\omega') \rangle \, \mathrm{d}\omega' \end{aligned} \tag{3.54}$$

Unless stated otherwise, all power spectra in this thesis are calculated in this way.

Since the mechanical position $\delta x(t)$ is proportional to the real part of the mechanical annihilation operator [Eq. (3.28)], the power spectral density of mechanical position is obtained from the Wiener-Khinchin theorem [50]:

$$S_{xx}(\omega) = \int_{-\infty}^{\infty} \langle \delta x(t) \delta x(0) \rangle e^{i\omega t} \mathrm{d}t = \left\langle |\delta x(\omega)|^2 \right\rangle . \tag{3.55}$$

---

[5] A wide-sense stationary random process is a random processes which has constant 1st moment (*i.e.* the mean) and autocovariance, and finite 2nd moment for all times.

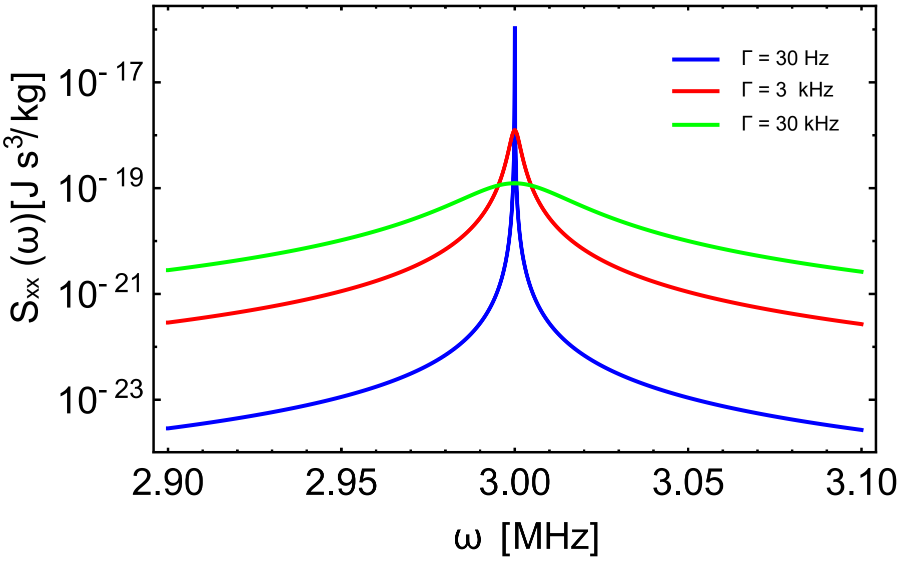

Figure 3.5: Power spectral density of a mechanical oscillator with $m = 1$ picogram, $\Omega_m/2\pi = 3$ MHz, $T = 300$ K, and various damping rates Γ: 30 Hz (blue), 3 kHz (red), 30 kHz (green). Note that the integrated power spectral density is the same for all the traces.

Let us first discuss a mechanical oscillator assumed to be in thermal equilibrium of temperature T and without the optomechanical interaction, the integration of the power spectral density yields the variance $\langle \delta x^2 \rangle$ of the mechanical position for a thermally driven oscillator in equilibrium with a bath at temperature T. The equipartition theorem leads to $\langle \delta x^2 \rangle = k_B T/(m\Omega_m^2)$, which can lead us to the amplitude of the mechanical oscillator in thermal equilibrium. Let us follow the assumption that the mechanical oscillator is only driven by thermal force F_{th}, which according to the *fluctuation-dissipation theorem* obeys the temporal correlation rule $\langle F_{\text{th}}(t) F_{\text{th}}(t') \rangle = 2m\Gamma k_B T \delta(t - t')$ and has the power spectral density $S_{\text{FF}}(\omega) = 2m\Gamma k_B T$ obtained from the Fourier transform of the correlation rule [59]. With the power spectral density of the thermal driving force, $\delta x(\omega) = \chi_m(\omega) F_{\text{ex}}(\omega)$ leads to the power spectral density of the mechanical motion at temperature T: $S_{xx}(\omega) = 2m\Gamma k_B T |\chi_m|^2$, where m is the mass of the mechanical oscillator, k_B is the Boltzmann constant, T is the temperature of the thermal bath, Γ is the mechanical damping rate, and χ_m is the mechanical susceptibility. The power spectral density of a mechanical oscillator thermalized to 300 K is plotted in Fig. 3.5, for different mechanical damping rates Γ.

Similarly, solving the linearized equations of motion for the quantum operators [Eq. (3.36)], we can obtain the solution of the mechanical annihilation operator $b(\omega)$. From the inverse process of Eq. (3.53) we have the steady-state variance of the mechanical oscillator lowering operator as below:

$$\langle |b(t)|^2 \rangle = \frac{1}{2\pi} \int_{-\infty}^{\infty} S_{bb}(\omega)\, \mathrm{d}\omega, \tag{3.56}$$

which is equal to the average occupancy of the mechanical oscillator.

For convenience, let us assume a simplified optomechanical interaction which only cools or heats the mechanical oscillator by changing the mechanical linewidth from the intrinsic linewidth Γ to the effective linewidth Γ_{eff}, which is defined as $\Gamma \pm 4g^2/\kappa$ and the sign corresponding to laser detuning by $\mp\Omega_m$. In addition, we also make the assumption that the optical damping rate Γ_{opt} is approximately not frequency-dependent near the mechanical resonance frequency, for example a system in the resolved sideband regime with laser detuning $|\Delta| = \Omega_m$, where $\Gamma_{\text{opt}} = \pm C\Gamma$. Then the solution of the equation [Eq.(3.36b)] of motion for the mechanical annihilation operator takes the form:

$$b(\omega) = \frac{\sqrt{\Gamma}\, b_{in}(\omega)}{-i(\omega - \Omega_m) + \Gamma_{\text{eff}}/2} \tag{3.57}$$

From the temporal correlation [Eq. (3.26)] of the mechanical thermal noise $b_{in}(t)$, we get the correlation relation in frequency domain as: $\frac{1}{2\pi}\langle b_{in}^{\dagger}(\omega) b_{in}(\omega')\rangle = n_{th}\delta(\omega + \omega')$ [6]. With this, the mechanical occupancy under the simplified optomechanical interaction is:

$$\begin{aligned} n_b &= \frac{1}{2\pi}\int_{-\infty}^{\infty}\frac{1}{2\pi}\int_{-\infty}^{\infty}\langle b^{\dagger}(\omega)b(\omega')\rangle\, \mathrm{d}\omega'\mathrm{d}\omega \\ &= \frac{1}{2\pi}\int_{-\infty}^{\infty}\frac{\Gamma n_{th}}{(\omega+\Omega_m)^2 + (\Gamma_{\text{eff}}/2)^2}\mathrm{d}\omega \\ &= \frac{\Gamma\, n_{th}}{\Gamma_{\text{eff}}}\frac{1}{\pi}\int_{-\infty}^{\infty}\frac{\Gamma_{\text{eff}}/2}{(\omega+\Omega_m)^2 + (\Gamma_{\text{eff}}/2)^2}\mathrm{d}\omega \\ &= \frac{\Gamma\, n_{th}}{\Gamma_{\text{eff}}}\,. \end{aligned} \tag{3.58}$$

This means that when the mechanical oscillator is coupled to two independent baths (an optical bath and an environment thermal bath) the equilibrium mechanical occupancy is the mean of the two bath occupancies weighted by the respective coupling rates (Γ and $\Gamma_{opt} = \pm C\Gamma$) [52]. Additionally, when the laser is red-detuned by Ω_m, Eq. (3.58) is reduced to be $n_b = n_{th}/(1+C)$, which proves that if the cooperativity is larger than the thermal occupancy the mechanical mode can be cooled to its ground state.

3.2 Superfluid Helium-4

Unlike liquid, solid and gas phases, superfluidity is a quantum-mechanical phase of matter. Simply speaking, when a gas which obeys Bose–Einstein statistics is cooled below a critical temperature T_λ, all the constituent atoms of the Bose gas are in the quantum ground state, and the interatomic distance becomes comparable to the thermal de Broglie wavelength [$\lambda_{\text{th}} = h/(mv)$], such that the wave packet of the matter wave of each constituent atom overlaps and interferes with one another [60]. Consequently via cooling below the critical temperature a Bose gas undergoes Bose-Einstein condensation, and becomes a macroscopic quantum object with long range coherence, and can be described by one unique wavefunction [61]

$$\Psi(\vec{r}, t) = \sqrt{\rho_s(\vec{r}, t)/m}\; e^{i\phi(\vec{r}, t)}, \tag{3.59}$$

---

[6] This equation is derived via expressing the operators $b_{in}^{\dagger}(\omega)$ and $b_{in}(\omega')$ as the Fourier transform of the corresponding operators in the time domain. Note that $e^{i\omega' t}$ and $2\pi\delta(\omega+\omega')$ are a Fourier transform pair as the exponent has a positive sign in the Fourier transform definition in the thesis.

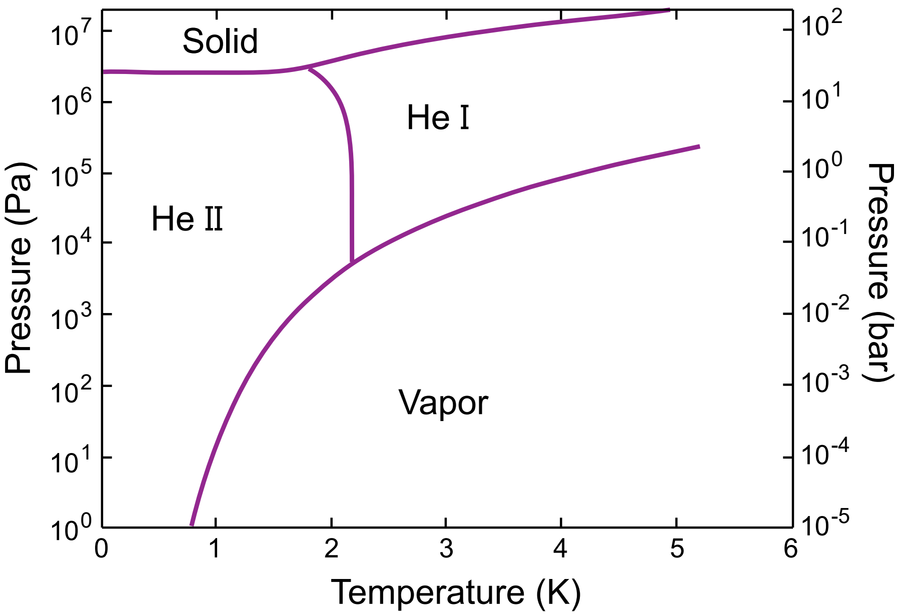

Figure 3.6: Helium-4 phase diagram. Adapted from [62].

where m is the mass of one atom, $\rho_s(\vec{r}, t)$ is the density distribution of the condensate, and $\phi(\vec{r}, t)$ is the phase of the wavefunction. The spatial gradient of $\phi(\vec{r}, t)$ gives the velocity of the condensate:

$$\vec{v}_s = \hbar/m\vec{\nabla}\phi. \tag{3.60}$$

The first discovered superfluid was superfluid helium-4, when Keesom and Kapitza observed the abnormally high thermal conductivity and low viscosity of liquid helium below the lambda point (2.17 K) [15, 63]. This superfluid phase is conventionally termed as Helium II, while the normal fluid phase above 2.17 K is termed as Helium I, as is shown in the phase diagram of helium-4 (Fig. 3.6). This phase transition from normal fluid to superfluid was first explained as Bose-Einstein condensation of helium-4 atoms by London [64]. Following that Tisza and Landau proposed the two-fluid model, and developed the hydrodynamics of superfluid helium-4 based on the two-fluid model [65, 66]. The two-fluid model states superfluid is composed of two components: a superfluid component and a normal fluid component, which can also be understood as each helium-4 atom below 2.17 K has a certain probability of being in the Bose-Einstein condensate state. As shown in Fig. 3.7 below the lambda point, the fractional density of the superfluid component increases, and eventually the superfluid component density is equal to the liquid helium density, meaning every atom in the liquid helium has a unity probability of being in the BEC state [67]. Note that unlike BEC of dilute Bose gas which has a micron-scale quantum coherence length (also termed as the healing length ξ), the typical healing length of superfluid helium-4 is at the Angstrom-scale [68, 69].

$$\xi(T) = 0.34(1 - \frac{T}{T_\lambda})^{-0.67} \tag{3.61}$$

The typical healing length at our experimental temperatures of 20 mK is around 0.4 nm. Note that the healing length diverges for T approaching T_λ from below.

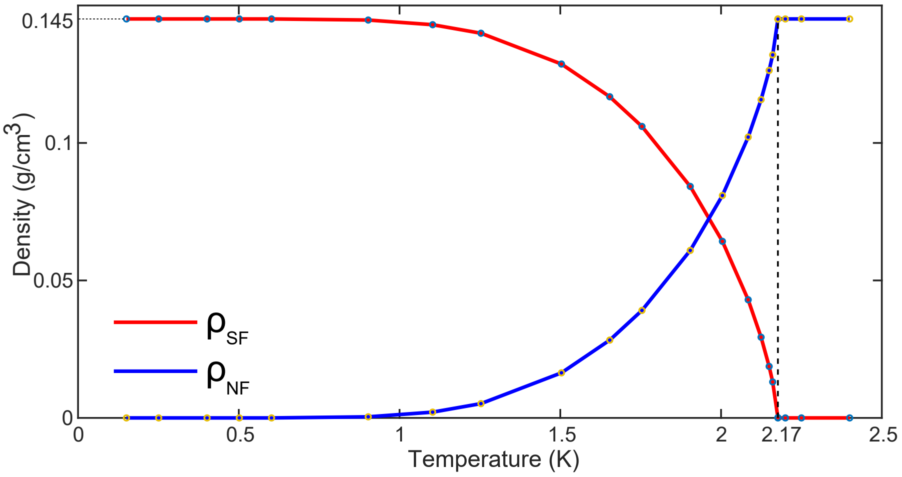

Figure 3.7: Density of the superfluid and normal fluid components of liquid helium-4 (ρ_{SF} and ρ_{NF} respectively), as a function of temperature, with data from [62] .

3.2.1 Superfluid Josephson Effect

The Josephson effect is widely used in superconducting circuits to build qubits (superconducting quantum interference devices (SQUIDs)) for quantum computing. The Josephson effect is the dissipationless tunnelling of electron Cooper pairs between two superconductors separated by a thin insulating layer, as predicted Josephson [70]. The direct supercurrent with amplitude less than the critical current flows with zero-voltage drop across the junction (DC Josephson effect). In the case that a constant voltage V is established across the junction, there is a sinusoidal supercurrent with frequency linearly dependent on the voltage (AC Josephson effect).

The Josephson effect in superfluid helium-4 happens in a similar way. Fig. 3.8 illustrates a superfluid "Josephson junction" composed of two macroscopic reservoirs of superfluid helium in equilibrium and separated by a thin membrane with a nanosized orifice. Since the two superfluid reservoirs are separated by the thin membrane, they evolve adiabatically and independently with their individual wavefunctions. The phase difference $\Delta\phi$ of the two wavefunctions during the evolution is determined by the chemical potential difference $\Delta\mu$ between the two superfluid

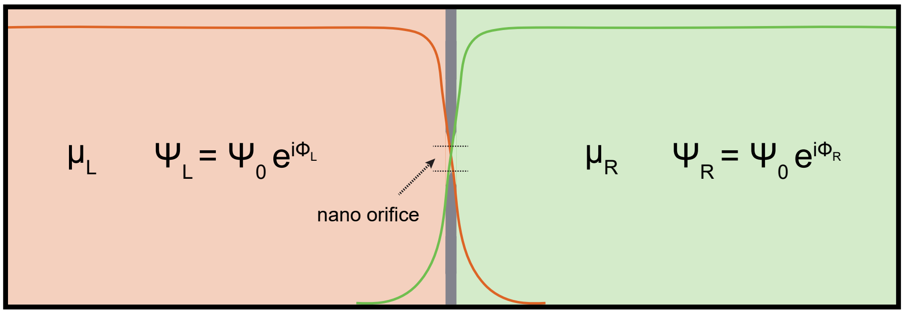

Figure 3.8: Quantum interference between two weakly connected superfluid reservoirs where the nano orifice working as a superfluid Josephson junction.

reservoirs, following the Josephson-Anderson equation [71]:

$$\frac{d\Delta\phi}{dt} = -\frac{\Delta\mu}{\hbar}, \tag{3.62}$$

where $\Delta\mu$ is the chemical potential defined as:

$$\Delta\mu = m_{\mathrm{He}}(\Delta P/\rho_s - s\Delta T) \tag{3.63}$$

with ρ_s the superfluid mass density, ΔP the pressure difference, s the entropy per unit mass and ΔT the temperature difference. The nano orifice in the thin membrane weakly links the two wavefunctions, such that the "evanescent field" of each wavefunction extends into the other superfluid reservoir. Although the characteristic length of the "evanescent field" is equal to the healing length ξ on the order of a few Angstroms, the interference between the two wavefunctions due to such "evanescent coupling" results in the quantum tunnelling of helium atoms through the membrane barrier, which is the superfluid Josephson effect. Similar to the AC Josephson effect in superconductors, if a constant chemical potential difference $\Delta\mu$ is applied across the weak link, there will be a sinusoidal superfluid flow [$I_J = I_c sin(\Delta\phi + \phi_0)$] through the nano orifice. The Josephson effect in superfluid was first predicted by P. W. Anderson as phase slippage [72, 73], which is the 2π phase decrease of the superfluid wave function when superfluid flows above the critical velocity in a 'strong link'. This phase slippage phenomenon was observed by Avenel and Varoquaux with a nano orifice slightly larger than the superfluid healing length [74]. The big orifice they used acts as the "strong link", so that when superfluid flow reaches the critical velocity, a vortex will be shed and the 2π phase slippage will decrease the superfluid velocity abruptly [Eq. (3.60)]. Since the 1990s the Packard group at University of California, Berkeley fabricated the nanosized orifice at the scale of the superfluid ^{3}He healing length (tens of nanometers) [75]. With that they invented a bulk superfluid interferometer/gyroscope analogous to a SQUID, and observed the interference exhibited as the sinusoidal Josephson current [76–79]. Further, they found the transition from the phase slippage regime to the sinusoidal Josephson oscillation using the temperature dependence of the healing length [68] and directly measured the quantum phase gradient in superfluid helium-4 flow [80].

3.2.2 Superfluid Fountain Effect

The superfluid fountain effect is also called the superfluid *thermomechanical effect*. It is the direct manifestation of the two-fluid model, and results from the phase gradient origin of superfluid velocity [60]. The historical experiment demonstrating the superfluid fountain effect is described as following. Two vessels both contain superfluid helium. One vessel is assumed be at 0 K and zero pressure. The two vessels are connected by a so-called superleak, which is a fine porous plug, such that the superfluid component with zero viscosity can flow through it, but the normal component is blocked [81]. When the temperature in the other vessel is

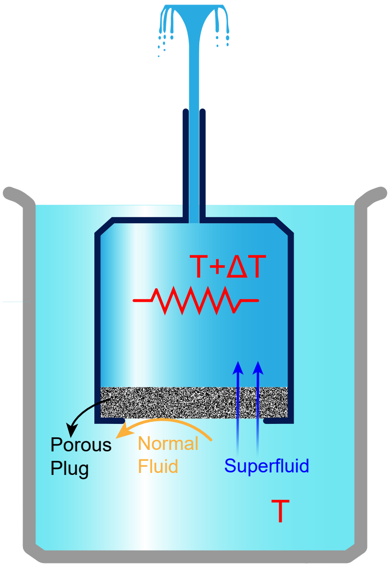

Figure 3.9: Illustration of the superfluid fountain effect, adapted from [82]

increased, there will be a chemical potential difference between the superfluid in the two vessel, and subsequently a phase gradient inducing superfluid to flow toward the heat source. After superfluid flows through the fine power, the high temperature in the other vessel turns superfluid into normal fluid. This eventually raises the pressure in the heated vessel and the helium inside can squirt like a fountain. We will see in Chapter 4 how this effect can be leveraged to apply strong forces at the micro-scale.

3.2.3 Acoustic Excitations in Superfluid

Among all the excitations in superfluid helium-4, there are mainly three types of acoustic excitations, and they are named first sound (density wave), second sound (temperature wave) and third sound. Third sound waves are a type of excitation unique to superfluid thin films [18, 84–88], whereas the first and second sound waves exist only in bulk superfluid, where the bulk form of superfluid is not assumed to be incompressible. As illustrated in Fig. 3.10 a third sound wave is exhibited as film thickness fluctuations of the superfluid component, while the normal fluid component (not shown) is viscously clamped to the substrate. Additionally, since the superfluid component does not carry entropy, the crests where there is more superfluid component have slightly lower temperature, and the troughs have slightly high temperature, such

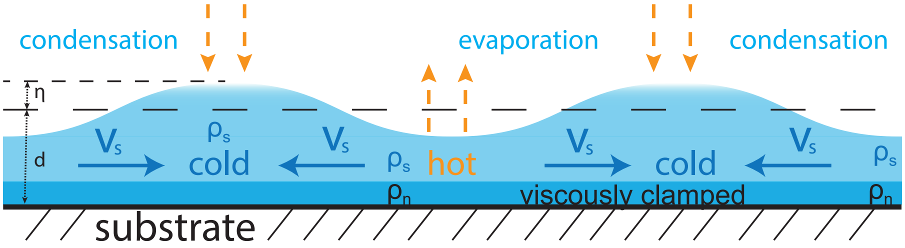

Figure 3.10: Illustration of third sound on a thin superfluid film, adapted from [83].

Table 3.1: Van der Waals coefficients α_{vdw} for liquid helium on different substrate materials [2].

Material	α_{vdw} $[m^5 s^{-2}]$
Silica	2.6×10^{-24}
CaF2	2.2×10^{-24}
Silicon	3.5×10^{-24}
MgO	2.8×10^{-24}

that the third sound wave also exhibits temperature alternations, accompanied by evaporation and condensation [84]. With zero superfluid viscosity, third sound waves are expected to have ultra-low loss. It is believed the evaporation and condensation process, the thermal contact with the substrate and interactions with vortices might cause third sound loss [89,90]. However, the loss mechanisms are still not perfectly understood. Third sound waves are analogous to shallow water waves, but their restoring force is the van der Waals interaction between the helium atoms and the substrate, instead of gravity for shallow water waves [91]. For superfluid thin films the van der Waals potential at the film surface is:

$$U(d) = -\frac{\alpha_{\text{vdw}}}{d^3}, \tag{3.64}$$

where α_{vdw} is the van der Waals coefficient characterizing the strength of the attractive force and is summarized for several substrates in Table 3.2.3, and d is the film thickness. The van der Waals force per unit mass is the gradient of the potential along the direction of the film thickness [92, 93]:

$$g_{\text{vdw}} = \frac{3\alpha_{\text{vdw}}}{d^4}. \tag{3.65}$$

Since the healing length [Eq. (3.61)] of superfluid helium-4 is only a few Angstroms, classical hydrodynamic theory is still valid to describe superfluid third sound waves down to truly microscopic dimensions, with no need to worry about the complicated microscopic quantum theory of superfluid helium-4. Assuming the superfluid film is incompressible, and in the limits of long wavelength $\lambda_3 \gg d$ and small wave amplitude $\eta \ll d$, conservation of mass and momentum as the basic laws of classical hydrodynamics give the continuity equation [94]:

$$\frac{\partial \eta}{\partial t} = -d\,\vec{\nabla} \cdot \vec{v}, \tag{3.66}$$

and the Euler equation:

$$\frac{\partial \vec{v}}{\partial t} = -g\vec{\nabla}\eta, \tag{3.67}$$

where g is the linearized van der Waals acceleration at the film surface [Eq. (3.65)]. Substituting the Euler equation into the continuity equation and eliminating $\vec{v}$ yields the wave equation of third sound:

$$\frac{\partial^2 \eta}{\partial t^2} - d\,g\nabla^2\eta = 0, \tag{3.68}$$

from which the third sound speed c_3 can be derived as:

$$c_3 = \sqrt{d\,g} = \sqrt{\frac{3\alpha_{\text{vdw}}}{d^3}}\,. \tag{3.69}$$

Table 3.2: First eight values of the frequency parameter $\zeta_{0,n}$ for fixed and free boundary conditions. In the case of fixed (free) boundary conditions, these correspond to the zeroes of $J_0(J_0')$.

	n = 1	n = 2	n = 3	n = 4	n = 5	n = 6	n = 7	n = 8
Free	3.832	7.016	10.174	13.324	16.471	19.616	22.760	25.904
Fixed	2.405	5.520	8.654	11.792	14.931	18.071	21.212	24.353

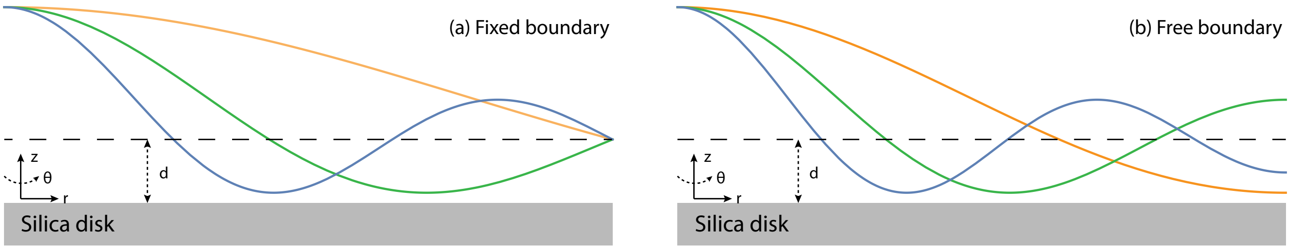

Figure 3.11: Illustrated cross-section of third sound modes of a thin superfluid film of average thickness d confined on a silica disk: (a) first three order Bessel modes of fixed boundary condition; (b) first three order Bessel modes of free boundary condition.

Assuming the time dependent amplitude $\eta(r,\theta,t)$ in Eq. (3.68) has solutions which obey the simple harmonic oscillator equation $\ddot{\eta}+\Omega_3^2\eta=0$, where Ω_3 is the third sound resonance frequency, the solutions must meet the relation of wave number K: $\Omega_3=c_3K$. With the assumption of harmonic time dependence, solving the wave equation with appropriate boundary conditions gives the solutions corresponding to third sound modes.

The experiments in this thesis focus on the third sound modes confined on the surface of a silica disk of radius R. Solving the wave equation [Eq. (3.68)] with circular geometry boundary conditions yields the Bessel mode profile in cylindrical coordinates (r,θ) [3]:

$$\eta_{m,n}(r,\theta,t)=\eta_0 J_m\left(\zeta_{m,n}\frac{r}{R}\right)e^{i(m\theta\pm\Omega_3 t)}, \tag{3.70}$$

where m and n are the azimuthal and radial mode numbers respectively, η_0 is the amplitude of the mode, J_m is the Bessel function of the first kind of order m, $\Omega_3=(\zeta_{m,n}c_3)/R$ is the mode frequency, θ is the angular direction, the ± sign in the exponential function denotes the travelling direction (clockwise or counter-clockwise) of the mode, and $\zeta_{m,n}$ is a frequency parameter, which is dependent on the mode order and boundary conditions, as displayed in Table 3.2.3.

There are two types of boundary conditions for the Bessel modes: the fixed $[\eta(R)=0]$ boundary condition, where there is no displacement at $r=R$ [Fig. 3.11(a)]; the free $[\partial_r\eta(R)=0]$ boundary condition, also know as the 'no flow' boundary condition, where the radial velocity of superfluid flow is 0 at the boundary [Fig. 3.11(b)]. The first three rotationally invariant Bessel mode profiles for the two boundary conditions are plotted in Fig. 3.11. In the case of free boundary condition the radial component of the flow velocity ($\vec{v}_3\sim\vec{\nabla}\eta$) at the boundary is zero, which means there is no fluid flowing across the boundary during the oscillation of a free-boundary condition mode, and thus the volume of the superfluid inside the mode boundary is conserved. This is indirectly illustrated in the profiles of the Bessel modes (especially obvious for the fundamental mode) in Fig. 3.11. In the illustration the free boundary condition is volume conserving, as the area underneath each free boundary mode profile curve is constant over time, while the fixed boundary condition is not volume conserving. However, in the experiments the boundary conditions are not fixed for the same host geometry, they can transition between each other, and a superposition of them can exist depending on the superfluid film thickness. For example, the transition from the free to fixed boundary condition has been observed in circular helium-3 third sound resonators, when the film thickness is increased to above ~ 200 nm [95, 96]. In our superfluid optomechanical resonator with thin films (typically below 20 nn thickness) and sharp 'knife-edge' disk rim [97], the superfluid flow between the top and lower surfaces is expected to be negligible, and thus the third sound modes supported by the disk top surface are expected to have free boundary condition, which is consistent with previous works on circular helium-4 third sound resonators [87, 92].

3.2.4 Quantized Vortices in Two Dimensional Superfluid

A quantized vortex in superfluid helium is the quantized circulation of superfluid flow around a topological defect, which could be made of excited particles, air, vacuum, etc. The diameter of a vortex core in superfluid helium-4 is typically of the order of a few Angstroms, as determined by the healing length [Eq. (3.61)]. The existence of quantized vortices was first suggested by Lars Onsager, and further developed by Richard Feynman [98]. As mentioned previously in Eq. (3.59) superfluid can be described by a macroscopic wavefunction $\Psi(\vec{r}, t)$, and the superfluid velocity is proportional to the gradient of the phase of the wavefunction [Eq. (3.60)]. The origin of superfluid velocity as the phase gradient leads to two consequences. First, the superfluid flow must be strictly irrotational [69]:

$$\vec{\nabla} \times \vec{v}_s = \frac{\hbar}{m_{\mathrm{He}}} \vec{\nabla} \times \left(\vec{\nabla}\phi\right) \equiv 0. \tag{3.71}$$

Second, the superfluid circulation around any closed loop will accumulate a phase shift. As required by the precondition that the superfluid wavefunction is single valued, the phase shift must be zero if the enclosed region is simply connected, or an integer times of 2π if the region is multiply connected. As a result, the superfluid circulation must be quantized [83]:

$$\oint \vec{v}_s \cdot \mathrm{d}\vec{l} = \frac{\hbar}{m_{\mathrm{He}}} \oint \vec{\nabla}\phi \cdot \mathrm{d}\vec{l} = n\kappa, \tag{3.72}$$

where $\kappa = \frac{h}{m_{\mathrm{He}}}$ is the superfluid circulation quantum, n is an integer corresponding to the number of vortices inside the closed loop, and m_{He} is the atomic mass of helium-4.

Again since the dimensions in which the superfluid quantumness matters are within the healing length, it is valid to use classical hydrodynamics to describe superfluid vortex dynamics down to very microscopic dimensions. Owing to the incompressible, inviscid and irrotational superfluid flow, the potential flow theory allows us to use the phase ϕ of the superfluid wavefunction as the velocity potential function to satisfy conservations of mass and momentum, and thus in two dimensional plane the superfluid velocity components in r and θ directions are respectively $\vec{v}_r = \frac{\partial \phi}{\partial r}$ and $\vec{v}_\theta = \frac{1}{r}\frac{\partial \phi}{\partial \theta}$. The streamfunction Ψ is linked to ϕ via the Cauchy-Riemann equations. The velocity potential ϕ and streamfunction Ψ of a two dimensional point vortex with circulation κ are respectively given by [94]:

$$\phi = \frac{\kappa}{2\pi}\theta, \tag{3.73}$$

$$\Psi = -\frac{\kappa}{2\pi}\ln\left(r\right), \tag{3.74}$$

and the corresponding velocity field of the point vortex in an infinite two dimensional plane is:

$$\vec{v}_\theta(r) = -\frac{d\Psi}{dr} = \frac{\kappa}{2\pi r}\hat{e}_\theta, \tag{3.75}$$

where $\hat{e}_\theta$ is the tangential unit vector and r is the distance from the vortex core.

Chapter 4

Optical Force Enhanced by Superfluid

This chapter is based on the work published by the American Physical Society:
D. L. McAuslan, G. I. Harris, C. Baker, Y. Sachkou, **X. He**, E. Sheridan, and W. P. Bowen, Microphotonic Forces from Superfluid Flow, *Physical Review X*, 6(2):021012, 2016.

Conventional cavity optomechanics studies the interaction between the motions of a mechanical oscillator and an optical resonator. This chapter presents superfluid optomechanics, where the mechanical motions are acoustic waves in superfluid, instead of strain waves in bulk solids or motion of dielectric slabs. In the first section, the research background of superfluid optomechanics is introduced, and the motivations for using superfluid for optomechanics experiments are explained. In the second section, a conventional optomechanical feed-back cooling experiment demonstrates that superfluid flow is able to enhance optical forcing on the mechanical resonator, and thus increases the cooling efficiency. The third section explains the coupling mechanism between superfluid motions and light, and theoretically estimates the optomechanical coupling rate based on perturbation theory. The fourth section is the theoretical and experimental investigations of quantized vortex detection in two dimensional superfluid film using this superfluid optomechanical system. The last section concludes this chapter.

4.1 Research Background and Motivations

With the development of laser physics in the past a few decades, optical forces which are usually minute, have broad applications in photonic circuits [99,100], micromanipulation [101,102], and biophysics. In the field of cavity optomechanics, optical forces, including radiation pressure forces, photothermal forces, optical gradient forces, and electrostrictive forces, have enabled practical applications including: 1) high precision sensing of forces, fields and mass [39,103,104], particularly represented by the ground-breaking work of gravitational wave detection [8], 2) information processing techniques like all-optical routing [105], non-volatile mechanical memories [106], etc. Besides practical applications, optical forces also have been widely used to

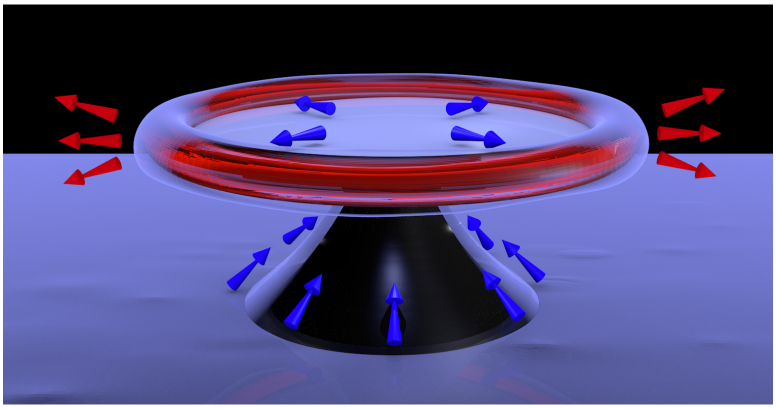

Figure 4.1: Artistic illustration of the optical force resulted from the recoil of the evaporated helium atoms. The blue arrows are superfluid flow, and the red arrows are evaporated helium-4 atoms. (Image courtesy of Dr Christopher G. Baker)

demonstrate fundamental science, for example generation of squeezed states in a Bose-Einstein condensate [107], ponderomotive squeezing [108], ground state cooling of a macroscopic mechanical oscillator [10], coherent state swapping [109].

In this section, a new type of optical forcing realised by superfluid convective flow is demonstrated to have an order-of-magnitude stronger mechanical actuation than radiation pressure. This convective flow of superfluid is frictionless, and is generated in response to a local heat source, as explained by the *fountain effect* in § 3.2. The momentum of the flowing helium-4 atoms is transferred to a mechanical element via collision and recoil, resulting in kinetic forcing. In our case a Whispering Gallery Mode (WGM) silica toroid resonator is coated with a thin superfluid film as shown in Fig. 4.1. The heat source is localised along the circumference of the mechanical oscillator, which the toroid resonator, whereby the incident superfluid atoms are evaporated from the surface. The momentum transfer from superfluid flow and recoil of evaporated helium-4 atoms induces a photoconvective force, which is similar to, but stronger than the standard photothermal force. It also has several additional advantages over the photothermal force. First, the photoconvective force from superfluid is not only able to provide strong actuation capabilities, but is also able to work at cryogenic temperatures, which are necessary to quench thermal noise for quantum experiments. Second, the large thermal conductivity of superfluid helium-4 in this case could be used to greatly reduce the localised heating of the mechanical element, which often degrades cryogenic quantum optomechanics experiments [110]. Third, superfluid flow, once initiated, has been observed to be very persistent [111]. This unique flow persistence is able to apply endurable pressure on a mechanical element, even after the optical field is removed, which could act as non-volatile optomechanical memory [106].

4.2 Photoconvective Force Mediated by Superfluid Flow

The configuration of of the superfluid photoconvective forcing experiment is illustrated in Fig. 4.1. A nano-meter scale superfluid helium film self-assembly coats a microtoroidal WGM resonator, due to the van der Waals interaction between superfluid helium-4 atoms and the substrate material. When laser light is coupled to the resonator via a tapered fiber (not shown), the optical absorption inside the resonator locally heats the microtoroid periphery (red glow). Due to the thermomechanical effect of superfluid, the local heating generates superfluid flow through the pedestal towards the resonator periphery (blue arrows). At the periphery, the recoil of the evaporated helium atoms (red arrows) exerts a force onto the toroid, directed radially inwards and with a magnitude given by

$$\begin{aligned} F_{\text{radial}} &= -\frac{d(m\, v_{\text{radial}})}{dt} \\ &= 4\dot{m}\, v_{\text{radial}}/\pi^2, \end{aligned} \tag{4.1}$$

where $\dot{m}$ is the mass flow rate of the evaporated helium atoms. The net radial velocity v_{radial} is from the integration of isotropically evaporated atoms in the outwards facing half-space with a root-mean-square (rms) velocity of

$$v_{\text{rms}} = \sqrt{\frac{3k_B\, T_{\text{evap}}}{m_{\text{He}}}}\,, \tag{4.2}$$

where T_{evap} is the temperature of the evaporated atoms and m_{He} is the mass of a helium-4 atom.

In steady state, the mass flow rate $\dot{m}$ is determined by equating the optical heating load to the energy dissipated evaporation of helium-4 atoms. In contrast to bulk systems, which dissipate through normal fluid counter-flow, the energy in thin superfluid films is dissipated via evaporation, due to the viscous clamping of normal fluid component to the surface [84]. So in steady state, the superfluid mass flow rate given an absorbed optical power P_{abs} is $\dot{m} = P_{\text{abs}}/(L - \langle\mu_{\text{vdW}}\rangle)$, where L is the latent heat of evaporation and $\langle\mu_{\text{vdW}}\rangle)$ is the van der Waals potential of the superfluid film. Inserting the mass flow rate equation and Eq. (4.2) into Eq. (4.1) yields the inward radial force from the recoil of the evaporated helium-4 atoms:

$$F_{\text{radial}} = \frac{4}{\pi^2}\sqrt{\frac{3k_B\, T_{\text{evap}}}{m_{\text{He}}}}\;\frac{P_{\text{abs}}}{L - \langle\mu_{\text{vdW}}\rangle} \tag{4.3}$$

Note that, similar to photothermal forces [38], this radial force equation is not related to the cavity finesse, allowing applications of photoconvective forces in the cases where there is only a weak cavity, or even no cavity. For comparison, assuming the magnitude of intracavity power equal to the absorbed optical power P_{abs} here, the radiation pressure force is $F_{\text{RP}} = P_{\text{abs}}\mathcal{F}/c$ [1], where $\mathcal{F}$ is the finesse of the cavity and c is the speed of light. For evaporation of superfluid at 1 K, the ratio $F_{\text{radial}}/F_{\text{RP}} \sim 4 \times 10^5/\mathcal{F}$ indicates the superfluid convective force is similar in magnitude to the radiation pressure force with a cavity finesse of around 400 000. Whereas the cavity finesse in this experiment is 53 000, predicting that the superfluid convective force is nearly 1 order of magnitude larger than the radiation pressure force.

---

[1] When a photon is absorbed, the momentum kick from the photon to the absorbent is $\hbar\kappa$. Given an absorbed optical power P_{abs} at steady state, the photon flux to be absorbed is $P_{\text{abs}}/(\hbar\omega)$, leading to a radiation pressure applied on the absorbent of P_{abs}/c. The intracavity optical power is enhanced by cavity finesse to be $P_{\text{abs}}\mathcal{F}$. Thus, given the absorbed optical power P_{abs}, the radiation pressure exerted on the cavity is $P_{\text{abs}}\mathcal{F}/c$.

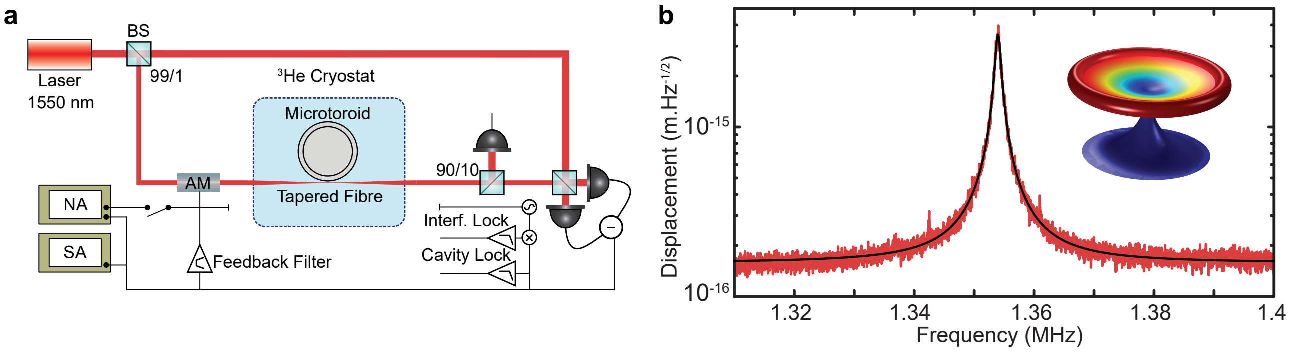

Figure 4.2: (a) Electronic control and measurement setup and homodyne optical setup used to investigate the superfluid photoconvective forcing. A WGM optical cavity placed inside a sample chamber of a helium-3 cryostat forms a part of an all-fibre interferometer built for the balanced homodyne detection scheme. Electronic filters and amplification stages are implemented for the feedback cooling experiment. The interferometer and the cavity locking is utilized for stability of the interferometer phase and the laser frequency respectively. BS – fibre beamsplitter, AM – amplitude modulator, SA – spectrum analyser, NA – network analyser, PD – photodetector. (b) Displacement profile of the microtoroid flexural mode at 3 K. Inset: FEM simulated displacement profile of the microtoroid flexural mode. Figure is reproduced from Ref. [1] with modifications.

4.3 Experimental Setup

The setup shown in Fig. 4.2(a) is used to experimentally demonstrate the superfluid photoconvective force is 1 order of magnitude stronger than the radiation pressure force. A microtoroidal WGM resonator resides in the superfluid-tight sample chamber of a helium-3 closed-cycle cryostat (Oxford Triton). Inside the sample chamber laser light at 1555.08 nm is coupled to a high-Q optical mode (linewidth $\kappa/2\pi = 23.5$ MHz) of the resonator via a tapered fiber. The microtoroid is also a mechanical resonator, since its geometry defines a number of intrinsic mechanical modes with frequency ranging from 1 to 50 MHz. With the homodyne detection method shown in the setup, the mechanical thermal motion is detected as the phase fluctuation in the signal arm, when laser light is locked on resonance with the optical mode. In principle, the radial forces originated from both radiation pressure and superfluid convective flow interact most efficiently with the radial breathing mechanical mode of the toroid. However, the radial breathing mode's frequency is 40 MHz, which is too high for superfluid flow to respond. In the experiment the photoconvective force from superfluid flow is observed to only respond up to 2 MHz, possibly due to the breakdown of superfluidity when the flow speed is above the Landau critical velocity [112]. Therefore, this experiment is done with the first-order flexural mode at $\Omega/2\pi = 1.35$ MHz, with a mechanical linewidth of $\Gamma/2\pi = 530$ Hz at the base temperature (559 mK) of the cryostat. The single-photon optomechanical coupling rate of this mechanical mode is $g_0/2\pi = 12.3$ Hz. This mode is simulated using finite element modelling (FEM), and its displacement profile is shown in the inset of Fig. 4.2(b).

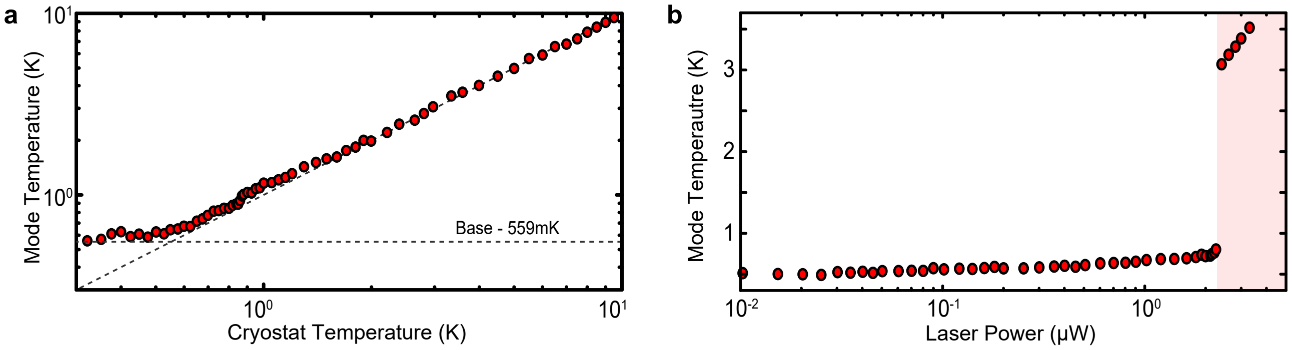

Figure 4.3: (a) Flexural mode temperature vs cryostat temperature as the cryostat is cooled from 10 to 0.32 K. The microtoroid reaches a base temperature of 0.56 K with 100 nW of injected optical power. (b) Mode temperature of the flexural mode as the probe laser is increased from 10 nW to 3.3 μW . Below 2.2 μW the temperature increases slightly as the laser power is increased. Above 2.2 μW the superfluid boils off, causing a sharp rise in mode temperature. Figure is reproduced from Ref. [1] with minor modifications.

4.4 Experimental Results

4.4.1 Calibration of the Microtoroid Temperature

The superfluid film is condensed from low-pressure helium-4 gass (19 mBar at 2.9 K) in the superfluid-tight sample chamber at the base temperature of the cryostat. This gas pressure which determines film thickness, is chosen to avoid frequency overlapping between superfluid sound modes and toroid mechanical modes [18]. The helium-4 in the sample chamber undergoes phase transition directly from gas into superfluid phase at 850 mK, coating all the inner surfaces of the sample chamber including the microtoroid with a self-assembling superfluid film. The flexural mode is used to do the thermometry of the microtoroid as the cryostat temperature is varied from 10 K to 320 mK. The temperature of the flexural mode is obtained from the integrated power spectral density of the homodyne photocurrent. As shown in Fig. 4.3(a), the microtoroid is very well thermalized to the cryostat from 10 K down to 600 mK; whereas, at lower cryostat temperatures the microtoroid temperature is dominated by the optical absorption of 100 nW of injected laser power, as shown by the plateau of toroid temperature. This temperature difference can be explained by the thermal gradient between the microtoroid (where the optical absorption happens) and the thermometer of the cryostat.

The effects of optical absorption induced heating on the toroid is investigated via the toroid mechanical mode temperature versus optical power. As shown in Fig. 4.3(b) the mechanical mode temperature barely increases with laser power, and eventually an abrupt rise happens when the superfluid film is boiled off at a threshold optical power. Varying the laser power by 2 orders of magnitude from 10 nW to 2.1 μW, the mode temperature only increases slightly from 510 mK to 730 mK. When the laser power is above 2.2 μW, the mode temperature abruptly increases to 3 K as indicated by the red shading in Fig. 4.3(b), which corresponding to the threshold power of superfluid boiloff in this configuration. This threshold phenomenon occurs because the optical absorption induced evaporation rate is larger than the replenishing rate from superfluid flow. This upper limit of the replenishing rate is ultimately set by Landau's critical velocity of superfluid flow, eventually leading to the superfluid boiloff at the periphery where the optical mode resides. Thereby, the microtoroid is no longer well thermally anchored to the environment due to the significant reduction of thermal conductivity from superfluid boiloff, resulting in a large temperature gradient between the microtoroid and the thermometer on the cryostat coldplate.

4.4.2 Enhanced Driven Response

The photoconvective forces can be naturally described by the photothermal interaction from superfluid. Therefore, a theoretical description of a generic photothermal force is first introduced.

The equation of motion of the mechanical mode position $x(t)$ is given as below:

$$m_{\text{eff}}\left[\ddot{x}(t)+\Gamma\dot{x}(t)+\Omega^2 x(t)\right]=F_{\text{th}}(t)+F_{\text{op}}(t), \tag{4.4}$$

where Γ is the mechanical decay rate, Ω is the mechanical resonance frequency and $m_{\text{eff}} = \int d\mathbf{r}\rho U(\mathbf{r})/|\max(U(\mathbf{r}))|$ is the effective mass which is calculated using the density ρ and the displacement profile $U(\mathbf{r})$ given from FEM simulations. There are two forces exerted on the mechanical oscillator: an optical force F_{op} and thermal noise $F_{th} = \sqrt{2\Gamma_m m_{\text{eff}} k_b T}\ \xi(t)$, where $\xi(t)$ is the unit white noise drive with the temporal correlation as $\langle \xi^*(t)\xi(t')\rangle = \delta(t-t')$.

The photothermal effect can be treated as a random fluctuating force, and its temporal correlations have a similar form to that of the thermal noise, since this effect is generated by the thermal response to the random absorption of photons [113]. The optical force in Eq. (4.4), F_{op} is decomposed into two terms: photothermal force and radiation pressure

$$\begin{aligned} F_{\text{op}}(t) &= F_{\text{rp}}(t)+F_{\text{pt}}(t) && (4.5)\\ &= \hbar g_0\left[a(t)^\dagger a(t)+\frac{\beta A}{\tau_t}\int_{-\infty}^{t}\mathrm{d}u\, e^{-\frac{t-u}{\tau_t}}a(u)^\dagger a(u)\right], && (4.6)\end{aligned}$$

where g_0 is the single photon optomechanical coupling rate, τ_{t} is the photothermal response time and A is the absorption coefficient given by the ratio of absorbed to circulating optical power. β is a dimensionless factor to quantify the strength of the radiation pressure normalized photothermal effect: $F_{\text{pt}} = \frac{\beta A}{1+i\omega\tau_{\text{t}}}F_{\text{rp}}$. To linearize the total optical force, the intracavity field annihilation operator is expressed as a coherent amplitude with quantum fluctuations i.e. $a(t)=\alpha+\delta a(t)$. Neglecting the second order fluctuations $(\delta a^\dagger(t)\delta a(t))$ and stationary terms $(\alpha^*\alpha)$ in the optical force, the expression of the total optical force in Fourier domain is:

$$F_{\text{op}}(\omega)=2\hbar g_0\alpha\left[1+\frac{\beta A}{1+i\omega\tau_{\text{t}}}\right]\delta X^+(\omega), \tag{4.7}$$

where $\delta X^+(\omega)=\frac{1}{2}(\delta a^\dagger(\omega)+\delta a(\omega))$ is the amplitude fluctuations of the intracavity field that drives the mechanical motion. The two terms within the brackets of Eq. 4.7 are the radiation

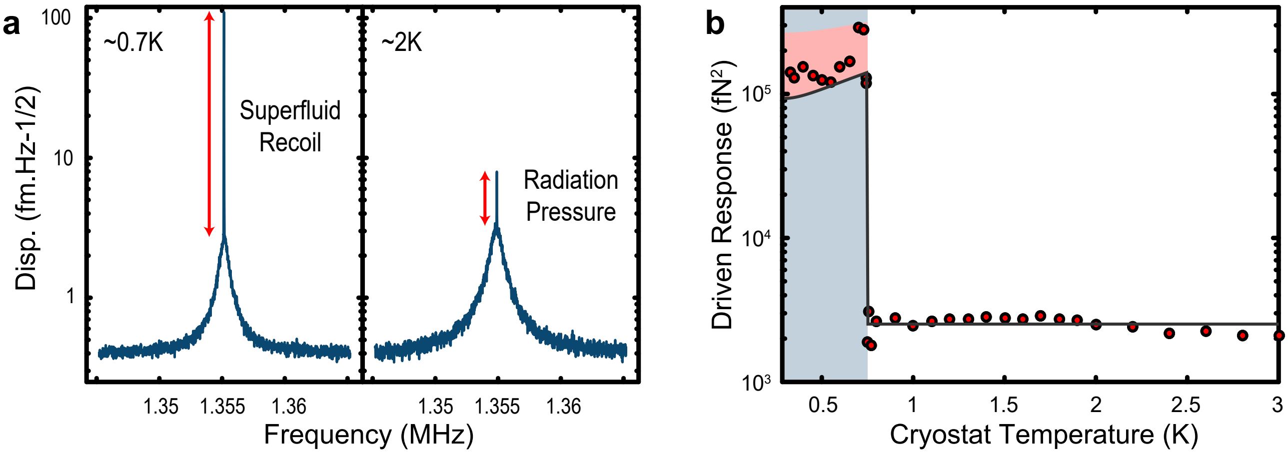

Figure 4.4: (a) Displacement spectrum of the flexural mode at 0.7 K and 2 K with a coherent drive applied via optical amplitude modulation. The response to coherent drive is shown to increase with the presence of superfluid helium; (b) Driven response of the flexural mode as the cryostat is cooled (red points), showing a step increase in response at the superfluid transition temperature. Black line represents a theoretical fit to the data. The gray shaded area indicates that a superfluid layer has formed on the microtoroid surface. The pink shaded area represents the theoretical force if T_{evap} is up to 1 K higher than the mode temperature. Figure is reproduced from Ref. [1] with minor modifications.

pressure and photothermal terms respectively, while the coefficient in the front is normalized by the strength of radiation pressure force. We arrive at this equation by approximating the time integral for the photothermal effect [Eq. (4.6)] by a convolution with a Heaviside step function $H(t)$ before the Fourier transform. Thereby the functional form of the photothermal force is effectively reduced to a low pass filter with a corner frequency determined by the characteristic thermalization time, which tells basically how fast the photothermal effect can respond. In this experiment, the superfluid photoconvective force is able to respond up to around 2 MHz, *i.e.* $\tau_t^{-1} \approx 2$ MHz.

To experimentally investigate the superfluid photoconvective force of this configuration, the flexural mode is driven by applying a constant optical amplitude modulation at the frequency of the mode, while the cryostat temperature is varied from 3 K to 0.325 K (see Fig. 4.4). The reason why this mode can be driven by the optical amplitude modulation is that the modulation can apply a resonant force through superfluid flow below the superfluid transition temperature, and through radiation pressure above the transition temperature. The drive from the resonant force is analogous to amplifying a pendulum's motion by applying a force at the pendulum oscillating frequency. The response of the flexural mode to this drive is measured using homodyne detection of the phase quadrature of the output light. Above the superfluid transition temperature, the optical force is only from radiation pressure [right of Fig. 4.4(a)], and it is shown in Fig. 4.4(b) that the response to the drive mediated by radiation pressure is independent of temperature. However, once the superfluid film is formed [the blue shading of Fig. 4.4(b)], the response of the flexural mode to the drive sharply increases by 21 dB to a maximum of 540 fN [the left plot of Fig. 4.4(a)], indicating that below the transition temperature the optical force mediating the drive is not dominated by radiation pressure. This large optical forcing of 540 fN is from the photoconvective flow of superfluid. The overlap between the flexural mode and the radial evaporative force is calculated using FEM simulation to be 0.037%, which gives a total superfluid photoconvective force of 1.46 nN below the superfluid transition temperature. This sharp increase of the driven response in Fig. 4.4(b) agrees very well with theoretical predictions, corresponding to a superfluid convective force 11 times larger than the radiation pressure. In the blue shading area of Fig. 4.4(b) the measured superfluid photoconvective force decreases with the temperature. This phenomenon is due to the evaporated atoms having reduced rms velocity [Eq. (4.2)] at lower temperatures, which manifests as a weaker recoil force onto the microtoroid. This reduction in the recoil force with temperature decrease can be fairly accurately described by Eq. (4.3), with the superfluid evaporation temperature T_{evap} equal to the measured microtoroid mode temperature T_m. Although the observed superfluid forces are observed to be maximally 60% larger than the theoretical prediction, this discrepancy can be explained by the temperature difference between the helium film and the evaporated atoms. It has been shown in the literature that the temperature of the evaporated helium-4 atoms from a superfluid thin film is around 1 K higher than the film temperature, depending on the power applied to heat the film [114, 115]. To account for the temperature uncertainty of the evaporated atoms, the pink shading is included in Fig. 4.4(b) showing the recoil force from the atoms evaporated at temperatures from the mode temperature T_m to $T_m + 1$ K.

4.4.3 Feedback Cooling Using Superfluid Photoconvective Force

Feedback cooling is a well studied approach in the cavity optomechanics community to demonstrate the cooling of mechanical modes, and the actuation forces can be both optical forces, or external forces like the electrical gradient force [116–118]. One application of the strong superfluid photoconvective forces is to feedback cool the flexural mechanical mode. Before reporting on the experimental demonstration of feedback cooling, the theory of feedback cooling mechanism is first briefly introduced as below.

In homodyne detection, the motion of the mechanical oscillator imprints phase fluctuations on the signal arm of the homodyne detection interferometer, and is eventually exhibited on the photocurrent expressed as

$$\begin{aligned} \delta i(\omega) &= G_{\mathrm{det}} \delta \tilde{x}(\omega) && (4.8) \\ &= G_{\mathrm{det}} \left(\delta x(\omega) + \delta N(\omega) \right), && (4.9) \end{aligned}$$

where $\delta N(\omega)$ is measurement noise including both optical shot noise and electronic noise, and G_{det} is the total gain included in the detection apparatus (including the detector, interferometer response and optomechanical interaction). Particularly in this experiment, the measurement noise is dominated by the optical shot noise, which is flat in the power spectrum and proportional to the optical power in the local oscillator arm. The photocurrent is fed back into an amplitude modulator in the setup [see Fig. 4.2(a)] before the microtoroid to generate an optical force [see Eq. (4.7) for why amplitude modulation can generate optical forces]. A feedback optical force is generated from the cavity-response scaled amplitude modulation, ultimately proportional to the photocurrent, namely $F_{\mathrm{fb}}(\omega) \propto \delta i(\omega)$. Thus the feedback force in Fourier domain has a form:

$$F_{\mathrm{fb}}(\omega) = -g\chi^{-1}(\Omega)\delta\tilde{x}(\omega) \tag{4.10}$$

where g is the feedback gain (including the effects from detection, actuation and filtering), and the term $\chi^{-1}(\Omega)$ is the spectral response of the feedback gain to make it unitless and facilitate factorization into the mechanical susceptibility in following steps. Substituting the feedback force equation into Eq. (4.4), and taking the Fourier transform of both sides yields

$$\delta x(\omega) \;=\; \chi'(\omega)\left[F_{th}(\omega) - g\chi^{-1}(\Omega)\delta N(\omega)\right], \tag{4.11}$$

where $\chi'^{-1}(\omega) = m_{\mathrm{eff}}^{-1}\left[\Omega^2 - \omega^2 + i\Gamma'\Omega\right]^{-1}$ is the mechanical susceptibility with modified linewidth $\Gamma' = \Gamma\,(1+g)$ depending on the feedback (gain and phase). Then the mechanical mode temperature is calculated from the integral of photocurrent power spectral density $S_{\tilde{x}\tilde{x}}(\omega) = \langle|\delta\tilde{x}(\omega)|^2\rangle$:

$$\tilde{T} \;=\; \int_{-\infty}^{\infty} \mathrm{d}\omega\; S_{\tilde{x}\tilde{x}}(\omega) \tag{4.12}$$

$$\;=\; \left(1 - \frac{g(g+2)}{\mathrm{SNR}}\right)\frac{1}{1+g}T_0, \tag{4.13}$$

where T_0 is the initial temperature and the signal-to-noise ratio (SNR) is the ratio between the mechanical signal peak power and noise level in the power spectral density: $\mathrm{SNR} = S_{\tilde{x}\tilde{x}}(\Omega_m)/S_{NN}(\Omega_m)$. The derivation of this equation has followed the idea of Eq. (3.58) that the integral of a normalized Lorentzian function is unity.

To obtain an accurate estimation of T, one must consider the correlations between the measurement noise and the mechanical motion, because the temperature estimate $\tilde{T}$ and the feedback is derived from the same photocurrent. These correlations obscure the actual mode temperature T. However, the correlations only occur at high gain and the obscuration can be compensated using the SNR and gain. Therefore, the actual mode temperature, represented by the dashed line in Fig. 4.5(a), can be shown to be

$$T = \frac{\mathrm{SNR} + g^2}{\mathrm{SNR} - g(g+2)}\tilde{T}. \tag{4.14}$$

To experimentally demonstrate the feedback cooling mediated by the strong photoconvective forces in our configuration, the homodyne photocurrent is filtered and amplified at different stages, and is then fed into an Mach-Zehnder modulator (MZM) to amplitude modulate the laser light coupling to the toroid resonator [see Fig. 4.2(a)]. The phase of the feedback loop is carefully tuned to ensure the feedback force opposes the instantaneous velocity of the flexural

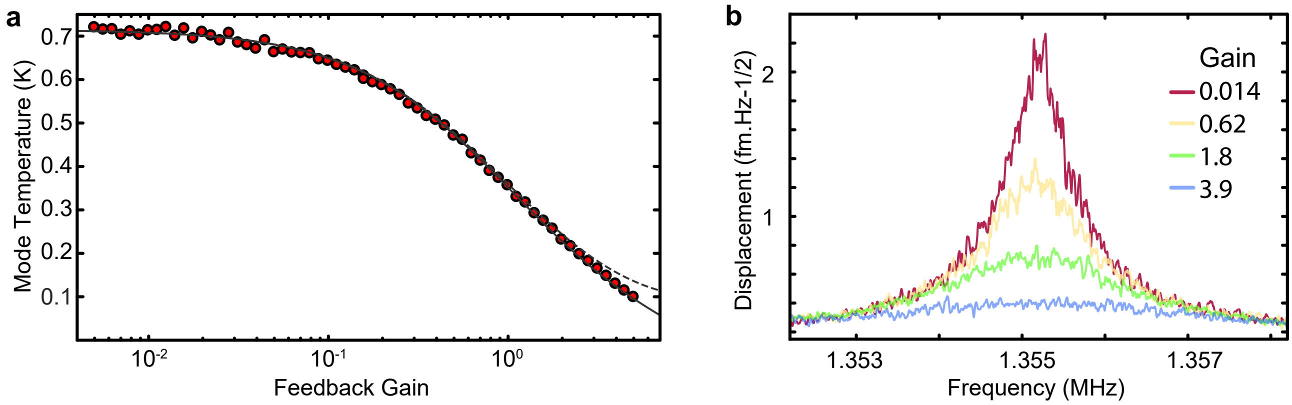

Figure 4.5: (a) Feedback cooling of the flexural mode from 715 mK to 137 mK using superfluid-mediated photoconvective forcing. With a fixed probe power of 1.9 μW , the feedback gain is varied over 3 orders of magnitude, showing good agreement with the estimated mode temperature from in-loop measurements (solid line). The out-of-loop mode temperature is then inferred by a transformation (dashed line) that is derived in the Supplemental Material [36]; (b) Displacement spectrum of the flexural mode with varying feedback gain. Figure is reproduced from Ref. [1].

mode, otherwise the thermal motion of the mode will be amplified. The initial flexural mode temperature T_0 here is 715 mK. As the feedback gain increases in Fig. 4.5(b), the power spectral density of the mode gets broadened, and its amplitude decreases. This results demonstrate that the mode temperature decreases with the feedback gain, and the experimental results are perfectly fitted by the theory curve (solid line) in Fig. 4.5(a). As shown by the calibrated mode temperature curve (dashed line) the flexural mode is eventually cooled to 137 mK, corresponding to a mechanical occupancy of 2110 ± 40 phonons.

The final phonon occupancy in feedback cooling generally depends on two factors: the optomechanical coupling rate, which determines the conditional variance of the mechanical oscillator under given measurement, and the maximum strength of the force which mediates the feedback cooling [52]. In the photoconvective feedback cooling experiment here, the optomechanical coupling rate of the flexural mode is fairly low ($g_0/2\pi = 12.3$ Hz), limiting the final phonon occupancy. However, given the mechanical mode and cryostat temperature here, the maximum strength of the feedback force is 1.46 nN, making the superfluid feedback force not a limiting factor for phonon numbers above $n \approx 0.015$. Thus, the mechanical mode of the resonator can be ground state cooled using the superfluid photoconvective force, if our microtoroid parameters are improved to be similar to previous works [109, 119]. Further, the superfluid photoconvective force together with backaction evading or non-linear measurements could also be applied to generate non-classical mechanical states [11, 120–123].

4.5 Conclusion

This chapter describes the experiments and theory on the superfluid thin film optomechanical resonator based on previous publications [1]. First, it demonstrates that the superfluid photo-convective force based on the fountain effect is able to enhances the optical forcing exerted onto the mechanical motions of the optical resonator by 1 order of magnitude, and thus enhance the feedback cooling capability with a final mechanical mode temperature of 137 mK.

Chapter 5

Superfluid Optomechanics and Its Application for Quantized Vortex Detection

This chapter is based on the works published by IOP Publishing:
C. G. Baker, G. I. Harris, D. L. McAuslan, Y. Sachkou, **X. He** and W. P. Bowen, Theoretical framework for thin film superfluid optomechanics: towards the quantum regime, New Journal of Physics, 18(12):123025, 2016.
S. Forstner, Y. Sachkou, M. Woolley, G. I. Harris, **X. He**, W. P. Bowen, C. G. Baker, Modelling of vorticity, sound and their interaction in two-dimensional superfluids, New Journal of Physics, 21(5):053029, 2019.
and the work submitted for publication and is available on the arXiv:
Y. P. Sachkou, C. G. Baker, G. I. Harris, O. R. Stockdale, S. Forstner, M. T. Reeves, **X. He**, D. L. McAuslan, A. S. Bradley, M. J. Davis, W. P. Bowen, Coherent vortex dynamics in a strongly-interacting superfluid on a silicon chip, arXiv 1902.04409, 2019.

Conventional cavity optomechanics studies the interaction between the motions of a mechanical oscillator and an optical resonator. This chapter presents superfluid optomechanics, where the mechanical oscillator is the acoustic waves in superfluid, instead of strain waves in solids. In the first section, the research background of superfluid optomechanics is introduced, and the motivations for using superfluid for optomechanics experiments are explained. The second section explains the coupling mechanism between the superfluid acoustic waves and light, and theoretically estimates the optomechanical coupling rate based on perturbation theory. The third section is the theoretical and experimental investigations of quantized vortex detection in a thin superfluid film using this superfluid optomechanical system. The last section concludes this chapter.

5.1 Research Background and Motivations

As introduced in Chap. 3, conventional cavity optomechanics is a great platform for high precision sensing, information processing and testing fundamental physics, etc., but its performance is more or less limited by 1) bulk heating of the mechanical oscillator due to optical absorption, 2) mechanical loss, 3) low optomechanical coupling due to poor overlap of the optical field with the mechanical motions, 4) small zero point motion. A lot of research efforts have been focused on overcoming these issues, but still people have to compromise among these four factors, which really hinders optomechanical experiments to approach the quantum coherent regime.

One way to get around these drawbacks of the conventional optomechanics is to utilize superfluid helium to form mechanical oscillators, because superfluid has advantages over its solid counterparts: 1) it has extremely low optical absorption [17], 2) in principle zero mechanical loss (zero viscosity) [15], 3) supports perfect overlap between the optical field and mechanical motions, due to the self-assembling nature of superfluid [18], 4) it can be very flexibly engineered to couple of atomic-layer thick film to obtain low effective mass (large zero point motion), 5) the mechanical oscillators it supports exhibit strong Duffing nonlinearities, 6) it can be coupled quantized vortices [22,92,124,125], 7) interact with electrons floating on the superfluid film [126], enriching the variety of physics accessible via optomechanics.

Superfluid optomechanics was first started in Keith Schwab's group at Caltech, using a niobium superconducting cavity filled with 39.3 cm^3 bulk superfluid helium-4 [16]. Acoustic modes (first sound) with gram-scale effective mass in the bulk superfluid have been observed to have Q up to 7×10^6. The superfluid density fluctuations generated by first sound waves modulate the permittivity inside the superconducting microwave cavity, resulting into the coupling between the acoustic modes and microwave photons. However, due to low optomechanical coupling rate, no dynamical backaction has been observed in this optomechanical system. First sound modes in bulk superfluid have also been utilized for optomechanics experiment in Jack Harris's group, where the optical cavity is a 67.3 μm long Fabry-Perot cavity formed by two optical fibre tips with Distributed Bragg Reflector (DBR) coating [17]. When the optical cavity is cooled down to below 100 mK with helium-4 gas, the helium is condensed to superfluid phase and conformally fills the hollow optical cavity, thereby the Fabry-Perot cavity supports both the optical modes and longitudinal superfluid density acoustic modes, allowing near-perfect overlapping between optical field and the mechanical mode. Because of a much smaller mode volume, the optomechanical interaction strength is much stronger than the previous case. Additionally, owing to the low optical absorption and high thermal conductivity of superfluid, the optomechanical coupling is predominantly from the unitary electrostrictive force of light, with the single photon coupling rate extracted from experiment having two components: the electrostrictive coupling rate of around 3 kHz, and the non-unitary photothermal coupling rate of around 1 kHz.

Different from those bulk superfluid optomechanics experiments, a new superfluid optomechanics configuration has been developed in our group that uses femtogram-scale thin superfluid helium-4 films that self-assembles on the surface of a toroidal whispering-gallery-mode resonator. Taking the advantage of high-precision sensing allowed by cavity optomechanics, Brownian motion of superfluid third sound modes have been able to be tracked and controlled in real-time [18]. The optomechanical interactions in this experiment are dominated by the non-unitary photothermal effects, due to small radiation pressure from weak evanescent coupling of superfluid acoustic modes with intracavity optical field. However, with modest improvements radiation pressure is expected to dominate. Although the optomechanical interaction has the photothermal component, the large interaction strength still highly motivates us in two aspects. On one hand, the high sensitivity allowed by strong superfluid optomechanical interaction really motivates us to probe excitations (phonons, vortices, etc.), since all previous investigations of superfluid excitations are based on either driving the system far out of equilibrium or average effect over a long period of time. On the other hand, the non-unitary imperfection of the strong optomechanical interaction motivates us to optimize the system to reduce the photothermal effect in order to push this superfluid optomechanical system into a fully quantum regime.

5.2 Theoretical Study on Light-Sound Interaction in Superfluid

Previous chapter introduces a conventional optomechanics experiment, in which superfluid is used to enhance the optical forcing applied on a toroid mechanical mode. Thus the system can be termed superfluid enhanced conventional optomechanics. Here, mode perturbation theory is used to prove that ultra-strong direct interactions between light and superfluid sound modes are experimentally achievable, which is termed superfluid optomechanics. This section introduces the improvement of the superfluid thin film optomechanical resonator, by optimizing the overlapping between superfluid film and optical field to maximize the dispersive radiation-pressure optomechanical coupling. Using perturbation theory, the dependence of the optomechanical coupling rate to resonator dimensions and superfluid film thickness is thoroughly studied. In addition, the expressions for the effective mass and zero-point motion of superfluid third sound acoustic modes are analytically derived.

5.2.1 Optimization of Light-Superfluid Coupling

The optomechanical resonator made of a circular whispering gallery mode (WGM) resonator coated with superfluid thin film is shown in the artistic illustration in Fig. 5.1. There is a type of acoustic waves existing in the superfluid thin film, termed as third sound which is thoroughly introduced in § 3.2.3. The third sound waves are exhibited as film thickness fluctuations. Although the relative permittivity of liquid helium is relatively low ($\epsilon_r = 1.058$), light experiences a slightly larger effective refractive index in regions with a thicker superfluid

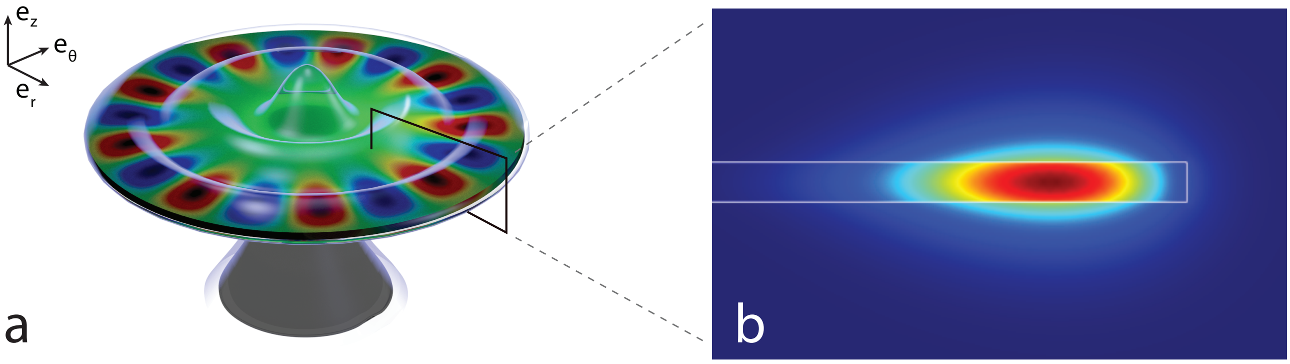

Figure 5.1: (a) Artistic illustration of a disk-shaped optomechanical resonator supporting an optical resonance (red and blue) coated with self-assembling superfluid thin film. (b) Cross-section of the finite element method (FEM) simulated optical intensity profile of the WGM optical mode. Figure is reproduced from Ref. [2].

film, and a lower effective refractive index in regions with a thinner film, because of the optical mode's evanescent field outside the cavity. This leads to the dispersive coupling between the intracavity optical field and the acoustic waves illustrated in Fig. 5.1, where the superfluid film thickness fluctuations generated by a third sound wave modulate the effective refractive index of the cavity, and consequently change the cavity path length. This dispersive coupling can be described by the frequency shift shift $\Delta\omega$ of a WGM mode in the presence of superfluid thin film. Using perturbation theory, the frequency shift has a functional form [127]:

$$\frac{\Delta\omega}{\omega_0} = -\frac{1}{2}\frac{\int_{\text{film}}(\epsilon_{\text{sf}}-1)|\vec{E}(\vec{r})|^2 d^3\vec{r}}{\int_{\text{all}}\epsilon_r(\vec{r})|\vec{E}(\vec{r})|^2 d^3\vec{r}}, \tag{5.1}$$

where ω_0 is the original optical resonance frequency with no superfluid, $\vec{E}(\vec{r})$ is the electric field distribution of the WGM mode without the perturbation from superfluid, $\epsilon_r(\vec{r})$ is the relative permittivity, and the relative permittivity of liquid helium ϵ_{sf} is 1.058. The numerator is an integral over the volume of the superfluid film on the resonator surface, and the denominator is over the whole calculation space. Thus, Eq. (5.1) can be understood as the ratio between the electromagnetic (EM) energy of the optical mode evanescently distributed in the superfluid film and the total energy of the optical mode. This understanding is the basic idea of the perturbation theory.

Fig. 5.2(a) shows the FEM simulated electric field intensity profile of a transverse electric (TE) WGM of wavelength $\lambda = 1.5\,\mu m$ supported in a silica micro-disk of 40 μm radius and 2 μm thickness. The solid line is the electric field intensity distribution over the vertical axis represented by the dashed line, which goes through the center of the optical mode. The intensity distribution over the vertical axis shows that the intracavity optical field is tightly confined inside the silica resonator, while there is weak evanescent field distributed at the top and lower interfaces where the superfluid film resides. This weak evanescent field at the interfaces leads to optomechanical coupling between the superfluid film and intracavity optical field, as dictated by Eq. (5.1). The optomechanical coupling can be improved through optimizing the

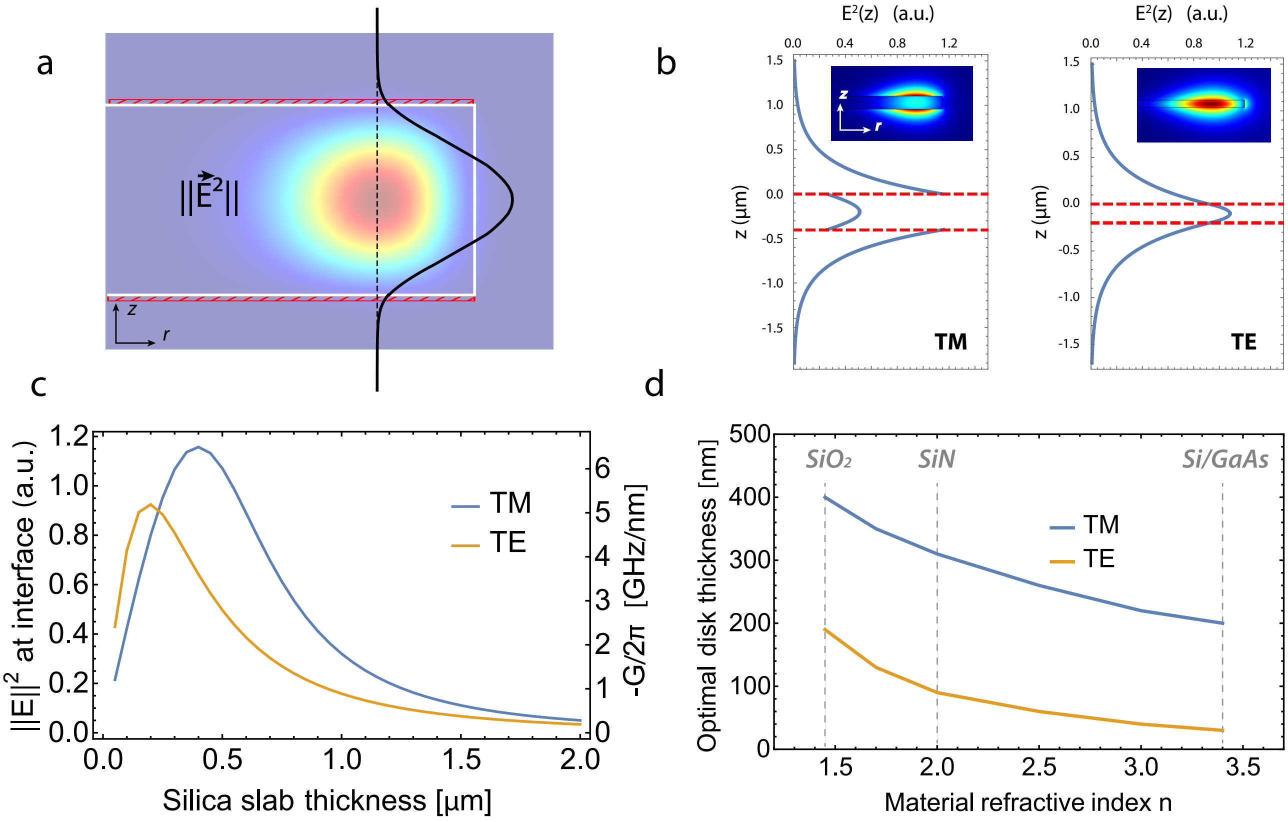

Figure 5.2: (a) FEM simulation showing the radial cross-section of a TE WGM of wavelength 1.5 μm confined in a silica disk of 40 μm radius and 2 μm thickness. Overlayed in black is a plot of the $|\vec{E}|^2(z)$ mode profile along the dashed black line going through the center of the WGM. The red region indicates the superfluid film on top and bottom. (b) Vertical mode profiles $|\vec{E}|^2(z)$ for a 1.5 μm wavelength TM (resp. TE) WGM confined in a 400 nm (200 nm) thick, 40 μm radius disk. The dashed red lines mark the disk upper and lower boundaries. Inset: FEM radial cross-section of $|\vec{E}|^2$ for each WGM. (c) Value of E^2 at the interface calculated using the Effective Index Method, for TM (blue) and TE (orange) polarized modes. Right axis: optical frequency shift per nm of superfluid $G/2\pi$. (d) Indicative optimal disk thickness for maximal field at the interface and superfluid detection, as a function of disk material refractive index. Figure is reproduced from Ref. [2].

resonator thickness and WGM polarization to maximize the evanescent field at the top and lower interfaces. Fig. 5.2(b) compares the vertical intensity distribution of a transverse magnetic (TM) polarized WGM in a 400 nm thick 40 μm radius silica disk, and a TE WGM in a 200 nm thick disk of the same radius. This figure shows that with a smaller disk thickness the WGM gets less confined by the silica material and is more exposed to the superfluid region, resulting to a larger resonance frequency shift of the WGM for a given magnitude of film thickness fluctuation.

This effect is systematically studied with the calculations shown in Fig. 5.2. The calculations of the TE and TM mode profiles inside a slab waveguide with different thickness (normalized such that $\int_{-\infty}^{\infty} \epsilon_r E^2 dz = 1$) are done using the effective index method (EIM), and the value of E^2 at the interface is recorded at each thickness. The result of the calculations shows that for each polarization the electric field intensity at the interface reaches a maximum when the disk thickness decreases to a certain thickness (roughly around 0.2 to 0.4 μm depending on the polarization). Below this optimal disk thickness the electric field intensity at the interface starts to drop again, because the disk is too thin that the electromagnetic wave is poorly confined along z axis. Then the same calculation is repeated for the slab waveguide with different values of refractive index, and the optimal thickness for TE and TM WGMs are plotted in Fig. 5.2. It is not surprising that the higher the material refractive index is, the smaller the optimal thickness required to have maximal evanescent field at the disk interface. For example, the optimal thickness for the TM mode in a silicon or gallium arsenide disk is around 200 nm, which is around half of the optimal thickness for silica disk. Although the result starts to be inaccurate due to the limitations of the EIM, they are still very useful if we are going to optimize the resonator geometries for strong optomechanical coupling between superfluid and light. What's more, these calculation results show that the optimal disk thickness for the TM mode is larger than that for the TE mode. As shown by the mode profiles along over vertical direction in Fig. 5.2, there is a step increase of the TM mode's electric field intensity outside the disk. This step increase is required by the continuity of the electric displacement field ($D_z = \epsilon_r E_z$), since the dominant field component of the TM mode is E_z, which is perpendicular to the top and lower interfaces. The step increase of the TM mode's electric field intensity outside the disk allows the TM mode stronger optomechanical coupling than the TE mode with the same disk thickness.

The characteristic decay length of the evanescent field in the vertical direction is on the order of hundred nanometers [see Fig. 5.2(b)], so the decay of E^2 is negligible over the superfluid film thickness typically of 1 to 30 nm. Therefore, rearranging Eq. (5.1) yields the optomechanical resonance frequency shift per mechanical displacement $G = \Delta\omega_0/\Delta z$:

$$G = \frac{\Delta\omega_0}{\Delta z} = -\frac{\omega_0}{2}\frac{\int_{\text{interface}}(\epsilon_{\text{sf}} - 1)|\vec{E}(\vec{r})|^2 d^2\vec{r}}{\int_{\text{all}} \epsilon_{\text{r}}(\vec{r})|\vec{E}(\vec{r})|^2 d^3\vec{r}}, \tag{5.2}$$

where the integral in the numerator is over the resonator top interface, assuming there is only superfluid film coated on the top interface. Applying Eq. (5.2) only to the vertical direction gives $G/2\pi$ as a function of resonator thickness in the right axis of Fig. 5.2(c). As is shown in the figure, careful design of the resonator thickness is very crucial, since the G of the TM mode can be improved by 20 times when the silica disk thickness changes from 2 to 0.4 μm. Thereby, large G of up to 6 GHz/nm is a experimentally achievable with this superfluid optomechanical resonator, although liquid helium's optical properties are close to those of vacuum ($\epsilon_r = 1.058$, n = 1.029) [62]. Additionally, the G of this optomechanical resonator is not only large in magnitude, but is also independent of resonator radius, and superfluid film thickness (as long as the thickness is within 30 nm, which is true for most experimental cases).

Similarly, the couplings (G and G_{vertical}) between light and the superfluid films on the lower interface and the vertical sidewall can also be calculated using EIM. In experiments, when the thickness of the superfluid film covering the WGM resonator varies uniformly, the optical resonance shift would be $2G + G_{\text{vertical}} > 10$ GHz/nm. From an experimental point of view, assuming an optical mode of a 2×10^6 Q , with a 10 GHz/nm coupling rate, a 10 pm film thickness change (*i.e.* $\frac{1}{36}$th of a helium monolayer [128]) would change the resonance frequency of the mode by one linewidth. Compared with widely used capacitive detection methods [88, 129], the sensitivity to superfluid film thickness here is around two orders of magnitude larger.

5.2.2 Superfluid Third Sound Modes

The basics of third sound waves [18, 84–86, 88, 130] has been introduced in §3.2.3. They are similar to shallow water waves, exhibited as film thickness fluctuations, as shown in the left of Fig. 5.3. Here in this section more details about third sound are introduced, specifically the mode profile and the effective mass of acoustic resonant modes of third sound.

The optical disk resonator not only supports WGMs, but also confines third sound waves on its top surface, forming third sound modes. The mode profile of the third sound modes is determined by the geometry of the confinement. As shown in Fig. 5.3(a), given the circular geometry of the disk, the mode profile has a functional form of Bessel functions from Eq. (3.70):

$$\eta_{m,n}(r,\theta,t) = \eta_0 J_m\left(\zeta_{m,n}\frac{r}{R}\right) e^{i(m\theta \pm \Omega t)}, \tag{5.3}$$

where m and n are the azimuthal and radial mode numbers respectively, η_0 is the amplitude of the mode, J_m is the Bessel function of the first kind of order m, $\Omega = (\zeta_{m,n}c_3)/R$ is the mode frequency, θ is the angular direction, the ± sign in the exponential function denotes the travelling direction (clockwise or counter-clockwise) of the mode, and $\zeta_{m,n}$ is a frequency parameter, which is dependent on the mode order and boundary conditions, as displayed in Table 3.2.3. The discussions below are focused on the rationally invariant Bessel modes, as they modulate the optical cavity length most efficiently and thus has the largest optomechanical coupling [38].

Before we proceed to calculate the effective mass and zero point motion, let us revisit the boundary conditions of the third sound modes on a disk resonator from § 3.2.3. The two types of boundary conditions for rotationally invariant Bessel modes are: the fixed ($\eta(R) = 0$) boundary condition, where there is no displacement at the boundary; the free ($\partial_{\mathrm{r}}\eta(R) = 0$) boundary condition, also know as 'no flow' boundary condition, where the radial velocity of superfluid flow is 0 at the boundary. The first three rotationally invariant Bessel modes' profiles are plotted in Fig. 5.3(b). In addition to illustrating the boundary conditions, profiles of these modes (especially the fundamental mode) can also indirectly show that the Bessel modes with the free boundary condition is volume conserving, while the ones with fixed boundary condition is not.

The effective mass m_{eff} is an important parameter in optomechanics, as it is required to calculate the single photon optomechanical coupling rate g_0:

$$g_0 = Gx_{\mathrm{zpf}} = G\sqrt{\frac{\hbar}{2m_{\mathrm{eff}}\Omega}}\ , \tag{5.4}$$

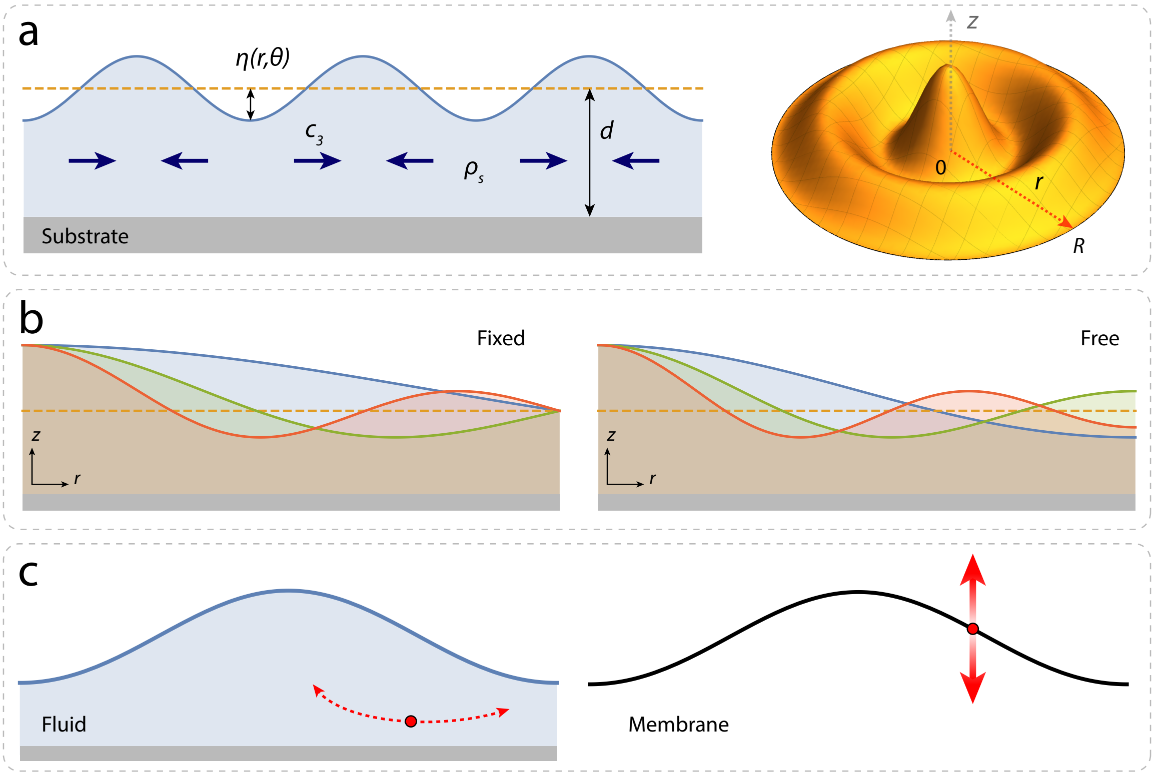

Figure 5.3: Superfluid third sound. (a) Left: schematic illustration of a superfluid third sound wave with profile $\eta(\vec{r})$ on a film of mean thickness d (dashed orange line). The normal fluid component [46] is viscously clamped to the surface, while the superfluid component ρ_s oscillates mostly parallel to the substrate (blue arrows). Right: plot of the surface profile for the (m = 0; n = 3) Bessel mode with free boundary conditions. (b) Radial profile $\eta(r)$ along the dashed red line in (a) for the (m = 0; n = 1) –blue–, (m = 0; n = 2) –green– and (m = 0; n = 3) –red– Bessel modes with fixed (left) and free (right) boundary conditions. (c) Comparison between the trajectory described by a 'particle' in a fluid (left) and a solid membrane (right).Figure is reproduced from Ref. [2].

where x_{zpf} is the zero point motion of the mechanical mode, Ω is the mechanical resonance frequency. The effective mass of a continuum mechanical system can be calculated by shrinking its volume to a reduction point $\vec{A}$, and treating the system with an equivalent point mass m_{eff} at the reduction position $\vec{A}$ with velocity $v(\vec{A})$ having the same amount of kinetic energy E_k. Mathematically, the definition of the effective mass of a continuous mechanical system is:

$$m_{\text{eff}} = \frac{2E_k}{v_A^2} = \frac{\int_V \rho v^2(\vec{r}) d^3\vec{r}}{v^2(\vec{A})} \tag{5.5}$$

Applying the general definition of effective mass to rotationally invariant modes of circular solid mechanical resonator of thickness d, the effective mass of the modes for a point on the resonator boundary is [131]:

$$m_{\text{eff,solid}} = 2\pi\rho d \frac{\int_0^R r\eta^2(r) dr}{\eta^2(R)}, \tag{5.6}$$

where the velocity $v(\vec{r})$ for both in- and out-of-plane mechanical modes is assumed to be independent of the z direction. However, the velocity field in superfluid film is related to its hydrodynamic equations, making it hard to get the analytical expression for the velocity field. Thus, to avoid solving hydrodynamic equations, equipartition theorem is used to replace the kinetic energy term in Eq. (5.5) with the van der Waals potential energy of the third sound modes of amplitude $\eta(r,\theta)$. This replacement is valid because equipartition theorem requires that the increase of the van der Waals potential energy due to the film thickness increase by the third sound amplitude $\eta(r,\theta)$ is equal to the kinetic energy:

$$\begin{aligned} E_k = E_{\text{pot}} &= \rho \int_{\theta=0}^{2\pi} \int_{r=0}^{R} \left(\int_{z=0}^{d+\eta(r,\theta)} U(z)dz \right) r dr d\theta - \rho \int_{\theta=0}^{2\pi} \int_{r=0}^{R} \left(\int_{z=0}^{d} U(z)dz \right) r dr d\theta \\ &= \rho \int_{0}^{2\pi} \int_{0}^{R} \left(\int_{d}^{d+\eta(r,\theta)} U(z)dz \right) r dr d\theta, \end{aligned} \tag{5.7}$$

where $U(z)$ is the van der Waals potential energy [Eq. (3.64)] of a unit mass of the film [10]:

In the limit that the third sound amplitude is very small compared to the average film thickness $\eta \ll d$, the increase of the van der Waals potential of a unit mass due to the third sound amplitude can be approximated by the first two terms of the Taylor expansion of the integral over the vertical axis z in Eq. (5.7), thus we have:

$$\int_{d}^{d+\eta(r,\theta)} U(z)dz = -\frac{\alpha_{\text{vdw}}\eta(r,\theta)}{d^3} + \frac{3\alpha_{\text{vdw}}\eta^2(r,\theta)}{2d^4}. \tag{5.8}$$

Then Eq. (5.7) is simplified as:

$$E_{\text{pot}} = 2\pi\rho \int_0^R dr\, r \left(-\frac{\alpha_{\text{vdw}}\eta(r,\theta)}{d^3} + \frac{3\alpha_{\text{vdw}}\eta^2(r,\theta)}{2d^4} \right). \tag{5.9}$$

Focusing on the volume conserving free (‘no flow’) boundary condition ($\int_0^R r dr \eta(r) = 0$), the effective mass of a point on the film surface at $r = R$ is:

$$m_{\text{eff}} = \frac{2E_{\text{pot}}}{v^2(R)} = \frac{6\pi\rho\alpha_{\text{vdw}} d^{-4} \int_0^R r\eta^2(r)dr}{\eta^2(R)\Omega^2}. \tag{5.10}$$

With $\Omega = \frac{\zeta c_3}{R}$ and third sound velocity [Eq. (3.69)]:

$$m_{\text{eff}} = \left(\frac{\rho}{\rho_{\text{s}}}\right) \left(\frac{R}{d}\right)^2 \frac{1}{\zeta^2} \times 2\pi\rho d \frac{\int_0^R r\eta^2(r)dr}{\eta^2(R)}, \tag{5.11}$$

which turns out to be the effective mass of a solid mechanical oscillator scaled by a prefactor proportional to $(R/d)^2$. Interesting result from this equation is that in contrast to the effective mass m_{eff} of a solid circular membrane mechanical oscillator (like its real mass), the effective mass of a third sound resonator on a superfluid film actually scales as R^4/d, which means third sound modes supported by thicker and heavier films will have smaller effective mass, and thus larger zero point motion. This huge scaling difference between a solid mechanical oscillator and a liquid mechanical oscillator are contributed by two factors: 1) the extremely nonlinear van der Waals restoring force; 2) as illustrated in Fig. 5.3(c), the microscopic motion of a unit mass of the liquid resonator is nearly horizontal, while the unit mass in a solid resonator has

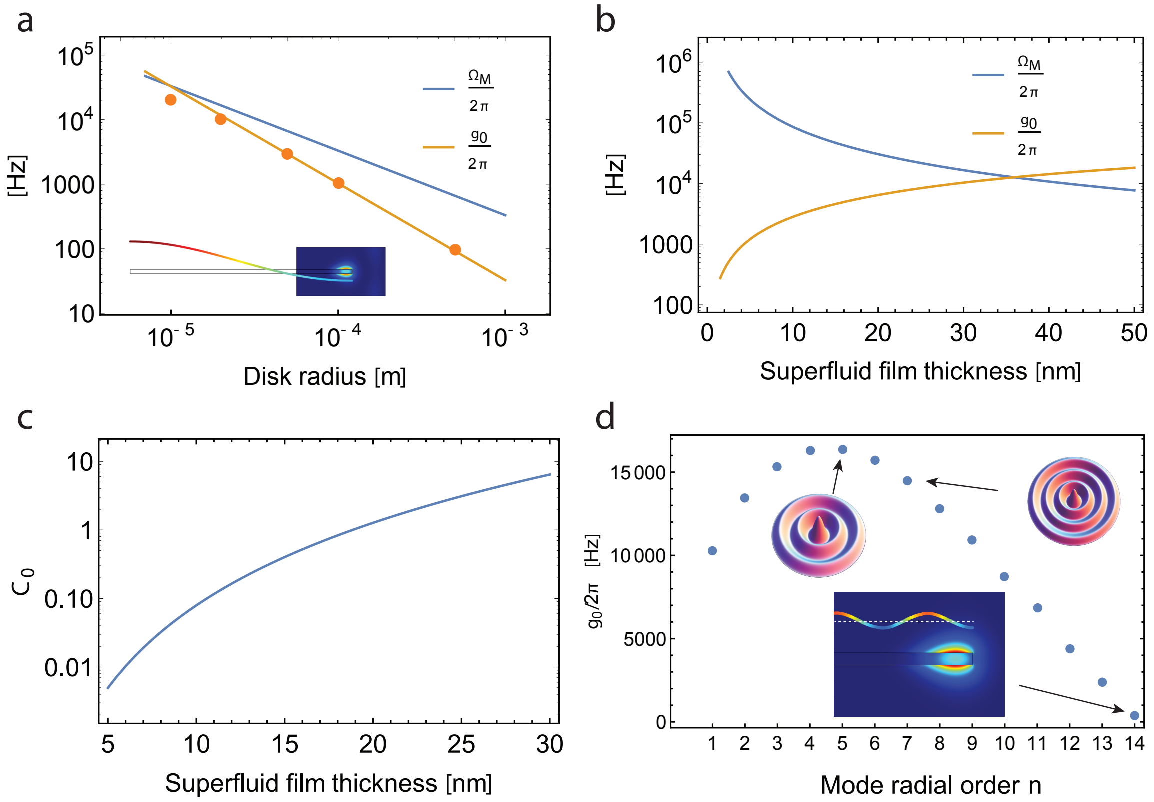

Figure 5.4: Optomechanical parameters.(a) Single photon optomechanical coupling strength $g_0/2\pi$ and mechanical frequency $\Omega/2\pi$ for the fundamental (m = 0; n = 1) third sound mode as a function of resonator radius, for a d = 30 nm thick superfluid film. Solid line: analytical formula, points: individual FEM simulations. Inset: FEM simulation displaying the WGM overlayed with the third sound mode displacement profile (colored line). (b) $\Omega/2\pi$ (blue) and $g_0/2\pi$ (orange) as a function of film thickness for a $R = 20\,\mu$m disk. (c) Predicted single photon optomechanical cooperativity C_0 as a function of film thickness d, for a $R = 20\,\mu$m disk. (d) Influence of third sound radial mode order n on $g_0/2\pi$, for $R = 20\,\mu$m and d = 30 nm. Inset: mechanical surface deformation profiles and FEM simulation showing the WGM mode overlayed with the displacement profile of the (m = 0; n = 14) third sound mode. All results are for free boundary conditions. Figure is reproduced from Ref. [2]

only vertical trajectory. In addition to the inverse scaling with superfluid film thickness, the proportion of the third sound mode effective mass to R^4 means that there can be a 5×10^8 effective mass reduction, when the resonator is decreased from a centimeter-scale to 40 μm radius resonator.

5.2.3 Superfluid Optomechanical Coupling Rate

In the previous section we investigated the optomechanical resonance frequency shift per mechanical displacement G and the effective mass of third sound modes. Here the optomechanical coupling rate g_0 is studied based on Eq. (5.4). In Fig. 5.4(a) both the resonance frequency $\Omega/2\pi$ and $g_0/2\pi$ of the fundamental ($m = 0$; $n = 1$) third sound mode are shown to have a linear relation with disk radius. The yellow solid line is the g_0 directly calculated using Eq. (5.4) and Eq. (5.11) assuming a constant $G/2\pi$ of 6.6 GHz/nm. This assumption is only valid for cases of disk radius above 20 μm, where the micro sized radial extension of the WGM is small compared to R, and thus the displacement of the fundamental Bessel mode over the optical mode region can still be approximated as flat surface fluctuations [see inset of Eq. (5.4)]. Whereas for high radial order Bessel modes on small radius resonator, this approximation is no longer valid, and g_0 needs to be calculated in a more general approach through the overlap integral of the optical field and the third sound displacement field:

$$g_0 = -\frac{\omega_0}{2}\frac{\int_{\text{interface}} q(\epsilon_{\text{sf}}-1)|\vec{E}(\vec{r})|^2 d^2\vec{r}}{\int_{\text{all}} \epsilon_r(\vec{r})|\vec{E}(\vec{r})|^2 d^3\vec{r}}, \tag{5.12}$$

where $q = \frac{\eta(r)}{\eta(R)}x_{\text{zpf}}$ is the zero point motion x_{zpf} normalized third sound displacement profile at R. The orange dots in Fig 5.4(a) are the FEM simulation results using the general g_0 calculation method. As is shown, the solid line from the analytical calculation agrees with the full simulation very well with disk radius larger than 20 μm. Below 20 μm disk radius, the full simulation results start to become smaller than the analytical results, as the constant G assumption is no longer valid. More importantly, this figure shows that our superfluid optomechanical resonator could reach the ultra-strong coupling regime where $g_0 > \Omega$, as g_0 increases faster than the third sound frequency Ω with smaller resonator radius R.

The effect of superfluid film thickness d on both g_0 and Ω is shown in Fig. 5.4(b) for a 20 μm radius resonator. As the third sound resonance frequency Ω is proportional to $d^{-3/2}$ and g_0 proportional to $d^{5/4}$, g_0 increases with film thickness, and Ω decreases with film thickness, eventually resulted into ultra-strong coupling regime with $g_0 > \Omega$ for 34 nm film thickness. Fig. 5.4(c) plots the effect of film thickness on the single photon cooperativity $C_0 = 4g_0^2/(\kappa\Gamma)$. Assuming an optical linewidth $\kappa/2\pi = 20\text{MHz}$ (Q = 10^7) as demonstrated in thin silica disk optical resonator of the same radius [35], and a mechanical Q_m of 4000 as demonstrated in our previous work with microtoroid resonators [13], the single photon cooperativity reaches 1 with around 20 nm thickness, indicating that the strong optomechanical coupling is easily achievable with this optomechanical resonator with thick superfluid films. These excellent performances of large cooperativities and single photon optomechanical coupling rate can bring a wide range of applications to this optomechanical system, like high precision sensing of acoustic excitations in superfluid film [50], ground state cooling of acoustic modes [10], and reaching strong light superfluid interaction [109, 132].

5.3 Vortex Detection Based on Superfluid Optomechanics

Here I show that two dimensional vortex dynamics can also be optically probed using this platform, where the third sound waves bridge the interaction between light and vortices. Probing vortex dynamics in two dimensional superfluid helium-4 is motivated by several reasons: 1) in two dimensional superfluid systems the topological phase transition (BKT transition)

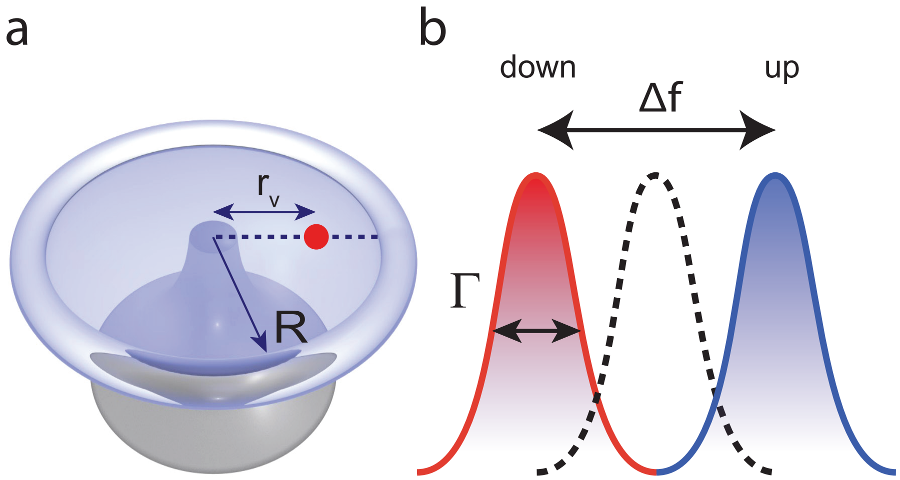

Figure 5.5: (a) Schematic of a microtoroidal resonator of radius R= 30μm covered with a superfluid helium thin film, with one quantized vortex offset from the disk origin. The red dot indicates the vortex core. (b) Illustrated frequency splitting of a Bessel mode due to the presence of a vortex. Figure is reproduced from Ref. [3].

allowed by quantized vortices has not been well studied experimentally [19, 133]; 2) there is a broad range of interesting physics in superfluid dynamics, like Onsager vortices, which are collective vortex dipoles with negative temperature and large-scale order [134, 135]. So far the experiments on superfluid dynamics have focused on weakly-interacting many-body systems (Bose-Einstein condensates formed with ultra-cold gases) [136]. Furthermore, since the Gross-Pitaevskii equation cannot give a valid microscopic model in the strongly-interacting regime, strongly-interacting superfluids do not have a microscopic model [137]. Thus experimentally probing vortices in strongly-interacting two dimensional superfluid is important and can help us understand superfluid dynamics.

5.3.1 Vortex-Sound Interactions

Here we consider a simple model as illustrated by Fig. 5.5(a), where a vortex denoted by the red dot residing in a two dimensional superfluid thin film coated on a microtoroidal resonator. The vortex interacts with third sound waves dispersively, namely adding or subtracting the vortices will change the resonance frequencies of the third sound modes. This dispersive interaction is due to the vortex induced change of the background flow field and the density (thickness) profile of the superfluid thin film, consequently leading to the modification of the eigen acoustic modes supported by the superfluid film, and the lift-up of the degeneracy of the clockwise and counter-clockwise rotating third sound waves, shown as the frequency splitting in in Fig. 5.5(b). The change of the acoustic eigen frequency is associated with the change of the energy stored in the acoustic mode. Because of the equipartition theorem, we use the kinetic energy change of the acoustic mode's flow field to approximate the change of its total energy. Therefore, this interaction can be simply understood as the overlap integral of the vortex and sound velocity fields.

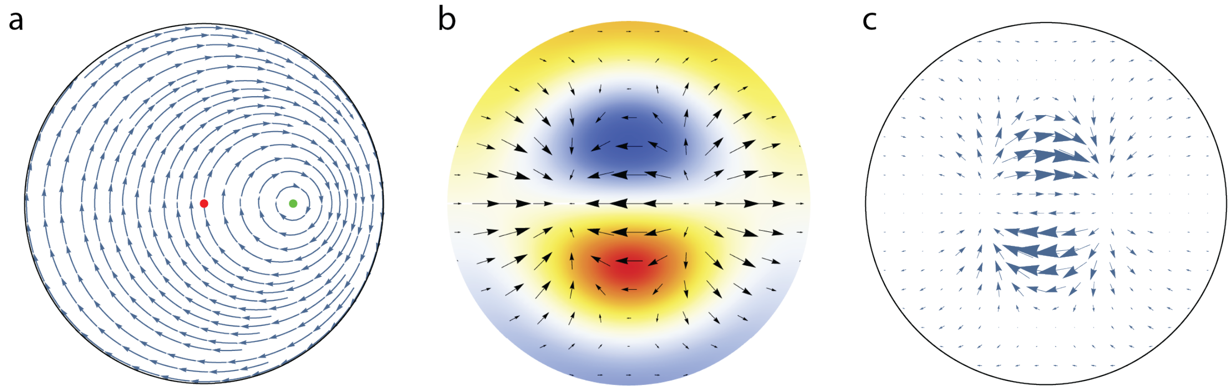

Figure 5.6: (a) Streamlines of $\vec{v}_v(\vec{r})$ for a CW vortex (green dot) offset from the origin (red dot) in a circular domain. ($X_1 = 0.5R$; $X_2 = 2R$). (b) Black arrows represent the instantaneous superfluid flow field $\vec{v}_3(\vec{r})$, for a clockwise-rotating ($m = 1$; $n = 2$) Bessel-mode with free boundary condition. Surface plot shows the associated surface deflection $\eta(\vec{r})$ (color code: red = positive, blue=negative). CW nature can be seen by noticing that fluid starting to accumulate ahead of the red peak, where $\vec{\nabla} \cdot \vec{v}_3 < 0$. The velocity field is positive under the peaks, negative under the troughs, and irrotational, *i.e.* with $\oint \vec{v}_3 \cdot \vec{dl} = 0$ for all contours inside the superfluid. (c) Vector field of $\vec{v}_3(\vec{r}) \times \eta(\vec{r})$. While from symmetry one sees that $\iint \vec{v}_3 \cdot \vec{v}_v = 0$, multiplication by the surface deflection profile $\eta(\vec{r})$ leads to a non-zero energy shift of the CW/CCW third-sound waves, see Eq. (5.19). Figure is reproduced from Ref. [3].

The streamfunction of a point vortex is given in Eq. (3.74), and its form for a circular geometry can be described with Cartesian coordinates by:

$$\Psi = -\frac{\kappa}{2\pi}\left(\ln\left(\sqrt{(x-X_1)^2+y^2}\right) - \ln\left(\sqrt{(x-X_2)^2+y^2}\right)\right), \tag{5.13}$$

and the components of its velocity field can be derived from the streamfunction as below:

$$v_{vx} = \frac{\partial \Psi}{\partial y}; \qquad \text{and} \qquad v_{vy} = -\frac{\partial \Psi}{\partial x}. \tag{5.14}$$

An example of the vortex velocity field is given by Fig. 5.6.

The displacement profile η of a travelling Bessel mode is introduced in Eq. (5.3), and the corresponding flow velocity field is:

$$\vec{v}_3 = \pm \frac{i\, c_3^2}{\Omega\, h_0} \vec{\nabla} \eta \tag{5.15}$$

where the ± sign denotes the travelling direction of the Bessel mode. Using this equation the velocity field of a clockwise rotating Bessel mode (m = 1, n = 2) is plotted in Fig. 5.6.

Generally, for a flow induced by either vortices or acoustic motions, the kinetic energy of the flow field is given by:

$$E = \frac{1}{2} \int \rho\, \vec{v}^2(\vec{r}) d^3(\vec{r}), \tag{5.16}$$

where ρ is the fluid density and $\vec{v}$ is the velocity field in the flow. This means that by integrating the velocity field over the whole superfluid volume, we can calculate the kinetic energy carried by the acoustic motion or vortices. Therefore the kinetic energy difference of the Bessel mode rotating in the same direction with the vortex and its direction-degenerate Bessel mode rotating against the vortex is given below:

$$\Delta E\left(t\right)=\frac{1}{2}\,\rho\int_{\theta=0}^{2\pi}\int_{r=0}^{R}\int_{z=0}^{h_0+\eta(r,\theta,t)}\left(\left|\left|\vec{v}_3\left(\vec{r},\,t\right)+\vec{v}_v\left(\vec{r}\right)\right|\right|^2-\left|\left|\vec{v}_3\left(\vec{r},\,t\right)-\vec{v}_v\left(\vec{r}\right)\right|\right|^2\right)r\,dr\,d\theta\,dz \tag{5.17}$$

Since the velocity fields are vectorial, this equation is valid for any sound mode and any vortex position. Assuming $\vec{v}_3$ and $\vec{v}_v$ are constant in the z direction, because there is no friction between the inviscid superfluid film and the substrate, Eq. (5.17) is reduced to be:

$$\Delta E\left(t\right)=2\rho\int_{\theta=0}^{2\pi}\int_{r=0}^{R}\vec{v}_3\left(r,\theta,\,t\right)\cdot\vec{v}_v\left(r,\theta\right)\left(h_0+\eta\left(r,\theta,t\right)\right)r\,dr\,d\theta \tag{5.18}$$

As shown in Fig. 5.6, v_{vx} is an odd function of θ, v_{vy} is an even function of θ, v_{3x} is an even function of θ, and v_{3y} is an odd function of θ. The parity difference of these velocity components over θ makes the integral $\int\vec{v_3}\cdot\vec{v_v}d\theta=0$. So cancelling the average film height h_0, the equation above is reduced to be:

$$\Delta E\left(t\right)=2\rho\int_{\theta=0}^{2\pi}\int_{r=0}^{R}\vec{v}_3\left(r,\theta,t\right)\cdot\vec{v}_v\left(r,\theta\right)\eta\left(r,\theta,t\right)r\,dr\,d\theta \tag{5.19}$$

The product of the two vector fields $\vec{v_3}\cdot\vec{v_v}d$ is basically the unnormalized projection of $\vec{v_v}$ onto $\vec{v_3}$, which can be understood as the change of the Bessel mode flow velocity due to the presence of the vortex flow velocity. Thus the whole integral is the surface-averaged Doppler shift of the Bessel mode flow kinetic energy, weighted by the displacement amplitude η of the Bessel mode. Then we average the kinetic energy change over a Bessel mode oscillation period T:

$$\langle\Delta E\rangle=\frac{1}{T}\int_0^T\Delta E\left(t\right)dt=2\,\rho\int_r\int_\theta r\,dr\,d\theta\left(v_{v\,r}\,\frac{1}{T}\int_0^T v_{3\,r}\,\eta\,\mathrm{d}t\right)+\left(v_{v\,\theta}\,\frac{1}{T}\int_0^T v_{3\,\theta}\,\eta\,\mathrm{d}t\right), \tag{5.20}$$

where the vectorial velocity fields are decomposed into the components for radial and angular directions. Comparing Eqs. (5.3,5.15) with the third sound flow velocity components below, we find that v_{3r} is out of phase with η, while $v_{3\theta}$ is in phase.

$$v_{3r}(r,\theta,t)=i\eta_0\frac{c_3^2R}{\zeta_{m,n}h_0}J_m\left(\zeta_{m,n}\frac{r}{R}\right)e^{i(m\theta\pm\Omega t)} \tag{5.21}$$

$$v_{3\theta}(r,\theta,t)=\eta_0\frac{c_3^2R}{\zeta_{m,n}h_0}\frac{m}{r}J_m\left(\zeta_{m,n}\frac{r}{R}\right)e^{i(m\theta\pm\Omega t)} \tag{5.22}$$

Thus, the first integral in Eq. (5.20) is averaged to be zero over time, and the second integral is resulted to be $\frac{1}{2}|v_{3\theta}||\eta|$. Inserting Eqs. (5.3,5.22) in to the result yields:

$$\langle\Delta E\rangle=\frac{\rho\,m\,c_3^2}{\Omega\,h_0}\int_{r=0}^{R}r\,dr\,\eta_0^2\,\frac{J_m^2\left(\zeta_{m,n}\frac{r}{R}\right)}{r}\int_{\theta=0}^{2\pi}v_{v\,\theta}\,d\theta, \tag{5.23}$$

which we rewrite, with $\eta\left(r\right)=\eta_0\,J_m\left(\zeta_{\mathrm{m,n}}\,\frac{r}{R}\right)$, as:

$$\langle\Delta E\rangle=\frac{\rho\,m\,c_3^2}{\Omega\,h_0}\int_{r=0}^{R}\frac{dr}{r}\,\eta^2\left(r\right)\int_{\theta=0}^{2\pi}v_{v\,\theta}\,r\,d\theta \tag{5.24}$$

We find that the second integral over θ is equivalent to a closed contour integral $\oint \vec{v_v} d\vec{l}$ over a circle of radius r centered at the origin of the resonator. Eq. (3.72) tells that the closed contour integral is equal to the circulation quanta κ if it encloses the vortex core, and to zero if it does not. So the region within radius r does not contribute to the $\langle \Delta E \rangle$. Neglecting this region, we get a modified radial integration lower bound:

$$\langle \Delta E \rangle = \frac{\rho \, m \, c_3^2 \, \kappa}{\Omega \, h_0} \int_{r=\text{offset}}^{R} \frac{dr}{r} \, \eta^2 \left(r \right) \tag{5.25}$$

Since the energy E of a harmonic oscillator is proportional to Ω^2, so we have $\frac{\Delta E}{E} = 2\frac{\Delta \Omega}{\Omega}$ and the splitting Δf (in Hz) equals:

$$\Delta f = \frac{\Omega}{4\pi} \frac{\Delta E}{E}, \tag{5.26}$$

with the kinetic energy E of the Bessel mode flow field, for $m > 0$, given by [63]:

$$E = \frac{1}{2} \int \rho \, v^2 \left(\vec{r} \right) d^3 \left(\vec{r} \right) = \frac{\pi \, \rho \, c_3^2}{2 \, h_0} \int_0^R \eta^2 \left(r \right) r \, dr \tag{5.27}$$

Combining Eqs.(5.24,5.27) yields:

$$\Delta f = \frac{\kappa \, m}{2 \, \pi^2} \frac{\int_{\text{offset}}^{R} \frac{dr}{r} \, \eta^2 \left(r \right)}{\int_0^R dr \, r \, \eta^2 \left(r \right)} \tag{5.28}$$

This result shows that the vortex-induced splitting of a Bessel mode is not influenced by the superfluid parameters (film thickness, density), and it is linear with the circulation quanta (the quantity of vortices) in a way that the splitting generated by an ensemble of vortices is equal to the sum of the splittings generated by each single vortex at its position. In addition to the circulation quanta, the radial position of each vortex also affects the total splitting. As shown by Eq. (5.28), if a vortex drifts away from the center of the resonator, the contribution of this vortex to the total splitting decreases. Furthermore, the splittings of different Bessel modes induced by the same ensemble of vortices are also different. Some Bessel modes are more sensitive to vortices, and thus have larger splittings, while some Bessel modes are less sensitive to vortices. Therefore, monitoring different Bessel modes enables us to identify both the vortex number and their distribution in radial direction.

5.3.2 Experimental Detection of Vortices in a Thin Superfluid Film

The vortex detection experiment is based on the experimental setup shown in Fig. 4.2. The toroidal resonator is cooled with helium-4 gas to the base temperature of the helium-3 cryostat, thereby the helium-4 is condensed into superfluid, coating the resonator with a thin superfluid film. The laser light is locked on resonance with the resonator and the output light from the resonator is measured using homodyne detection method, such that the motions of the third sound waves on the resonator are imprinted as phase fluctuations of the output light and eventually exhibited as the oscillations of the homodyne photocurrent.

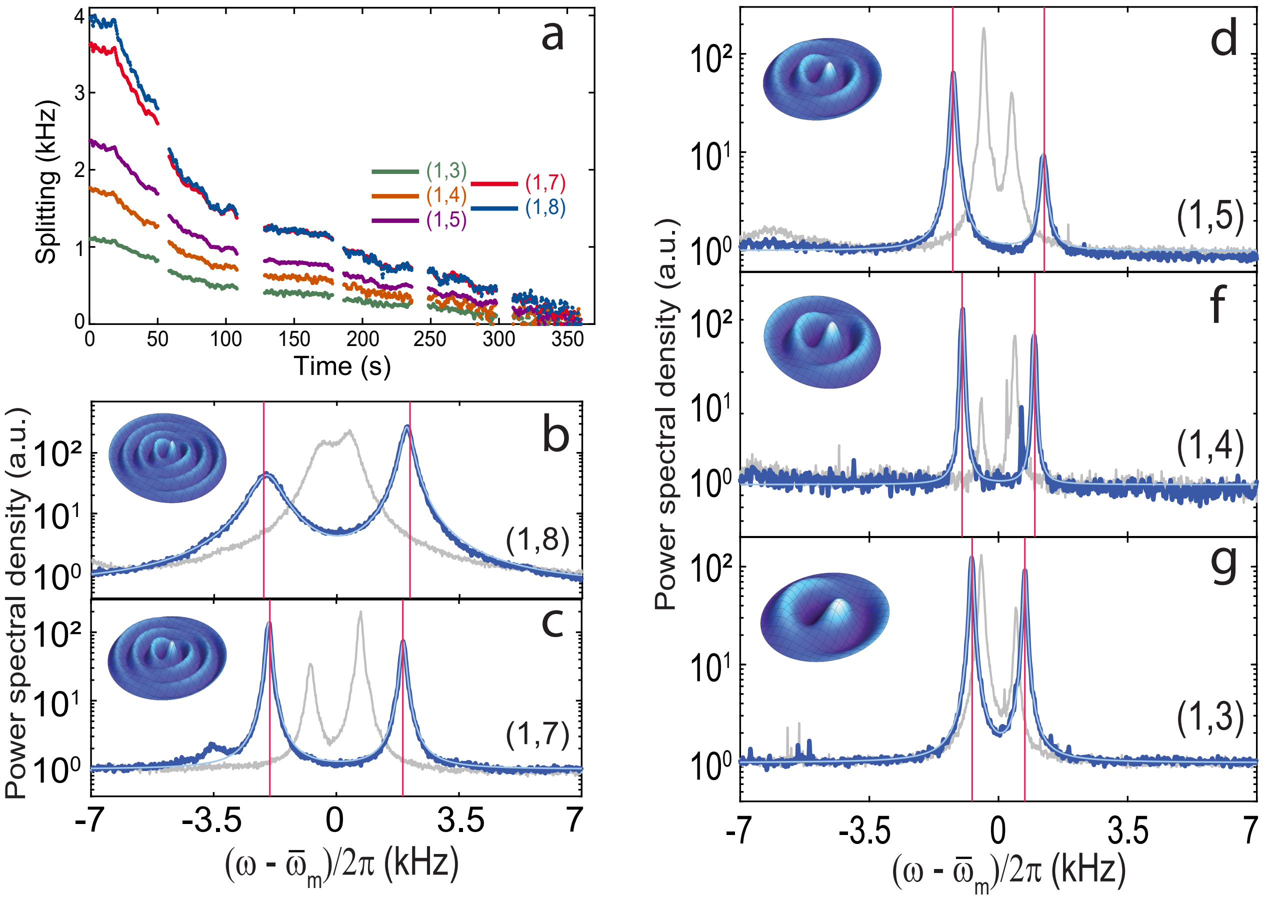

Figure 5.7: (a) Decay of frequency splittings of the (1,3), (1,4), (1,5), (1,7) and (1,8) thrd sound modes, respectively corresponding to the bottom-to-top traces. The data was taken with a large bandwidth and high memory-depth oscilloscope. During taking the data six continuous measurements were taken, separated by data-saving periods of approximately ten seconds each. (b)-(g) power spectra of different third sound modes before and after the frequency splitting decay. Figure is reproduced from Ref. [5].

When the system is in equilibrium, the third sound mode spectra obtained from the homodyne photocurrent display stable splittings, because the stationary geometry-imperfections lift up the degeneracy between clockwise and counter-clockwise third sound modes. The geometric splittings are shown as the gray curves in the experimental mechanical spectra in Fig. 5.7(b-g). Using Finite Element Modelling (FEM) the third sound modes are identified fairly accurately as shown in the insets of Fig. 5.7(b-g). However, when we drive the system out of equilibrium by injecting high laser power, the large superfluid flow due to the fountain effect or large third sound mode amplitude causes superfluid velocity above the critical velocity, and eventually sheds vortices on the resonator. Then we reduce the laser power or recover the laser frequency and interferometer lockings of the experimental setup, and measure the spectrum of the third sound modes in real-time. The generation of vortex ensemble brings the system out of equilibrium, leading to larger frequency splittings of the third sound modes than the stationary geometric imperfections induced splittings, as dictated by the vortex-position dependent splitting function (Eq. (5.28)). In Fig. 5.7(b-g) the large splittings are shown by the blue curves of the power spectra from the photocurrent signal right after vortices are shed. Via annihilation and vortex-vortex interaction, the vortex ensemble evolve into new equilibrium with lower system energy. Thus the third sound mode splittings decrease during the vortex evolution. Fig. 5.7(a) shows the evolution of the splittings over time. This evolution of the splittings is directly related to the vortex dynamics through the theory elaborated in the previous section (§ 5.3.1). The observed mode splittings in this experimental run agree very well with point vortex simulations of the initial metastable state of vortex dipole containing 17 free vortices with a total kinetic energy of $K_{\text{total}} = 7.8^{+0.6}_{-0.3}$ aJ, or 16 vortices with $K_{\text{total}} = 8.3^{+0.2}_{-0.6}$ aJ. The analysis of the simulations and the experimental results is elaborated in Ref. [5]. This experiment demonstrates that we are able to monitor in real-time the vortex number and the distribution of the vortex ensemble. In future experiments, with higher sensitivity (by increasing light-sound and vortex-sound couplings) and larger measurement bandwidth of this superfluid optomechanical system, it would be possible to detect single quantized vortex in two dimensional strongly-interacting superfluid.

5.4 Conclusion

This chapter describes a new cavity optomechanical system composed of a disk WGM resonator coated with thin superfluid films is theoretically developed. The theoretical estimation shows that the optomechanical coupling of the sound in superfluid films with light can be larger than the acoustic frequency, pushing the superfluid optomechanical system into quantum regime. Last, the coupling between sound and quantized vortices in two dimensional superfluid is theoretically elaborated. With the vortices bridged by the sound to the light field, the superfluid optomechanical system is experimentally demonstrated to be able to probe the coherent evolution of a vortex ensemble, which matches very well with point vortex simulations of the initial metastable state of 17 free vortices with a total kinetic energy of $K_{\text{total}} = 7.8^{+0.6}_{-0.3}$ aJ, or 16 vortices with $K_{\text{total}} = 8.3^{+0.2}_{-0.6}$ aJ.

Chapter 6

Ultra-low Threshold Brillouin Lasing

This chapter is based on the work submitted for publication and is available on the arXiv:
X. He, G. I. Harris, C. G. Baker, A. Sawadsky, Y. P. Sachkou, Y. Sfendla, S. Forstner, W. P. Bowen, Strong optical coupling through superfluid Brillouin lasing, arXiv 1907.06811, 2019.

In this chapter, we present the experiment on Brillouin lasing in a superfluid optomechanical system. This experiment studies the Brillouin interaction between travelling acoustic waves on the surface of a thin superfluid film and the intracavity optical field. First, the research background of Brillouin scattering is introduced. In the second section, a theoretical model is formulated based on coupled mode theory to explain the Brillouin interaction in a thin superfluid film. Next, we explain the experimental setup, and present experimental results. The final section concludes the chapter.

6.1 Research Background and Motivations

With recent improvement in the strength of interactions between optical fields and mechanical oscillators, using cavity optomechanics it has become possible to control and manipulate phonons -the energy quanta of mechanical motion- via radiation pressure using cavity optomechanics. The radiation-pressure mediated control of phonons has been key in a wide range of fundamental physics experiments, including ground state cooling, squeezing and entanglement of macroscopic mechanical oscillators [9–14]. Further, the ability to control and readout phonons with high precision has enabled many practical applications, such as precision sensing of mass [6], force [7], and gravitational waves [8], coherent frequency conversion [138], information storage [139, 140], injection locking of oscillators [141], etc. An alternative approach to control phonons is to utilise Brillouin scattering of light by acoustic waves [142].

Brillouin scattering is a type of inelastic scattering of light, commonly observed in fibre communication, where the Brillouin frequency shift causes spectral broadening. Brillouin scattering exists in optical fibres and waveguides because of the thermally populated acoustic waves

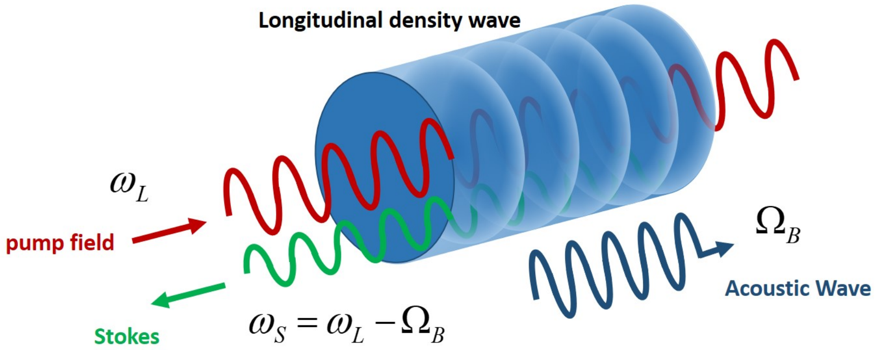

Figure 6.1: Illustration of Brillouin scattering process in an optical fiber, where a longitudinal acoustic wave generates compression and rarefaction of the fibre core material. Red: initial laser light with ω_L denoting its frequency; green: backscattered Stokes light with ω_S denoting its frequency; blue: Brillouin acoustic wave with Ω_B denoting its frequency.

which propagate in them [143–145]. As illustrated in Fig. 6.1 an acoustic wave in an optical fiber causes a strain field in the fibre core material resulting in alternating rarefaction and compression. The mechanical deformation exhibited as rarefaction and compression changes the permittivity of the fiber core material via the photoelastic effect for isotropic materials [146]:

$$\Delta(\epsilon^{-1})_{ij} = p_{ijkl} S_{kl}, \tag{6.1}$$

where p_{ijkl} is the photoelastic tensor and S_{kl} is the linear strain [147]. Thus, the refractive index is typically higher in high density regions and lower in low density regions. In this way the acoustic wave is able to create a refractive index grating travelling in the same direction as the light.

In the particular case where the acoustic wave (shown in blue in Fig. 6.1) has a wavelength equal to half of the light wavelength ($\lambda_B \approx \lambda_p/2$), the refractive index grating generated by this particular density wave acts as an efficient Bragg mirror for the light (red arrow with frequency ω_L in Fig. 6.1) propagating in the optical fiber. When this acoustic wave is travelling in the same direction as the light, the refractive index grating reflects red-shifted light (Stokes: green arrow in Fig. 6.1) due to the Doppler effect, and the frequency shift is equal to the frequency of the acoustic wave, which is called as the *Brillouin shift*:

$$f_B = \frac{2 n_{\text{eff}} v_a}{\lambda_p}, \tag{6.2}$$

where v_a is the acoustic velocity within the material, n_{eff} is the effective refractive index experienced by the pump light of freespace wavelength λ_p. Similarly, if this particular acoustic wave propagates in the opposite direction to the laser light, the refractive index grating reflects blue-shifted light (anti-Stokes, not displayed in Fig. 6.1). What's more, due to electrostriction, whereby the electric field of the light induces strain within a material proportional to the square of the electric field, the beating of the reflected Stokes light with the initial laser light drives the co-propagating acoustic wave, leading to the reflection of more Stokes light. This phenomenon can be described by the Brillouin intensity gain coefficient g_B of the material [148]:

$$g_B = \frac{2\pi n^7 p_{12}^2}{c\lambda_p^2 \rho v_a \Delta f_B} \ [\mathrm{m/W}], \tag{6.3}$$

where p_{12} is the longitudinal elasto-optic coefficient, ρ the density, Δf_B the full-width at half maximum (FWHM) of the acoustic wave and c the vacuum velocity of light. With more Stokes light reflected, this forms a positive feedback.

Generally, researchers use an optical cavity to resonantly enhance the interaction between light and the Brillouin acoustic wave by engineering the cavity to have two optical modes with frequency spacing equal to the Brillouin shift (or engineering the free spectral range (FSR) of the cavity to be the Brillouin shift). If the pump power coupled to the cavity is increased above a threshold power, the positive feedback from the Brillouin gain eventually amplifies the co-propagating wave to a strong and coherent amplitude, much stronger than a thermally driven acoustic wave, which is termed *Brillouin lasing*, and the Brillouin lasing threshold power in micro-cavities is [149, 150]:

$$P_{\mathrm{th}} = \frac{\pi^2 n^2 A_{\mathrm{eff}} L_{\mathrm{eff}}}{g_B Q_p Q_B \lambda_p^2}, \tag{6.4}$$

where A_{eff} is the optical mode area, L_{eff} is the round-trip length of the cavity, Q_p and Q_B are respectively the quality factor of the pump and Stokes optical modes. A different Brillouin gain coefficient depending on the device design can be defined as $G_B = g_B/A_{\mathrm{eff}}$. Using this parameter, the Brillouin amplification rate per photon is given [151]:

$$g_0 = \frac{\hbar\omega_p c^2 G_B}{2n^2 L_{\mathrm{eff}}}. \tag{6.5}$$

In contrast to the amplification of the co-propagating acoustic wave detailed here, as explained theoretically in § 6.2.2 the beating of the anti-stokes with the initial laser light attenuates the counter-propagating acoustic wave, leading to less anti-Stokes reflection. This cooling effect of the counter-propagating acoustic wave is also predicted by the theory developed in the following section.

6.1.1 Overview of Existing Brillouin Systems

Researchers have invented various kinds of platforms using different materials to exploit the Brillouin interaction between light and sound as briefly summarized in Fig. 6.2. Harnessing of the Brillouin interaction has been demonstrated in a variety of practical and scientific applications. In Peter Rakich's group suspended optomechanical silicon waveguides are used to harness the strong Brillouin non-linearity of silicon. The suspended waveguide is connected to the substrate via sparse thin tethers, which greatly reduce the acoustic loss through the substrate. The length of the Brillouin interaction region is increased to centimetre scale to increase the Brillouin gain. Two spatial optical modes and a Brillouin elastic wave are collocated in the optomechanical waveguide. By leveraging the symmetry-breaking of Stokes and anti-Stokes

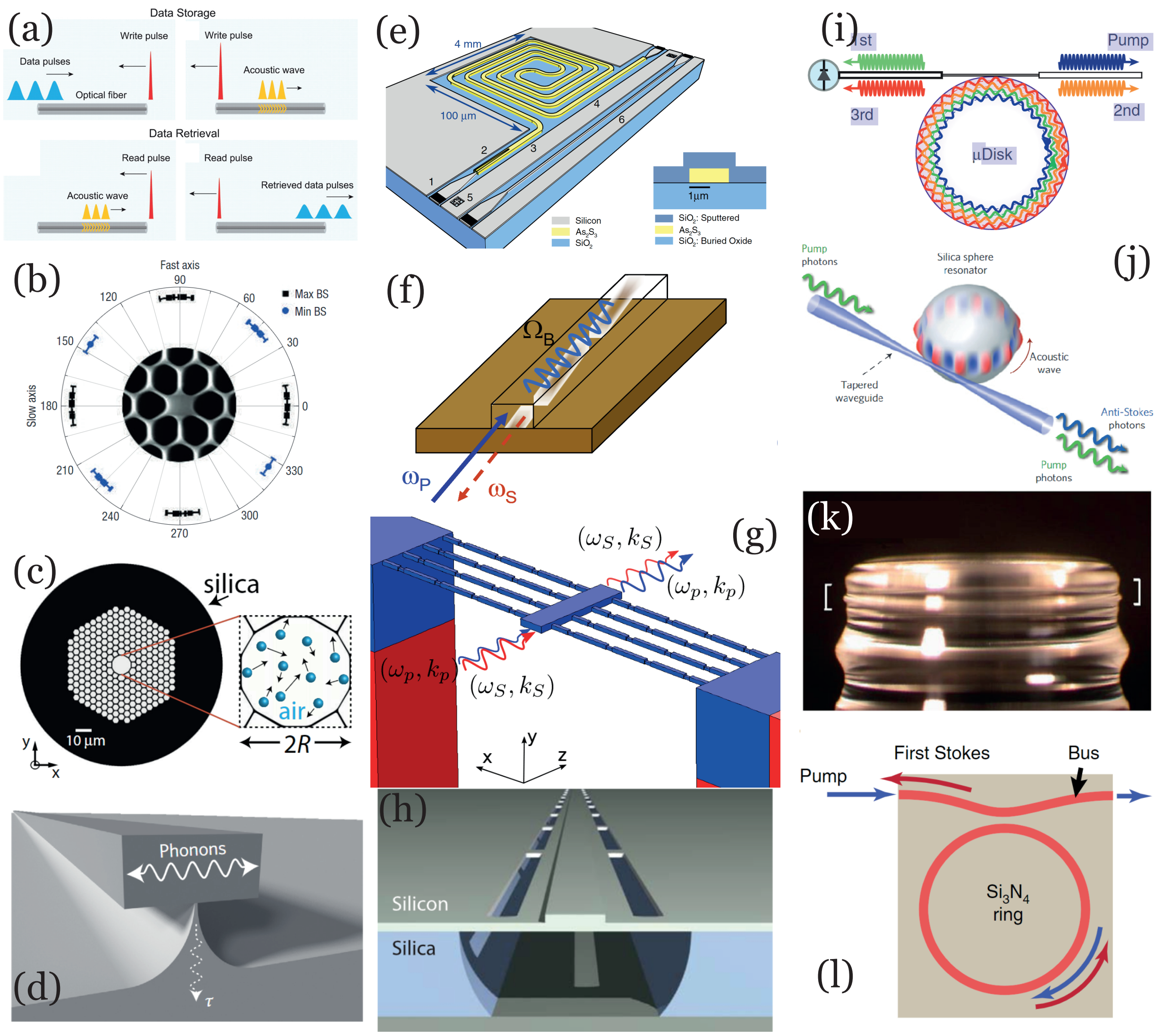

Figure 6.2: A few examples of the wide variety of Brillouin systems realized with different platforms and materials: (a) Stored light using Brillouin scattering in an optical fiber [152]. (b) Small-core photonic crystal fibre [153]. (c) Brillouin scattering from the vibrating air in a hollow-core fiber [154]. (d) Suspended Silicon wire waveguide [155]. (e) Integrated spiral As_2S_3 rib waveguide [156]. (f) As_2S_3 chalcogenide waveguide [157]. (g) Silicon waveguide isolated from the substrate on a narrow fin [158]. (h) Racetrack resonator with suspended Brillouin-gain regions [159]. (i) WGM optica microdisk resonator [160]. (j) WGM silica microsphere resonator [161], (k) Milimeter scale WGM CaF_2 resonator [162]. (l) Centimeter scale Si_3N_4 ring resonator [151].

processes produced by phase matching in intermodal Brillouin scattering, a band of travelling-wave phonons are cooled for the first time in linear waveguide systems without an optical cavity or discrete phonon modes [163]. Further, a racetrack optical cavity is fabricated with two suspended optomechanical waveguides and two unsuspended curving waveguides, where the two spatial optical modes have a frequency difference equal to the Brillouin elastic wave frequency of 6 GHz. By pumping the higher frequency spatial optical mode, the other spatial optical mode is populated by the coherent forward scattered Stokes light, which is the Brillouin scattering. By further increasing the pump power above the Brillouin lasing threshold power of 10.6 mW, they have observed that the strong Stokes light is able to produce linewidth narrowing of the elastic wave [159].

Although silicon is compatible with the current complementary metal–oxide–semiconductor (CMOS) technology, its Brillouin gain is relatively low, due to low photoelastic nonlinearity and large acoustic loss [164]. Especially the acoustic loss resulted from the higher stiffness of silicon than that of the insulator substrate complicates the fabrication process of optomechanical silicon waveguides, because the silicon waveguides need to be fabricated to be isolated from the substrate to overlap better the optical and elastic waves, and more importantly avoid the leak of acoustic energy to reduce the acoustic loss. To get around the drawback of silicon waveguides, As_2S_3 waveguides of strong nonlinearity are intensively investigated in Eggleton's group at University of Sydney to generate stimulated Brillouin scattering on-chip, which leads to wide range of applications, such as optical isolator, coherent photonic-phononic memory, phase shifter and et al. [157,165–168]. The large non-linearity of As_2S_3 allows standard optical waveguide fabrication and full integration into photonic circuits.

In addition to waveguides, Whispering Gallery Mode (WGM) resonators have also been studied to enhance Brillouin scattering in low nonlinearity materials. One example is that a sub-Hertz Brillouin laser in an integrated Si_3N_4 ring resonator from a group at University of California, Santa Barbara. They have demonstrated that the linewidth of the Brillouin laser can be significantly reduced to 0.7 Hz [151]. Using conventional semiconductor processing methods, millimeter-scale diameter ultrahigh-Q disk resonators were fabricated in Kerry Vahala's group at Caltech. These resonators are fabricated without the typical reflow process to form high Q silica microtoroid or microsphere resonators [169,170]. Despite this, the on-chip disk resonators not only have the highest reported Q (875 million) for diameters larger than 500 μm, but also enable a very fine control of the free spectral range (see § 2.4), which is very challenging to do reproducibility in the reflow process. With these two advantages a low threshold Brillouin laser is demonstrated in Reference [150]. By improving this ultrahigh-Q disk resonator Brillouin laser they were also able to demonstrate a microwave synthesizer and an optical gyroscope by realising cascaded Brillouin lasing [160, 171]. Although silica has very low optical loss, its Brillouin non-linearity is very small. By using high non-linearity materials like CaF_2 the Brillouin lasing threshold is significantly reduced to 3 μW, and cascaded Brillouin lasing is observed with BaF_2 [162,172].

The Brillouin interaction has also been exploited to achieve the strong coupling between light and sound for cavity optomechanics experiments. In Peter Rakich's group, a high Q (quality factor) Fabry-Perot optical cavity with a bulk acoustic resonator inside is utilised to realise Brillouin strong coupling. The Fabry-Perot cavity is fine-tuned to have a dispersively engineered mode spacing equal to the Brillouin frequency, which selectively biases the system for the Stokes process over the anti-Stokes process, when the pump light is on resonance with the higher frequency mode. In this way, they have achieved a multi-photon optomechanical cooperativity [Eq. (3.27)] larger than 1, and observed the lasing and optical cooling of the acoustic mode. Similarly, but instead of using a Fabry-Perot cavity with a bulk acoustic resonator, Brillouin optomechanics experiments have also been realised with WGM silica microresonators, which confine both acoustic and optical WGMs along the circumference of the device. Using this platform, Gaurav Bahl's group have observed strong optomechanical coupling (with multi-photon optomechanical coupling rate g larger than both optical κ and mechanical Γ linewidths) and spontaneous Brillouin cooling of the acoustic WGM [161]. These achievements have proven that along with the conventional optomechanical coupling, the Brillouin interaction provides a new way to coherently control and generate quantum states of mechanical oscillators.

In addition to the successful applications of Brillouin scattering in solid materials, stimulated Brillouin scattering in liquid materials was first found by focusing laser beam onto water and methanol droplets in 1988 [173]. Due to the absence of resonant enhancement from an optical cavity, low Brillouin non-linearity and high acoustic damping in liquid droplets, the generation of stimulated Brillouin scattering in this experiment was very difficult. Directly immersing optomechanical systems in liquid was very challenging, but it is advantageous to use an optical cavity to enhance the weak Brillouin interaction in liquid. Thus, in one of Gaurav Bahl's work a hybrid approach is taken to use a hollow core silica capillary resonator, where the WGM optical modes are confined at the circumference of the hollow core silica capillary with around 30 μm thickness, while the liquid is confined in the hollow core [174]. The acoustic modes of this system are also supported by the silica capillary. Thus, in this experiment the Brillouin lasing is similar to the aforementioned WGM resonator based Brillouin laser, where the silica resonators co-host both optical WGM and acoustic WGM. The difference of this experiment is that the liquid inside the capillary can provide additional damping and frequency shift to the acoustic WGM.

Very recently the resonantly enhanced Brillouin lasing has also been observed in 140 μm diameter silicone oil droplets stably suspended at a fibre tip in Gagliardi's group [175]. Since the droplet is very stable, laser light is directly coupled from free space to the circumference of the droplet. The Brillouin acoustic mode is also an acoustic WGM confined at the circumference of the droplet. This scheme allows direct interaction of light and sound in the liquid, but the large acoustic damping due to the liquid viscosity and the large size of the device lead to a relatively high lasing threshold power of around 0.2 mW. Generally FSR engineering is challenging in solid optical resonators and is even more so for liquid optical resonators, but in this experiment the large optical linewidth and relatively low Brillouin shift relieved this Brillouin system from FSR engineering, with both Stokes and pump light to be resonant with the same optical mode as illustrated in Fig. 6.3.

As mentioned in Chap. 5, to get around the high acoustic damping from the viscosity of normal liquid, in Jack Harris's group, superfluid helium was used explore Brillouin interaction between light and sound [17]. In the experiment the optical cavity is a Fabry-Perot cavity formed between two optical fibre tips coated with Distributed Bragg Reflector (DBR) mirrors. When the optical cavity is cooled down to below 100 mK with helium-4 gas, the helium gas is condensed to superfluid phase and conformally fills the hollow optical cavity, thereby the Fabry-Perot cavity supports both the optical modes and longitudinal superfluid density acoustic modes, allowing near-perfect overlap between them. Since both the optical and acoustic modes are standing waves rather than travelling waves, there is no symmetry breaking of Stokes and anti-Stokes processes, leading to a modulation of the effective cavity length of the standing optical mode by the spatial variation of helium density associated with the standing acoustic wave, which is essentially a standard optomechanical interaction. Owing to the low optical absorption and high thermal conductivity of superfluid, the optomechanical coupling is predominantly from the unitary electrostrictive force of light, with the single photon coupling rate extracted from experiment having two components: the electrostrictive coupling rate of around 3 kHz, and the non-unitary photothermal coupling rate of around 1 kHz.

Although excellent results have been achieved with solid and liquid materials, there are still disadvantages in these experiments. In solid material, the Brillouin interaction typically relies on weak optical electrostrictive forces [16,17,146,162,171,176,177] (potentially boosted by radiation pressure forces at the nanoscale [178]) to strain a high Young's modulus solid material, leading to weak optomechanical coupling strength (g_0). High Brillouin non-linearity materials like CaF_2 indeed allow large optomechanical coupling strength, but are not compatible with conventional semiconductor processing techniques. A second disadvantage with solid material is that the large Brillouin shift from the high Young's modulus requires either complicated mode engineering across free spectral ranges to to ensure both pump and Stokes fields are on resonance (see Fig. 6.3(a)) [142, 159, 161, 177]. The liquid Brillouin experiments described above also present several disadvantages. First, if the optical and acoustic modes are confined by a thick silica resonator, the influence of the liquid at the resonator interface has extremely weak influence on both optical and acoustic modes. Second, if both the optical and acoustic modes are confined by the liquid resonator, the optical absorption and viscosity of normal liquid generate high loss rate for light and sound respectively, leading to inefficient Brillouin scattering. This leaves several milestones yet to be demonstrated, including the strong Brillouin interaction between light and ultra-low frequency acoustic waves,, and Brillouin-interaction induced strong coupling between optical cavity modes.

Compared with the Brillouin experiments with solid materials, two key features distinguish our experimental approach. First, the Brillouin active component is not silica, but rather a thin superfluid film that resides on the surface and is evanescently coupled to the whispering gallery modes (WGM) of the microdisk. Regions of high light intensity inside the resonator continuously deform the superfluid interface by drawing in more superfluid by means of an optical gradient force [179, 180], resulting in a periodically modulated refractive index grating which scatters pump light, as illustrated in Fig. 6.3(c). The superfluid film has an exceedingly weak restoring force[1], affording a compliant dielectric interface that easily conforms in the

---

[1] the van der Waals pressure, is typically on the order of hundreds of Pa to ∼1 kPa, compared with typically tens to hundreds of GPa bulk modulus for solid materials like SiO_2, Si and Si_3N_4.

Table 6.1: v_a longitudinal acoustic velocity. Note that the typical Brillouin shift wavelength pump light depends on the effective refractive index and crystal direction.

material	v_a (m/s)	n	typical $\Omega_B/2\pi$ (GHz)	g_B (m/W)
As_2S_3 [144]	~2400	2.44	7	7.2×10^{-10}
Ge [181]	~3500	4.02	6	3.2×10^{-10}
Si [144, 155]	~8433	3.42	9	$\sim2.4\times10^{-10}$
Si_3N_4 [151]	~8550	1.96	11	$\sim2.8\times10^{-14}$
SiO_2 [182]	~5960	1.45	11	1.73×10^{-11}
As_2Se_3 [183]	~2250	2.8	8	6×10^{-9}
CaF_2 [162]	~6600	1.43	12	2.8×10^{-11}
Bulk superfluid [17]	~230	1.028	~0.3	N/A
Thin superfluid film (this work)	~ 5	1.028	~0.01	N/A

presence of optical forces [1,2,18]. This allows the single photon coupling rate to be substantially higher than solid Brillouin systems. Second, this weak restoring force also corresponds to a much smaller sound velocity in the superfluid film than in solids (m/s vs km/s) as shown in Table 6.1.1. As a result, a low Brillouin frequency in the MHz range instead of more than ten GHz in solids makes the Stokes and anti-Stokes photons reside well within the optical linewidth (see Fig. 6.3 (b)). Therefore, we can leverage the advantage of three mode resonant enhancement by scattering into the naturally degenerate WGM that propagates in the direction opposite to the pump. This avoids the fabrication complexity associated to mode engineering across free-spectral-ranges, or higher order modes, and allows the device to be further miniaturized while maintaining resonant enhancement. These features have enabled an extremely low Brillouin lasing threshold of 1.8 μW, and a phonon mediated strong coupling between degenerate optical modes.

Compared with other Brillouin experiments with liquid materials, the work described here is a hybrid approach, where the optical mode is essentially confined by a thin silica disk resonator while the acoustic mode is confined by the superfluid film. Motion in the film couples to the optical mode by perturbing its evanescent field. This hybrid approach has four advantages. First, the low optical absorption of silica and superfluid helium generally leads to high Q optical modes in at near-infrared wavelengths. Second, the viscosity of superfluid helium nearly vanishes at the fridge base temperature of around 10 mK, potentially enabling high Q acoustic modes. Third, the evanescent field of the optical mode is very strong in the superfluid region, owing to the small disk thickness (below 2 μm). Thus, the coupling of the acoustic mode to the optical mode is very strong. Due to these three factors, this hybrid Brillouin system has the lowest lasing threshold among all Brillouin systems to date. Last, the circular geometry of the disk resonator allows travelling optical and acoustic waves, potentially leading to certain interesting physics of non-reciprocity.

Moreover, this hybrid Brillouin system shows that the Brillouin acoustic mode when drive to a large amplitude, induces strong coupling of two degenerate optical modes. The coherent

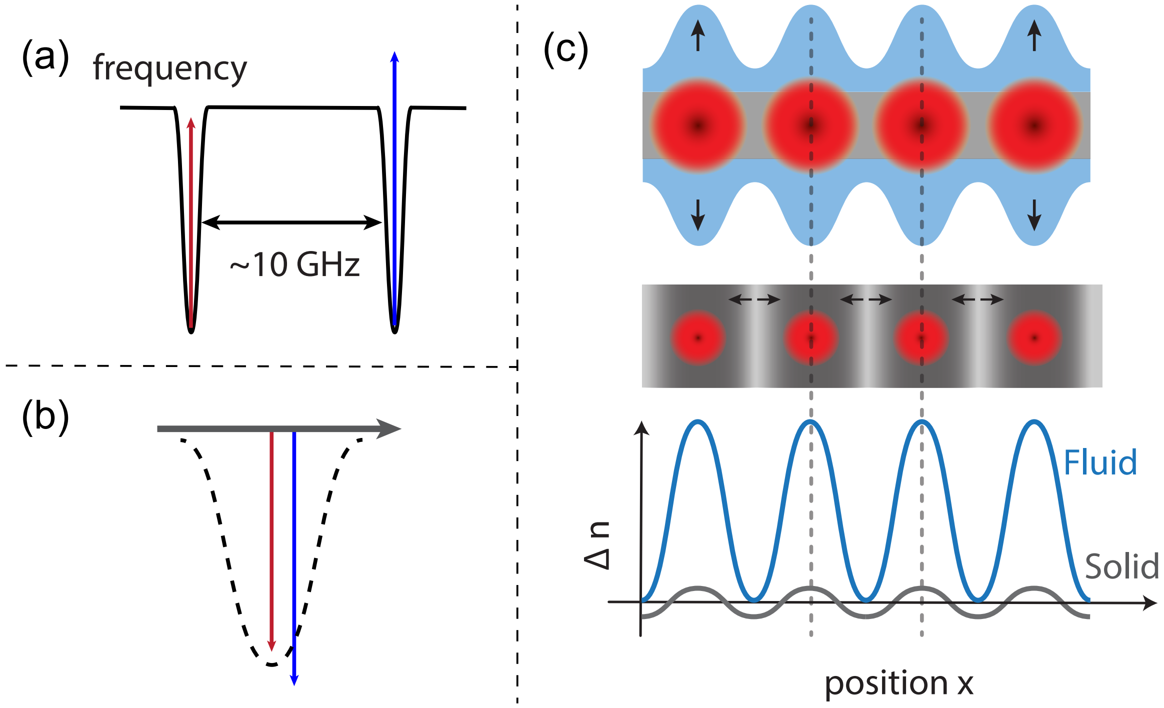

Figure 6.3: (a) Due to large sound velocity in solid materials, the Stokes (red) and pump (blue) are on resonance with two different optical modes; (b) due to the reduced speed of sound in the superfluid, both pump (blue) and Stokes (red) are resonant with the same high Q WGM; (c) schematic illustration of the Brillouin interaction in our superfluid system (top) and in a solid material where the optical field is responsible for compression and rarefaction of the medium (middle). Due to the fluid interface's larger compliance, the optically driven refractive index modulation (bottom) is larger in the fluid case.

coupling between the two optical modes can be switched on and off by the optically pumped Brillouin lasing. In terms of information processing, this Brillouin lasing configuration is acting as a router, where the pump light is able to control the information transfer between the two optical modes. This can have potential applications, such as a mechanically mediated quantum state transfer, applicable to reconfigurable all-optical quantum circuits [184]. In addition, studying the Brillouin process in superfluid could improve our understanding of the origin of dissipation in superfluid helium.

6.2 Theoretical Modelling

6.2.1 Model of Brillouin Scattering

Fig. 6.4 provides an overview of the hybrid Brillouin system. A silica microdisk supporting high-Q optical WGM resonances is coupled to a tapered fibre and cooled to millikelvin temperatures in a sealed sample chamber within a dilution refrigerator. Helium-4 gas injected into the chamber forms a nanometer-thick self-assembling superfluid film coating the microresonator. The pump light is coupled to the optical mode (a_k) propagating in clockwise (CW) direction, while Stokes and anti-Stokes light is backscattered into the naturally degenerate optical mode

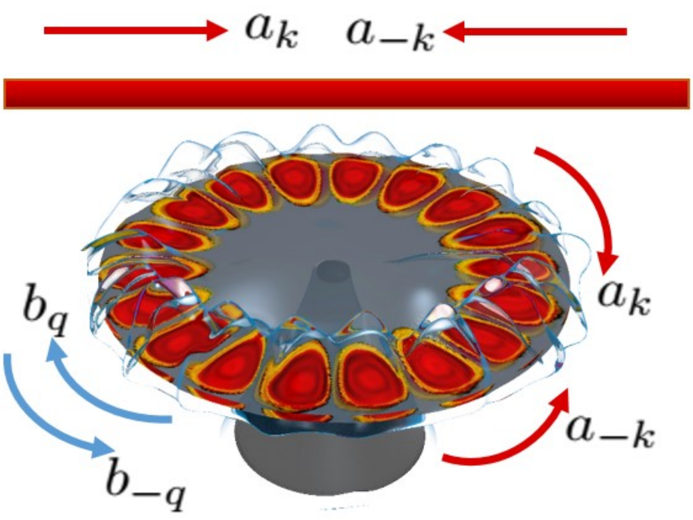

Figure 6.4: Illustration of the superfluid Brillouin optomechanical system composed of an optical micro-disk resonator, a layer of superfluid thin film covering the disk, and a tapered optical fibre coupling laser light into the resonator. Red arrows denote the two optical modes propagating in opposite directions, with $a_{k(-k)}$ corresponding to the lowering operator of the optical mode in clockwise (counter-clockwise) direction (the subscript k is the wavenumber of the optical modes, and the sign in front of k indicates the direction); blue arrows denote the clockwise and counter-clockwise acoustic modes with $b_{q(-q)}$ corresponding to their lowering operators.

(a_{-k}) propagating in the direction opposite to the pump light.

The microdisk, in addition to supporting WGM optical modes, provides confinement for acoustic waves in the superfluid film —named third sound [84]— which manifest as film thickness fluctuations with a restoring force provided by the attractive van der Waals interaction between the helium atoms and the resonator as described in §. 3.2.3. Given the circular geometry, these sound waves take the form of drumhead modes defined by Bessel functions, which evanescently perturb the WGM field thus modulating the resonator's effective length [2]. In this Brillouin experiment, we focus on a particular high azimuthal order Bessel mode (like an acoustic WGM mode) which resides at the rim of the microdisk. This Bessel mode has twice the azimuthal order of the optical mode in order to have perfect overlap between the optical and acoustic modes[2]. It is always valid to decompose this WGM acoustic mode into two travelling acoustic modes in opposite directions (b_q co-propagates with the pump light and b_{-q} against the pump light). As shown in the Section 6.2.2 this four mode system can be studied by coupled mode theory [185].

---

[2] such that each peak in the superfluid matches an extremum in the optical intensity as illustrated in Fig. 6.3(a)

6.2.2 Hamiltonian Formalism

Here I detail the analytical Brillouin scattering theory, which describes the superfluid Brillouin system in the *non-depleted pump regime*[3], an approximation valid below the lasing threshold. The general interaction Hamiltonian is determined by the overlap integral of the optical and acoustic fields [2, 186]. It is derived below, based on a perturbation theory approach. The energy shift ΔE experienced by the optical field due to the presence of the superfluid is given by:

$$\Delta E = \int_0^R \int_0^{2\pi} \int_0^{d_0+\eta(r,\theta)} \frac{1}{2}\,\varepsilon_0\,(\varepsilon_{\mathrm{sf}}-1)\,|E|^2\, r\,\mathrm{d}r\,\mathrm{d}\theta\,\mathrm{d}z, \tag{6.6}$$

where $\varepsilon_0 = 8.85\times 10^{-12}$ F/m is the vacuum permittivity, $\varepsilon_{\mathrm{sf}}$ is the relative permittivity of superfluid helium, η is the out-of-plane displacement of the superfluid surface beyond a mean height d_0 due to the acoustic wave (third sound), E is the WGM electric field and R is the radius of the disk resonator. Given the film thickness is only a few nanometres, the electric field can be treated as constant over the height of the film. Thus the volume integral Eq. (6.6) can be reduced to an integral over the surface of the disk resonator:

$$\Delta E = \int_0^R \int_0^{2\pi} \frac{1}{2}\,\varepsilon_0\,(\varepsilon_{\mathrm{sf}}-1)\,(d_0+\eta\,(r,\theta))\,|E|^2\, r\,\mathrm{d}r\,\mathrm{d}\theta \tag{6.7}$$

Rewriting this expression in terms of photon and phonon annihilation and creation operators:

$$\Delta E = \int_{\mathrm{surface}} \frac{1}{2}\,\varepsilon_0\,(\varepsilon_{\mathrm{sf}}-1)\left[\underbrace{\Psi_b(\vec{r})\left(b_q+b_q^\dagger+b_{-q}+b_{-q}^\dagger\right)}_{\mathrm{AC}} + \underbrace{d_0}_{\mathrm{DC}}\right]\left[|\Psi_a(\vec{r})|^2|a_k+a_{-k}|^2\right]\,\mathrm{d}A. \tag{6.8}$$

Here $\Psi_a(\vec{r}) = E\,(\vec{r})\sqrt{\frac{\hbar\omega}{\int \frac{1}{2}\,\varepsilon_0\,\varepsilon_{\mathrm{sf}}\,E^2\,\mathrm{d}V}}$ is the electric amplitude per photon, $\Psi_b(\vec{r})$ is the acoustic amplitude in the ground state, a_k (b_q) and a_{-k} (b_{-q}) are respectively the photon (phonon) annihilation operators acting on the forwards and backwards propagating optical (acoustic) modes. This equation shows the transition from classical optical energy shift to quantum interaction Hamiltonian, and explains the essence of the physics in this experiment. To avoid the confusion between quantum operators and their corresponding classical mean values, the connection between the acoustic displacement and acoustic field annihilation and creation operators is $\eta = \Psi_b(\vec{r})\left\langle b_q+b_q^\dagger+b_{-q}+b_{-q}^\dagger\right\rangle$, and similarly for the WGM electric field and intracavity optical mode annihilation and creation operators $E = \Psi_a(\vec{r})\,\langle a_k+a_{-k}\rangle$. The subscripts k (q) refer respectively to the wavenumbers of the optical (acoustic) wave and the signs in front of k and q indicate the propagation direction, with the convention that the optical pump travels in the positive direction. In the limit that the Brillouin frequency is much smaller than the optical frequency ($\Omega_B \ll \omega_{\mathrm{opt}}$), momentum and energy conservations require that $q = 2k$ for the Brillouin process.

The acoustic term in Eq. (6.8) can be decomposed into two components: a DC component proportional to the mean film thickness d_0 which gives the DC shift of the optical resonance

---

[3] this assumption states that the power in the pump beam is not altered by the Brillouin scattering process

frequency due to the superfluid helium film covering the resonator, and an AC component describing the interaction of the surface acoustic wave with the intracavity optical field. Neglecting the DC part, the interaction Hamiltonian takes the form:

$$\begin{aligned} H_{\text{int}} &= -\int_{\text{surface}} \frac{1}{2}\varepsilon_0\,(\varepsilon_r - 1)\,\Psi_b(\vec{r})|\Psi_a(\vec{r})|^2\,\mathrm{d}A\,(b_q + b_q^\dagger + b_{-q} + b_{-q}^\dagger)|a_k + a_{-k}|^2 \\ &= -\hbar\,g_{0,\text{rp}}\,(b_q + b_q^\dagger + b_{-q} + b_{-q}^\dagger)(a_k^\dagger + a_{-k}^\dagger)(a_k + a_{-k}), \end{aligned} \tag{6.9}$$

where $g_{0,\text{rp}}$ is the single photon optomechanical coupling rate [2, 50], and the minus sign just depends on how we choose the positive direction for the mechanical motion axis (see Fig. 3.1):

$$g_{0,\text{rp}} = \int_{\text{surface}} \frac{1}{2}\varepsilon_0\,(\varepsilon_{\text{sf}} - 1)\;\Psi_b(\vec{r})\,|\Psi_a(\vec{r})|^2\,\mathrm{d}A \tag{6.10}$$

The interaction Hamiltonian is further reduced by energy and momentum conservation arguments to the following form:

$$H_{\text{int}} = -\hbar\,g_{0,\text{rp}}(b_q^\dagger a_k a_{-k}^\dagger + b_{-q} a_k a_{-k}^\dagger + b_{-q}^\dagger a_k^\dagger a_{-k} + b_q a_k^\dagger a_{-k}) \tag{6.11}$$

The first two terms correspond respectively to the Stokes and anti-Stokes scattering process for the forward propagating optical field a_k, while the third and fourth terms correspond respectively to the Stokes and anti-Stokes process acting on the counter-propagating optical field a_{-k}.

Note that in many other works [142, 161], the resonator's optical spectrum is engineered such that pump and Stokes fields are resonant with two distinct optical modes separated by the Brillouin shift. Compared with the pump and Stokes, the non-resonant anti-Stokes field experiences a very low optical density of states and can therefore be neglected. Here, because of the small Brillouin shift ($\sim$ 6 MHz), we must keep both the Stokes and anti-Stokes terms. In addition, the frequencies of the two counter-propagating optical modes are degenerate, such that the frequencies of a_k and a_{-k} are both treated as Δ in the full Hamiltonian description in a frame rotating at the laser frequency ω_L, where Δ is defined as $\omega_L - \omega_k$:

$$\begin{aligned} H = &\underbrace{-\hbar\Delta a_k^\dagger a_k - \hbar\Delta a_{-k}^\dagger a_{-k}}_{\text{optical}} + \underbrace{\hbar\Omega_B b_q^\dagger b_q + \hbar\Omega_B b_{-q}^\dagger b_{-q}}_{\text{mechanical}} \\ &\underbrace{-\hbar g_{0,\text{rp}}(b_q a_k^\dagger a_{-k} + b_{-q}^\dagger a_k^\dagger a_{-k} + b_{-q} a_{-k}^\dagger a_k + b_q^\dagger a_{-k}^\dagger a_k)}_{\text{Brillouin interaction}} \end{aligned} \tag{6.12}$$

6.2.3 Calculation of Optomechanical Coupling Rate G

In the experiment the optical modes are supported by a disk microresonator (see § 6.3) We compute the optomechanical coupling strength $G = \frac{\partial\omega_0}{\partial x}$ using FEM modelling software (COMSOL Multiphysics). The silica microresonator dimensions are measured with a scanning electron microscope (SEM) and summarized in Table 6.2. We simulate the optical eigenmodes of the structure, which for thin disks are defined by their transverse electric (TE) or transverse magnetic (TM) polarization, and radial and azimuthal mode orders (p, m) [38]. The electric field

Parameter	Symbol	Value	Units	source
Disk radius (top)	R_t	30.6	μm	SEM
Disk radius (bottom)	R_b	38.6	μm	SEM
Disk wedge angle	-	14	degrees	SEM
Film thickness	d	6	nm	cavity shift
		8	nm	Brillouin frequency
WGM azimuthal number	m_{opt}	186	-	FEM
Mechanical azimuthal number	m	372	-	-
Optomechanical coupling rate	$G/2\pi$	-2.17×10^{18}	Hz/m	FEM
Brillouin mode zero-point motion	x_{ZPF}	9.5×10^{-15}	m	analytical estimation
Single photon coupling strength	$g_{0,\text{pt}}/2\pi$	122	kHz	fit to measurement
	$g_{0,\text{rp}}/2\pi$	11	kHz	simulation

Table 6.2: Experimental parameters. SEM: Scanning Electron Microscope; FEM: Finite Element Method.

(E) distribution of the ($p = 1$, $m = 186$) quasi-TE mode of the microdisk is plotted as an inset in Fig. 6.12(b). G is computed from the E field distribution through [2]:

$$G = \frac{-\omega_0}{2} \frac{\iint_{\text{interface}} (\varepsilon_{\text{sf}} - 1)\, E^2(\vec{r})\, \mathrm{d}^2\vec{r}}{\iiint_{\text{all}} \varepsilon_r(\vec{r})\, E^2(\vec{r})\, \mathrm{d}^3\vec{r}}, \tag{6.13}$$

where ε_r is the relative permittivity and $\varepsilon_{\text{sf}} = 1.058$ is the relative permittivity of superfluid helium. The numerator surface integral is performed over both top and bottom resonator boundaries, while the normalizing denominator volume integral is performed over all space. We find values of $G/2\pi$ clustered around -2.2×10^{18} Hz/m for TE modes and around -2.4×10^{18} Hz/m for TM modes, with little influence of the WGM radial order. The higher values of $|G|$ for TM modes is due to their stronger field at the interface due to the E field discontinuity [2]. We identify our experimental WGM as a ($p = 1, m = 186$) quasi-TE WGM, as shown in the inset of Fig. 6.12(b). As mentioned above, the optomechanical coupling G has a marked dependence on the wedge angle. Indeed, while the fundamental TE mode's $|G|/2\pi \sim 2.2$ GHz/nm for a 14 degree wedge angle, this value increases to 2.5 GHz/nm for a 12 degree wedge, and drops to 1.5 GHz/nm for a 20 degree wedge angle. The contribution to the total G from top and bottom disk interfaces is well balanced, with respectively 51% and 49 % of the total coupling rate coming from top and bottom for the fundamental TE mode.

6.2.4 Estimation of Single Photon Optomechanical Coupling Rate g_0

Calculation of the single-photon optomechanical coupling rate $g_0 = |G|\, x_{\text{ZPF}}$ [50] requires the Brillouin mode zero-point motion x_{ZPF}. The Brillouin eigenmode can be well approximated through a high-order azimuthal Bessel mode of a disk, for which the zero-point motion can be calculated analytically [2]. The surface displacement η of the travelling Brillouin wave on both

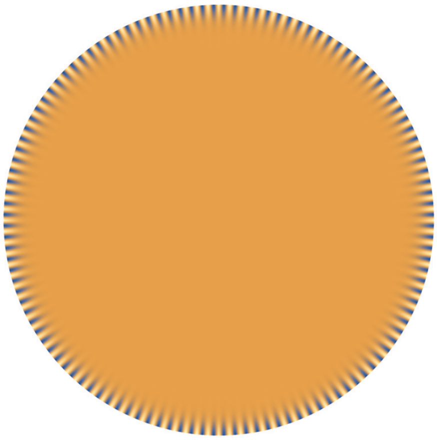

Figure 6.5: Example displacement profile of an acoustic whispering gallery-type mode (superfluid Brillouin wave) of the kind used in the experiments. For clarity, we show here the displacement $\eta_{120,1}(r,\theta)$ of the $m = 120$ Bessel mode with free boundary conditions at the resonator edge [5], which has ~ 3 times fewer nodes than the experimental $m = 372$ Bessel mode. The displacement is essentially localized on the resonator edge, such that the eigenmode is not perturbed by the presence of the pedestal on the microdisk underside.

top and bottom surfaces of the disk is given by:

$$\eta_{m,n}(r,\theta,t) = \eta_0 \, J_m\left(\zeta_{m,n}\frac{r}{R}\right)\cos\left(m\theta \pm \Omega\, t\right), \tag{6.14}$$

where m and n are respectively the azimuthal and radial mode numbers, η_0 the mode amplitude, J_m the Bessel function of the first kind of order m, and $\zeta_{m,n}$ a frequency parameter depending on the mode order and the boundary conditions [2]. Energy and momentum conservation for the Brillouin scattering process imply that the Brillouin mode azimuthal order be twice that of the optical WGM, *i.e.* $m = 2\,m_{\mathrm{opt}} = 2 \times 186 = 372$ (see Table 6.2). Such a mode has its displacement localized on the periphery of the resonator, well colocalized with the optical field intensity, forming a type of acoustic whispering gallery mode, as shown in Fig. 6.5. Note that since the excitations exist on both the top and underside of the disk, the collective excitation of the film on top and bottom has twice the effective mass, and hence $1/\sqrt{2}$ the zero-point motion of a mode residing only on the disk top surface. The azimuthal overlap between optical and mechanical fields leads to a further factor two reduction: $\frac{1}{2\pi}\int_0^{2\pi} 2\cos^2(\theta)\cos(2\theta)\,\mathrm{d}\theta = \frac{1}{2}$. Combined, and assuming perfect radial overlap, this estimation provides, for the WGM mode used in the experiments a value of $g_{0,\mathrm{rp}}/2\pi = 11$ kHz. We ascribe the discrepancy with the experimentally extracted value from the lasing threshold (Sec 6.4.4) to some degree to uncertainties in the geometry (wedge angle, sidewall roughness) as well as potential photothermal contributions [18] which may increase the effective optomechanical coupling.

6.2.5 Equations of Motion for Brillouin Interaction

From the Hamiltonian in § 6.2.2 we derive the equations of motion. Including the drive a_{in} of the pump field, the photothermal coupling ($g_{0,\mathrm{pt}} = g_{0,\mathrm{tot}} - g_{0,\mathrm{rp}}$), the native cavity backscattering κ_b, the thermal drive b_{in} (b_{-in}) of the acoustic fields b_q (b_{-q}) respectively [52,142] and dissipation, we obtain:

$$\dot{a}_k = i\Delta a_k - \frac{\kappa}{2}a_k + ig_{0,\mathrm{rp}}(b_q a_{-k} + b_{-q}^\dagger a_{-k}) + i\kappa_b a_{-k} + \sqrt{\kappa_{ext}}\ \alpha_{in} \tag{6.15a}$$

$$\dot{a}_{-k} = i\Delta a_{-k} - \frac{\kappa}{2}a_{-k} + ig_{0,\mathrm{rp}}(b_{-q} a_k + b_q^\dagger a_k) + i\kappa_b a_k \tag{6.15b}$$

$$\dot{b}_q = -i\Omega_B b_q - \frac{\Gamma}{2}b_q + ig_{0,\mathrm{tot}}\, a_{-k}^\dagger a_k + \sqrt{\Gamma}\ b_{in}(t) \tag{6.15c}$$

$$\dot{b}_{-q} = -i\Omega_B b_{-q} - \frac{\Gamma}{2}b_{-q} + ig_{0,\mathrm{tot}}\, a_k^\dagger a_{-k} + \sqrt{\Gamma}\ b_{-in}(t), \tag{6.15d}$$

where κ is the optical decay rate, κ_{ext} the coupling rate of the optical cavity to the tapered fibre, n_q (n_{-q}) the thermal occupation of the co-propagating (counter-propagating) acoustic field, Γ the intrinsic mechanical damping rate, and $b_{in}(t)$ the thermal drive, which obeys the Markovian noise process such that $\langle b_{in}^\dagger(t) b_{in}(t')\rangle = n_q\,\delta(t-t')$ and $\langle b_{in}(t) b_{in}^\dagger(t')\rangle = (n_q+1)\delta(t-t')$ [52]. Note that light can drive the acoustic wave through both the radiation pressure and photothermal interactions, but the acoustic wave affects the intracavity optical field only through dispersive coupling which can not be mediated by photothermal interaction.

Although the coupled equations [Eq. (6.15)] of motion have four modes and are nonlinear, we can solve them via two approaches. The first approach is to use a Matlab ODE solver to numerically simulate the full equations of motion with no approximation (see Sec. 6.4.4 for details of numerical simulations). The second approach is to analytically solve them with linearization. We linearize the equations of motion by assuming that a_k is a non-depleted pump, and its steady state is not affected by the dynamics of the system. Then the equations of motion can be linearized by assuming a_k is not strongly affected by its time-variant part δa_k, but is dominated by it average coherent amplitude α_k given by the steady state solution. First neglecting the Brillouin interaction and back scattering, and solving the steady-state of the pump light from Eq. (6.15a) and Eq. (6.15b), we get:

$$\alpha_k = \sqrt{n_{cav,k}} = \left| \frac{\sqrt{\kappa_{ext}}\ \alpha_{in}}{-i\Delta + \kappa/2} \right| . \tag{6.16}$$

Here we define $n_{cav,k}$ as the intracavity photon number for the steady state solution of the pump light: $n_{cav,k} = |\alpha_k|^2$.

To simplify the analytical model we perform full simulations of the equations of motion (Eq. (6.15)) to understand at what level the different forms are important. We find from the full simulations that given the amplitude of the input field a_{in} the solutions of the full equations of motion depend only on the product of $g_{0,\mathrm{rp}}$ and $g_{0,\mathrm{tot}}$ regardless of individual values. Furthermore, the simulations also show that the backscattering effectively decreases the pump field intracavity photon number $n_{cav,k}$, and actively cools the co-propagating acoustic wave b_q. Therefore, in order to analytically solve the equations of motion to understand the underlying dynamics of the system, we neglect the backscattering dynamics and rather define a parameter ξ to quantify the effects of the native backscattering on the intracavity photon number, such that with the presence of the native backscattering, the intracavity photon number is modified as $\xi n_{cav,k}$, and the average intracavity field amplitude as $\sqrt{\xi}\ \alpha_k$.

Then we replace the effects of the native backscattering by substituting α_k with $\sqrt{\xi}\ \alpha_k$, Subtracting the steady state solutions from Eqs. (6.15), and neglecting all the optical noise and higher order terms in the time-variant variables, the Fourier transformed equations of motion are:

$$-i\omega a_{-k}(\omega) = i\Delta a_{-k} - \frac{\kappa}{2}a_{-k} + i\sqrt{\xi}\ g_{\mathrm{rp}}b_{-q} + i\sqrt{\xi}\ g_{\mathrm{rp}}b_q^\dagger \tag{6.17a}$$

$$-i\omega b_q(\omega) = -i\Omega_B b_q - \frac{\Gamma}{2}b_q + i\sqrt{\xi}\ g_{\mathrm{tot}}a_{-k}^\dagger + \sqrt{\Gamma}\ b_{in}(\omega) \tag{6.17b}$$

$$-i\omega b_{-q}(\omega) = -i\Omega_B b_{-q} - \frac{\Gamma}{2}b_{-q} + i\sqrt{\xi}\ g_{\mathrm{tot}}^* a_{-k} + \sqrt{\Gamma}\ b_{-in}(\omega), \tag{6.17c}$$

where $g_{\mathrm{rp\,(tot)}} = \alpha_k g_{0,\mathrm{rp\,(tot)}}$ is the pump field boosted optomechanical coupling rate, $b_{in}^\dagger(\omega)$ is the Fourier transform of the complex conjugate of $b_{in}(t)$ following the convention of this thesis such that $b_{in}^\dagger(\omega) = [b_{in}(-\omega)]^\dagger$, and the auto-correlations of the thermal drives at Markovian limit, $b_{in}(\omega)$ and $b_{in}(\omega)$, have such functional forms:

$$\langle b_{in}^\dagger(\omega) b_{in}(\omega')\rangle = 2\pi\, n_q\, \delta(\omega+\omega') \tag{6.18a}$$

$$\langle b_{in}(\omega) b_{in}^\dagger(\omega')\rangle = 2\pi(n_q+1)\delta(\omega+\omega') \tag{6.18b}$$

$$\langle b_{in}^\dagger(\omega) b_{-in}(\omega')\rangle = 0. \tag{6.18c}$$

Solving the equations of motion yields the dynamical solution of the co-propagating acoustic wave:

$$\begin{aligned} b_q(\omega) &= \frac{\frac{-\xi g_{0,\mathrm{rp}} g_{0,\mathrm{tot}} n_{cav,k}\sqrt{\Gamma}\ b^\dagger_{-in}(\omega)}{(i\omega+i\Omega_B-\Gamma/2)(-i\omega+i\Delta+\kappa/2)-\xi g_{0,\mathrm{rp}} g_{0,\mathrm{tot}} n_{cav,k}} + \sqrt{\Gamma}\ b_{in}(\omega)}{-i\omega + i\Omega_B + \Gamma/2 - \frac{\xi g_{0,\mathrm{rp}} g_{0,\mathrm{tot}} n_{cav,k}}{-i\omega+i\Delta+\kappa/2+\frac{\xi g_{0,\mathrm{rp}} g_{0,\mathrm{tot}} n_{cav,k}}{-i\omega-i\Omega_B+\Gamma/2}}} \\ &= \frac{-\xi g_{0,\mathrm{rp}} g_{0,\mathrm{tot}} n_{cav,k}\sqrt{\Gamma}\ b^\dagger_{-in}(\omega)\chi_q(\omega)}{B(\omega)} + \sqrt{\Gamma}\ b_{in}(\omega)\chi_q(\omega), \end{aligned} \tag{6.19}$$

where we define

$$\chi_q^{-1}(\omega) = -i\omega + i\Omega_B + \Gamma/2 - \frac{\xi g_{0,\mathrm{rp}} g_{0,\mathrm{tot}} n_{cav,k}}{-i\omega + i\Delta + \kappa/2 + \frac{\xi g_{0,\mathrm{rp}} g_{0,\mathrm{tot}} n_{cav,k}}{-i\omega-i\Omega_B+\Gamma/2}}, \tag{6.20}$$

and

$$B(\omega) = (i\omega + i\Omega_B - \Gamma/2)(-i\omega + i\Delta + \kappa/2) - \xi g_{0,\mathrm{rp}} g_{0,\mathrm{tot}} n_{cav,k} \tag{6.21}$$

to simplify the notations of this equation.

The power spectrum of the co-propagating acoustic wave is calculated from the auto-correlation function of its solution Eq. (6.19). With the thermal noise correlations given in

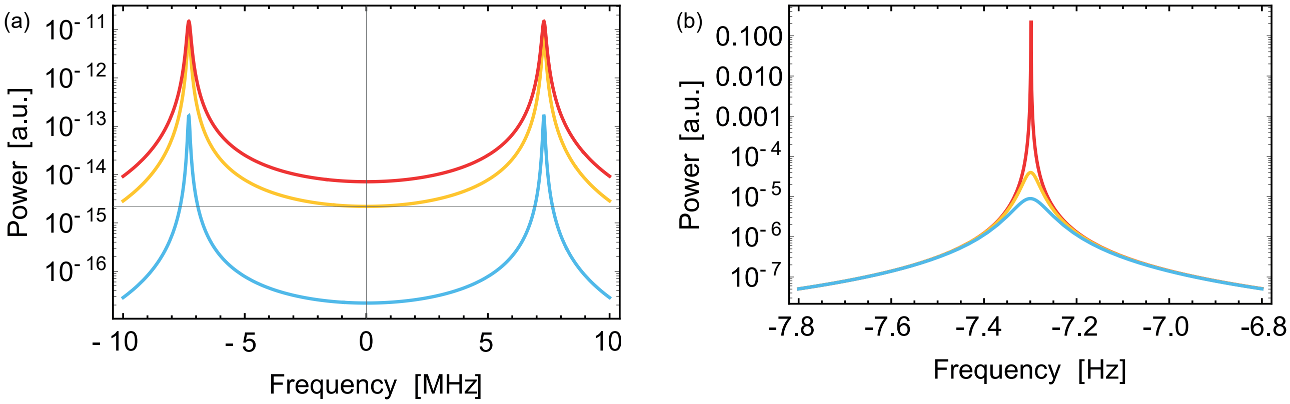

Figure 6.6: (a) Power spectra of the co-propagating wave b_q at different pump powers based on the first term of Eq. (6.22); (b) Power spectra of the co-propagating wave b_q at different pump powers based on the second term of Eq. (6.22). Red: 1.8 μW; yellow: 1 μW; blue: 0.1 μW.

Eqs. (6.18), the co-propagating wave power spectrum is calculated as following:

$$\begin{aligned} S_{b_q b_q}(\omega) &= \frac{1}{2\pi}\int \mathrm{d}\omega' \, \langle b_q^\dagger(\omega) b_q(\omega')\rangle \\ &= \frac{1}{2\pi}\int \mathrm{d}\omega' \, \langle [b_q(-\omega)]^\dagger b_q(-\omega)\rangle \\ &= \frac{(\xi g_{0,\mathrm{rp}} g_{0,\mathrm{tot}} n_{cav,k})^2 \, \Gamma(n_{-q}+1)|\chi_q(-\omega)|^2}{|B(-\omega)|^2} + \Gamma \, n_q |\chi_q(-\omega)|^2. \end{aligned} \tag{6.22}$$

From the results above $S_{b_q b_q}(\omega)$ has two terms: one is related with the thermal noise of the acoustic wave (b_{-q}) that counter-propagates with the pump light, the other is related to the co-propagating wave's (b_q) own thermal noise. The first term shows that the mechanical waves travelling in opposite directions are coupled to each other via light.

Fig. 6.6 plots the power spectra of the co-propagating acoustic at different input powers, with the following parameters: acoustic resonance frequency $\Omega_B/2\pi = 6.37$ MHz, laser (pump) frequency $w_L/2\pi = 193$ THz, fiber-to-cavity coupling rate $\kappa_{ext} = 180$ MHz, backscattering-modified total optical mode linewidth $(\kappa + \frac{4\kappa_b^2}{\kappa})/2\pi = 363$ MHz [4], the radiation pressure optomechanical coupling rate $g_{0,\mathrm{rp}}/2\pi$ is estimated to be 11 kHz in § 6.2.4 , optical detuning $\Delta = \Omega_B$, intrinsic mechanical linewidth $\Gamma/2\pi = 85 \pm 6$ kHz, the factor for the backscattering effect $\xi = 0.2$ and $g_{0,\mathrm{pt}}/2\pi = 122$ kHz.

However, sinc that the optical cavity linewidth κ is much larger than the acoustic resonance frequency, the first term of the power spectrum of b_q in Fig. 6.6(a) is negligible compared to the second term. Then the dynamical solution of $b_q(\omega)$ is reduced to be:

$$b_q(\omega) = \sqrt{\Gamma} \, b_{in}(\omega)\chi_q(\omega). \tag{6.23}$$

In addition, in the denominator of $\chi_q^{-1}(\omega)$, the optical linewidth dominates over other terms around the acoustic resonance frequency. So the denominator of b_q can be further approximated

---

[4] The real part of the denominator of Eq. (2.22) gives the backscattering modified optical linewidth, showing backscattering broadens the optical mode.

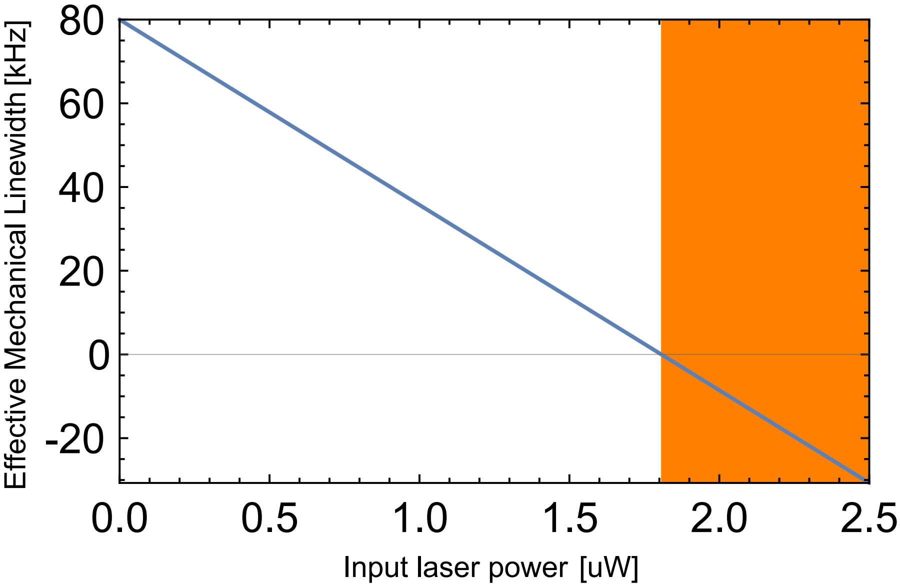

Figure 6.7: Effective mechanical linewidth Γ_{eff} of the forward propagating acoustic wave versus input laser power (blue line), plotted using Eq. (6.26). The orange shading corresponds to the region above the Brillouin lasing threshold, for which the analytical theory is no longer valid.

as:

$$\chi_q^{-1}(\omega) = -i(\omega - \Omega_B) + \Gamma/2 - \frac{\xi g_{0,\text{rp}} g_{0,\text{tot}} n_{cav,k}}{-i\omega + i\Delta + \kappa/2}. \tag{6.24}$$

The first two terms are related with the original mechanical resonance of the co-propagating wave. The last term describes how the interaction with light influences the co-propagating wave. For convenience, the last term is denoted as

$$\Sigma_{b_q}(\omega) = i\delta\Omega_B(\omega) - \frac{\Gamma_{opt}(\omega)}{2} = \frac{-\xi g_{0,\text{rp}} g_{0,\text{tot}} n_{cav,k}}{-i\omega + i\Delta + \kappa/2}, \tag{6.25}$$

where the influence of light on the acoustic wave is decomposed into two parts: the imaginary part $\delta\Omega_B(\omega)$ is related to the acoustic resonance frequency change (frequency pulling, or optical spring effect) by light; the second part $\Gamma_{opt}(\omega)/2$ is related with the acoustic linewidth change (optical damping) generated by light. Again, due to large optical linewidth κ, $\Sigma_{b_q}(\omega)$ is mainly determined by the optical linewidth around the acoustic resonance frequency. Particularly, when the pump laser is marginally blue detuned by the acoustic frequency ($\Delta = \Omega_B$), the imaginary part diminishes, with light only affecting the acoustic linewidth. Thus, when $\Delta = \Omega_B$, the effective acoustic linewidth is defined as

$$\Gamma_{\text{eff}} = \Gamma - \frac{4\xi g_{0,\text{rp}} g_{0,\text{tot}} n_{cav,k}}{\kappa}. \tag{6.26}$$

This is the intrinsic acoustic linewidth reduced by an optical damping term, which is, in the limit of no phothermal effect ($g_{0,\text{tot}} = g_{0,\text{rp}}$), equal to the optical measurement rate [52]. Using the same experimental parameters for Fig. 6.6, the effective linewidth versus input laser power is plotted in Fig. 6.7. This figure shows that the effective acoustic linewidth has a linear relation with the input laser power, and reaches zero at around 1.8 μW, where the spontaneously

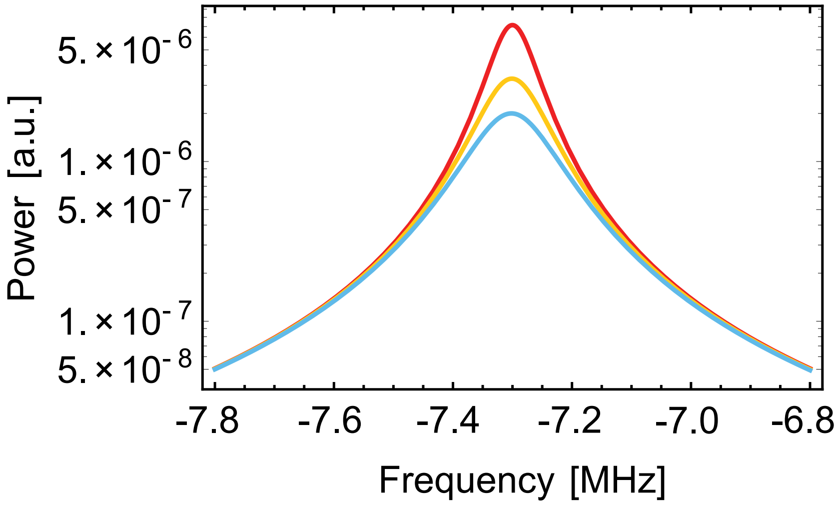

Figure 6.8: Power spectra of the counter-propagating acoustic wave versus input laser power, showing the optical damping of the counter-propagating acoustic wave, plotted using Eq. (6.30). Blue: 1.8 μW; yellow: 1 μW; red: 0.1 μW.

thermally excited Brillouin acoustic wave is optically amplified to a large coherent amplitude, i.e. Brillouin lasing. The observation of Brillouin lasing implies a multiphoton cooperativity of $C = 1$, an important threshold for the realization of quantum state transfer protocols.

Using the same method of deriving and simplifying the solution of $b_q(\omega)$, from the equations of motion in Eqs. (6.17) the solution of the counter-propagating acoustic wave $b_{-q}(\omega)$ is obtained:

$$b_{-q}(\omega) = \frac{\sqrt{\Gamma}\, b_{-in}(\omega)}{-i\omega + i\Omega_B + \Gamma/2 + \frac{\xi g_{0,\mathrm{rp}} g_{0,\mathrm{tot}} n_{cav,k}}{-i\omega - i\Delta + \kappa/2}}. \tag{6.27}$$

Similarly, the last term in the dominator is defined as

$$\Sigma_{b_{-q}}(\omega) = \frac{\xi g_{0,\mathrm{rp}} g_{0,\mathrm{tot}} n_{cav,k}}{-i\omega - i\Delta + \kappa/2}, \tag{6.28}$$

which can also be decomposed into a real part and an imaginary part. At the limit of large optical linewidth κ, when the optical detuning Δ is roughly $-\Omega_B$, the imaginary part related with frequency pulling is neglected. This approximation leads to the effective acoustic linewidth in Eq. (6.27)

$$\Gamma_{\text{eff}-} = \Gamma + \frac{4\xi g_{0,\mathrm{rp}} g_{0,\mathrm{tot}} n_{cav,k}}{\kappa}. \tag{6.29}$$

Different from the effective linewidth of the co-propagating acoustic wave, the effective linewidth of the counter-propagating acoustic wave in Eq. (6.29) increases linearly with the pump laser power. This means that light exerts a damping force on the counter-propagating acoustic wave. This is shown in the counter-propagating acoustic wave power spectra below achieved in a similar approach of deriving Eq. (6.22):

$$S_{b_{-q}b_{-q}}(\omega) = \Gamma\, n_{-q} |\chi_{-q}(-\omega)|^2, \tag{6.30}$$

where

$$\chi_{-q}^{-1}(\omega) = -i\omega + i\Omega_B + \Gamma/2 + \frac{\xi g_{0,\mathrm{rp}} g_{0,\mathrm{tot}} n_{cav,k}}{-i\omega - i\Delta + \kappa/2}. \tag{6.31}$$

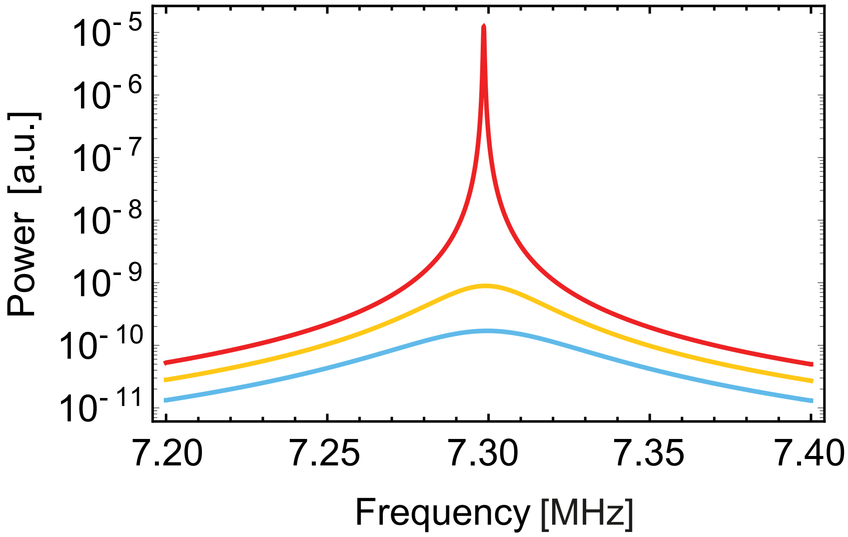

Figure 6.9: Analytical calculation of the reflected light power spectrum in the non-depleted pump regime from Eq. (6.33), showing the lasing of the Stokes sideband. Curves corrspond to $P_{in} = 0.5\,\mu$W (blue); $P_{in} = 1\,\mu$W (yellow) and $P_{in} = 1.8\,\mu$W (red - at phonon lasing threshold).

After the analysis of the two acoustic waves b_q and b_{-q}, inserting the simplified solutions (Eq. (6.23) and Eq. (6.27)) back into the equations of motion Eq. (6.17), the solution of the backscattered optical field a_{-k} yields

$$a_{-k}(\omega) = \frac{i\sqrt{\xi}\; g_{0,\mathrm{rp}}\alpha_k(b_{-q}(\omega) + b_q^\dagger(\omega))}{-i\omega - i\Delta + \kappa/2}, \tag{6.32}$$

which is the sum of the two acoustic waves filtered by the optical cavity response.

The power spectrum of the reflected light is calculated using the self-correlation of Eq. (6.32):

$$\begin{aligned} S_{a_{-k}a_{-k}}(\omega) &= \frac{1}{2\pi}\int_{-\infty}^{\infty} d\omega' \langle [a_{-k}(-\omega)]^\dagger a_{-k}(\omega')\rangle \\ &= \xi g_{0,\mathrm{rp}}^2 n_{cav,k}|\chi_{-k}(-\omega)|^2 \left(\Gamma\,(n_q+1)|\chi_q^*(-\omega)|^2 + \Gamma\, n_{-q}|\chi_{-q}(-\omega)|^2\right), \end{aligned} \tag{6.33}$$

where $\chi_q^{-1}(\omega)$ is from Eq. (6.24), $\chi_{-q}(\omega)$ is from Eq. (6.31), and $\chi_{-k}(\omega)$ is:

$$\chi_{-k}^{-1}(\omega) = -i\omega - i\Delta + \kappa/2. \tag{6.34}$$

Note that in the co-propagating acoustic wave part of Eq. (6.33), it's the complex conjugate $\chi_q^*(-\omega)$ instead of $\chi_q(-\omega)$, because it is $b_q^\dagger(\omega)$ in the solution of $a_{-k}(\omega)$ [Eq. (6.32)]. Eq. (6.33) also shows that the backscattered light power spectrum is the power spectrum of the acoustic waves scaled by the spectral response of the cavity.

Below the Brillouin lasing threshold, the co-propagating wave is amplified, while the counter-propagating wave is optically attenuated. Unless there is certain type of saturation mechanism showing a substantial amount of pump light is scattered backward to pump the counter-propagating wave, the counter-propagating wave induced sideband (anti-Stokes sideband) is extremely weak. Thus only the Stokes sideband is plotted in the power spectra of the reflected light in Fig. 6.9.

Note that this analytical result is valid as mentioned in the non-depleted pump regime, and only describes the behaviours below the threshold. The above threshold behaviour can be explained in the numerical simulation of the equations of motion without non-depleted pump approximation. Nevertheless, this analytical approach is able to predict the dynamics and estimate the performance of the system below the lasing threshold, for example the Brillouin optomechanical coupling rate and lasing threshold. With experimental measurements of Brillouin linewidths at different input powers [Eq. (6.26)], this analytical approach can also help extract the intrinsic acoustic linewidth.

6.2.6 Theory on Brillouin Induced Strong Optical Coupling

Here we calculate the modified eigenfrequencies of a pair of optical cavity modes introduced by mechanically mediated scattering between them. For simplicity, we neglect the two interacting terms in the full Hamiltonian [Eq. (6.12)] for anti-Stokes scattering, as the Brillouin interaction is dominated by Stokes scattering and the anti-Stokes scattering in it is suppressed.

$$\hat{H} = \hbar\omega_k a_k^\dagger a_k + \hbar\omega_{-k} a_k^\dagger a_{-k} - \hbar g_0 \left(a_k^\dagger a_{-k} b_q + a_k a_{-k}^\dagger b_q^\dagger \right), \tag{6.35}$$

where ω_k and ω_{-k} are the bare eigen frequencies of the two optical modes, and the associated a is the lowering operator of each mode. g_0 is the usual vacuum optomechanical coupling rate, and b_q is the lowering operator for the co-propagating acoustic wave, where the counter-propagating wave is neglected. k and q are respectively the wave numbers of the optical modes and acoustic wave, with the signs in the front indicating directions. The bare mechanical Hamiltonian has been neglected here because we will instead just assume that the mechanical oscillator oscillates at some frequency and at some amplitude (the exact frequency will turn out not to matter, but should be expected to be very close to the bare mechanical resonance frequency).

This Hamiltonian models the Brillouin interaction of particular interest to this experiment, but also a broader class of "photon-phonon translator" type systems such as introduced by the Painter group [187].

Equations of motion

From the Hamiltonian we directly obtain the equations of motion for the coupled optical cavity modes in the absence of dissipation. While dissipation can have the effect of shifting the eigen mode frequencies, for high quality optical cavities, as is the relevant case for this experiment, this is a negligible effect. Neglecting the dissipation allows a simpler calculation.

The equations of motion are found to be:

$$\dot{a}_k = -i\omega_k a_k + i g_0 a_{-k} b_q \tag{6.36}$$

$$\dot{a}_{-k} = -i\omega_{-k} a_{-k} + i g_0 a_k b_q^\dagger \tag{6.37}$$

Then we treat the mechanical oscillator classically (we're interested in the light scattered due to its coherent oscillation rather than fluctuations) by substituting b_q with $\beta_q e^{-i\Omega t}$. β_q is the amplitude of oscillation and Ω can be thought of as the mechanical resonance frequency though in fact our results do not require this (of course, the further away from resonance the harder it will typically be to drive the oscillator to a given amplitude). We take β_q to be real, without loss of generality. This just determines the phase of the mechanical oscillation. Defining the *mechanical-amplitude boosted optomechanical coupling rate* $g_{\text{opt}} = \beta_q\, g_0$, we then obtain

$$\dot{a}_k = -i\omega_k a_k + i g_{\text{opt}} e^{-i\Omega t} a_{-k} \tag{6.38}$$

$$\dot{a}_{-k} = -i\omega_{-k} a_{-k} + i g_{\text{opt}} e^{i\Omega t} a_k. \tag{6.39}$$

The terms on the right are coherent coupling terms that act to hybridise the two optical modes. This results in a new pair of orthogonal eigenmodes with shifted frequencies.

To determine the shifted eigenmode frequencies we postulate solutions of the following form:

$$a_k \rightarrow \alpha_k e^{-i\omega t} \tag{6.40}$$

$$a_{-k} \rightarrow \alpha_{-k} e^{-i\omega t} \tag{6.41}$$

where ω is the oscillation frequency. Again we are neglecting the fluctuations in the fields which do not alter the eigen frequencies, with the α's representing the coherent amplitude of each field. We then find

$$-i\omega a_k = -i\omega_k \alpha_k + i g_{\text{opt}} e^{-i\Omega t} \alpha_{-k} \tag{6.42}$$

$$-i\omega a_{-k} = -i\omega_{-k} \alpha_{-k} + i g_{\text{opt}} e^{i\Omega t} \alpha_k. \tag{6.43}$$

In matrix representation this can be written as

$$\mathbf{M} \cdot \boldsymbol{\alpha} = \mathbf{0}, \tag{6.44}$$

where

$$\mathbf{M} = \begin{bmatrix} \omega_k - \omega & -g_{\text{opt}} e^{-i\Omega t} \\ -g_{\text{opt}} e^{i\Omega t} & \omega_{-k} - \omega \end{bmatrix}$$

and

$$\boldsymbol{\alpha} = \begin{bmatrix} \alpha_k \\ \alpha_{-k} \end{bmatrix}$$

Non-trivial ($\boldsymbol{\alpha} \neq 0$) solutions to this matrix equation only exist when $\mathbf{M}$ is invertible and has a determinant equal to zero. This gives a condition on the frequency ω:

$$|\mathbf{M}| = (\omega_k - \omega)(\omega_{-k} - \omega) - g_{\text{opt}}^2 = 0, \tag{6.45}$$

which does not depend explicitly on the oscillation frequency Ω of the mechanical element. Note that there is an implicit dependence, since achieving a large β_q and therefore g_{opt} is easier for oscillation frequencies near the mechanical resonance frequency. Similarly, choosing appropriate bare optical frequencies can greatly enhance the ability of radiation pressure to drive the mechanical response.

Solving this equation for ω gives two new shifted eigen frequencies $\omega_\pm$ given by

$$\omega_\pm = \bar{\omega} \pm \sqrt{\Delta^2/4 + g^2} \ , \tag{6.46}$$

where $\bar{\omega} = (\omega_k + \omega_{-k})/2$ is the average of the two bare resonance frequencies and $\Delta = \omega_k - \omega_{-k}$ is their difference.

We can observe that when $g_{\text{opt}} \gg \Delta$ the splitting between the resonances is given by $\delta = \omega_+ - \omega_- = 2g_{\text{opt}}$ as expected for strong coupling. However, in the reverse regime where $g \ll \Delta$, $\delta = \Delta + g_{\text{opt}}^2/\Delta$. In this case, the first term (Δ) is just the initial splitting of the resonances. The shift in splitting due to the mechanically-mediated coupling is g_{opt}^2/Δ, suppressed compared to the regime where $g_{\text{opt}} \gg \Delta$ by a factor of $2\,\Delta/g_{\text{opt}}$. In this superfluid Brillouin lasing experiment, the initial splitting of the two optical modes is zero, so the strong optical coupling is observed.

6.3 Experimental Setup

To investigate the Brillouin interaction between the phase-matched optical field and acoustic wave in superfluid. We cool down a silica disk microresonator with helium-4 gas in a indium-sealed sample chamber inside a dilution refrigerator. Laser light is coupled to the resonator by feeding through optical fibers into the fridge. Silica microdisks are fabricated from a 500 μm-thick silicon handling wafer topped by a two-micron thick thermal oxide layer (Virginia Semiconductor). Disks are defined in the silica layer through a combination of photolithography (AZ1518 positive resist and HMDS adhesion promoter) and hydrofluoric acid (HF) wet-etch. A

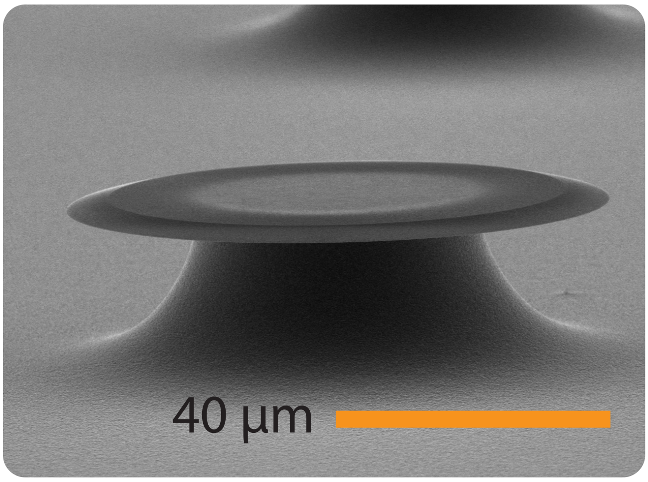

Figure 6.10: Scanning Electron Microscope (SEM) image of a silica WGM resonator on the silicon chip (radius 40 μm, thickness 2 μm).

subsequent XeF_2 gas-phase release selectively etches the silicon material and leaves the silica disks isolated from the substrate atop a silicon pedestal, as shown in Fig. 6.10.

Unlike in previous experimental work [1, 18], the fabricated microdisks undergo no laser reflow step to form a microtoroidal resonator, and maintain their wedged outer sidewalls. This wedge shape serves a dual purpose: beyond enhancing the optical Q (over a vertical sidewalled microdisk) by making the device less sensitive to fabrication-induced roughness [150], it also serves to deconfine the optical mode and maximize the optical field intensity at the top and bottom disk interfaces where the superfluid film resides, as shown in Fig. 6.12. Indeed, the value of the WGM electric field at the silica interface is the parameter which should be optimized in order to maximize the optomechanical coupling rate between light and superfluid [2], see § 6.2.3. Fabricated devices show a number of WGM families, with optical Qs in the 10^5 to low 10^7 range.

The experimental setup is shown in Fig. 6.11. The microresonator chip is positioned inside a superfluid-tight sample chamber at the bottom of a Bluefors dilution refrigerator (base temperature 10 mK). Helium-4 gas injected into the superfluid tight sample chamber forms a nanometer-thick self-assembling superfluid film coating the microresonator. Laser light is injected into the dilution fridge through an optical fiber and is evanescently coupled into the microresonators via a tapered optical fiber [18]. The Stokes and anti-Stokes light backscatterd by the acoustic waves are collected using a circulator, and eventually beats with the Local Oscillator (LO), the frequency of which is up-shifted by 80 MHz using an Acousto-Optic Modulator (AOM). The beat of Stokes and anti-Stokes light with LO is sent to a large bandwidth balanced photodetector (PD). This forms a heterodyne detection of the backscattered signal. Due to the beat with LO, the anti-Stokes light shows sideband below the AOM frequency (80 MHz) on

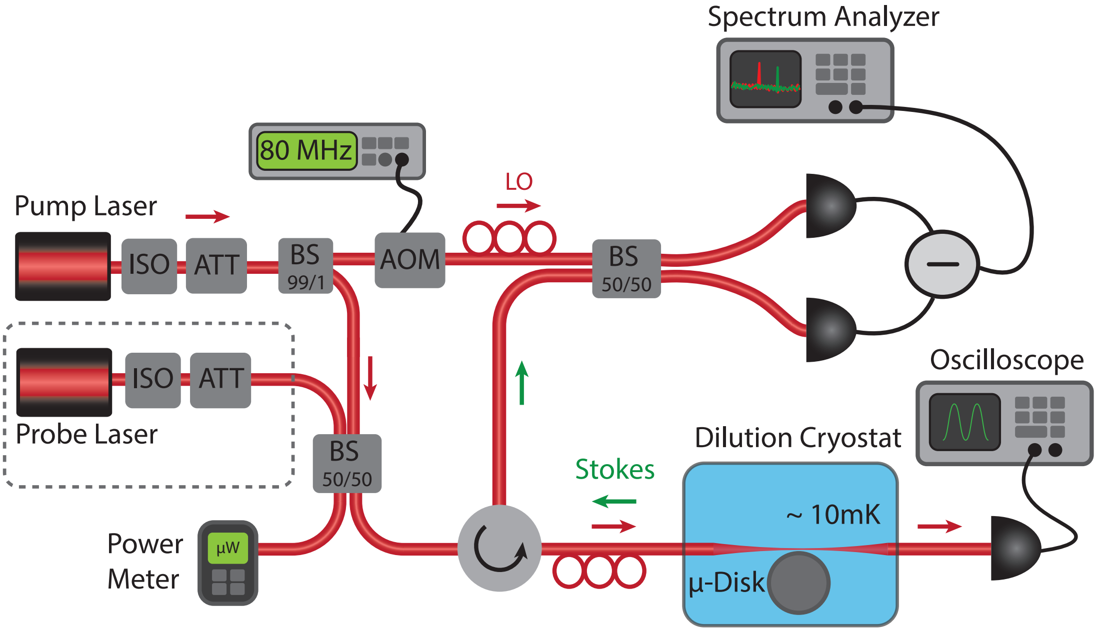

Figure 6.11: Schematic of the experimental setup. BS: beamsplitter; AOM: acousto-optic modulator; blue box represents the sample chamber in the dilution refrigerator.

the Spectrum Analyser, while the Stokes sidebands are above the AOM frequency. Inside the sample chamber, precise fiber positioning is achieved through Attocube nanopositioning stages. The fiber taper rests on support pads microfabricated on the chip alongside the resonators [1], in order to eliminate taper drift and fluctuations. The experimental measurements are performed with the pulse-tube cooler switched off to minimize vibrations. The sample chamber contains a small volume of micronized alumina powder in order to increase the effective chamber surface area (by $\sim$ 10 m^2), leading to more precise film thickness control and greater film thickness stability [87]. While at base temperature, helium-4 gas can be continuously injected from the top of the cryostat into the sample chamber through a thin capillary. This allows for varying of the film thickness, and thus in-situ tuning of the Brillouin frequency.

6.4 Experimental Results

6.4.1 Characterization of Superfluid Film Thickness

We first calibrate the superfluid film thickness to determine the third sound velocity. The thickness of the superfluid film covering the microresonator can be assessed through two independent means:

- First, through the magnitude of the WGM wavelength-shift across the superfluid transition temperature. When sweeping the cryostat temperature down from 1.1 K to 0.2 K, all WGMs acquire a positive wavelength shift corresponding to the increased optical path length due to the condensation of the superfluid film on the resonator surface[5], as shown in Fig. 6.12. Each WGM experiences a frequency shift $\frac{G}{2\pi}\Delta x$, where $G = \frac{\partial \omega_0}{\partial x}$ is the optomechanical coupling strength describing the optical cavity angular resonance frequency shift per unit deposited superfluid film thickness on the resonator boundary Δx [2, 50]. The value of G is WGM dependent, and can be calculated through FEM modelling, as detailed in § 6.2.3 below. With the knowledge of G, the magnitude of the experimentally measured WGM frequency shift can be converted into a deposited film thickness.

- Second, through the Brillouin frequency. The Brillouin wavelength is imposed by the wavelength of light through $\lambda_B \approx \lambda_{\text{light}}/2$, where λ_{light} is the wavelength of light in the silica given by λ_0/n_{eff}, *i.e.* the freespace wavelength λ_0 divided by the WGM effective index. The Brillouin frequency $\Omega_B/2\pi = c_3/\lambda_B$ thus informs us on the speed of sound in the superfluid c_3, which is given by [84]:

$$c_3 = \sqrt{3\,\frac{\rho_s}{\rho}\,\frac{\alpha_{\text{vdw}}}{d^3}}\;. \tag{6.47}$$

Here the ratio ρ_s/ρ is nearly one at the low temperature used in our experiments, $\alpha_{\text{vdw}} = 2.6\times10^{-24}$ m^5 s^{-2} describes the van der Waals interaction between the helium atoms in the

---

[5] Indeed, the magnitude of the thermo-optic shift [188] over this temperature range can be neglected.

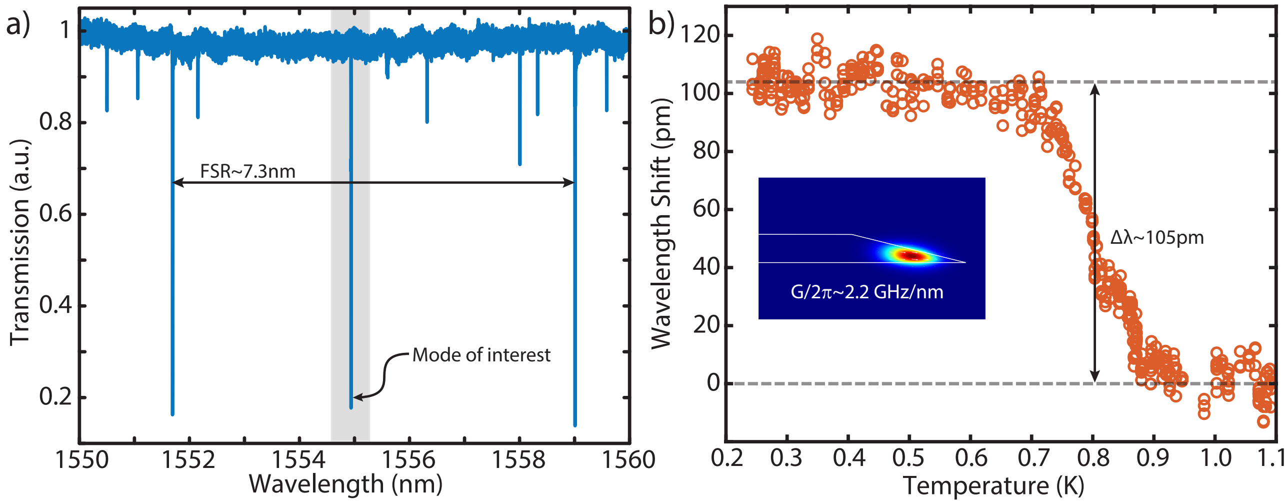

Figure 6.12: a) Microdisk optical spectrum, showing a number of high-Q WGMs separated by a $\sim$ 7 nm free-spectral-range (FSR). WGM highlighted in gray near 1555 nm is the one used in the experiments. b) WGM wavelength shift as a function of fridge temperature, for the mode highlighted in (a). The vertical scatter in the data points is due to the 20 pm repeatability error in the motor sweep of our tunable laser diode. Inset displays the electric field norm of the $(p = 1,\, m = 186)$ quasi-TE mode of the structure.

superfluid and the silica disk [2] and d is the superfluid film thickness. The experimentally measured Brillouin frequency thus provides a second independent estimate of the film thickness in the experiments.

The film thickness estimation through these two methods is provided in Table 6.2. We ascribe the discrepancy to uncertainties in the exact device geometry. Indeed, variations in wedge angle of a few degrees can shift G by over 30%, by altering the mode confinement of the WGM and its interaction with the superfluid film. Surface roughness on the microresonator, not taken into account in the simulations, may also increase the effective surface area of the resonator and result in uncertainties in the G.

6.4.2 Influence of Surface Tension

In thin superfluid films, there are two types of forces which can act as the restoring force of surface acoustic waves: van der Waals force and surface tension. The acoustic waves that these two type of restoring forces correspond to are respectively third sound and ripplons. The type of the acoustic wave in our system can be determined using the dispersion relation of thin superfluid films. The dispersion relation giving the angular frequency Ω of a superfluid wave under the influence of van der Waals and surface tension restoring forces is:

$$\Omega = \sqrt{\frac{3\,\alpha_{\mathrm{vdw}}\,k^2}{d^3} + \frac{\sigma\,k^4\,d}{\rho}}\,, \qquad (6.48)$$

where $\sigma = 3.54 \times 10^{-4}$ N/m is the superfluid ^{4}He surface tension [189] and $k = 2\pi/\lambda = \zeta_{m,n}/R$ the angular wavenumber. We plot this frequency $\Omega/2\pi$ in Fig. 6.13, along with the limiting

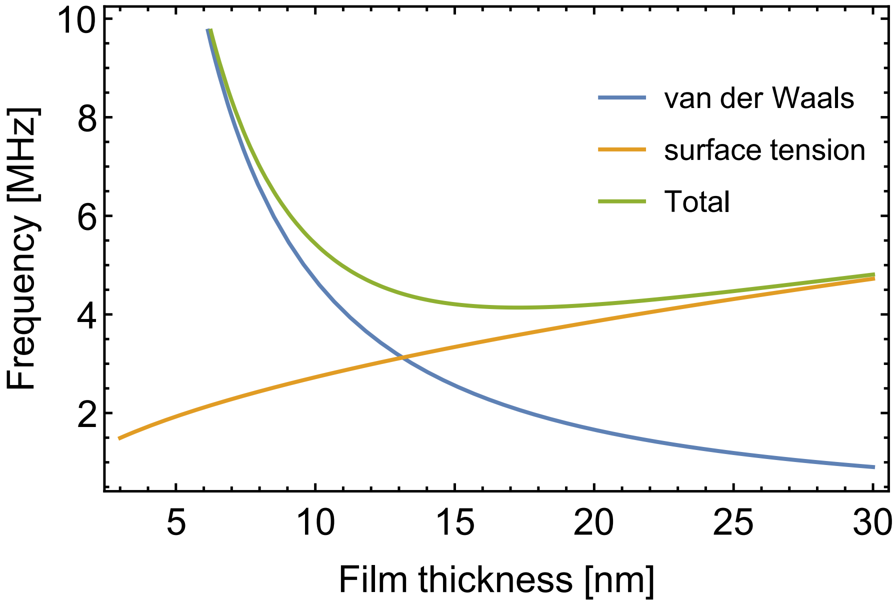

Figure 6.13: Frequency $\Omega/2\pi$ of Brillouin wave in the presence of both van der Waals and surface tension restoring forces (green), as well as the limiting cases of the frequency $\Omega_{\mathrm{vdw}}/2\pi$ of a pure van der Waals wave (third sound - blue) and the frequency $\Omega_\sigma/2\pi$ of a pure surface tension wave (ripplon - orange). Values plotted with $k = 10^7$, corresponding to the Brillouin wavenumber in our experiments.

cases of a pure van der Waals wave (third sound) of frequency $\Omega_{\mathrm{vdw}}/2\pi = \frac{1}{2\pi}\sqrt{\frac{3\,\alpha_{\mathrm{vdw}}\,k^2}{d^3}}$, and a pure surface tension wave (ripplon) of frequency $\Omega_\sigma/2\pi = \frac{1}{2\pi}\sqrt{\frac{\sigma\,k^4\,d}{\rho}}$. For the film thickness used in the experiment, the dominant restoring force is the van der Waals interaction, and the Brillouin wave can be well approximated by a third sound mode. For thicker films (> 13 nm), the restoring force becomes dominated by surface tension, and the wave crosses over into a ripplon-like regime.

6.4.3 Transition from Standing-Wave ‘Optomechanics-like’ Interaction to Travelling-Wave ‘Brillouin-like’ Interaction

There has been a recent push to theoretically unify the fields of cavity optomechanics and Brillouin scattering [190]. While both fields deal with the inelastic interaction of photons with a mechanical degree of freedom (phonons), the Brillouin scattering paradigm generally refers to the interaction between a travelling optical field and a travelling mechanical wave which causes a periodic refractive index modulation [see Fig. 6.14(a)]. In contrast, the optomechanical paradigm —as illustrated by the archetypal Fabry-Perot cavity with a movable end-mirror Fig. 3.1 — typically refers to the interaction between a standing optical field and a standing mechanical wave, as illustrated in Fig. 6.14(b).

We show here that these two regimes can be accessed on the same device, and that the switch can be performed in-situ, simply by tuning the position of the coupling fiber taper in order to transition from a standing to a travelling intracavity optical field. Indeed, our microresonator

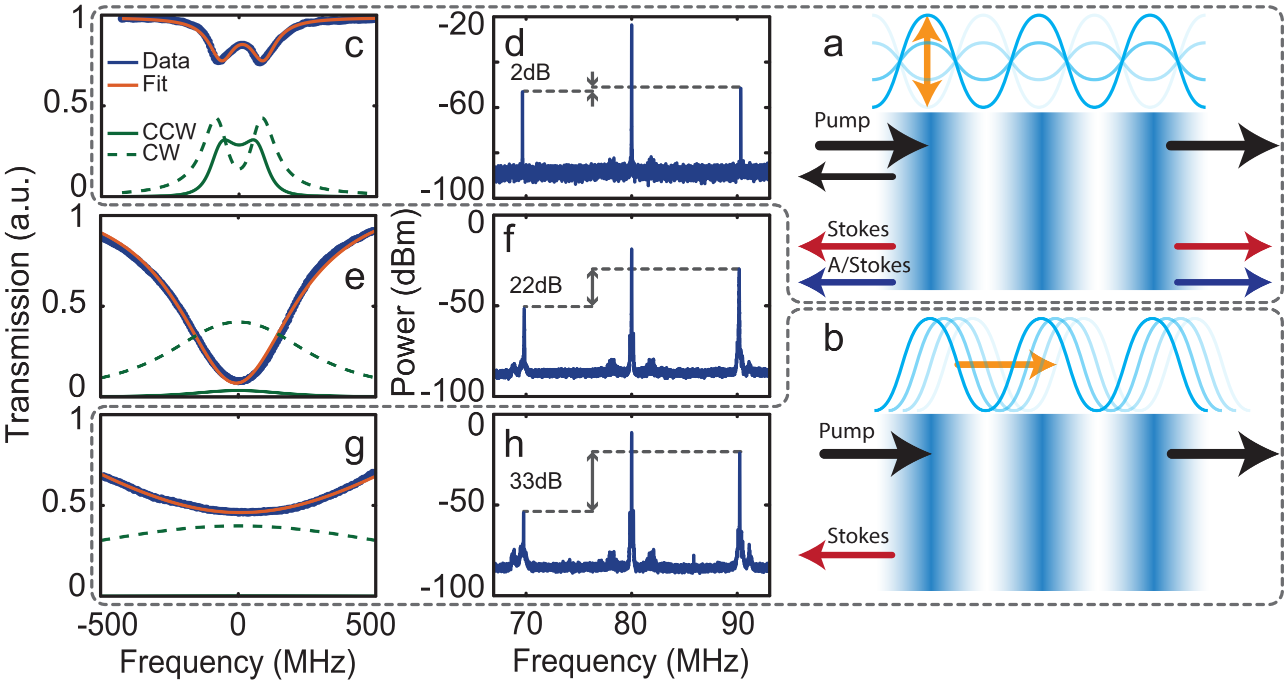

Figure 6.14: (a) Illustration of 'optomechanics-like' interaction where the pump is scattered by a standing refractive index grating whose strength is modulated in time, leading to symmetric Stokes and anti-Stokes sideband generation. (b) Schematic illustration of a travelling wave 'Brillouin-like' interaction, where the pump scatters off a moving refractive index grating, leading to single Stokes sideband generation. (c),(e),(g): normalized WGM transmission spectra for increasing fiber taper coupling strength (blue line). The dashed and solid green lines respectively refer to the photon numbers of the forwards and backwards travelling directions $|a_k|^2$ and $|a_{-k}|^2$ (arbitrary units). By increasing the coupling the optical field changes from predominantly standing to predominantly travelling: $|a_k|^2/|a_{-k}|^2$ at zero detuning goes from 0.53 (c) to 11.7 (e) and 162.4 (g). (d), (f) and (h): heterodyne power spectra respectively corresponding to the cases (c), (e) and (g), illustrating the transition from symmetric to asymmetric sideband generation.

possesses some native backscattering due to geometric imperfections such as sidewall roughness, which introduces a coupling between forwards and backwards propagating directions. This rate is experimentally measured to be $\kappa_b/2\pi = 75$ MHz, on the order of the intrinsic linewidth $\kappa_{int}/2\pi = 104$ MHz, and manifests as the optical resonance taking on a characteristic doublet lineshape [42], as shown in the blue trace in Fig. 6.14(c). The 'Optomechanics-like' interaction occurs when the pump is scattered by a standing refractive index grating whose strength is modulated in time, leading to symmetric Stokes and anti-Stokes sideband generation.

Based on coupled-mode theory formalism (see § 2.5), one can compute the relative amount of light travelling in the forwards and backwards direction as a function of detuning in this regime, as shown in the green traces in Fig. 6.14(c)-(g). Due to the backscattering rate κ_b being of comparable magnitude to the loss rate κ, both circulation directions are similarly populated, leading to a predominantly standing optical field, as described in Fig. 6.14(b). Indeed, we verify that in this regime the Stokes and anti-Stokes sidebands are comparable in magnitude, as shown in Fig. 6.14(d).

Next, we increase the coupling rate κ_{ext} of the cavity by approaching the fiber taper. As the cavity was previously undercoupled, this increases the depth of the transmission dip, while broadening the width of the resonance, as shown in Fig. 6.14(e). In this regime, the backscattering rate κ_b is no longer larger than the linewidth $\kappa = \kappa_{int} + \kappa_{ext}$, and the forwards propagating field is predominantly populated (green curves), leading to a predominantly travelling optical field. This can be understood by looking at Eqs. (2.20, 2.21). Both propagation directions experience a loss rate $\kappa = \kappa_{int} + \kappa_{ext}$ which depends on κ_{ext}. However, while increasing κ_{ext} increases both the loss rate and the pump rate of the forwards field (see Eq. (2.20)), it only increases the loss rate of the backwards propagating mode, which is pumped at a fixed rate proportional to κ_b (see Eq. (2.21)). Increasing the coupling rate to the taper therefore biases the system towards a forwards travelling optical field and a situation analogous to the Brillouin case described in Fig. 6.14(a). Indeed, in this coupling regime the asymmetry between Stokes and anti-Stokes sidebands reaches 22 dB, as shown in Fig. 6.14(f). Further increasing the taper coupling rate well into the overcoupled regime (Fig. 6.14(g)) leads to an even higher ratio of forwards to backwards optical intensity ($|a_k|^2/|a_{-k}|^2 = 162$ on resonance), and a sideband asymmetry reaching 33 dB (Fig. 6.14(h)).

6.4.4 Brillouin Lasing Measurement and Simulation

Backwards Brillouin scattering is an inelastic process, whereby each Stokes scattered photon is accompanied by the emission of one phonon into the forward travelling acoustic wave. This optical pumping results in a modified effective mechanical linewidth Γ_{eff} for the acoustic wave, which, based on the quantized interaction Hamiltonian in the non-depleted pump regime, can be expressed analytically as Eq. (6.26), with n_{cav} the intra-cavity photon number, $\kappa = \kappa_{int} + \kappa_{ext}$ the loaded optical linewidth, g_0 the single photon optomechanical coupling rate (including

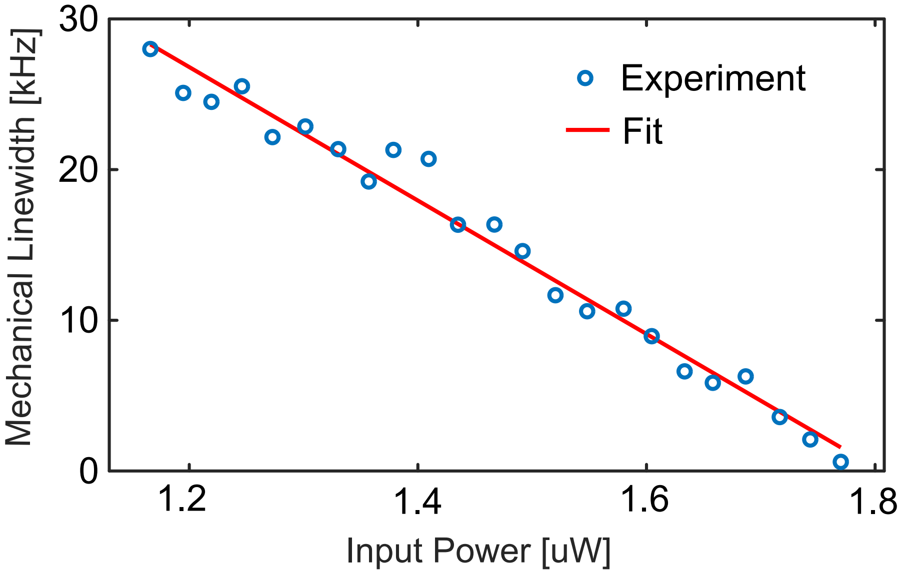

Figure 6.15: Effective acoustic linewidth Γ_{eff} vs input power, along with fit by Eq.(6.26).

both radiation pressure and photothermal interactions) and Γ the intrinsic linewidth of the co-propagating wave. When the effective linewidth reaches zero, spontaneously occurring thermal excitations in the superfluid film are optically amplified to a large coherent amplitude, *i.e* phonon lasing.

To experimentally measure the onset of lasing we select an optical mode at $\lambda = 1555$ nm with intrinsic linewidth $\kappa_{int}/2\pi = 104$ MHz. This mode is natively split due to geometrical imperfection (backscattering coupling rate between clockwise (CW) and counter-clockwise (CCW) WGM $\kappa_b/2\pi = 75$MHz). We observe that changing the cavity coupling strength κ_{ext} through the taper position enables us to tune the optical field from a standing wave to a travelling wave, resulting in a change to the coupling of the corresponding standing or travelling acoustic wave (see Supplemental Material for more details). For the rest of this work we operate in the overcoupled regime ($\kappa_{ext}/2\pi = 180$ MHz corresponding to a loaded $Q \simeq 7 \times 10^5$) in order to overcome the native backscattering and ensure a travelling-wave Brillouin excitation.

We measure the Stokes and Anti-Stokes signals in the reflected light via a heterodyne detection scheme, as shown Fig. 6.11. Fig. 6.16 plots the Stokes signal peak power as a function of input laser power, while Fig. 6.15 shows the Stokes linewidth versus input power, along with a fit through Eq. (6.26), yielding an intrinsic acoustic linewidth of $\Gamma/2\pi = 85 \pm 6$ kHz and a Brillouin lasing threshold power of 1.8 μW. Further, the numerical simulation of the full equations of motion (Eq. (6.15)) gives a photothermal single photon coupling rate of $g_{0,\mathrm{pt}}/2\pi =$ 122 kHz and a backscattering factor ξ (defined in Eq. (6.17)) of 0.2 with the 1.8 μW lasing threshold power and $g_{0,\mathrm{rp}}/2\pi$ fixed to be the finite element modelling result of 11 kHz (see § 6.2.3). The improved optical overlap with the superfluid excitations [2] in these devices means the optomechanical coupling is dominated by the radiation-pressure interaction, in contrast to

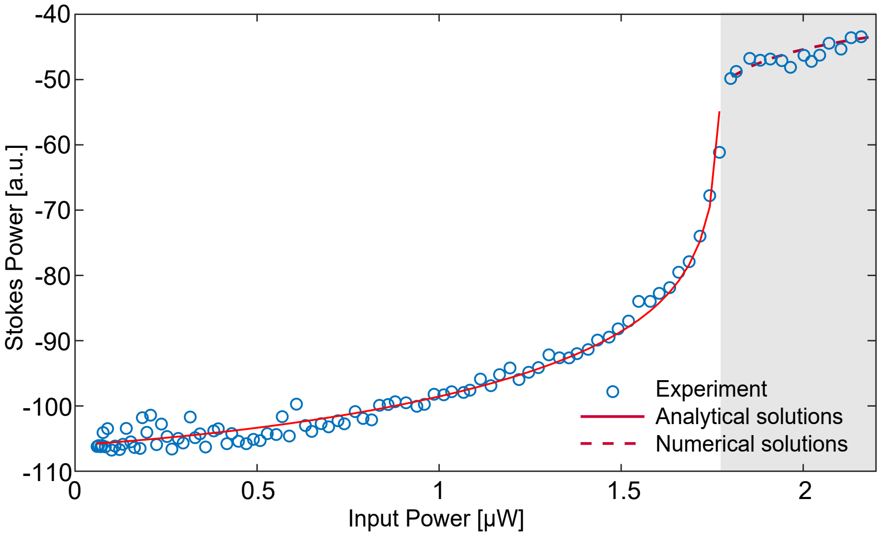

Figure 6.16: Stokes sideband peak power versus input laser power (blue circles). Solid red line is an analytical fit to the data in the non-depleted pump regime, while dashed red line is a fit obtained by numerically solving the full equations of motion). Shaded region above 1.8 μW marks the onset of Brillouin lasing.

Parameter	Symbol	Value	Units
Acoustic damping rate	$\Gamma/2\pi$	85	kHz
Acoustic (Brillouin) frequency	$\Omega_B 2\pi$	6.3	MHz
Laser detuning	Δ	0	MHz
Intrinsic cavity decay rate	$\kappa_{\text{int}}/2\pi$	104	MHz
Input coupling (external) cavity decay rate	$\kappa_{\text{ext}}/2\pi$	180	MHz
Backscattering decay rate	$\kappa_{\text{b}}/2\pi$	75	MHz
Single photon coupling strength (radiation pressure)	$g_{0,\text{rp}}/2\pi$	11	kHz
Single photon coupling strength (photothermal)	$g_{0,\text{pt}}/2\pi$	122	kHz

Table 6.3: System parameters used in numerical simulation.

our earlier work with silica microtoroids, where the optomechanical coupling was dominated by non-conservative photothermal effects [18]. As pointed out earlier, the fluid's greater compliance accounts for the coupling rate $g_{0,\text{rp}}$ being close to three orders of magnitude larger than what is achieved using the electrostrictive interaction in similar sized silica microspheres [161].

Using the extracted values of $g_{0,\text{pt}}$ and Γ, the functional form of the Stokes sideband peak power is fitted to analytical solutions (solid red line in Fig. 6.16), with only measurement transduction efficiency and detector noise as free parameters. The linewidth vanishes at 1.8 μW, corresponding to the Brillouin lasing threshold.

While this microwatt-range value is amongst the lowest reported Brillouin lasing thresholds [162], Eq. (6.26) reveals a quadratic dependence of the lasing threshold on cavity Q, through the decrease in κ and corresponding increase in n_{cav}. Reducing the optical linewidth to 20 MHz ($Q = 10^7$) through a better control of sidewall roughness [150] would reduce the threshold down to nano-Watts. Pico-Watt range lasing would even be accessible with a modest improvement in acoustic dissipation, significantly below what can be achieved with solid state systems.

Beyond the lasing threshold, the pump light is depleted by scattering off the strong superfluid travelling refractive index grating, such that the linearised theory is no longer valid. The above-threshold behaviour is therefore fitted by numerically solving the full equations of motion of the optical and acoustic fields.

The full equations of motion [Eq. (6.15)] are numerically solved in the time domain using a Matlab numerical solver function (ode23s), with the thermal noise terms $\sqrt{\Gamma}\ b_{in}(t)$ and $\sqrt{\Gamma}\ b_{-in}(t)$ replaced by an initial weak amplitude (initial "kick"), as we are not doing stochastic simulation. The initial weak amplitude is valid, because the optical input amplifies the co-propagating acoustic wave through the Brillouin interaction, and the initial weak amplitude only affects the very start of the simulation, not the steady state of the system reaching lasing regime.

The numerical simulation returns the solutions of the four variables respectively for the four fields for a given simulation time interval. The simulation parameters are summarized in Table 6.3. Fig. 6.17(a) and (b) directly plot the temporal solutions of the co-propagating acoustic wave (b_q) for 0.03 ms simulation time at 1.2 μW and 1.8 μW input power, respectively.

The displacement is oscillating at 6.3 MHz, so the envelope in the two plots shows how the zero-point-motion normalized acoustic amplitude evolves. In Fig. 6.17(a) the Brillouin amplification at 1.2 μW input power can not compensate the acoustic damping (Γ), so the simulation result shows the decay of the co-propagating acoustic wave after the "kick" given at the start of the simulation. Whereas, when the input power is set at around 1.8 μW, the Brillouin amplification compensates the acoustic damping, so that the initial "kick" generated acoustic amplitude does not decay over simulation time, which means the effective mechanical linewidth Γ_{eff} [Eq. (6.26)] reaches zero at this input power.

With $g_{0,\text{rp}}/2\pi$ fixed to 11 kHz, and the system parameters extracted from the experiment summarized in Table 6.3, the 1.8 μW lasing threshold from the numerical simulation agrees with the experimentally measured lasing threshold, when $g_{0,\text{pt}}/2\pi$ in the simulation is tuned to 122 kHz. Further, we need to note that the full numerical simulation takes into account the native backscattering (κ_b) observed in the experiment, whereas in the analytical approach the parameter ξ is introduced to take into account the two effects of the backscattering together: decreasing the pump field intracavity photon number $n_{cav,k}$, and actively cooling the co-propagating acoustic wave b_q. By feeding the $g_{0,\text{pt}}$ extracted from the full numerical simula-

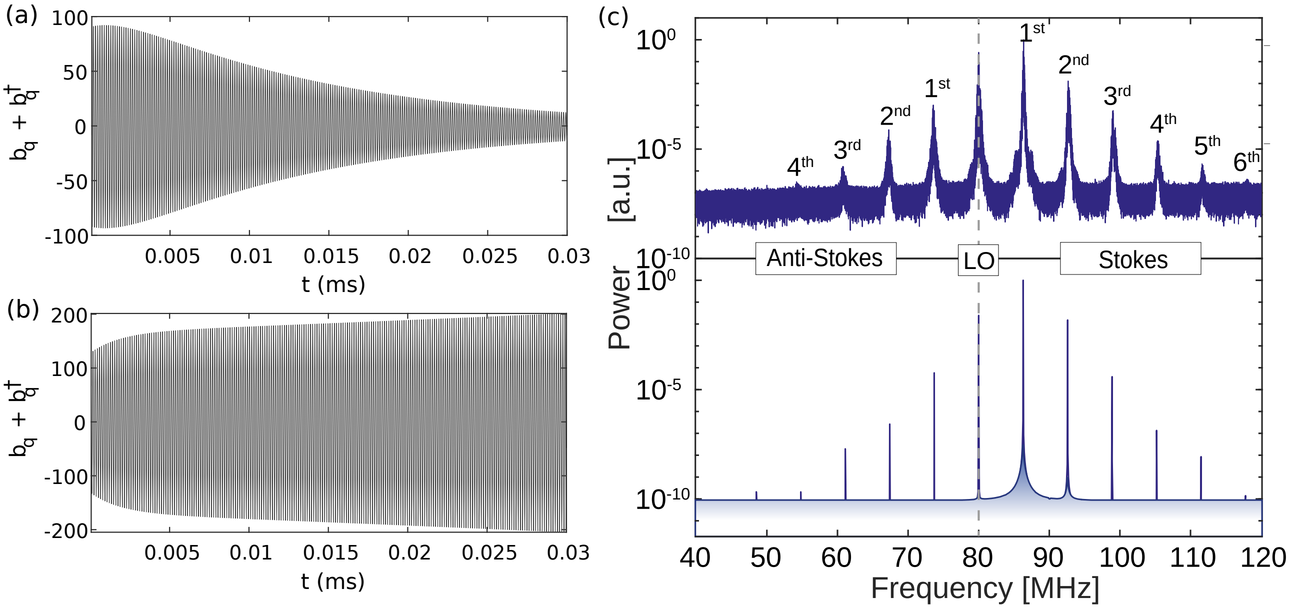

Figure 6.17: (a) Temporal evolution of the zero-point-motion normalized displacement of the co-propagating acoustic wave at 1.2 μW input power (the decaying envelope shows the co-propagating wave is ringing down after the initial "kick" at the start of the simulation, because there is no thermal drive in the simulation.); (b) Temporal evolution of the zero-point-motion normalized- displacement of the co-propagating acoustic wave at around 1.8 μW input power (the envelope shows that the mechanical amplitude is almost constant over time, because the Brillouin amplification at 1.8 μW compensates the acoustic damping rate.); (c) Multiple harmonics from Brillouin lasing measured at 5.65 μW input power, (top: experimental spectrum; bottom: numerical simulation). The small amount of native coupling between CW and CCW WGMs explains why all Stokes and Anti-Stokes orders are visible in the backscattered light. Note that Stokes sidebands appear at higher frequencies due to the heterodyne detection.

tion lasing threshold of 1.8 μW back to the experimental mechanical linewidth fit (Fig. 6.15), ξ is determined to be 0.2, with the intracavity photon number calculated using Eq. (6.16). Note that $g_{0,\mathrm{pt}}$ and ξ are not independent parameters, we need both the numerical simulation and the experimental mechanical linewidth fit to determine them.

We can not only do the simple temporal analysis of the acoustic amplitude evolution, but also do the spectral analysis of the numerical simulation solutions by performing Fourier transform in Matlab. The peak power of the simulated power spectra of the backscattered field (a_{-k}) gives a good agreement to the measured Stokes power scaling (dashed red curve in Fig. 6.16), and also provides a confirmation of the saturation mechanism: above threshold, the counter-propagating Stokes field becomes strong enough to initiate its own Brillouin lasing process. At 5.65 μW input power the simulated power spectrum of the backscattered field shows higher harmonics to the 6th order, with an excellent agreement to the experimental result showing in Fig. 6.17.

6.4.5 Experimental Demonstration of Strong Optical Coupling

The lasing of the co-propagating acoustic wave generates creates a large refractive index grating travelling at the speed of sound, mediating a coupling between the initially quasi-degenerate CW and CCW propagating optical fields. If this coupling is sufficiently strong, it will lift their degeneracy resulting in a new set of optical eigenfrequencies given by Eq. (6.49), where $g_{\mathrm{opt}} = g_0\,\beta$ is the *phonon boosted* optomechanical coupling rate:

$$\omega_{\pm} = \bar{\omega} \pm \sqrt{\Delta^2/4 + g_{\mathrm{opt}}^2}\ . \tag{6.49}$$

Here $\bar{\omega} = (\omega_k + \omega_{-k})/2$ is the average of the two bare optical resonance frequencies and $\Delta = \omega_k - \omega_{-k}$ is their original difference. The strong pump depletion above the lasing threshold, visible in Fig. 6.17, hints towards strong coupling between the CW and CCW propagating optical fields. To measure this effect, a weak tunable diode probe laser is added to the heterodyne setup shown in Fig. 6.11. While the pump laser is set on resonance with the optical mode, the probe laser is repeatedly swept at 100 Hz across the optical resonance. The transmitted optical photodetector signal is low-pass filtered (filter bandwidth = 20 kHz) and averaged 256 times on an oscilloscope in order obtain the optical cavity spectrum, free from any potential modulation due to the Brillouin lasing process.

Fig. 6.18 shows the optical resonance measured with this pump-probe setup. With the pump laser off (Fig. 6.18(a)), the optical mode appears non-split. Next, the pump laser is switched on, injecting 5 μW of optical power. Since the pump power is above threshold, this initiates spontaneous Brillouin lasing, as verified through the reflected light power spectrum. Due to the large refractive index grating generated by the Brillouin lasing process, the probe laser now detects two distinct cavity resonances (Fig. 6.18(a)): a lower frequency resonance (red) sensing the peaks of the superfluid Brillouin wave, and a higher frequency resonance (blue) —spatially shifted by $\lambda_B/2$— sensing the troughs, see inset of Fig. 6.18(b). The magnitude of

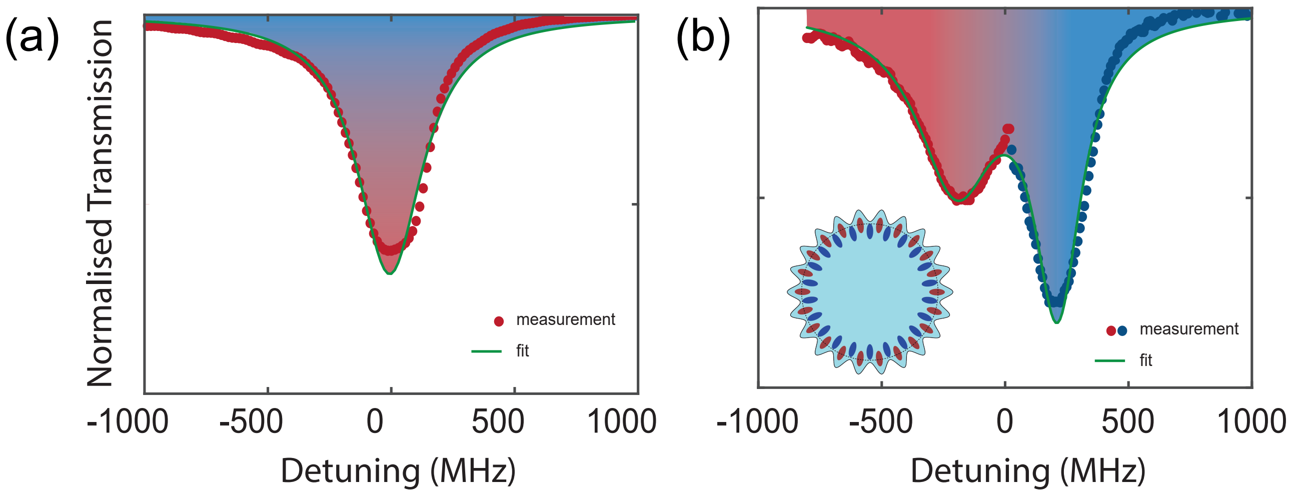

Figure 6.18: (a) With the pump laser off, the optical mode measured by the probe beam is non-split. (b) At 5 μW pump power, the lasing of Brillouin wave splits the optical mode into a doublet.

the splitting provides the coupling rate $(g_{\mathrm{opt}}/2\pi)$=187 MHz, larger than the intrinsic linewidth of the optical mode.

In contrast to solid systems where optical modes are separated by many GHz (i.e. large Δ), here the combination of a compliant low-frequency fluid interface with the high optomechanical coupling rate afforded by microscale confinement enables, for the first time, the observation of mechanically-mediated strong optical coupling between degenerate modes. This could open up the possibilities of low power, superfluid based, optical switches and reconfigurable optical circuits [184].

6.4.6 Orthogonality of WGMs in Brillouin Mediated Strong Coupling

The whispering gallery modes form the complete orthogonal eigenmode bases of the electromagnetic field confined inside the optical resonator. Because of this orthogonality, the superfluid surface deformation (and its associated refractive index modulation) caused by driving one WGM should in principle leave other WGMs unaffected. This is indeed what we observe in the experiments. Fig. 6.19(a) shows a transmission spectrum of our microresonator, with the WGM used in the experiments (m = 186) highlighted in red. The WGM of the same mode family with the next azimuthal order (m+1 = 187), separated from the first by a free spectral range, is highlighted in green. Using the pump-probe setup shown in Fig. 6.11, we use the strong pump tuned to the m WGM to initiate Brillouin lasing. In this regime, the weak probe scanned over the m WGM reveals a doublet splitting (Fig. 6.19(b)), a manifestation of the strong coupling between forwards and backwards propagating directions mediated by the superfluid index grating. In contrast, sweeping over the adjacent $m + 1$ WGM in the same lasing regime shows this mode remains unaffected and maintains its Lorentzian shape, see Fig. 6.19(c).

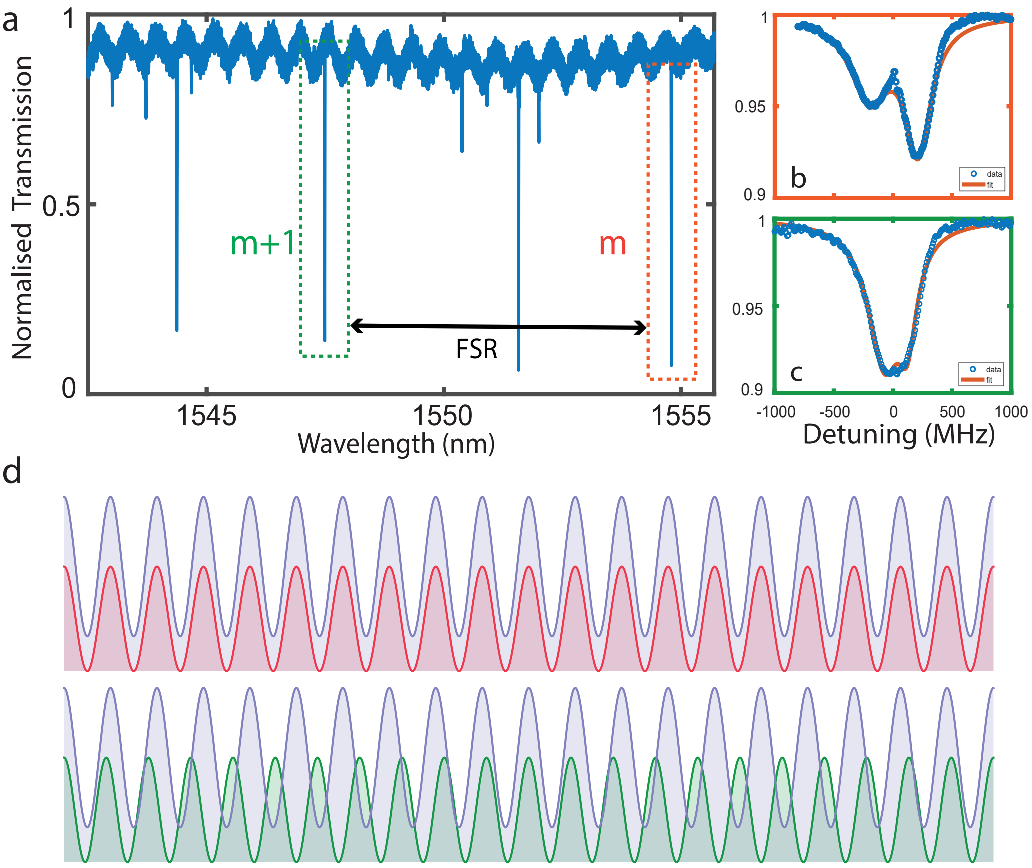

Figure 6.19: a) Normalized cavity transmission spectrum, showing the optical mode used in the experiments ($m = 186$) near 1555 nm (dashed red box), along with the next azimuthal order WGM ($m + 1 = 187$) separated in wavelength by an FSR (dashed green box). In the presence of the strong refractive index grating created by pumping mode m above the Brillouin lasing threshold, the adjacent optical mode $m + 1$ measured by the probe laser remains unsplit (b), while the pumped mode reveals strong mechanically induced optical coupling (c). d) Schematic illustration of mode orthogonality between mode $m = 10$ (red) and its associated refractive index modulation (blue) and mode $m + 1 = 11$ (green).

A schematic illustration of this orthogonality is shown in Fig. 6.19(d), with lower azimuthal orders plotted here for clarity. The top panel shows the intensity profile, proportional to E^2, of the $m = 10$ WGM along the circumference of the resonator (red), along with the associated superfluid film deformation generated by the Brillouin scattering process (blue). The lower panel shows this same surface deformation (blue) along with the field intensity of the $m+1 = 11$ WGM. Because of the WGM orthogonality, the refractive index modulation created by mode m leads to net change in optical path length for the $m + 1$ WGM, and hence no energy shift (Eq. (6.6)) and a zero g_0 and g_{opt}, (see § 6.2.6).

6.5 Conclusion

This chapter describes the experiment of ultra-low threshold Brillouin lasing based on the superfluid optomechanical disk resonator. First the research background of Brillouin lasers is reviewed, with platforms from optical fibers to silicon nanowires, from nonlinear optical waveguides to optical resonators, with materials from solid to liquid, etc. The advantages and disadvantages of different platforms and materials are compared. For example, compared with conventional optical fiber and waveguide Brillouin systems, As_2S_3 nonlinear optical waveguides and silicon suspended optomechanical waveguides of higher Brillouin nonlinearity are intensively investigated for integrated Brillouin laser applications. Compared with solid materials, liquid materials have advantages like low speed of sound which leads to the low Brillouin shift, and large mechanical compliance which leads to the large coupling rate. The research background summary gives a broad view of this field, and helps us find the motivation for realizing Brillouin lasing in the superfluid optomechanical system.

Following the research background of Brillouin scattering, the theoretical modelling and experimental results of the superfluid Brillouin optomechanical system are described. In the theoretical modelling part we develop the interaction Hamiltonian for the intracavity optical field and the superfluid third sound based on the perturbation theory, which manifests the essence of the physics of this experiment. In order to quantify the Brillouin interaction strength, we numerically calculate the radiation pressure single photon optomechanical coupling rate $g_{0,\mathrm{rp}}$ to be 11 kHz based on the experimental parameters of the superfluid optomechanical disk resonator. In addition to the theoretical modelling, we introduce the experimental setup of the heterodyne measurement of the Brillouin backscattered light. With this setup, we first show that the optical frequency shift per unit mechanical displacement $G/2\pi$ can be measured by decreasing the cryostat temperature through the superfluid transition temperature. Second, we demonstrate that by tuning the taper-cavity coupling rate to change the intracavity field from standing to travelling wave, we can transition from standard optomechanics to travelling Brillouin optomechanics. This is shown by the experimental result that the difference between Stokes and anti-Stokes sidebands is only 2 dB with weak taper-cavity coupling, whereas the difference is 33 dB when the taper-cavity coupling is strong. Third, by measuring the power spectra of the Stokes sideband at different input laser power, we determine the Brillouin lasing threshold of 1.8 μW, and the measured linear relation between the Stokes sideband linewidth and input optical power agrees very well with Eq. (6.26) obtained from the analytical approach. Furthermore, we perform full numerical simulation of the nonlinear equations of motion which take into account the native resonator backscattering. Combining the experimental results of the Stokes linewidth and the numerical simulation the photothermal optomechanical coupling rate $g_{0,\mathrm{pt}}$ and the native resonator backscattering parameter ξ are determined to be 122 kHz and 0.2, respectively. Last, taking advantage of the ultra-strong Brillouin interaction in the superfluid optomechanical system, we demonstrate that the Brillouin backscattering can mediate strong coupling of the two counter-propagating degenerate optical modes. The experimental results show that with high pump laser power the optical mode displays normal mode splitting larger than the intrinsic optical linewidth.

Further improvements for the superfluid Brillouin experiment are possible, although the

Brillouin lasing threshold is already the lowest in the literature. First of all, lowering the acoustic dissipation and optical linewidth by smoothing the sidewall of our current devices could reduce the threshold power into picowatt range. Second, depending on whether future experiments investigate quantum or classical applications, the photothermal optomechanical coupling should be correspondingly reduced or enhanced. For example, one possible solution to reduce the photothermal effect is to utilize the optical resonator made of a circular slot-waveguide, where the optical field and superfluid co-locate in the slot between the dielectric material. Using the slot-waveguide ring resonators, the optical absorption of the resonator material can be minimized. Furthermore, the native backscattering due to the resonator geometry imperfections can be avoided with better nano fabrication technique. Without the native backscattering, the Brillouin lasing threshold can be further reduced, and the system can have potential applications, such as non-reciprocal optical devices and precision Brillouin gyroscopes.

Chapter 7

Conclusion

In this thesis I have presented the research work on superfluid optomechanics, where the techniques of cavity optomechanics are leveraged to probe the superfluid excitations, such as third sound and vortices. Owing to the strong coupling between light and superfluid motion in this system, it can be potentially used to cool sound modes down to their energy ground state, and to detect single quantized vortices in a nm-thick superfluid film. These potential applications can help people understand the physics of strongly-interacting superfluids, which has not been well studied.

7.1 Summary

Chapter 1 introduces the essence of cavity optomechanics. This chapter also presents the motivations and brief overview (*e.g.* high precision sensing and macroscopic quantum state generation, etc.) for the research in this field. Based on conventional optomechanical systems, a superfluid optomechanical system is introduced, where the advantages of superfluid helium expand the technique of cavity optomechanics to a new and unexplored field.

Chapter 2 briefly summarizes several very useful experimental concepts and techniques, such as shot noise and detection methods (§ 2.3), optical cavities with the coupled mode theory and the input-output relation (§ 2.4), frequency locking methods (§ 2.6), and the nanofabrication process for on-chip WGM resonators (§ 2.7).

Chapter 3 goes through the basic concepts and theories for cavity optomechanics and superfluid. We first formally introduces the canonical quantization respectively for a mechanical oscillator and a single cavity optical mode (§ 3.1.1). Based on the separate Hamiltonians for the mechanical oscillator and the cavity mode, we introduce the optomechanical interaction Hamiltonian for a Fabry-Perot cavity with a movable mirror (§ 3.1.2). Then the equations of motion are derived from the full optomechanical Hamiltonian. We solve the equations of motion for both the steady state (§ 3.1.4) and the dynamics (§ 3.1.5), and present several characteristic phenomena of cavity optomechanics, including optomechanical bistability, optical spring effect, optomechanical cooling, optomechanically induced transparency/ amplification, which are widely observed in experiments and are useful to calibrate optomechanical systems. Then the spectral analysis of the dynamical solution of the equations of motion is introduced (§ 3.1.5). Furthermore we go through the phenomenological description of superfluid helium (§ 3.2), derive the wave equation for third sound acoustic waves on the surface of a thin superfluid film (§ 3.2.3), and briefly explains the quantization of circulation (quantized vortices) in a thin superfluid film (§ 3.2.4).

Chapter 4 presents the experimental work on the superfluid enhanced optical force. The optical force is termed photoconvective force, which mediated by the superfluid fountain effect, where the helium atoms flow toward the optically heated region and evaporate. The photoconvective force resulted from the recoil of the evaporated helium atom is estimated to be one order of magnitude larger than radiation pressure force given the optical cavity condition (§ 4.2). Then a homodyne detection setup is used to measure a mechanical mode of the microtoroid resonator. By monitoring this mechanical mode we are able to calibrate the mode temperature, which is also used as the thermometer for the cryostat (§ 4.4.1). Next, the driven response of the optical force is measured at temperatures both above and below the superfluid transition temperature, showing that the photoconvective force is 11 times larger than the radiation pressure force (§ 4.4.2). Last, feedback cooling of the mechanical mode is performed using the strong photoconvective force, and we show that the phonon occupancy of the mechanical mode can be cooled down to of 2110 ± 40 (§ 4.4.3).

Chapter 5 presents the work on an optomechanical system composed of a WGM resonator and surface acoustic waves on the thin superfluid film coated on the resonator. We first theoretically estimate the optomechanical coupling rate based on the mode perturbation theory, showing that the optical frequency shift per unit mechanical displacement (G) can be up to 6 GHz/nm (§ 5.2.1). Then the acoustic modes confined on the circular geometry of the resonator are analysed and the zero point motion of the acoustic modes is calculated (§ 5.2.2). Based on the G and the zero point motion, the single optomechanical coupling rate can be larger than the mechanical frequency of the acoustic waves (§ 5.2.3). Using this high performance superfluid optomechanical system we theoretically and experimentally demonstrate that vortex dynamics in the thin superfluid film can be probed by monitoring the frequency splittings of the acoustics waves, and the experimental result shows the coherent evolution of 17 vortices (§ 5.3.1).

Chapter 6 presents the experiment on the ultra-low threshold Brillouin lasing in a thin superfluid film. We first introduce the background and state of the art of Brillouin scattering systems (§ 6.1). Then based on the coupled mode theorem the dynamics of the superfluid Brillouin system with a WGM disk resonator is theoretically modelled, showing that the acoustic wave travelling in the same direction with the pump field will be amplified, and the acoustic linewidth linearly decreases with the pump power, eventually leading to Brillouin lasing (§ 6.2). In the experiment, we first calibrate the film thickness from two independent methods:

the optical frequency shift from a given G, and the acoustic frequency shift. From this we also confirm the G to be 2.17 GHz/nm. Then the Brillouin acoustic mode is measured using a heterodyne detection setup. The Brillouin lasing threshold is observed at 1.8 μW, which gives a radiation pressure $g_{0,rp}$ of 11 kHz, and a photothermal $g_{0,pt}$ of 122 kHz. In addition, we demonstrate the transition from conventional optomechanics to Brillouin optomechanics by tuning the intracavity optical field from standing wave to travelling wave, with the tuning implemented by changing taper-cavity coupling strength. Last, the experiment also shows that the Brillouin wave with large amplitude is able to mediate the strong coupling between the direction-degenerate optical modes (§ 6.3).

7.2 Future Outlook

Here in this section I mention two possible improvements to the current superfluid optomechanics experiment in our lab.

Being able to probe and control surface acoustic waves on a thin superfluid film is truly one of the great advantages of this experiment. Based on this capability, we have demonstrated cooling and Brillouin lasing of the surface acoustic modes, and by optimizing the system parameters we would be able to demonstrate ground state cooling of the surface acoustic modes, detect quantized vortices, and study topological phase transition in strongly interacting superfluids. These potential applications make this optomechanical system really a fantastic platform to study the interdisciplinary field between quantum physics and condense matter physics. Whereas, due to the double-edge sword of the thin superfluid film's self-assembling nature, the boundary condition of the acoustic modes might be dependent on the pedestal of the WGM resonator. This is not a clearly defined boundary condition, and leads to several painful issues in the experiment. First, there are many "unexpected" modes appearing in the acoustic mode spectrum. Second, the Bessel type acoustic modes defined by the circular geometry of the WGM resonator are valid for sure, but need some corrections. Third, the unclear boundary condition also limits the mechanical Q of the acoustic modes. Fourth, this also hinders future experiments, since the effective mass of the modes might be hard to calibrate. Thus, I think it is really necessary to "carve" some pattern (or design some thin tethers) on the WGM resonator to isolate the superfluid film which interacts with the optical field away from the rest of the film in the sample chamber.

The second point we can improve in the current experiment is the photothermal effect due to optical absorption in the silica resonator. Although the superfluid fountain effect can make the photothermal effect here more efficient, such that the photothermal interaction in our superfluid experiment is less non-unitary, it is still necessary to minimize the photothermal effect. There are several options to do so. For example, we can design certain type of optical cavity where light is confined in the vacuum within the dielectric material, such that the optical absorption only happens with the weak evanescent field in the dielectric material. Another example would be superconducting LC cavities like the electromechanical system with a drum capacitor in the References [9, 191], although the optomechanical coupling strength may be sacrificed to some extent due to the low dielectric constant of liquid helium.

Bibliography

[1] D. McAuslan, G. Harris, C. Baker, Y. Sachkou, X. He, E. Sheridan, and W. Bowen. Microphotonic Forces from Superfluid Flow. *Physical Review X*, 6(2):021012, 2016.

[2] C. Baker, G. Harris, D. McAuslan, Y. Sachkou, X. He, and W. Bowen. Theoretical framework for thin film superfluid optomechanics: Towards the quantum regime. *New Journal of Physics*, 18(12):0–12, 2016.

[3] S. Forstner, Y. Sachkou, M. Woolley, G. I. Harris, X. He, W. P. Bowen, and C. G. Baker. Modelling of vorticity, sound and their interaction in two-dimensional superfluids. *New Journal of Physics*, 21(5):053029, 2019.

[4] X. He, G. I. Harris, C. G. Baker, A. Sawadsky, Y. L. Sfendla, Y. P. Sachkou, S. Forstner, and W. P. Bowen. Strong optical coupling through superfluid Brillouin lasing. 2019.

[5] Y. P. Sachkou, C. G. Baker, G. I. Harris, O. R. Stockdale, S. Forstner, M. T. Reeves, X. He, D. L. McAuslan, A. S. Bradley, M. J. Davis, and W. P. Bowen. Coherent vortex dynamics in a strongly-interacting superfluid on a silicon chip. 2019.

[6] J. Chaste, A. Eichler, J. Moser, G. Ceballos, R. Rurali, and A. Bachtold. A nanomechanical mass sensor with yoctogram resolution. *Nature Nanotechnology*, 7(5):301–304, 2012.

[7] G. I. Harris, D. L. McAuslan, T. M. Stace, A. C. Doherty, and W. P. Bowen. Minimum Requirements for Feedback Enhanced Force Sensing. *Physical Review Letters*, 111(10):103603, 2013.

[8] B. P. Abbott and ... Observation of Gravitational Waves from a Binary Black Hole Merger. *Physical Review Letters*, 116(6):061102, 2016.

[9] J. D. Teufel, T. Donner, D. Li, J. W. Harlow, M. S. Allman, K. Cicak, A. J. Sirois, J. D. Whittaker, K. W. Lehnert, and R. W. Simmonds. Sideband cooling of micromechanical motion to the quantum ground state. *Nature*, 475(7356):359–363, 2011.

[10] J. Chan, T. P. M. Alegre, A. H. Safavi-Naeini, J. T. Hill, A. Krause, S. Gröblacher, M. Aspelmeyer, and O. Painter. Laser cooling of a nanomechanical oscillator into its quantum ground state. *Nature*, 478(7367):89–92, 2011.

[11] E. E. Wollman, C. U. Lei, A. J. Weinstein, J. Suh, A. Kronwald, F. Marquardt, A. A. Clerk, and K. C. Schwab. Quantum squeezing of motion in a mechanical resonator. *Science*, 349(August):952–955, 2015.

[12] J.-M. Pirkkalainen, E. Damskägg, M. Brandt, F. Massel, and M. Sillanpää. Squeezing of Quantum Noise of Motion in a Micromechanical Resonator. *Physical Review Letters*, 115(24):243601, 2015.

[13] R. Riedinger, A. Wallucks, I. Marinković, C. Löschnauer, M. Aspelmeyer, S. Hong, and S. Gröblacher. Remote quantum entanglement between two micromechanical oscillators. *Nature*, 556(7702):473–477, 2018.

[14] C. F. Ockeloen-Korppi, E. Damskägg, J.-M. Pirkkalainen, M. Asjad, A. A. Clerk, F. Massel, M. J. Woolley, and M. A. Sillanpää. Stabilized entanglement of massive mechanical oscillators. *Nature*, 556(7702):478–482, 2018.

[15] P. Kapitsa. Viscosity of Liquid Helium below the λ-Point. *Nature*, 141:74–74, 1938.

[16] L. A. De Lorenzo and K. C. Schwab. Superfluid optomechanics: Coupling of a superfluid to a superconducting condensate. *New Journal of Physics*, 16:2–5, 2014.

[17] A. D. Kashkanova, A. B. Shkarin, C. D. Brown, N. E. Flowers-Jacobs, L. Childress, S. W. Hoch, L. Hohmann, K. Ott, J. Reichel, and J. G. E. Harris. Superfluid Brillouin optomechanics. *Nature Physics*, 13(1):74–79, 2016.

[18] G. I. Harris, D. L. Mcauslan, E. Sheridan, Y. Sachkou, C. Baker, and W. P. Bowen. Laser cooling and control of excitations in superfluid helium. *Nature Physics*, 1506:4542, 2016.

[19] J. M. Kosterlitz and D. J. Thouless. Ordering, metastability and phase transitions in two-dimensional systems. *Journal of Physics C: Solid State Physics*, 6(7):1181–1203, 1973.

[20] Z. Hadzibabic, P. Krüger, M. Cheneau, B. Battelier, and J. Dalibard. Berezinskii–Kosterlitz–Thouless crossover in a trapped atomic gas. *Nature*, 441(7097):1118–1121, 2006.

[21] C. F. Barenghi, L. Skrbek, and K. R. Sreenivasan. Introduction to quantum turbulence. *Proceedings of the National Academy of Sciences of the United States of America*, 111 Suppl:4647–52, 2014.

[22] E. J. Yarmchuk, M. J. V. Gordon, and R. E. Packard. Observation of Stationary Vortex Arrays in Rotating Superfluid Helium. *Physical Review Letters*, 43(3):214–217, 1979.

[23] N. G. Parker, N. P. Proukakis, C. F. Barenghi, and C. S. Adams. Controlled Vortex-Sound Interactions in Atomic Bose-Einstein Condensates. *Physical Review Letters*, 92(16):160403, 2004.

[24] G. Wlazłowski, K. Sekizawa, P. Magierski, A. Bulgac, and M. M. Forbes. Vortex Pinning and Dynamics in the Neutron Star Crust. *Physical Review Letters*, 117(23):232701, 2016.

[25] K. J. Blow, R. Loudon, S. J. D. Phoenix, and T. J. Shepherd. Continuum fields in quantum optics. *Physical Review A*, 42(7):4102–4114, 1990.

[26] H. A. Bachor and T. C. Ralph. *A guide to experiments in quantum optics.* 2004.

[27] C. Shannon. Communication in the Presence of Noise. *Proceedings of the IRE*, 37(1):10–21, 1949.

[28] M. Fox. *Quantum Optics: An Introduction.* Oxford Master Series in Physics. OUP Oxford, 2006.

[29] A. M. Jayich, J. C. Sankey, B. M. Zwickl, C. Yang, J. D. Thompson, S. M. Girvin, A. A. Clerk, F. Marquardt, and J. G. E. Harris. Dispersive optomechanics: a membrane inside a cavity. *New Journal of Physics*, 10(9):095008, 2008.

[30] D. J. Wilson, C. A. Regal, S. B. Papp, and H. J. Kimble. Cavity Optomechanics with Stoichiometric SiN Films. *Physical Review Letters*, 103(20):207204, 2009.

[31] D. Hunger, T. Steinmetz, Y. Colombe, C. Deutsch, T. W. Hänsch, and J. Reichel. A fiber Fabry–Perot cavity with high finesse. *New Journal of Physics*, 12(6):065038, 2010.

[32] M. Cai, O. Painter, and K. J. Vahala. Observation of Critical Coupling in a Fiber Taper to a Silica-Microsphere Whispering-Gallery Mode System. *Physical Review Letters*, 85(1):74–77, 2000.

[33] E. M. Purcell, H. C. Torrey, and R. V. Pound. Resonance Absorption by Nuclear Magnetic Moments in a Solid. *Physical Review*, 69(1-2):37–38, 1946.

[34] D. W. Vernooy, A. Furusawa, N. P. Georgiades, V. S. Ilchenko, and H. J. Kimble. Cavity QED with high-Q whispering gallery modes. *Physical Review A*, 57(4):R2293–R2296, 1998.

[35] D. Armani, B. Min, A. Martin, and K. J. Vahala. Electrical thermo-optic tuning of ultrahigh-Q microtoroid resonators. *Applied Physics Letters*, 85(22):5439–5441, 2004.

[36] T. J. Johnson, M. Borselli, and O. Painter. Self-induced optical modulation of the transmission through a high-Q silicon microdisk resonator. *Optics Express*, 14(2):817, 2006.

[37] K. H. Lee, T. G. McRae, G. I. Harris, J. Knittel, and W. P. Bowen. Cooling and control of a cavity optoelectromechanical system. *Physical Review Letters*, 104(12):1–4, 2010.

[38] L. Ding, C. Baker, P. Senellart, A. Lemaitre, S. Ducci, G. Leo, and I. Favero. High Frequency GaAs Nano-Optomechanical Disk Resonator. *Physical Review Letters*, 105(26):263903, 2010.

[39] S. Forstner, S. Prams, J. Knittel, E. D. van Ooijen, J. D. Swaim, G. I. Harris, A. Szorkovszky, W. P. Bowen, and H. Rubinsztein-Dunlop. Cavity Optomechanical Magnetometer. *Physical Review Letters*, 108(12):120801, 2012.

[40] M. T. Hill, H. J. S. Dorren, T. de Vries, X. J. M. Leijtens, J. H. den Besten, B. Smalbrugge, Y.-S. Oei, H. Binsma, G.-D. Khoe, and M. K. Smit. A fast low-power optical memory based on coupled micro-ring lasers. *Nature*, 432(7014):206–209, 2004.

[41] W. R. Headley, G. T. Reed, S. Howe, A. Liu, and M. Paniccia. Polarization-independent optical racetrack resonators using rib waveguides on silicon-on-insulator. *Applied Physics Letters*, 85(23):5523–5525, 2004.

[42] M. Borselli, T. J. Johnson, and O. Painter. Beyond the Rayleigh scattering limit in high-Q silicon microdisks: theory and experiment. *Optics Express*, 13(5):1515, 2005.

[43] J. J. Sakurai and J. Napolitano. *Modern Quantum Mechanics.* Cambridge University Press, 2nd edition, 2017.

[44] C. Tapalian, J.-P. Laine, and P. A. Lane. Thermo-optical switches using coated microsphere resonators. *MRS Proceedings*, 694:K3.9, 2001.

[45] C. Baker, S. Stapfner, D. Parrain, S. Ducci, G. Leo, E. M. Weig, and I. Favero. Optical instability and self-pulsing in silicon nitride whispering gallery resonators. *Optics Express*, 20(27):29076, 2012.

[46] E. D. Black. An introduction to Pound–Drever–Hall laser frequency stabilization. *American Journal of Physics*, 69(1):79–87, 2001.

[47] A. J. Maker and A. M. Armani. Fabrication of silica ultra high quality factor microresonators. *Journal of visualized experiments : JoVE*, (65), 2012.

[48] C. Gerry and P. Knight. *Introductory Quantum Optics.* Cambridge University Press, 2004.

[49] D. F. Walls and G. J. Milburn. *Quantum optics.* Springer Berlin, 2nd edition, 2008.

[50] M. Aspelmeyer, T. J. Kippenberg, and F. Marquard. Cavity optomechanics. *Reviews of Modern Physics*, 86(4):1391–1452, 2014.

[51] C. Gardiner and P. Zoller. *Quantum Noise: A Handbook of Markovian and Non-Markovian Quantum Stochastic Methods with Applications to Quantum Optics.* Springer Series in Synergetics. Springer, 2004.

[52] W. P. Bowen and G. J. Milburn. *Quantum optomechanics.* CRC Press, 2015.

[53] T. P. Purdy, K. E. Grutter, K. Srinivasan, and J. M. Taylor. Observation of Optomechanical Quantum Correlations at Room Temperature. pages 1–13, 2016.

[54] F. Lecocq, J. B. Clark, R. W. Simmonds, J. Aumentado, and J. D. Teufel. Mechanically mediated microwave frequency conversion in the quantum regime. pages 1–5, 2015.

[55] K. Stannigel, P. Rabl, A. S. Sørensen, P. Zoller, and M. D. Lukin. Optomechanical Transducers for Long-Distance Quantum Communication. *Physical Review Letters*, 105(22):220501, 2010.

[56] M. Schmidt, M. Ludwig, and F. Marquardt. Optomechanical circuits for nanomechanical continuous variable quantum state processing. *New Journal of Physics*, 14(12):125005, 2012.

[57] M. J. Weaver, F. Buters, F. Luna, H. Eerkens, K. Heeck, S. de Man, and D. Bouwmeester. Coherent optomechanical state transfer between disparate mechanical resonators. *Nature Communications*, 8(1):824, 2017.

[58] A. V. Oppenheim, A. S. Willsky, and S. H. Nawab. *Signals and Systems (2nd Ed.).* Prentice-Hall, Inc., 1996.

[59] R. Kubo. The fluctuation-dissipation theorem. *Reports on Progress in Physics*, 29(1):255–284, 1966.

[60] J. F. Annett. *Superconductivity, Superfluids, and Condensates.* Oxford University Press, 2004.

[61] P. C. Hohenberg. Existence of long-range order in one and two dimensions. *Physical Review*, 1967.

[62] R. J. Donnelly and C. F. Barenghi. The Observed Properties of Liquid Helium at the Saturated Vapor Pressure. *Journal of Physical and Chemical Reference Data*, 27(6):1217–1274, 1998.

[63] W. Keesom and A. Keesom. On the heat conductivity of liquid helium. *Physica*, 3(5):359–360, 1936.

[64] J. F. Allen and A. D. Misener. Flow of Liquid Helium II. *Nature*, 141:75–75, 1938.

[65] L. Tisza. Transport Phenomena in Helium II. *Nature*, 141:913, 1938.

[66] L. Landau. Theory of the Superfluidity of Helium II. *Physical Review*, 60(4):356–358, 1941.

[67] K. B. Davis, M. O. Mewes, M. R. Andrews, N. J. van Druten, D. S. Durfee, D. M. Kurn, and W. Ketterle. Bose-Einstein Condensation in a Gas of Sodium Atoms. *Physical Review Letters*, 75(22):3969–3973, 1995.

[68] E. Hoskinson, Y. Sato, I. Hahn, and R. E. Packard. Transition from phase slips to the Josephson effect in a superfluid 4He weak link. *Nature Physics*, 2(1):23–26, 2005.

[69] W. I. Glaberson and K. W. Schwarz. Quantized Vortices in Superfluid Helium-4. *Physics Today*, 40(2):54–60, 1987.

[70] B. D. Josephson. Possible new effects in superconductive tunnelling. *Physics Letters*, 1(7):251–253, 1962.

[71] R. E. Packard. The role of the Josephson-Anderson equation in superfluid helium. *Rev. Mod. Phys.*, 70(2):641–651, 1998.

[72] P. W. Anderson. Considerations on the Flow of Superfluid Helium. *Rev. Mod. Phys*, 38(2):298–310, 1966.

[73] E. Varoquaux. Anderson's considerations on the flow of superfluid helium: Some offshoots. *Reviews of Modern Physics*, 87(3), 2015.

[74] O. Avenel and E. Varoquaux. Josephson effect and quantum phase slippage in superfluids. *Physical Review Letters*, 60(5):416–419, 1988.

[75] K. Schwab, J. Steinhauer, J. C. Davis, and R. E. Packard. Fabrication of a silicon-based superfluid oscillator. *Journal of Microelectromechanical Systems*, 5(3):180–186, 1996.

[76] K. Schwab, N. Bruckner, and R. E. Packard. Detection of the Earth's rotation using superfluid phase coherence. *Nature*, 386(6625):585–587, 1997.

[77] R. E. Packard and S. Vitale. Principles of superfluid-helium gyroscopes. *Phys. Rev. B*, 46(6):3540–3549, 1992.

[78] R. W. Simmonds, A. Marchenkov, E. Hoskinson, J. C. Davis, and R. E. Packard. Quantum interference of superfluid He-3. *Nature*, 412(6842):55–58, 2001.

[79] J. C. Davis and R. E. Packard. Superfluid He-3 Josephson weak links. *Rev. Mod. Phys.*, 74(3):741–773, 2002.

[80] Y. Sato, A. Joshi, and R. Packard. Direct Measurement of Quantum Phase Gradients in Superfluid He 4 Flow. *Physical Review Letters*, 98(19):195302, 2007.

[81] J. F. Allen and H. Jones. New Phenomena Connected with Heat Flow in Helium II. *Nature*, 141(3562):243–244, 1938.

[82] S. Fisher and G. Pickett. Up the magnetic pressure. *Nature*, 444(7121):832–833, 2006.

[83] D. R. Tilley and J. Tilley. *Superfluidity and superconductivity.* CRC Press, 1990.

[84] K. R. Atkins. Third and fourth sound in liquid helium II. *Physical Review*, 113(4):962–965, 1959.

[85] J. H. Scholtz, E. O. McLean, and I. Rudnick. Third sound and the healing length of He II in films as thin as 2.1 atomic layers. *Physical Review Letters*, 32(4):147–151, 1974.

[86] C. W. F. Everitt, K. R. Atkins, and A. Denenstein. Detection of Third Sound in Liquid Helium Films. *Physical Review Letters*, 8(4):161–163, 1962.

[87] F. M. Ellis and H. Luo. Observation of the persistent-current splitting of a third-sound resonator. *Phys. Rev. B*, 39(4):2703–2706, 1989.

[88] A. M. R. Schechter, R. W. Simmonds, R. E. Packard, and J. C. Davis. Observation of 'third sound' in superfluid 3He. *Nature*, 396(6711):554–557, 1998.

[89] D. Bergman. Hydrodynamics and Third Sound in Thin He II Films. *Physical Review*, 188(1):370–384, 1969.

[90] K. Penanen and R. E. Packard. A Model for Third Sound Attenuation in Thick 4He Films. *Journal of Low Temperature Physics*, 128(1/2):25–35, 2002.

[91] S. A. Thorpe and O. M. Phillips. The Dynamics of the Upper Ocean. *The Mathematical Gazette*, 52(381):317, 2007.

[92] F. M. Ellis and L. Li. Quantum swirling of superfluid helium films. *Physical Review Letters*, 71(10):1577–1580, 1993.

[93] P. Schuck and X. Viñas. Thomas-Fermi approximation for Bose-Einstein condensates in traps. *Physical Review A*, 61(4):043603, 2000.

[94] H. Lamb. *Hydrodynamics.* Cambridge University Press, 1993.

[95] A. Schechter. *Third sound in superfluid helium-3.* PhD thesis, University of California, Berkeley, 1999.

[96] A. Vorontsov and J. A. Sauls. Spectrum of Third Sound Cavity Modes on Superfluid 3He Films. *Journal of Low Temperature Physics*, 134(3/4):1001–1008, 2004.

[97] P. J. Shirron and M. J. DiPirro. Suppression of Superfluid Film Flow in the XRS Helium Dewar. In *Advances in Cryogenic Engineering*, pages 949–956. Springer US, Boston, MA, 1998.

[98] R. Feynman. Chapter II Application of Quantum Mechanics to Liquid Helium. *Progress in Low Temperature Physics*, 1:17–53, 1955.

[99] M. Li, W. H. P. Pernice, C. Xiong, T. Baehr-Jones, M. Hochberg, and H. X. Tang. Harnessing optical forces in integrated photonic circuits. *Nature*, 456(7221):480–484, 2008.

[100] J. Roels, I. De Vlaminck, L. Lagae, B. Maes, D. Van Thourhout, and R. Baets. Tunable optical forces between nanophotonic waveguides. *Nature Nanotechnology*, 4(8):510–513, 2009.

[101] A. Ashkin and J. Dziedzic. Optical trapping and manipulation of viruses and bacteria. *Science*, 235(4795):1517–1520, 1987.

[102] M. P. MacDonald, G. C. Spalding, and K. Dholakia. Microfluidic sorting in an optical lattice. *Nature (London)*, 426(6965):421–424, 2003.

[103] H. J. Mamin and D. Rugar. Sub-attonewton force detection at millikelvin temperatures. *Applied Physics Letters*, 79(20):3358–3360, 2001.

[104] J. Chaste, A. Eichler, J. Moser, G. Ceballos, R. Rurali, and A. Bachtold. A nanomechanical mass sensor with yoctogram resolution. *Nature Nanotechnology*, 7(5):301–304, 2012.

[105] J. Rosenberg, Q. Lin, and O. Painter. Static and dynamic wavelength routing via the gradient optical force. *Nature Photonics*, 3(8):478–483, 2009.

[106] M. Bagheri, M. Poot, M. Li, W. P. H. Pernice, and H. X. Tang. Dynamic manipulation of nanomechanical resonators in the high-amplitude regime and non-volatile mechanical memory operation. *Nature nanotechnology*, 6(11):726–732, 2011.

[107] C. Orzel, A. K. Tuchman, M. L. Fenselau, M. Yasuda, and M. A. Kasevich. Squeezed States in a Bose-Einstein Condensate. 291(March):2386–2390, 2001.

[108] D. W. C. Brooks, T. Botter, S. Schreppler, T. P. Purdy, N. Brahms, and D. M. Stamper-Kurn. Non-classical light generated by quantum-noise-driven cavity optomechanics. *Nature (London)*, 488(7412):476–480, 2012.

[109] E. Verhagen, S. Deléglise, S. Weis, A. Schliesser, and T. J. Kippenberg. Quantum-coherent coupling of a mechanical oscillator to an optical cavity mode. *Nature*, 482(7383):63–67, 2012.

[110] S. M. Meenehan, J. D. Cohen, G. S. MacCabe, F. Marsili, M. D. Shaw, and O. Painter. Pulsed Excitation Dynamics of an Optomechanical Crystal Resonator near Its Quantum Ground State of Motion. *Phys. Rev. X*, 5(4):41002, 2015.

[111] I. Rudnick, H. Kojima, W. Veith, and R. S. Kagiwada. Observation of Superfluid-Helium Persistent Current by Doppler-Shifted Splitting of Fourth-Sound Resonance. *Phys. Rev. Lett.*, 23(21):1220–1223, 1969.

[112] L. Landau. Theory of the superfluidity of helium II. *Physical Review*, 1941.

[113] J. Restrepo, J. Gabelli, C. Ciuti, and I. Favero. Classical and quantum theory of photothermal cavity cooling of a mechanical oscillator. *Comptes Rendus Physique*, 12(9-10):860–870, 2011.

[114] D. S. Hyman, M. O. Scully, and A. Widom. Evaporation from Superfluid Helium. *Physical Review*, 186(1):231–238, 1969.

[115] K. Andres, R. C. Dynes, and V. Narayanamurti. Velocity Spectrum of Atoms Evaporating from a Liquid He Surface at Low Temperatures. *Physical Review A*, 8(5):2501–2506, 1973.

[116] M. Poggio, C. L. Degen, H. J. Mamin, and D. Rugar. Feedback Cooling of a Cantilever's Fundamental Mode below 5 mK. *Physical Review Letters*, 99(1):017201, 2007.

[117] M. Pinard, P. F. Cohadon, T. Briant, and A. Heidmann. Full mechanical characterization of a cold damped mirror. *Physical Review A*, 63(1):013808, 2000.

[118] C. Schäfermeier, H. Kerdoncuff, U. B. Hoff, H. Fu, A. Huck, J. Bilek, G. I. Harris, W. P. Bowen, T. Gehring, and U. L. Andersen. Quantum enhanced feedback cooling of a mechanical oscillator using nonclassical light. *Nature Communications*, 7(1):13628, 2016.

[119] G. Anetsberger, R. Rivière, A. Schliesser, O. Arcizet, and T. J. Kippenberg. Ultralow-dissipation optomechanical resonators on a chip. *Nature Photonics*, 2(10):627–633, 2008.

[120] V. B. Braginsky, Y. I. Vorontsov, and K. S. Thorne. Quantum nondemolition measurements. *Science*, 209(4456):547–557, 1980.

[121] A. Szorkovszky, A. C. Doherty, G. I. Harris, and W. P. Bowen. Mechanical squeezing via parametric amplification and weak measurement. *Physical review letters*, 107(21):213603, 2011.

[122] J. D. Thompson, B. M. Zwickl, a. M. Jayich, F. Marquardt, S. M. Girvin, and J. G. E. Harris. Strong dispersive coupling of a high-finesse cavity to a micromechanical membrane. *Nature*, 452(7183):72–5, 2008.

[123] G. A. Brawley, M. R. Vanner, P. E. Larsen, S. Schmid, A. Boisen, and W. P. Bowen. Nonlinear optomechanical measurement of mechanical motion. *Nature Communications*, 7:10988, 2016.

[124] L. F. Gomez, K. R. Ferguson, J. P. Cryan, C. Bacellar, R. M. P. Tanyag, C. Jones, S. Schorb, D. Anielski, A. Belkacem, C. Bernando, R. Boll, J. Bozek, S. Carron, G. Chen, T. Delmas, L. Englert, S. W. Epp, B. Erk, L. Foucar, R. Hartmann, A. Hexemer, M. Huth, J. Kwok, S. R. Leone, J. H. S. Ma, F. R. N. C. Maia, E. Malmerberg, S. Marchesini, D. M.

Neumark, B. Poon, J. Prell, D. Rolles, B. Rudek, A. Rudenko, M. Seifrid, K. R. Siefermann, F. P. Sturm, M. Swiggers, J. Ullrich, F. Weise, P. Zwart, C. Bostedt, O. Gessner, and A. F. Vilesov. Shapes and vorticities of superfluid helium nanodroplets. *Science*, 345(6199):906–909, 2014.

[125] E. Fonda, D. P. Meichle, N. T. Ouellette, S. Hormoz, and D. P. Lathrop. Direct observation of Kelvin waves excited by quantized vortex reconnection. *Proceedings of the National Academy of Sciences of the United States of America*, 111(Supplement 1):4707–10, 2014.

[126] G. Yang, A. Fragner, G. Koolstra, L. Ocola, D. Czaplewski, R. Schoelkopf, and D. Schuster. Coupling an Ensemble of Electrons on Superfluid Helium to a Superconducting Circuit. *Physical Review X*, 6(1):011031, 2016.

[127] G. Anetsberger, O. Arcizet, Q. P. Unterreithmeier, R. Rivière, A. Schliesser, E. M. Weig, J. P. Kotthaus, and T. J. Kippenberg. Near-field cavity optomechanics with nanomechanical oscillators. *Nature Physics*, 5(12):909–914, 2009.

[128] E. S. Sabisky and C. H. Anderson. Verification of the Lifshitz theory of the van der Waals potential using liquid-helium films. *Physical Review A*, 7(2):790–806, 1973.

[129] W. E. Keller. Thickness of the Static and the Moving Saturated He II Film. *Physical Review Letters*, 24(11):569–573, 1970.

[130] F. M. Ellis and H. Luo. Observation of the persistent-current splitting of a third-sound resonator. *Physical Review B*, 39(4):2703, 1989.

[131] Jing Wang, Z. Ren, and C.-C. Nguyen. 1.156-GHz self-aligned vibrating micromechanical disk resonator. *IEEE Transactions on Ultrasonics, Ferroelectrics and Frequency Control*, 51(12):1607–1628, 2004.

[132] S. Gröblacher, K. Hammerer, M. R. Vanner, and M. Aspelmeyer. Observation of strong coupling between a micromechanical resonator and an optical cavity field. *Nature*, 460(7256):724–727, 2009.

[133] D. Bishop and J. Reppy. Study of the Superfluid Transition in Two-Dimensional He4 Films. *Physical Review Letters*, 40(26):1727–1730, 1978.

[134] L. Onsager. Statistical hydrodynamics. *Il Nuovo Cimento*, 6(S2):279–287, 1949.

[135] G. Gauthier, M. T. Reeves, X. Yu, A. S. Bradley, M. A. Baker, T. A. Bell, H. Rubinsztein-Dunlop, M. J. Davis, and T. W. Neely. Giant vortex clusters in a two-dimensional quantum fluid. *Science*, 364(6447):1264–1267, 2019.

[136] N. Navon, A. L. Gaunt, R. P. Smith, and Z. Hadzibabic. Critical dynamics of spontaneous symmetry breaking in a homogeneous Bose gas. *Science*, 347(6218):167–170, 2015.

[137] P. W. Anderson and N. Itoh. Pulsar glitches and restlessness as a hard superfluidity phenomenon. *Nature*, 256(5512):25–27, 1975.

[138] M. Forsch, R. Stockill, A. Wallucks, I. Marinkovic, C. Gärtner, R. A. Norte, F. van Otten, A. Fiore, K. Srinivasan, and S. Gröblacher. Microwave-to-optics conversion using a mechanical oscillator in its quantum groundstate. 2018.

[139] V. Fiore, Y. Yang, M. C. Kuzyk, R. Barbour, L. Tian, and H. Wang. Storing Optical Information as a Mechanical Excitation in a Silica Optomechanical Resonator. *Physical Review Letters*, 107(13):133601, 2011.

[140] C. Galland, N. Sangouard, N. Piro, N. Gisin, and T. J. Kippenberg. Heralded Single-Phonon Preparation, Storage, and Readout in Cavity Optomechanics. *Physical Review Letters*, 112(14):143602, 2014.

[141] C. Bekker, R. Kalra, C. Baker, and W. P. Bowen. Injection locking of an electro-optomechanical device. *Optica*, 4(10):1196, 2017.

[142] P. Kharel, G. I. Harris, E. A. Kittlaus, W. H. Renninger, N. T. Otterstrom, J. G. E. Harris, and P. T. Rakich. High-frequency cavity optomechanics using bulk acoustic phonons. *Science Advances*, 5(4):eaav0582, 2019.

[143] E. Ippen and R. Stolen. Stimulated Brillouin scattering in optical fibers. *Applied Physics Letters*, 21(11):539–541, 1972.

[144] Z. Bai, H. Yuan, Z. Liu, P. Xu, Q. Gao, R. J. Williams, O. Kitzler, R. P. Mildren, Y. Wang, and Z. Lu. Stimulated Brillouin scattering materials, experimental design and applications: A review. *Optical Materials*, 75:626–645, 2018.

[145] B. J. Eggleton, C. G. Poulton, and R. Pant. Inducing and harnessing stimulated Brillouin scattering in photonic integrated circuits. *Advances in Optics and Photonics*, 5(4):536, 2013.

[146] C. Baker, W. Hease, D.-T. Nguyen, A. Andronico, S. Ducci, G. Leo, and I. Favero. Photoelastic coupling in gallium arsenide optomechanical disk resonators. *Optics Express*, 22(12):14072, 2014.

[147] A. Feldman. Relations between electrostriction and the stress-optical effect. *Physical Review B*, 11(12):5112–5114, 1975.

[148] G. Agrawal. *Nonlinear Fiber Optics*. Elsevier Inc., 2006.

[149] T. Kippenberg, S. Spillane, B. Min, and K. Vahala. Theoretical and experimental study of stimulated and cascaded Raman scattering in ultrahigh-Q optical microcavities. *IEEE Journal of Selected Topics in Quantum Electronics*, 10(5):1219–1228, 2004.

[150] H. Lee, T. Chen, J. Li, K. Y. Yang, S. Jeon, O. Painter, and K. J. Vahala. Chemically etched ultrahigh-Q wedge-resonator on a silicon chip. *Nature Photonics*, 6(6):369–373, 2012.

[151] S. Gundavarapu, G. M. Brodnik, M. Puckett, T. Huffman, D. Bose, R. Behunin, J. Wu, T. Qiu, C. Pinho, N. Chauhan, J. Nohava, P. T. Rakich, K. D. Nelson, M. Salit, and D. J. Blumenthal. Sub-hertz fundamental linewidth photonic integrated Brillouin laser. *Nature Photonics*, 13(1):60–67, 2019.

[152] Z. Zhu, D. J. Gauthier, and R. W. Boyd. Stored light in an optical fiber via stimulated Brillouin scattering. *Science*, 318(5857):1748–50, 2007.

[153] P. Dainese, P. S. J. Russell, N. Joly, J. C. Knight, G. S. Wiederhecker, H. L. Fragnito, V. Laude, and A. Khelif. Stimulated Brillouin scattering from multi-GHz-guided acoustic phonons in nanostructured photonic crystal fibres. *Nature Physics*, 2(6):388–392, 2006.

[154] W. H. Renninger, R. O. Behunin, and P. T. Rakich. Guided-wave Brillouin scattering in air. *Optica*, 3(12):1316, 2016.

[155] R. Van Laer, B. Kuyken, D. Van Thourhout, and R. Baets. Interaction between light and highly confined hypersound in a silicon photonic nanowire. *Nature Photonics*, 9(3):199–203, 2015.

[156] B. Morrison, A. Casas-Bedoya, G. Ren, K. Vu, Y. Liu, A. Zarifi, T. G. Nguyen, D.-Y. Choi, D. Marpaung, S. J. Madden, A. Mitchell, and B. J. Eggleton. Compact Brillouin devices through hybrid integration on silicon. *Optica*, 4(8):847, 2017.

[157] R. Pant, C. G. Poulton, D.-Y. Choi, H. Mcfarlane, S. Hile, E. Li, L. Thevenaz, B. Luther-Davies, S. J. Madden, and B. J. Eggleton. On-chip stimulated Brillouin scattering. *Optics Express*, 19(9):8285, 2011.

[158] M. K. Schmidt, C. G. Poulton, G. Z. Mashanovich, G. T. Reed, B. J. Eggleton, and M. J. Steel. Suspended mid-infrared waveguides for Stimulated Brillouin Scattering. *Optics Express*, 27(4):4976, 2019.

[159] N. T. Otterstrom, R. O. Behunin, E. A. Kittlaus, Z. Wang, and P. T. Rakich. A silicon Brillouin laser. *Science*, 360(6393):1113–1116, 2018.

[160] J. Li, H. Lee, and K. J. Vahala. Microwave synthesizer using an on-chip Brillouin oscillator. *Nature Communications*, 4(1):2097, 2013.

[161] G. Bahl, M. Tomes, F. Marquardt, and T. Carmon. Observation of spontaneous Brillouin cooling. *Nature Physics*, 8(3):203–207, 2012.

[162] I. S. Grudinin, A. B. Matsko, and L. Maleki. Brillouin Lasing with a CaF2 Whispering Gallery Mode Resonator. *Physical Review Letters*, 102(4):043902, 2009.

[163] N. T. Otterstrom, R. O. Behunin, E. A. Kittlaus, and P. T. Rakich. Optomechanical Cooling in a Continuous System. *Physical Review X*, 8(4):041034, 2018.

[164] S. Nouri Jouybari. Brillouin gain enhancement in nano-scale photonic waveguide. *Photonics and Nanostructures - Fundamentals and Applications*, 29:8–14, 2018.

[165] C. G. Poulton, R. Pant, A. Byrnes, S. Fan, M. J. Steel, and B. J. Eggleton. Design for broadband on-chip isolator using stimulated Brillouin scattering in dispersion-engineered chalcogenide waveguides. *Optics Express*, 20(19):21235, 2012.

[166] M. Merklein, I. V. Kabakova, T. F. S. Büttner, D.-Y. Choi, B. Luther-Davies, S. J. Madden, and B. J. Eggleton. Enhancing and inhibiting stimulated Brillouin scattering in photonic integrated circuits. *Nature Communications*, 6(1):6396, 2015.

[167] M. Merklein, B. Stiller, K. Vu, S. J. Madden, and B. J. Eggleton. A chip-integrated coherent photonic-phononic memory. *Nature Communications*, 8(1):574, 2017.

[168] L. McKay, M. Merklein, A. C. Bedoya, A. Choudhary, M. Jenkins, C. Middleton, A. Cramer, J. Devenport, A. Klee, R. DeSalvo, and B. J. Eggleton. Brillouin-based phase shifter in a silicon waveguide. *Optica*, 6(7):907, 2019.

[169] S. M. Spillane, T. J. Kippenberg, and K. J. Vahala. Ultralow-threshold Raman laser using a spherical dielectric microcavity. *Nature*, 415(6872):621–623, 2002.

[170] D. K. Armani, T. J. Kippenberg, S. M. Spillane, and K. J. Vahala. Ultra-high-Q toroid microcavity on a chip. *Nature*, 421(6926):925–928, 2003.

[171] J. Li, M.-G. Suh, and K. Vahala. Microresonator Brillouin gyroscope. *Optica*, 4(3):346, 2017.

[172] G. Lin, S. Diallo, K. Saleh, R. Martinenghi, J.-C. Beugnot, T. Sylvestre, and Y. K. Chembo. Cascaded Brillouin lasing in monolithic barium fluoride whispering gallery mode resonators. *Applied Physics Letters*, 105(23):231103, 2014.

[173] J.-Z. Zhang and R. K. Chang. Generation and suppression of stimulated Brillouin scattering in single liquid droplets. *Journal of the Optical Society of America B*, 6(2):151, 1989.

[174] G. Bahl, K. H. Kim, W. Lee, J. Liu, X. Fan, and T. Carmon. Brillouin cavity optomechanics with microfluidic devices. *Nature communications*, 4(May):1994, 2013.

[175] A. Giorgini, S. Avino, P. Malara, P. De Natale, M. Yannai, T. Carmon, and G. Gagliardi. Stimulated Brillouin Cavity Optomechanics in Liquid Droplets. *Physical Review Letters*, 120(7):073902, 2018.

[176] R. W. Boyd. *Nonlinear Optics, Third Edition.* Academic Press, Inc., Orlando, FL, USA, 3rd edition, 2008.

[177] G. Enzian, M. Szczykulska, J. Silver, L. Del Bino, S. Zhang, I. A. Walmsley, P. Del'Haye, and M. R. Vanner. Observation of Brillouin optomechanical strong coupling with an 11 GHz mechanical mode. *Optica*, 6(1):7, 2019.

[178] C. Reinke, P. T. Rakich, Z. Wang, R. Camacho, and P. Davids. Giant Enhancement of Stimulated Brillouin Scattering in the Subwavelength Limit. *Physical Review X*, 2(1):011008, 2012.

[179] A. Ashkin, J. M. Dziedzic, J. E. Bjorkholm, and S. Chu. Observation of a single-beam gradient force optical trap for dielectric particles. *Optics Letters*, 11(5):288, 1986.

[180] Q. Lin, J. Rosenberg, X. Jiang, K. J. Vahala, and O. Painter. Mechanical Oscillation and Cooling Actuated by the Optical Gradient Force. *Physical Review Letters*, 103(10):103601, 2009.

[181] C. Wolff, R. Soref, C. Poulton, and B. Eggleton. Germanium as a material for stimulated Brillouin scattering in the mid-infrared. *Optics Express*, 22(25):30735, 2014.

[182] M. Nikles, L. Thevenaz, and P. Robert. Brillouin gain spectrum characterization in single-mode optical fibers. *Journal of Lightwave Technology*, 15(10):1842–1851, 1997.

[183] K. S. Abedin. Observation of strong stimulated Brillouin scattering in single-mode As2Se3 chalcogenide fiber. *Optics Express*, 13(25):10266, 2005.

[184] P. Zapletal, S. Walter, and F. Marquardt. Dynamically Generated Synthetic Electric Fields for Photons. 2018.

[185] C. Wolff, M. J. Steel, B. J. Eggleton, and C. G. Poulton. Stimulated Brillouin scattering in integrated photonic waveguides: Forces, scattering mechanisms, and coupled-mode analysis. *Physical Review A*, 92(1):013836, 2015.

[186] M. Tomes, F. Marquardt, G. Bahl, and T. Carmon. Quantum-mechanical theory of optomechanical Brillouin cooling. *Physical Review A - Atomic, Molecular, and Optical Physics*, 84(6), 2011.

[187] A. H. Safavi-Naeini and O. Painter. Proposal for an optomechanical traveling wave phonon–photon translator. *New Journal of Physics*, 13(1):013017, 2011.

[188] E. Gil-Santos, M. Labousse, C. Baker, A. Goetschy, W. Hease, C. Gomez, A. Lemaître, G. Leo, C. Ciuti, and I. Favero. Light-Mediated Cascaded Locking of Multiple Nano-Optomechanical Oscillators. *Physical Review Letters*, 118(6):1–6, 2017.

[189] R. J. Donnelly and C. F. Barenghi. The Observed Properties of Liquid Helium at the Saturated Vapor Pressure. *Journal of Physical and Chemical Reference Data*, 27(6):1217–1274, 1998.

[190] R. Van Laer, R. Baets, and D. Van Thourhout. Unifying Brillouin scattering and cavity optomechanics. *Physical Review A*, 93(5):1–15, 2016.

[191] K. Cicak, D. Li, J. A. Strong, M. S. Allman, F. Altomare, A. J. Sirois, J. D. Whittaker, J. D. Teufel, and R. W. Simmonds. Low-loss superconducting resonant circuits using vacuum-gap-based microwave components. *Applied Physics Letters*, 96(9):093502, 2010.

Appendix

.1 Cryogenic Designs

Cryogenic engineering takes a large amount of time for the superfluid optomechanics experiment, although it is not very critical to the physics behind the experiment. Most of the cryogenic engineering in the experiment can be categorized into two types: vacuum sealing and thermal isolation (or its opposite thermal link). Here I briefly summarize several important cryogenic designs for the superfluid optomechanics experiment.

Indium Sealing

Due to zero viscosity, superfluid helium can leak through microscopic openings that even air cannot leak through. Thus, in the experiment superfluid helium has to be generated by cooling helium gas in a specially sealed sample chamber. Usually the sealing is made by compressing a indium wire on the lip of a sample chamber lid as illustrated by the yellow circles between the sample chamber wall and the lid in Fig .1. When the indium wire is slowly compressed in the tiny gap by slowly and carefully screwing the lid onto the chamber, it forms a molecular bond with the surfaces of the sample chamber wall and lid. It is this molecular bond that seals the superfluid inside the chamber from leaking out. The indium sealing is widely used in

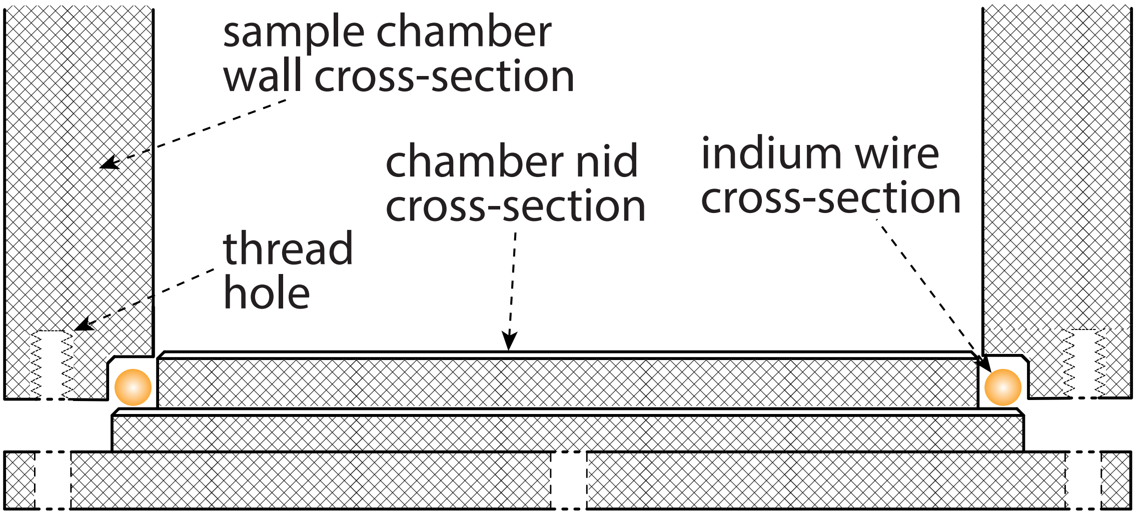

Figure .1: Illustration of the indium sealing for a superfluid-tight sample chamber.

the superfluid community, for both bulk and thin film superfluid experiments. The advantage of the indium sealing is that it is very robust to avoid superfluid leak, is easy to make, and is replaceable. The disadvantage is also obvious. It is quite hard to clean the indium sealing after the chamber is open. It is really mentally hard to clean the indium sealing many times, especially when the cryogenic setup inside the chamber is under test.

Optical/ Electrical Feedthrough

The indium sealing mentioned above is for large openings, such as sample chamber lids, windows, etc. Generally in experiments, measurements require to send certain optical and/or electrical signals into and out from the sample chamber by feeding through the corresponding optical fibers and electrical wires (*e.g.* coax cables, etc.) into the sample chamber. Ideally, it would be really great and convenient to use the vacuum feedthroughs at room temperature for cryogenic experiments. Unfortunately, often room temperature vacuum feedthroughs do not work at cryogenic temperatures due to thermal expansion/ shrinking. Although superfluid experiments have stricter requirement for feedthroughs than general experiments, I do find that in Schuster's group hermetic SMA connectors (GPO Male FD to GPO Male FD Thread-in Hermetic Feedthru by Corning Gilbert, DC-18 GHz) are used for feedthroughs of their superfluid sample chamber.

Here I only introduce a common cryogenic feedthrough solution for optical fibers and electrical wires as illustrated in Fig. .2. The yellow area is the cross-section of the sample chamber wall or the flange fixed on the sample chamber wall. Normally a several millimeter diameter opening is big enough to feed through one optical fiber or electrical wire. The first solution we try is just to glue the fiber in the opening from both sides. Although this solution works and is fairly reliable, it is still less endurable than the solution illustrated in Fig .2, where a thin stainless steel tube is laser welded at the small opening of the sample chamber. Generally laser welding between metals can be superfluid tight, but the welding process is too hot for optical

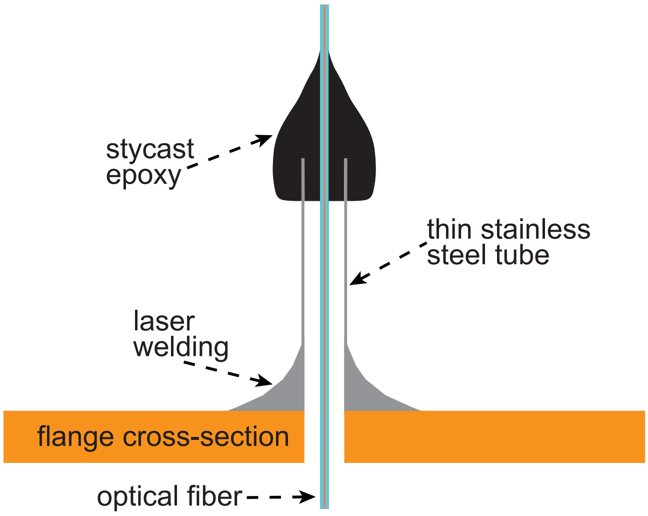

Figure .2: Illustration of optical fiber feedthrough for a superfluid-tight sample chamber.

fibers and electrical wires. With the thin stainless tube, the optical fiber can be glue at the end of the stainless tube using cryogenic Stycast epoxy. The advantage of this method of gluing is that during cool down, the Stycast epoxy will shrink a lot, but the stainless tube will not. Thus, the epoxy outside the tube will compress the tube, making it less likely to have a leak at the feedthrough region. Whereas in our first solution, when the epoxy shrinks more than the flange metal, this shear force will tear off the molecular bond between the epoxy and the flange. After several thermal cycles, leaks would happen in the feedthroughs with only epoxy.

Optical Fiber Taper Preparation

Optical fiber tapers are widely used in cavity optomechanics experiments to couple laser light from a fiber into an optical cavity. The fabrication process of fiber tapers is very mature and is standardized, but the taper used for cryogenic experiments needs a few extra cares, since the space for the experimental setup in a cryostat is usually limited, and the fragile taper has to undergo fairly large thermal shrinking during the cool-down to cryogenic temperatures. Taking into account these two factors, the fiber taper clamp has to be designed to be smaller than the ones for room temperature experiments, but not too small that the tapered region gets contaminated by the glue used to fix the fiber taper onto the clamp. For the thermal shrinking during the cool-down, the material for the taper clamp should be glass, which has roughly the same thermal expansion coefficient with the fiber core material. Additionally, from my experience the taper undergoes more thermal shrinking than the glass taper clamp, possibly due that the taper is so thin. Thus, I tension the taper a bit less for the superfluid experiments.

A: Every life is undergoing decoherence.
B: No, born to be classical!

Anonymous